9-1-1995

Construction and Characterization of an Extended Helicon Plasma Source

Russell Ford Jewett Jr.

Recommended Citation

Jewett, Russell Ford Jr.. "Construction and Characterization of an Extended Helicon Plasma Source." (1995). https://digitalrepository.unm.edu/ece_etds/461

CONSTRUCTION AND CHARACTERIZATION OF AN
EXTENDED HELCION PLASMA SOURCE - JEWETT

THE UNIVERSITY OF NEW MEXICO
ALBUQUERQUE, NEW MEXICO 87131

POLICY ON USE OF THESES AND DISSERTATIONS

Unpublished theses and dissertations accepted for master's and doctor's degrees and deposited in the University of New Mexico Library are open to the public for inspection and reference work. *They are to be used only with due regard to the rights of the authors.* The work of other authors should always be given full credit. Avoid quoting in amounts, over and beyond scholarly needs, such as might impair or destroy the property rights and financial benefits of another author.

To afford reasonable safeguards to authors, and consistent with the above principles, anyone quoting from theses and dissertations must observe the following conditions:

1. Direct quotations during the first two years after completion may be made only with the written permission of the author.
2. After a lapse of two years, theses and dissertations may be quoted without specific prior permission in works of original scholarship provided appropriate credit is given in the case of each quotation.
3. Quotations that are complete units in themselves (e.g., complete chapters or sections) in whatever form they may be reproduced and quotations of whatever length presented as primary material for their own sake (as in anthologies or books of reading) ALWAYS require consent of the authors.
4. The quoting author is responsible for determining "fair use" of material he uses.

This thesis/dissertation by Russell Ford Jewett jr. has been used by the following persons whose signatures attest their acceptance of the above conditions. (A library which borrows this thesis/dissertation for use by its patrons is expected to secure the signature of each user.)

NAME AND ADDRESS	DATE

UNIVERSITY OF NEW MEXICO
ALBUQUERQUE, NEW MEXICO 87131

POLICY ON USE OF THESES AND DISSERTATIONS

Unpublished theses and dissertations accepted for master's and doctor's degrees and deposited in the University of New Mexico Library are open to the public for inspection and reference work. *They are to be used only with due regard to the rights of the authors.* The work of other authors should always be given full credit. Avoid quoting in amounts, over and beyond scholarly needs, such as might impair or destroy the property rights and financial benefits of another author.

To afford reasonable safeguards to authors, and consistent with the above principles, anyone quoting from theses and dissertations must observe the following conditions:

1. Direct quotations during the first two years after completion may be made only with the written permission of the author.
2. After a lapse of two years, theses and dissertations may be quoted without specific prior permission in works of original scholarship provided appropriate credit is given in the case of each quotation.
3. Quotations that are complete units in themselves (e.g., complete chapters or sections) in whatever form they may be reproduced and quotations of whatever length presented as primary material for their own sake (as in anthologies or books of readings) ALWAYS require consent of the authors.
4. The quoting author is responsible for determining "fair use" of material he uses.

This thesis/dissertation by Russell Todd Jessee Jr. has been used by the following persons whose signatures attest their acceptance of the above conditions. (A library which borrows this thesis/dissertation for use by its patrons is expected to secure the signature of each user.)

NAME AND ADDRESS	DATE

Russell Ford Jewett, Jr.

Candidate

Chemical and Nuclear Engineering

Department

This dissertation is approved, and it is acceptable in quality and form for publication on microfilm:

Approved by the Dissertation Committee:

Harold M. Anderson, Chairperson

R W Boswell

Josef T Cecchi

Accepted:

Dean, Graduate School

SEP 01 1995

Date

Hanson, Ruth Janssen, MN

Candidate

Chemical and Factors Exploration

Title

This dissertation is approved, and it is acceptable in quality and form for publication on microfilm:

Approved by the Dissertation Committee:

Chairperson

Approved:

Dean, Graduate School

SEP 01 1995

Date

CONSTRUCTION AND CHARACTERIZATION OF AN EXTENDED HELICON PLASMA SOURCE

by

RUSSELL FORD JEWETT, JR.

Bachelor of Science, Physics, The University of North Carolina, 1990

DISSERTATION

Submitted in Partial Fulfillment of the
Requirements for the Degree of

DOCTOR OF PHILOSOPHY IN ENGINEERING

The University of New Mexico
Albuquerque, New Mexico

DECEMBER, 1995

For my best friend and wife,

Suzanne Jewett.

ACKNOWLEDGMENTS

The construction and characterization of a new type of plasma processing tool was a demanding task, which required technical expertise from a wide range of disciplines. This work would not have been possible without the support of my colleagues, and the sponsorship and personal attention from several organizations.

In particular I would like to recognize the following people at the University of New Mexico: Harold Anderson for his support and advice during all of my graduate work, Norm Roderick for his teaching ability, and Glen Deering for his support in the laboratory.

Rod Boswell, and his crew in Australia provided a great environment for learning about helicon plasma sources, and for starting the extended source project. Special thanks to Andrew Perry and Bert Ellingboe for their invaluable help on both experimental and theoretical techniques. Harold Persing was an excellent resource for the Langmuir probe development. Thanks to Robert Porteous for finding mistakes in my math, and to Joel Anderson and Gareth Williams for their invaluable help and friendship while constructing the first machines. And to my mate Rod Boswell, who made the Australian experience possible, I am most grateful.

I appreciate the sponsorship of the Semiconductor Research Corporation and Lam Research Corporation. Neil Benjamin and Stefano Mangano of Lam Research deserve special recognition for their inventiveness and creativity while working with me on this project. Thanks guys!

Finally, I would like to thank Suzanne Jewett for enduring all of the late nights and boring dinner conversations. She was and is my constant companion and wife.

I can only hope that my future work is blessed with such fine working colleagues and friends as these. Thank you all, again.

CONSTRUCTION AND CHARACTERIZATION OF AN EXTENDED HELICON PLASMA SOURCE

by

RUSSELL FORD JEWETT, JR.

ABSTRACT OF DISSERTATION

Submitted in Partial Fulfillment of the
Requirements for the Degree of

DOCTOR OF PHILOSOPHY IN ENGINEERING

The University of New Mexico
Albuquerque, New Mexico

DECEMBER, 1995

CONSTRUCTION AND CHARACTERIZATION OF AN EXTENDED HELICON PLASMA SOURCE

by

Russell Ford Jewett, Jr.

Bachelor of Science, Physics, The University of North Carolina, 1990

Doctor of Philosophy in Engineering, Engineering, The University of New Mexico, 1995

ABSTRACT

A new helicon source has been developed for plasma processing applications. The source is a modification of the traditional cylindrical helicon source design to rectangular geometry. In order to accomplish this, the antenna used for launching helicon waves is stretched in the direction perpendicular to the static magnetic field lines. This source was coupled to a long rectangular slab chamber which is used for the actual material processing. A static magnetic field of ~200 Gauss peak strength, pointing out from the source into the diffusion region, was applied to facilitate helicon wave propagation. 13.56 MHz rf power was used to excite the magnetized plasma along the slab, and a rectangular diffusion chamber was attached to the side of the new source.

Langmuir probes were used extensively to characterize the plasma produced in the new chamber. Careful attention was given to rf and other perturbing effects on Langmuir probe traces. Probes were constructed to minimize perturbing effects, and measurements of electron energy distribution functions, plasma and floating potentials, and density are presented for a variety of conditions. The

extended source is shown to produce large regions of 10^{12} cm^{-3} density plasma in argon under some weak magnetic field conditions.

Magnetic induction probes were used to examine the structure of waves in the extended chamber. A 10 x 10 x 50 cm source, with an appropriate antenna is shown to excite waves of 12 cm wavelength for certain magnetic field configurations. The theory of wave propagation along magnetic field lines in rectangular geometry is presented here for the first time. Favorable comparisons between the theoretical model and experimental results indicate that the model may be of use for designing improved extended sources.

This work shows that an extended helicon source can be used to generate large areas of uniform plasma in chambers of relatively small volume. Scaling of the slab source in either cylindrical ring- or rectangular-type chambers should have little effect on the physics of the source operation. Application of this technology may include areas outside of microelectronics processing, such as hardening layers for large objects, or plasma source ion implantation. Also included is a brief discussion of the work necessary to improve the applicability of this prototype tool for those plasma processing applications.

Table of Contents

LIST OF FIGURES

LIST OF TABLES

1. INTRODUCTION

The exacting fabrication processes used in the semiconductor and display manufacturing industries are driving the search for improved performance in plasma etch and deposition tools. Performance features necessary to fulfil future manufacturing needs have been identified by the Semiconductor Industry Association (SIA) and are summarized with the following list[1]:

- cost effectiveness
- manufacturability of 0.10 μm device feature sizes
- ability to process wafers as large as 400 mm
- maintenance of minimal particle counts (< 0.002 particles cm^{-2} for particles with diameters no more than 0.02 μm)
- high uniformity
- absolute process stability.

Cost effectiveness in the microelectronics market of today further requires plasma tools capable of high throughput, and hence high etch or deposition rates. But high etch rates and small feature size are opposing requirements. Processing must be done at low pressure and low plasma potential to ensure successful formation of small geometries and control over ion bombarding energies, yet must be performed in an environment containing a high density of charged particles and appropriate reactive species. In an effort to address such problems, plasma processing tool manufacturers have shifted emphasis from efforts to improve traditional parallel plate tools to implementation of less-traditional (and perhaps more exotic) types of plasma sources. The past five years have seen several commercial inductive sources introduced to the market,

including inductively coupled plasma (ICP), transformer coupled plasma (TCP), and radio frequency inductive (RFI). Electron cyclotron resonance (ECR) and helicon sources have also been introduced to the manufacturing community.

Conventional parallel plate reactors typically operate in the 10 mTorr to 50 Torr pressure regime, and achieve plasma densities of ~10^9-10^{10} cm^{-3}. Electron energy distribution functions can usually be described as Maxwellian, with ~5 eV mean electron energies[2]. Voltages of 1000V peak to peak or higher are applied to the wafer electrode at a frequency in the radio wave spectrum (RF). Power is capacitively coupled to the plasma through the wafer electrode. Electron mobility in plasmas is much larger than ion mobility, and in the process of losing electrons to walls or other conducting boundaries, the plasma develops a positive bias with respect to its surroundings. In addition, power is often coupled to the substrate through a series capacitor, requiring that the integrated ion and electron currents to the substrate must balance. A greater average voltage differential between the plasma and substrate is created in this arrangement. This average bias voltage appearing on the electrode can be as high as -500 V with respect to the chamber walls (ground). Higher processing rates are achieved by using higher powers, which result in higher bias potentials. Ions diffusing across the sheath to the substrate arrive with higher energies, and can cause device damage. As geometries get smaller, this effect becomes more important.

The "next-generation" sources are typically designed to operate in the 1 to 50 mTorr pressure regime, with increased plasma densities in the range 10^{10}-10^{13} cm^{-3}. Increased plasma density offers the capability to etch or deposit at higher

rates. Low pressure, low temperature discharges derive their usefulness from two primary features: (1) power is deposited using an external antenna coupled across a dielectric window, and (2) substrate bias and plasma production are decoupled. Mean electron energies are usually in the 2-10 eV range (which is comparable to those found in parallel plate discharges), but plasma to substrate potentials can be as low as the plasma potential (< 30 V), which minimizes damage to devices being processed. Decoupling the source and biasing supplies allows independent control over power deposited in the plasma and bias voltage between the plasma and the substrate. Higher density also means higher processing rates.

ECR, helicon and inductive sources each offer advantages over existing parallel plate tools, but deciding which source is the ideal tool for microelectronics manufacturing in the near term is more difficult. Each of these high density sources remain the subject of ongoing research. Each offers both unique advantages and unique problems to the manufacturing community. One area which previously has not been explored in depth is scaleability. As microelectronics manufacturing moves to larger substrates (as has slowly happened over the past 10 years), and as similar manufacturing techniques are applied to areas as diverse as flat-paneled displays, tool coatings, and ceramics, the need for very large area processing tools becomes more pressing. This dissertation focuses on creating a new large area source, based on existing helicon work, as a possible tool for processing very large substrates. Ideally, the new machine would have the same high density, low pressure operation characteristics as the ICP, ECR, and helicon sources discussed previously, but would also produce suitable processing plasmas over five to ten times the present area. Developing

such a tool is not simply a matter of scaling up an existing design. Rather, this task involves careful study of the present understanding of source operation and performance, and then adaptation of that knowledge to form a theoretical basis for the new design.

Boswell et al. have already successfully demonstrated the operation of a large argon helicon source called WOMBAT[3]. This being the only one of the three new sources built on such a large scale, and given helicon excitation has also been used on large scale fusion experiments, the new tool developed in this study was conceived to be based on the same excitation process. Existing helicon plasma processing designs have all been based in cylindrical geometry. Fusion experiments were done in toroidal geometry, which can also be modeled as a modified cylinder. Figure 1-1 shows a typical helicon source.[4] The usable processing area of the tool in Figure 1-1 would be ~190 cm^2, or about enough to process a 6" wafer. The new source was conceived to process substrates with an order of magnitude larger area. Rather than just a scaled version of the old source, the new source was conceived as a stretched out version of an existing design, as pictured in Figure 1-2. Helicon waves would have to be excited along a distributed length without cylindrical symmetry. Waves would propagate out from that slab source to feed a volume which no longer has cylindrical symmetry.

The new source would, of course, have to be able to produce high density plasmas at low pressure to be competitive with the sources now being brought to market. Accordingly, the goals for this project were as follows:

1. build an extended helicon source prototype suitable for testing a variety of antennas and RF power feeds,

2. determine by theory and experiment the nature of helicon wave propagation and antenna interaction in the extended source, and

3. develop suitable diagnostic tools to evaluate plasma characteristics, and hence source performance.

Figure 1-1. Conventional Helicon Source Used for Plasma Processing

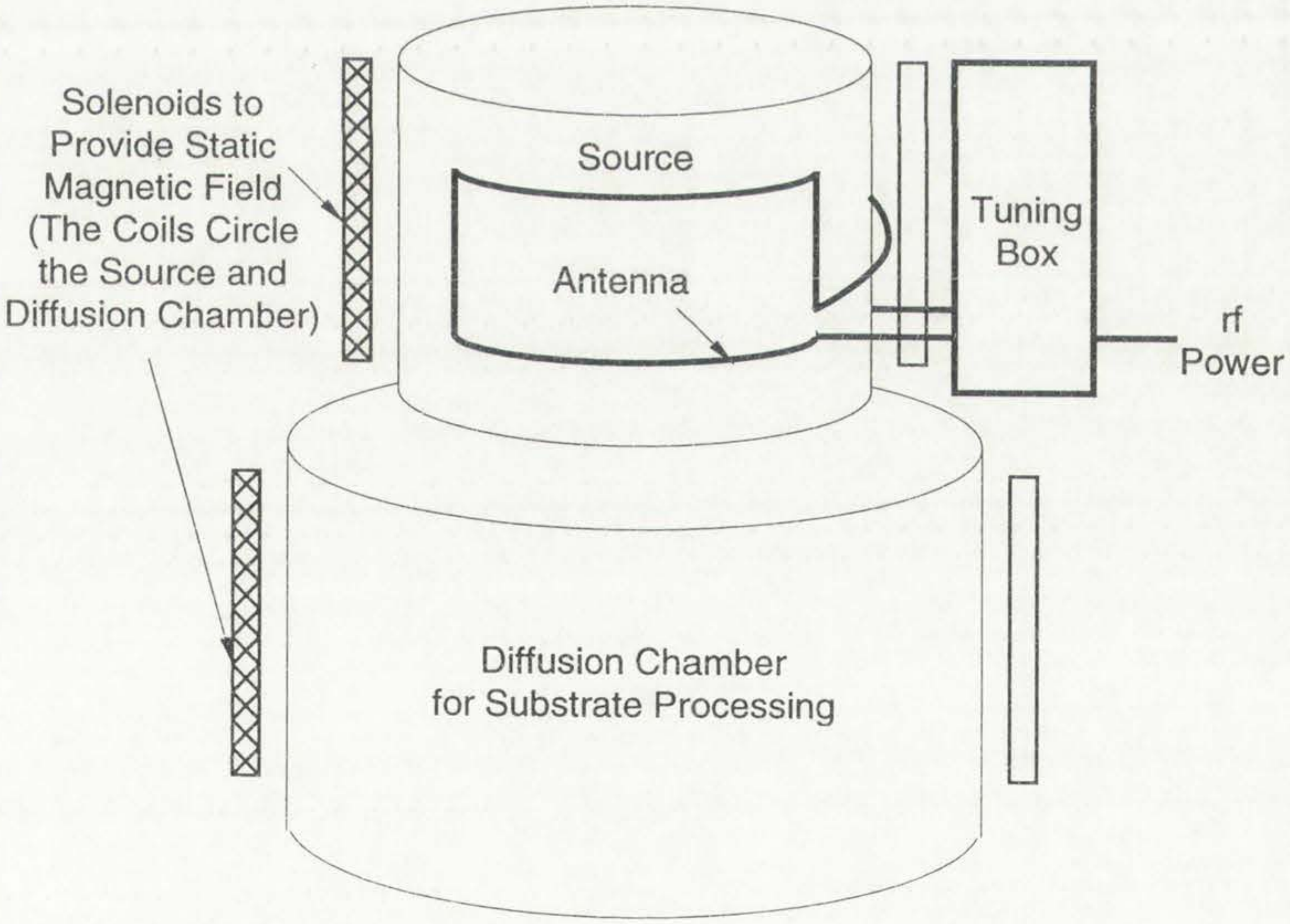

Figure 1-2. Proposed Extended Helicon Source

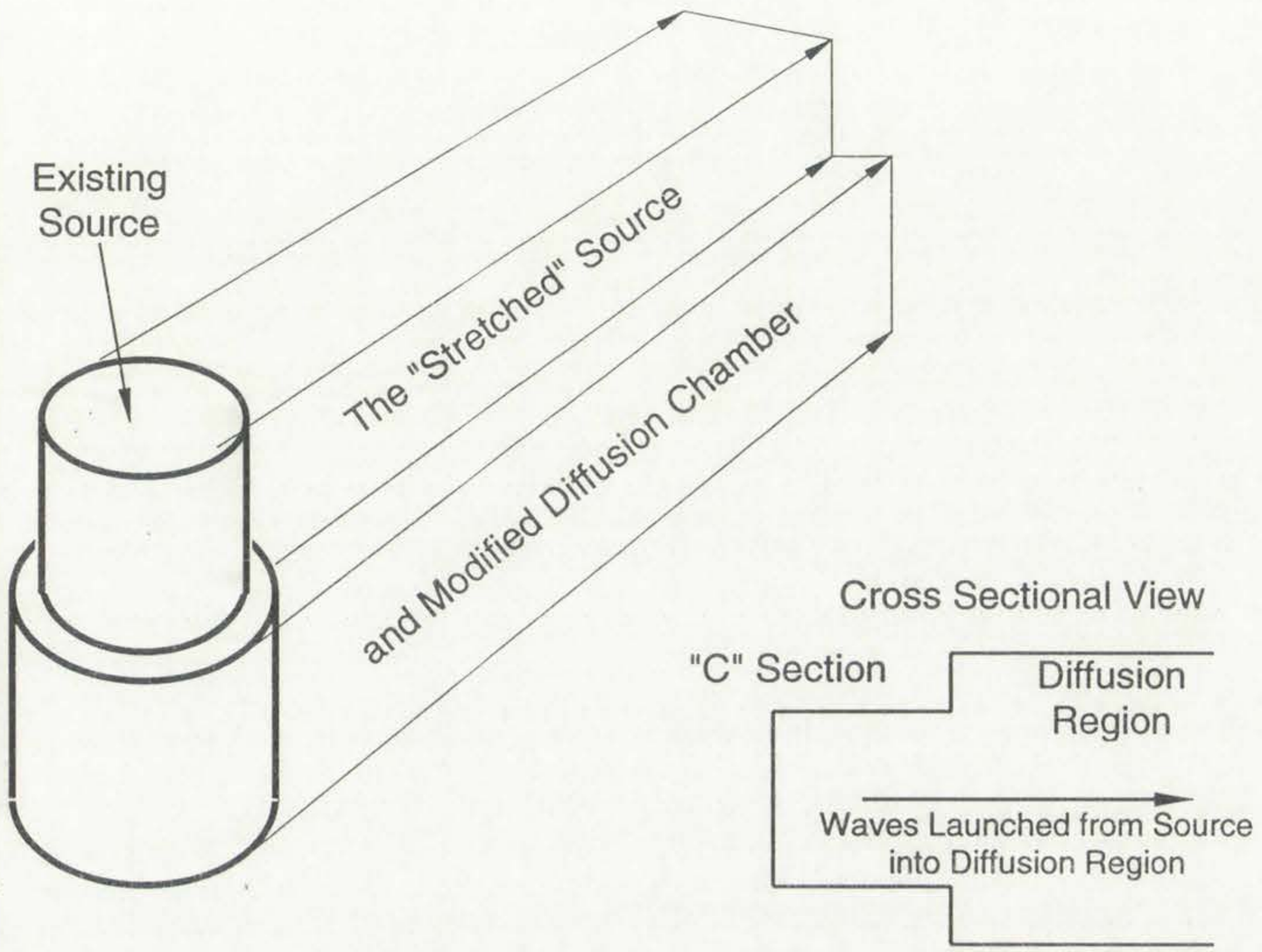

Given that the above goals could be accomplished, a set of measurement goals were also prepared to evaluate the industrial viability of the new tool. Specific measurements were outlined and are summarized as follows:

1. evaluate the production of plasma outside the source. A target density in argon of 1×10^{12} cm^{-3} measured 5 cm outside of the source opening was chosen,

2. measure uniformity along the length of the source. It was desirable to have <10% variation in density over 40 cm (measured 5 cm outside the source opening),

3. evaluate performance at several pressures. Ideally, the tool should be able to operate between 1 and 50 mTorr, and

4. address operability of source in a processing gas (CF_4) by trying to achieve 3×10^{11} cm^{-3} density in CF_4.

It was felt that achieving success in each of these goals would validate the applicability of this tool to plasma processing. In addition, success would justify further investigations of uses for this tool in semiconductor manufacturing. Given that the above objectives have been satisfied, a final goal of this project was to outline the scope of further research needed to bring this source prototype to a stage of development such that a commercial assessment can be made. The next chapter commences with a reexamination of the relevant physics of helicon waves in plasmas to better understand the performance abilities of the new system.

2. HELICON PLASMA SOURCES: THEORY AND PRACTICE

2.1 HELICON WAVES

Helicon waves were first investigated experimentally in solid state materials in the early 1960's.[5] Although the basic theory of these waves in solids was developed before 1970,[6] it was not until 1970 that the first gas plasma source predominantly excited by helicon waves was described by Boswell.[7] Since that time, they have been applied in gas laser media, gas lenses for high energy particle beams, and in plasma reactors designed for materials processing. Necessary for the understanding of the behavior of helicon sources is an understanding of what helicon waves are, and the conditions necessary for their propagation.

Helicon waves belong to the family of whistler waves, which are right-hand-circularly-polarized waves traveling along magnetic field lines in an ionized gas. The name "whistler" arises from the whistles heard on atmospheric monitoring equipment from time to time. They have been associated with the presence of thunderstorms. Lightening from these storms emits a broadband spectrum of radiation, some of which propagates to the ionosphere. The dielectric constant for whistler waves traveling along magnetic field lines in ionized gas is frequency dependent, with high frequencies traveling faster than low frequencies. A detector located some distance from the source will receive the higher frequency radiation first, and low frequencies later.[8] Two properties of the helicon wave that distinguish it from classical whistlers are (a) they are of lower frequency, and hence the motion of the guiding center of the electrons is sufficient to describe electron transport and (b) they are bounded waves.[5] (a) implies that Larmor gyrations around magnetic field lines are not important, but that the ExB drift is

the dominant factor for electron transport. In infinite geometry, helicon waves are right-hand-circularly-polarized (RHCP). It is evident that the medium in which they are observed must be birefringent; that the dispersion relations for right- and left- hand polarizations must be different. Just from this simple clarification of the naming convention, at least two requirements for the propagation of helicon waves are evident: (1) a static magnetic field must be present, and (2) the medium where the wave is found must be birefringent.

A derivation by Chen[5] shows that any magnetized plasma has a different dispersion relation for right- and left- hand waves traveling along field lines in a cylindrically bounded plasma. (A more general derivation for waves traveling at any angle with the field lines can be found in Swanson[9], but the simple treatment by Chen will be sufficient for this review). The linearized Maxwell equations are given by:

$$\nabla x \boldsymbol{E} = -\frac{\partial \boldsymbol{B}}{\partial t} \qquad (1)$$

$$\nabla x \boldsymbol{B} = \mu_0 \boldsymbol{j} \qquad (2)$$

$$\boldsymbol{E} = \boldsymbol{j} \; x \frac{\boldsymbol{B}_0}{q e n_0} \qquad (3)$$

where n_0 and $\mathbf{B}_0$ are the equilibrium density and magnetic field, and n, **B**, **E**, and **j** the perturbed density, magnetic field, electric field, and current, respectively. Using these equations implies that all of the current is carried by the guiding center motion of the electrons, which further implies that (a) the frequency ω is much higher than the lower hybrid frequency, so ion motion can be neglected,

(b) $\omega \ll \omega_c$, the electron cyclotron frequency, so that electron motion around the field lines can be neglected, and (c) the resistivity is zero. Equation (2) also assumes the displacement current is negligible. Equations (1)-(3) also imply the following:

$$\nabla \cdot \boldsymbol{B} = 0 \qquad (4)$$

$$\nabla \cdot \boldsymbol{j} = 0 \qquad (5)$$

$$\boldsymbol{j}_{\perp} = -qen_0 \frac{\boldsymbol{E} \, x \, \boldsymbol{B}_0}{B_0^2} \qquad (6)$$

A general perturbation of the form exp i(mθ + kz - ωt) is assumed. Equations (1) and (3) then give

$$i\omega \boldsymbol{B} = \nabla x \boldsymbol{E} = \nabla x \left(\frac{\boldsymbol{j} \; x \boldsymbol{B}_0}{qen_0} \right) = \frac{(\boldsymbol{B}_0 \cdot \nabla)\, \boldsymbol{j}}{qen_0} = \frac{ikB_0}{qen_0} \boldsymbol{j} \qquad (7)$$

which from (2) gives

$$\left(\frac{\omega \mu_0 qen_0}{kB_0} \right) \boldsymbol{B} = \nabla x \boldsymbol{B} \qquad (8)$$

The quantity in parenthesis in (8) will subsequently be referred to as α, and taking the curl of both sides of (8) yields the wave equation

$$\nabla^2 \boldsymbol{B} + \alpha^2 \boldsymbol{B} = 0 \qquad (9)$$

Note that substituting (9) into (2) gives

$$\mathrm{j} = \frac{\alpha}{\mu_0}\boldsymbol{B} \qquad (10)$$

which shows that the current is parallel to the perturbed magnetic field. Rendering equation (9) in cylindrical coordinates, and solving for B_z yields[5]

$$\frac{\partial^2 B_z}{\partial z^2} + \frac{1}{r}\,\frac{\partial B_z}{\partial r} + \left(\alpha^2 - k^2 - \frac{m^2}{r^2}\right) B_z = 0 \qquad (11)$$

This is Bessel's equation, and the finite solution at r=0 is

$$B_z = -2(\alpha^2 - k^2)^{-\frac{1}{2}} C J_m\left((\alpha^2 - k^2)^{\frac{1}{2}} r\right) \sin(m\theta + kz - \omega t) \qquad (12)$$

where C is a constant. Solutions for B_r and B_θ can be found by solving the appropriate portions of (9), and they are given by:

$$B_\theta = -0.5\,C(\alpha^2 - k^2)^{-\frac{1}{2}}((\alpha + k)\,J_{m-1} + (\alpha - k)\,J_{m+1})\,\sin(m\theta + kz - \omega t) \qquad (13)$$

$$B_r = 0.5\,C(\alpha^2 - k^2)^{-\frac{1}{2}}((\alpha + k)\,J_{m-1} + (\alpha - k)\,J_{m+1})\,\cos(m\theta + kz - \omega t) \qquad (14)$$

where the arguments of the Bessel functions are the same as in (12). Chen states that j_r=0 at an insulating boundary[5], so from (10), B_r=0. For a cylindrical insulating chamber of radius a, $B_r(a)$=0 yields the following two dispersion relations corresponding to the two fundamental modes (m=0,1) pictured in Figure 2-1.

$$\frac{\omega}{k} = \frac{\omega_c c^2}{\omega_p^2}\sqrt{\left(\frac{3.83}{a}\right)^2 + k^2} \qquad \text{m=0} \qquad (15)$$

$$\frac{B_0}{n_0} = \frac{q_e \mu_0 a}{3.83}\left(\frac{\omega}{k} + \frac{\omega a}{3.83^2}\right) \qquad \text{m=1} \qquad (16)$$

where c is the speed of light, ω_c is the cyclotron frequency ($^{qB}/_{m}$), and ω_p is the plasma frequency given by:

$$\omega_p = \left(\frac{n_0 q_e^2}{\varepsilon_0 m}\right)^{\frac{1}{2}} \qquad (17)$$

where ε_0 is the permittivity of free space.

Figure 2-1. m=0 and m=1 Radial Modes in Bz and B_Θ

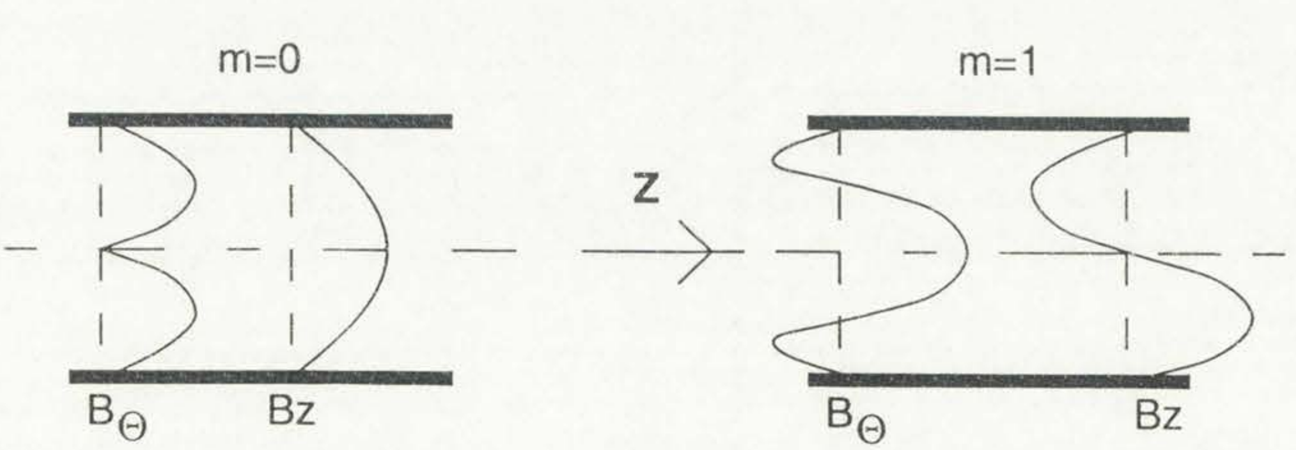

Figures 2-2 and 2-3 show the r and θ dependence of the electric field with z position for the m=0 and the m=1 modes, respectively[5]. Notice that the m=1 mode has a field pattern that does not change with position, but simply rotates as z changes to keep $\theta+kz$ a constant.

Landau damping is thought to be one of the dominant ways that a wave traveling along magnetic field lines transfers its energy to electrons in the plasma[5]. Even in the absence of collisions, electrons traveling close to the phase velocity of the wave interact with the local electric field of the wave. The wave increases the velocity of electrons traveling slightly slower than its phase velocity and slows down the population of electrons moving slightly faster. Since there is almost

Figure 2-2. 3-D Structure of m=0 mode

Electric filed line patterns for the m=0 mode. (a) 3-D representation; (b) crossections at $(k/\alpha)\,\mathrm{ctn}(kz-wt)=1/3$ (left) and $(k/\alpha)\,\mathrm{ctn}(kz-wt)=1/3$ (right).

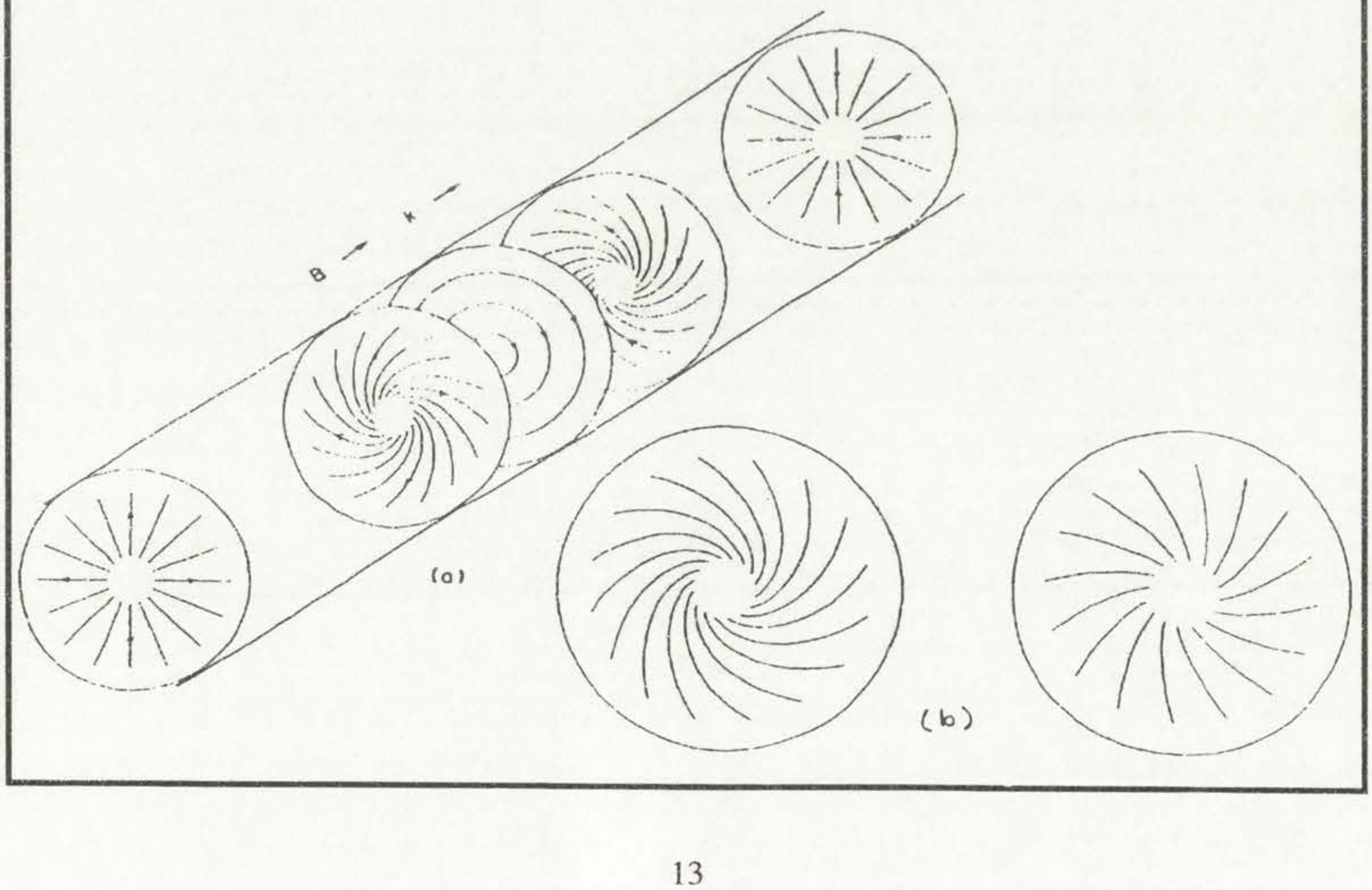

Figure 2-3. 3-D Structure of m=1 mode

Electric filed line patterns for the m=1 mode. (a) 3-D representation; (b) detailed pattern for $k/\alpha = 1/3$. Line spacing is indicative of field strength only at y=0.

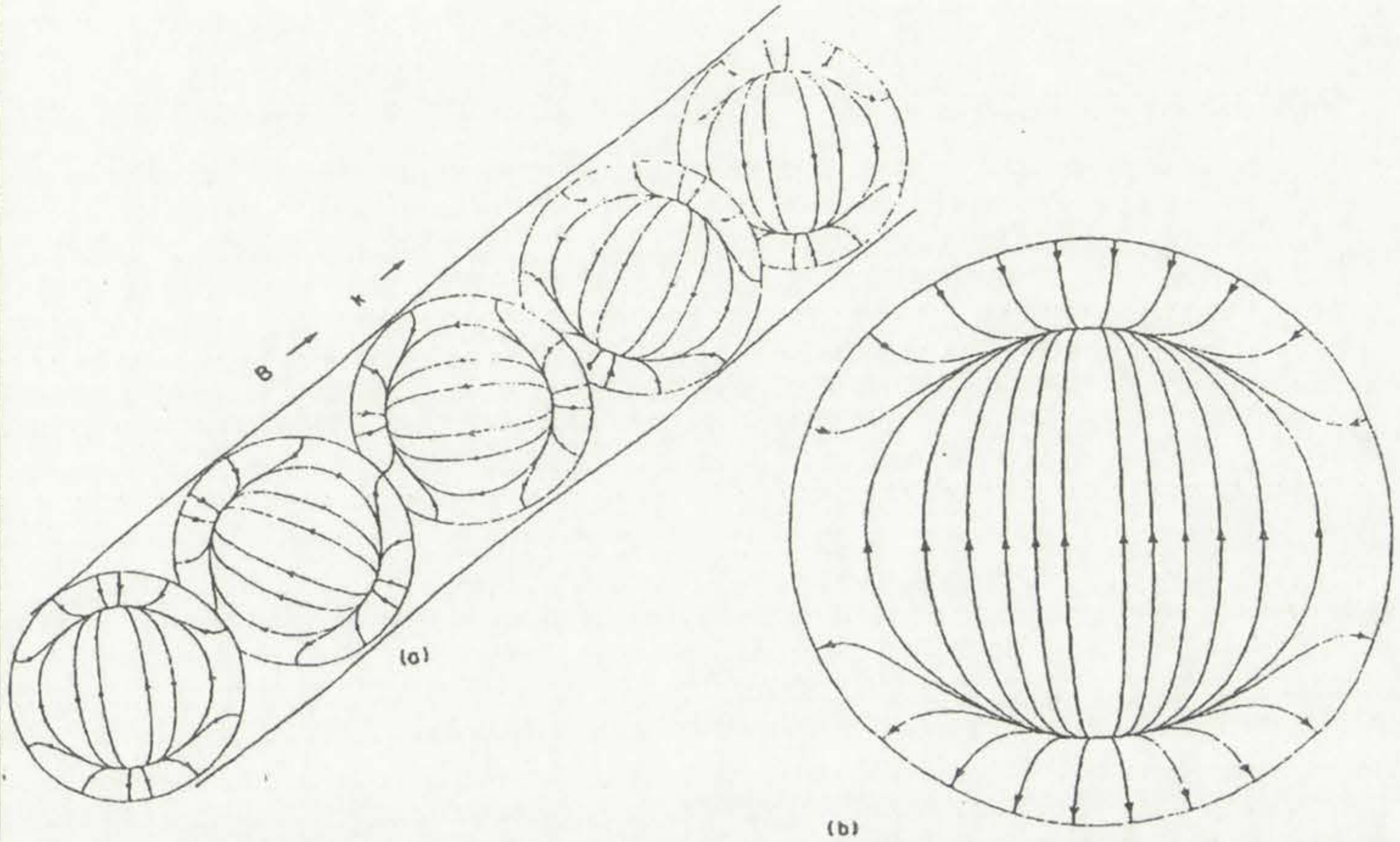

always a larger number of electrons with a velocity slightly slower than the wave than slightly faster, the wave loses energy in the process.

Sample density calculations are provided in Table 1 for several magnetic field values for the m=0 mode, assuming λ_z=16cm, and a=6cm. Note that the density calculated from the dispersion relation for these cases is significantly higher than is normally observed in parallel plate discharges.

Table 1. Sample Density Calculations.

Magnetic Field Value (Gauss)	Density (cm-3)
25	7.5×10^{11}
100	3.0×10^{12}
200	6.0×10^{12}

2.2 CHAMBER DESIGN

The helical wave field developed by helicon waves in large geometries make cylindrical chambers an obvious choice for helicon wave experiments. Chen and Boswell perform most of their high magnetic field experiments on long cylindrical glass tubes, as shown in Figure 2-4, surrounded by regularly spaced magnetic field coils concentric with the tube.[10,11] The solenoid coils produce a static magnetic field from 100 to 1500 Gauss (parallel to the long axis of the tube). The dispersion relations for cylindrical finite geometry derived by Chen[9] and shown here allow propagation of both left- and right- hand polarizations.[10] This result is quite different from the infinite geometry case, where the left-hand wave does not propagate.[12] These small diameter tube, high static field experiments are used to study fundamental plasma phenomena, including fully ionized gas behavior, laser, and helicon wave experiments.

In addition to the small diameter tube used for high magnetic field experiments, Boswell also has a larger reactor designed as a semiconductor manufacturing tool. Several variants on this design exist, some of which are being marketed. Boswell's basic configuration is shown in Figure 2-5.[4]

Figure 2-4. High Static Field Helicon Source

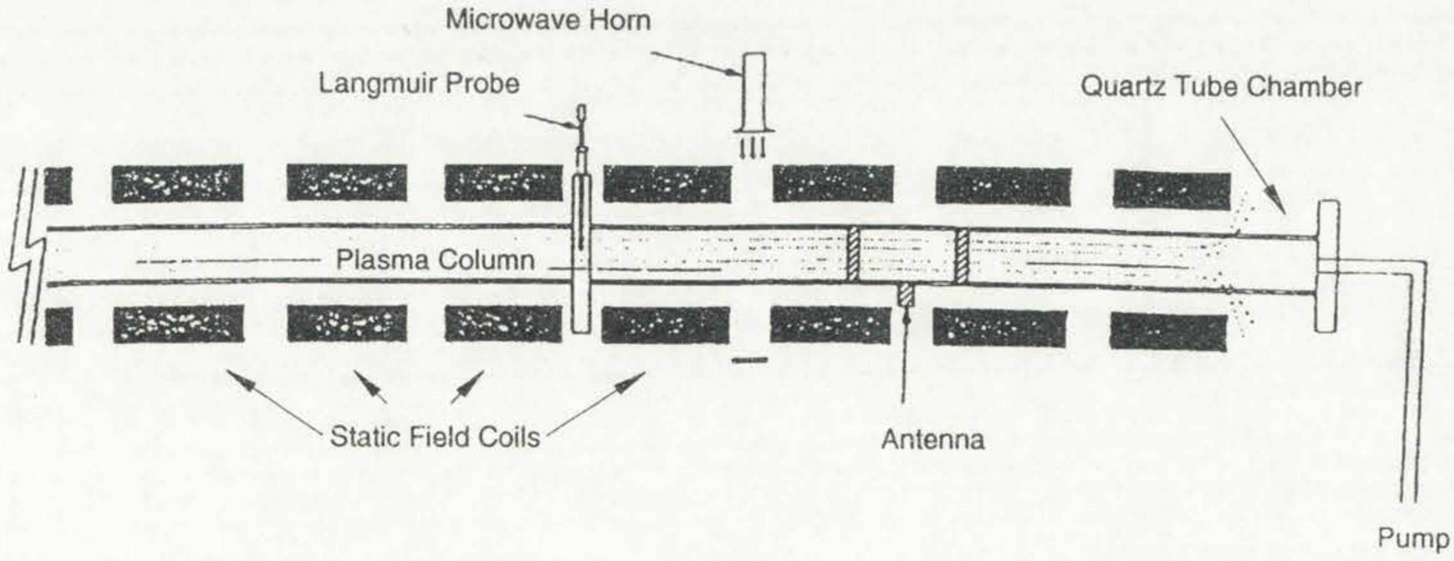

Figure 2-5. Boswell's Helicon Source for Plasma Processing

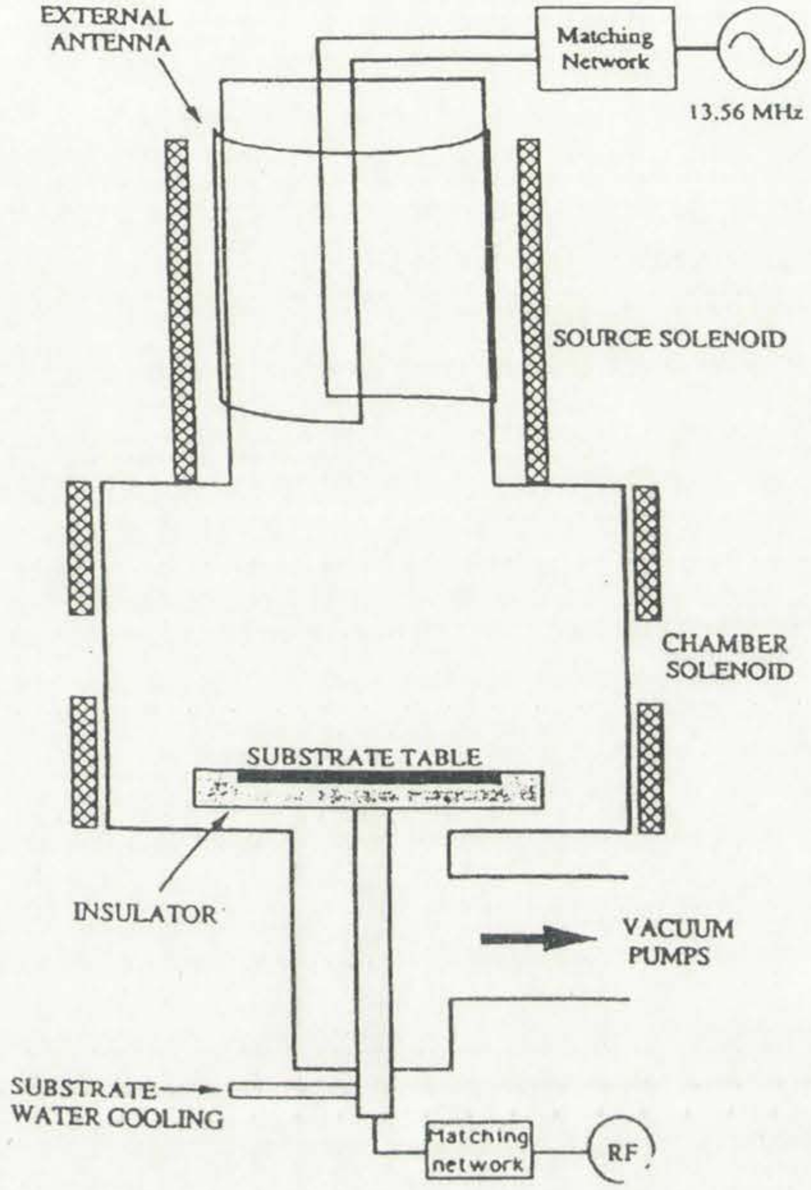

The semiconductor processing source shown in Figure 2-5 operates with a much lower static magnetic field than is used in the machine in Figure 2-4. Field values typically range from 50 to 100 Gauss. Note that the wafer processing region is separate from the source, complete with its own solenoid field coil. This configuration allows the source field strength to be markedly different from that of the chamber. The field in the source can be optimized for efficient antenna coupling, while the wafer is processed in a low field region optimized for uniform processing conditions. Source densities of 3×10^{11} cm^{-3} in SF_6, and up to 5×10^{12} cm^{-3} in Argon are attainable. This particular tool uses the 13.56 MHz industrial frequency and a Boswell type antenna (to be discussed in the next section).

2.3 ANTENNA CONSIDERATIONS

The discussion so far has centered on wave propagation and basic chamber design. The dispersion relation indicates that in a plasma with an appropriate density and static field, a helicon wave can be created merely by introducing a perturbation at the proper frequency. A simple rf current carrying wire located either in or near the plasma would suffice. That is not to say that such a wire would efficiently couple power into the plasma via helicon waves. In fact, the design of appropriate exciting antennas continues to be a relevant research problem.

There are presently three common types of antennae used in cylindrical and toroidal helicon excitation: the Nagoya type III, the Boswell, and the Shoji (or helical) type.[10] Each of these is pictured in Figure 2-6. The Nagoya type III antenna was used on the Nagoya bumpy torus research reactor in Nagoya, Japan. Excitation fields from this antenna excite waves with a mixture of right- and left-hand components. Downstream from the antenna, left- or right-hand helical wave structure, or mixtures of both, can be observed depending on operation characteristics.[10] Densities achieved with the Nogoya type antenna in Chen's reactor are almost identical to those achieved using the Boswell antenna.

The Boswell antenna, as pictured in Chen's paper, also excites both right- and left-handed waves equally, and is very similar to the Nagoya type III. However, there are several variants of the Boswell type that preferentially excite either of the two polarizations depending on the design. The variant actually used by Boswell, et al.[11] is pictured in Figure 2-6(d). Both the Boswell and Nagoya type

III designs have been used to excite plasmas (some of which are fully ionized) with densities of 2.5 x 10^{13} cm^{-3} using high static magnetic fields.[10,11]

The Shoji antenna, shown in Figure 2-6(c) differs from the Boswell and Nagoya III antennas because it is designed to couple directly to the left- or right-hand wave, depending on the antenna helicity. In finite geometry, both polarizations can satisfy the dispersion relation, so one would expect both Shoji antenna orientations to perform in a similar manner. Surprisingly, that is not the case. Chen performed experiments with both left- and right-helicity antennas, and found that only the right-handed antenna was able to produce measurable waves in the plasma column. Densities observed for the right-handed case were as high as achieved using either the Boswell or the Nagoya types (up to 10^{14} cm^{-3}) at the sacrifice of some stability.

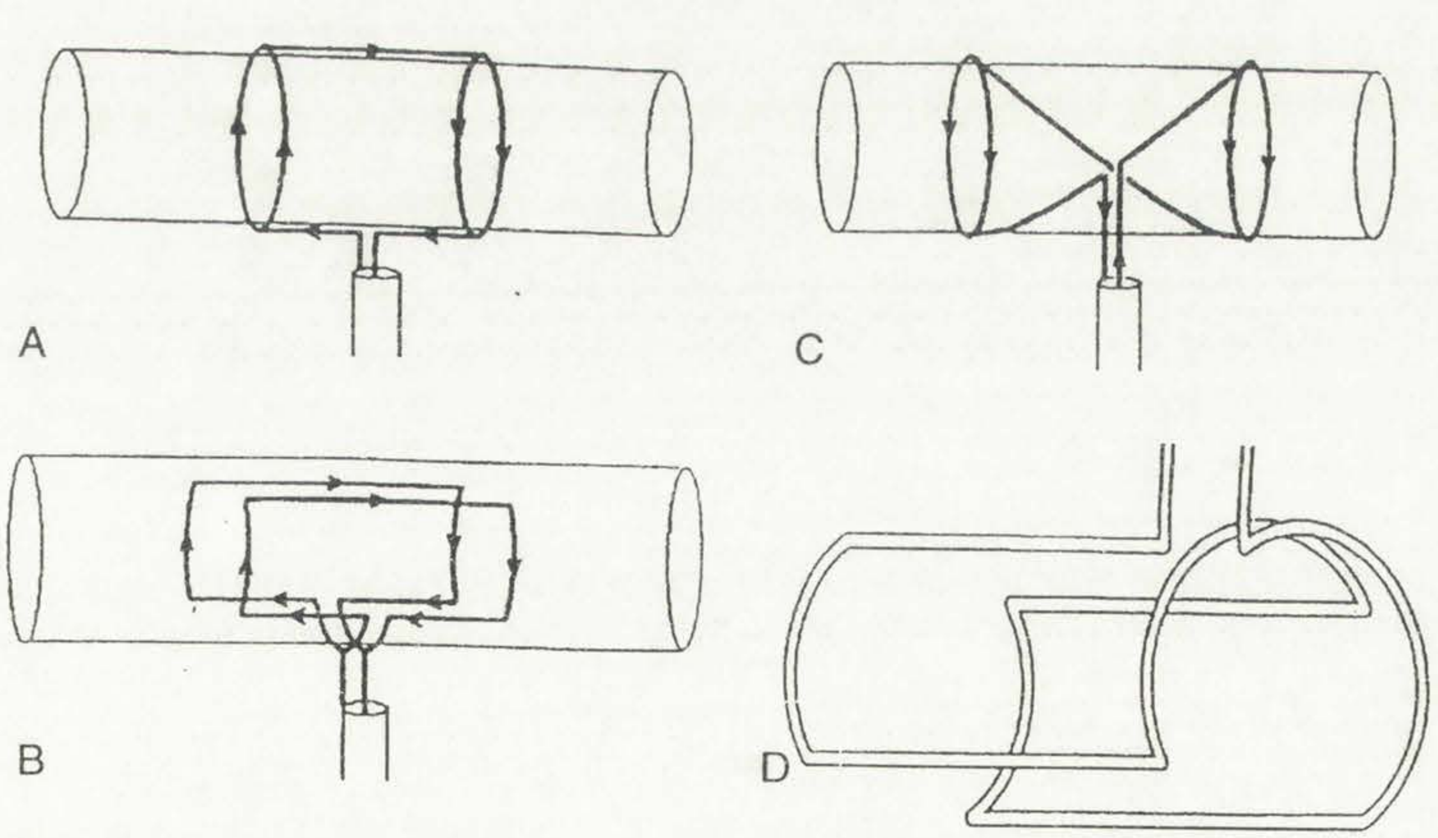

Figure 2-6. Helicon Antenna Types
A. Nagoya Type III
B. Modified Boswell
C. Shoji (helical)
D. Unmodified Boswell

Electrodeless plasmas excited via helicon waves are so markedly different from those used in parallel plate reactors that one might expect that the tuning networks used to achieve antenna resonance would also be different. They are not. Boswell and Shoji both use a conventional Pi network, where the antenna functions as the inductor between the capacitors.[10,11] A less expensive, and no less elegant method is used by Chen, where a system of rigid coaxial cables with tunable stubs is used to tune the antenna circuit for resonance.[10]

In general, there are several requirements which must be met for the design of helicon sources.

1. If the antenna is to be located external to the plasma, the chamber must be constructed of a material that is transparent to the oscillating fields of the driving antenna. Quartz, or other glass materials are appropriate materials, as they are clean and relatively inexpensive. Ceramics provide better resistance to heat cycling stresses and chemical attack and possess superior strength.

2. If the antenna is to be located internal to the plasma (as is the case in most fusion applications), the reactor can be made of any material, and is usually constructed of metal. The antenna, however, must be robust enough to withstand plasma bombardment and eddy currents induced in the wall of the chamber can present a significant power loss problem.

3. Care must be used when constructing an antenna to match the source geometry. Usually they should be built to couple to a particular mode of the reactor vessel.

4. Solenoidal field coils usually provide the static magnetic field needed for helicon wave propagation. They must be designed to allow RF connections to the antenna, and to provide a variety of magnetic field conditions.

Helicon sources have been constructed for a variety of applications. There are small diameter tubes (approximately 4 cm) used to study helicon waves in high field conditions, intermediate sized reactors for wafer processing, and large chambers (approximately 50-200 cm in diameter) used for fusion and other applications. All reactors in the literature are built with cylindrical or toroidal symmetry, but there is nothing inherent in the behavior of these waves to prevent their use in other geometries. They have demonstrated operation in a variety of gasses whose electrical characteristics vary markedly.

2.4 DIAGNOSTIC TECHNIQUES COMMONLY USED IN HELICON DISCHARGES

Electrodeless discharges for use in plasma processing differ significantly from their parallel plate counterparts. Densities can easily exceed 100 times that of parallel plate tools, and a magnetic field is always present. Therefore, some changes in the standard diagnostic tools are required, and some specialized probes are needed. Discussed here are two principal diagnostic probes: the Langmuir probe, the **B**-dot probe, the ion energy analyzer, and a microwave

interferometer. A brief discussion of the problems associated with each is also included.

2.4.1 Langmuir Probes

Langmuir probes have been used to study plasmas since the early part of the 20th century. In their simplest form, they are metal wires immersed in the plasma. The wire voltage is swept from a large negative potential, where all of the collected current comes from impinging ions, to a positive potential above the plasma potential, where all of the current is due to electrons. Contained in this trace is information about electron and ion density, electron energy distribution function (EEDF), and plasma and floating potentials. It is a powerful, yet simple tool, but requires some careful analysis to obtain credible values for plasma parameters. The simple probe described above works very well in DC discharges, but it needs to be modified before it can be used in plasmas where time dependent fields are present. In capacitive discharges, like RF parallel plate systems, it is necessary to construct the probe in such a way as to minimize probe to plasma capacitance effects.[13] Capacitance effects are smaller in helicon discharges, because the densities are sufficiently high enough to shield the bulk of the discharge from external fields. However, the helicon waves themselves introduce RF fluctuations in the plasma. Also, large RF fields may be found in the region of the plasma close to the antenna. It is just as important to consider high frequency effects on Langmuir probe measurements in helicon discharges as in parallel plate types. The use of inductive filters built into probe tips in addition to external filtering and careful termination is common, but measurements taken with uncalibrated Langmuir probes should be regarded as only approximate.[14] In addition, because the electron density can be as much as 10^{14}

cm^{-3} in reasonable magnetic fields, and because a significant fraction of electrons present have energies greater than 10 eV, sputtering of or deposition on the probe surface can produce inconsistent results.

A further requirement for the use of Langmuir probes to obtain accurate information about EEDF's is that the current-voltage trace be resolved very accurately. Most magnetized plasmas exhibit more complicated EEDF's than non-magnetized varieties. Usually this distribution can be interpreted as a bi-Maxwellian[15] or as a Maxwellian with a non-thermal tail.[11] 8-bit resolution (the standard for most digitizing oscilloscopes) is not sufficient to resolve some of these tails. A detailed discussion of trace analysis techniques used in the development of the new source is included with the experimental data.

Langmuir probe measurements are effected by RF in the plasma, are subject to errors in interpretation of the probe trace, and can perturb plasma conditions in the region of interest. In fact, the larger the probe, the stronger the perturbing effect. Miller, et al.[16] have shown that even probes with areas as small as 10 mm^2 introduce systematic errors when used to measure the density in an argon capacitively coupled discharge. Density measurements with a Langmuir probe were consistently lower than the line-integrated value obtained using a microwave interferometer. Therefore, careful attention was given to designing the probes used in this work to be as small as possible, yet still provide a reasonable signal. Sources of error, both in probe design and in trace analysis will be discussed in detail in this work.

2.4.2 B-dot Probes

The B-dot probe was designed to measure time varying magnetic fields within a plasma or other medium. It consists of a small wire loop which is insulated from, but immersed in the plasma. Oscillating magnetic fields in the plasma induce currents in the loop, which are proportional to the time derivative of the flux passing through loop. One would expect all three spacial components of the wave structure to exist in the plasma, and probes can be designed to look at all three simultaneously, as is shown in Figure 2-7.[17] If the probes also have the ability to move around in the chamber, and the plasma conditions are reproducible, then a map of the wave structure in the entire chamber can be constructed. It is also possible to quantify the performance of the antenna in use.[18]

Figure 2-7. B-dot probe for 3-axis measurements

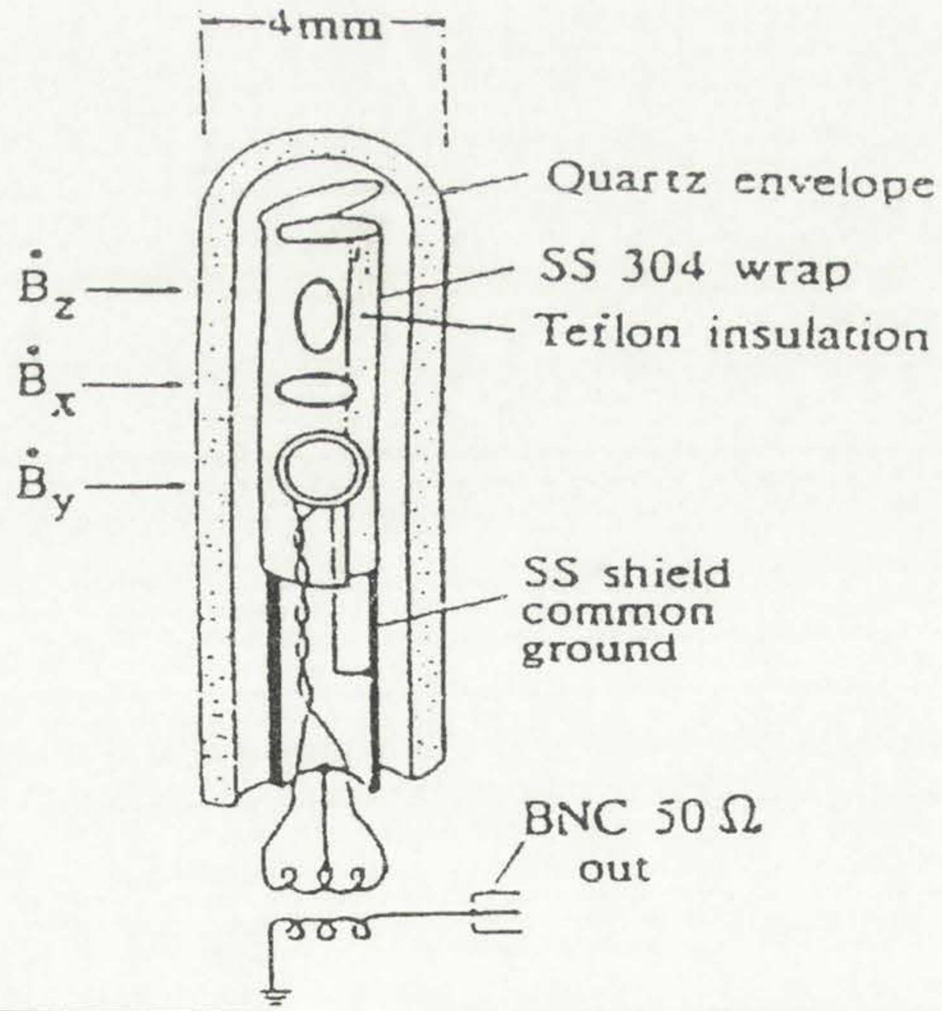

High frequency effects must also be considered in the design of **B**-dot probes, as was the case with Langmuir probes. The sensing loops and the lengths of wire needed to connect them to external instrumentation create a significant inductance, especially when large loops, or large numbers of loops, are used. As such, a small Helmholtz coil and a signal generator should be used to calibrate the probe for frequency response and sensitivity. This technique was used extensively during the development of the new source, and a detailed discussion of the probes used is included with the experimental data.

Other plasma diagnostic tools which have been used on helicon tools include ion energy diagnostics[19,20], microwave interferometers, and various type of optical diagnostics. As they were not used for this work, descriptions are not included here. The discussion now turns to properties of helicon discharges as measured by these devices.

2.5 CHARACTERISTICS OF HELICON DISCHARGES

The helicon source has been recognized as having distinct advantages over existing plasma processing equipment both in efficiency and density almost since the first chamber was constructed in 1970.[7] The efficient coupling created a natural curiosity as to the mechanism. Measurement of the EEDF seems to address the issue, but does not completely agree with the theory. It is important to note that a complete answer does not exist for this problem, rather it is still the focus of current research.

The helicon wave energy is thought to couple to electrons in the plasma via Landau damping. Collisional heating transfers energy to the bulk electrons, high, the [illegible] effects of [illegible] are considered in the design of B-dot probes, as was the [illegible] of [illegible]. The winding [illegible] and the lengths of wire needed to connect them to external instrumentation create a significant pickup [illegible], especially when large loops, or large numbers of loops are used. As such, a small Helmholtz coil and a digital generator should be used to calibrate the probe for frequency response and sensitivity. This technique was used extensively during the development of the new source, and a detailed discussion of the probes used is included with the experimental data.

Other plasma diagnostic tools which have been used on helicon tools include ion energy diagnostics, microwave interferometers, and various types of optical diagnostics. As they were not used for this work, descriptions are not included here. The discussion now turns to properties of helicon discharges as measured by these devices.

2.5 CHARACTERISTICS OF HELICON DISCHARGES

The helicon source has been recognized as having distinct advantages over existing plasma processing equipment both in efficiency and density almost since the first chamber was constructed in 1970. The efficient coupling created a natural curiosity as to the mechanism. Measurement of the EEDF seems to address the issue, but does not completely agree with the theory. It is important to note that a complete answer does not exist for this problem, rather it is still the focus of current research.

The helicon wave is widely [illegible] thought to [illegible] mechanisms in the plasma via Landau damping. Collisional heating transfers energy to the bulk electrons.

while collisionless heating selectively accelerates a group of electrons to energies much exceeding those found in the bulk. Chen[10] calculated that an electron which gets accelerated by collisionless Landau damping in an m=1 mode would have between 50-100 eV of energy if $n_e = 5 \times 10^{12}$ cm^{-3} and B_0=1000 G. In a similar geometry, but under different conditions, observation of non-thermal tails in the EEDF have been observed by Zhu and Boswell[11]. Figure 2-8 shows the electron energy distribution function observed in an Argon plasma with 800 Gauss of static field. There is an increased population of electrons at 45 eV. Although the peaked shape of the distribution at 45 eV indicates that simple Landau damping does not adequately describe the measurement, the observa-

Figure 2-8. EEDF's in a Highly Magnetized Helicon Discharge

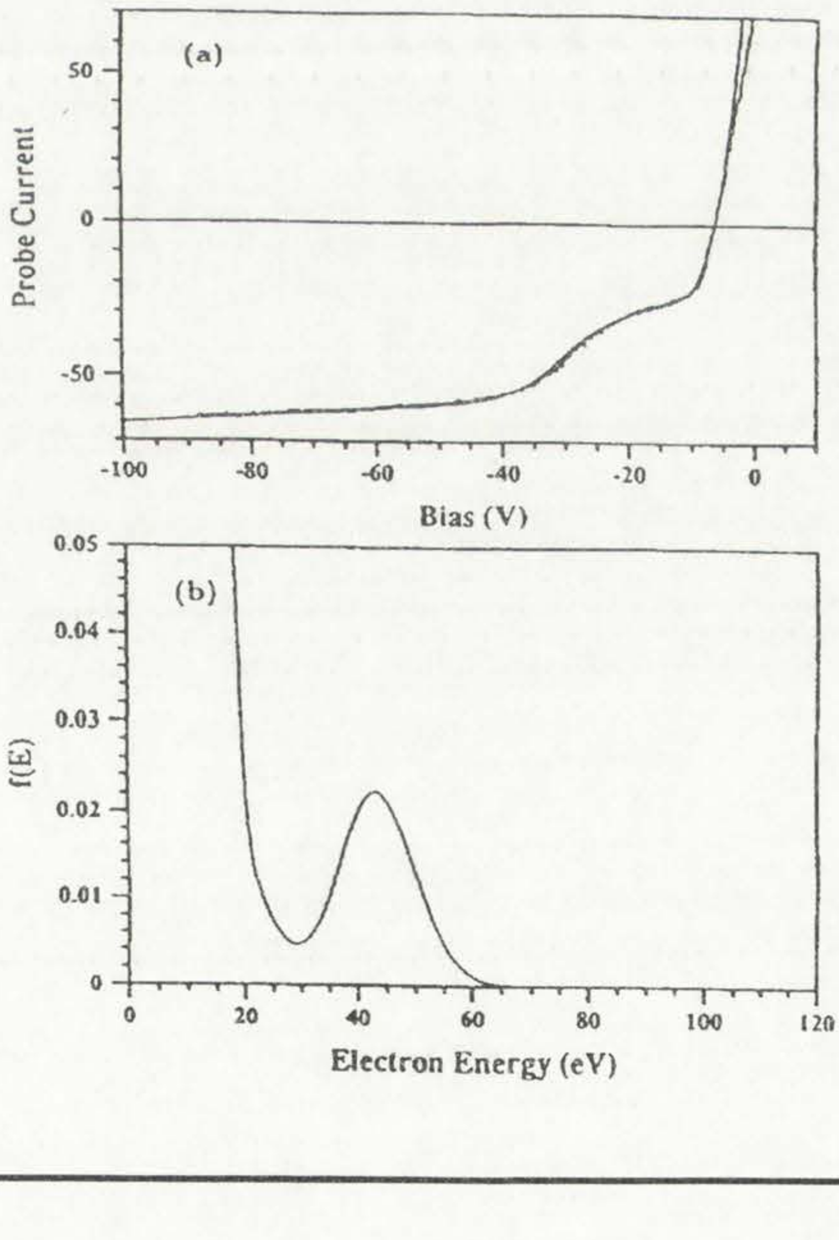

tion of warm electrons of approximately the expected energy lends credibility to the argument. Although there is still contention, Landau damping is the most likely explanation for the way energy is deposited into a helicon plasma, and readily explains observed efficiencies as high as 40%. Since the first ionization potential of Argon is 15.76 V, it is very easy to see why a helicon wave excited plasma is so efficient. If a two-temperature Maxwellian distribution is assumed, with 1% 18 eV electrons in a 2 eV bulk, the number of electrons with energies higher than 15.57 eV is 100 times that of a 2 eV single-temperature Maxwellian distribution. Multi-peaked EEDF's are known to be found in other types of magnetized plasmas, as well[12].

Charles[20] has performed experiments using ion energy diagnostics on the Boswell etching reactor. Using a stalk mounted ion energy analyzer, she measured the ion energy distribution functions shown in Figure 2-9. Note that the ions in this distribution function have rather high energies. This is because ions are collected after falling through the sheath around the stalk. Ions which

Figure 2-9. Sample Ion Energy Distribution Function in Helicon Etch Reactor

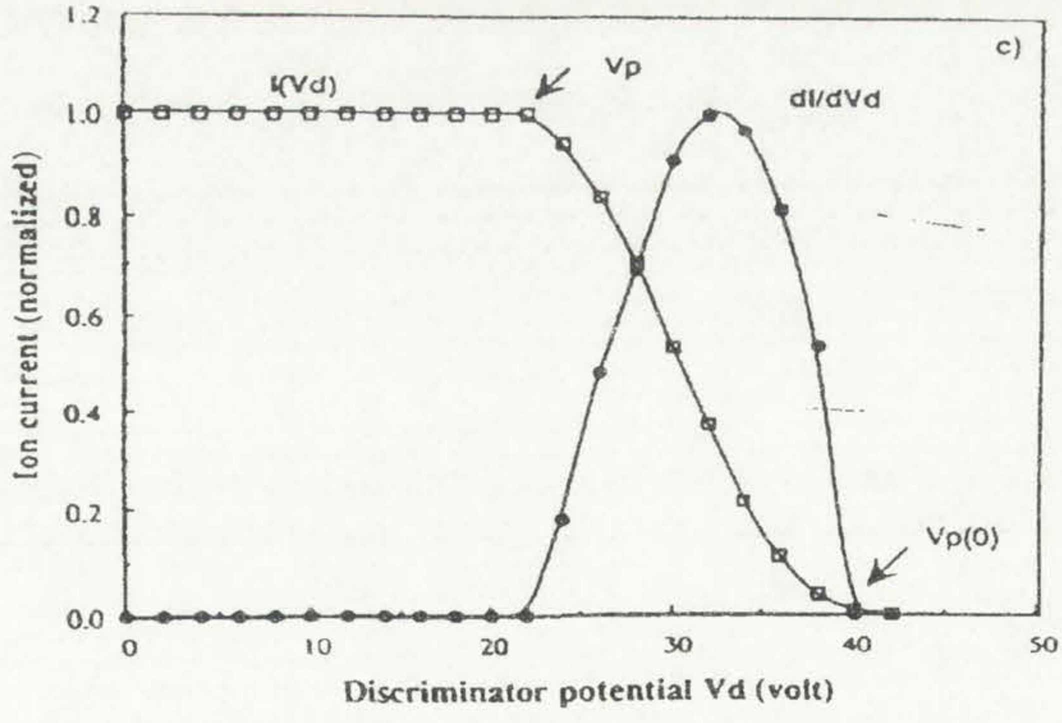

undergo no collisions in the sheath arrive with energies close to the plasma potential. Those with energies at the plasma potential are representative of local plasma conditions. Some ions can be collected whose energies are larger than the local plasma potential, and are representative of regions in the vicinity of the probe where the local potential may be slightly higher than the plasma potential. To determine the true IEDF in the bulk region, an additional measurement of the plasma potential, referenced to the energy analyzer ground, is needed.

Properties such as EEDF, IEDF and density affect the etch rate, anisotropy, and other parameters relevant to plasma processing in a complicated manner. Although helicon sources have been applied to plasma processing relatively recently, there have been a few preliminary experiments showing the capability of this source to perform industrial processes. The high magnetic field reactors, where much of the antenna and wave experiments were performed, would not be very useful for microelectronics applications, and the high electron energies observed would increase damage. (Etching or deposition would occur at huge rates, but device quality would be low). A compromise is found at lower magnetic fields, where electron and ion energy distribution functions and plasma potential are more suitable for sensitive devices, and densities are still 10-100 times that found in conventional parallel plate reactors with equivalent power input. Etch rates on silicon are 1.2 $^{\mu m}/_{min}$ at 3 mTorr and 0.2 $^{\mu m}/_{min}$ for conditions optimized for SiO_2 etching.[21] Figure 2-10 is an electron micrograph from the same paper showing a 1 μm feature etched in the helicon reactor. Selectivity ratios of Si to SiO_2 of 100 or more have been achieved.[22] The plasma uniformity in these conditions was better than 10% over a 15 cm diameter region. Recent experiments have shown that this uniform region can be extended to 30 cm but

no etching studies have been performed in that system.[23]

Figure 2-10. Anisotropic Etch Profile of a 1 micron Feature. Etched in Boswell Etch Reactor

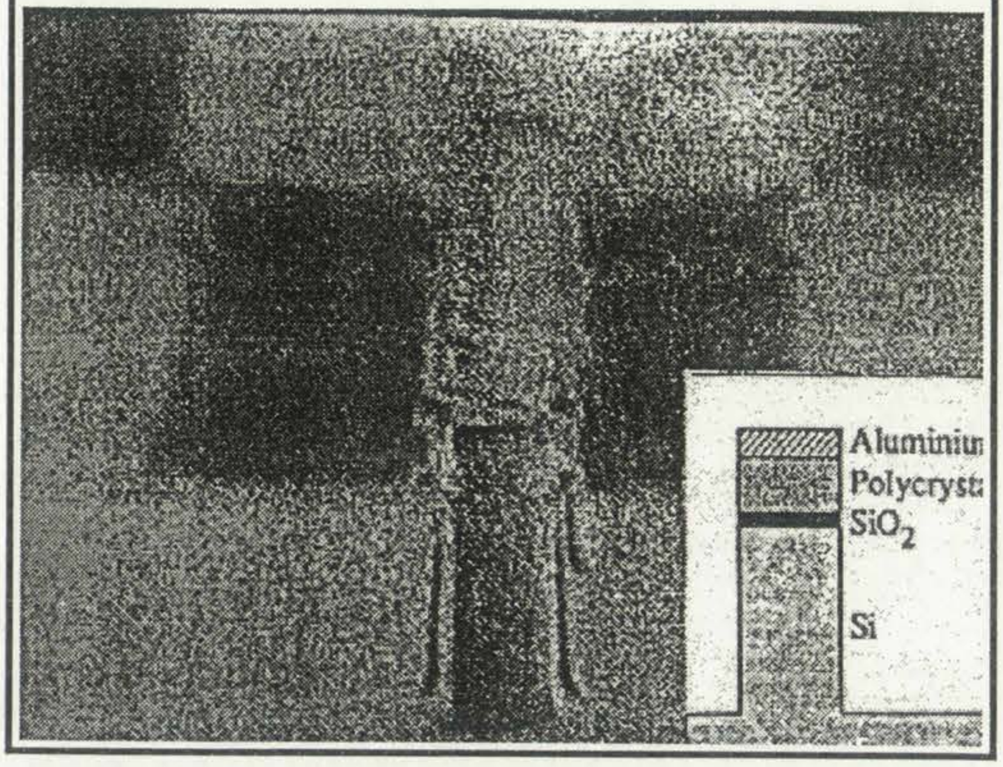

Damage concerns have been addressed by Tsukada, et al.[24] on 6" wafers processed in an oxygen plasma generated by a helicon source. It is shown that damage in helicon reactors is actually less than that observed in conventional parallel plate, ECR, or RFI systems, especially at higher powers. This effect is attributed to the lower plasma potential found in helicon discharges, which enables better control of the bias potential of the wafer being etched. The authors recommend helicon reactors for use in sub-half-micron MOSLSI processing.

The use of helicon sources in plasma processing is still novel, and more work needs to be performed before use in industrial processes. However, the high etch rates observed in the few processes where helicon sources have been tried, and the low damage incurred show them to be a viable option for the next generation of plasma processing tools.

2.6 OTHER APPLICATIONS OF HELICON WAVE EXCITATION

Although some of the applications of helicon wave enhanced discharges have already been discussed, a more general overview is necessary to show the possible applications of this science. The high density sources (shown earlier in Figure 2-4) used to study helicon wave production and propagation are directly applicable to the high energy laser field. Two other applications which have not been covered in depth are fusion devices and large area (or volume) devices.

Loewenhart, et al.[25] has used a helicon wave excitation scheme to pump power into SHEILA, a helical axis stellerator (heliac) fusion research reactor. The antenna, a modified Boswell type, "produce[d] plasma remarkably efficiently". A larger version of SHEILA, called H-1 (for Heliac-1) is presently undergoing start-up tests, and helicon waves will be used as part of the excitation scheme on this reactor, as well. It should be noted that even in the complicated twisted toroidal geometry of the heliac, Landau damping is thought to be the dominant energy deposition mechanism, particularly at higher powers.

A large, 1 m diameter vacuum vessel, 1.6 m long called WOMBAT (Waves On Magnetized Beams And Turbulence) has also been constructed for fundamental helicon wave studies.[3] A large helicon source (0.2 m diameter, 0.5 m long), equipped with a modified Boswell antenna, is attached to one end of the vacuum vessel, and a magnetic field is provided by two independent solenoids. Densities of up to 1.5 x 10^{12} cm^{-3} have been achieved using this chamber. Its size makes it an ideal candidate for a variety of experimental diagnostics, and it is currently being used to study 3-D helicon wave structure in various operating modes.

2.7 WAVES PARALLEL TO B_0 IN RECTANGULAR GEOMETRY

The dispersion relation derived for helicon waves in cylindrical geometry is not necessarily accurate for the source proposed for this project. As such, a reexamination of the relevant equations is in order. The linearized Maxwell equations (1)-(4) are used along with equations (5) and (6), and a perturbation of the form exp i(nx + my + kz - wt) is assumed. The analysis then proceeds as for deriving equation (9), the wave equation. The vector relation in (9) is then solved by examining each component, and relevant boundary conditions. X(x,y,z), Y(x,y,z), and Z(x,y,z) are introduced as general solutions of the wave equation in **x**, **y**, and **z**, respectively. Using (8) and (9) the following relations are obtained:

$$\begin{aligned} Z &= A_z\, exp(\, i\,(\, kz + mx + ny - \omega t)\,) \\ Y &= A_y\, exp(\, i\,(\, kz + mx + ny - \omega t + \phi_y)\,) \\ X &= A_x\, exp(\, i\,(\, kz + mx + ny - \omega t + \phi_x)\,) \end{aligned} \qquad (18)$$

where A_y, A_x, ϕ_y, and ϕ_x are functions of k, m, n and A_z given by

$$\left.\begin{aligned} A_y &= \left(\left(\frac{kn}{k^2 - \alpha^2} \right)^2 + \left(\frac{m\alpha}{k^2 - \alpha^2} \right)^2 \right)^{\frac{1}{2}} A_z \\ A_x &= \left(\left(\frac{km}{k^2 - \alpha^2} \right)^2 + \left(\frac{n\alpha}{k^2 - \alpha^2} \right)^2 \right)^{\frac{1}{2}} A_z \end{aligned}\right] \qquad (19)$$

$$\left.\begin{aligned} \phi_y &= \tan^{-1}\left(\frac{m\alpha}{kn} \right) \\ \phi_x &= \tan^{-1}\left(\frac{-n\alpha}{km} \right) \end{aligned}\right] \qquad (20)$$

It is evident from (20) that the solutions in (18) describe elliptically polarized waves, which is only circularly polarized when $^{m}/_{n}+^{n}/_{m}=^{\pi}/_{2}$, and $k=\alpha$. Further, given that m, n, and α can change with position since the density, wall materials and static field can change with position, the relative phase between the X and Y solutions may not be constant throughout the chamber.

For finite solutions, (18) has solutions of sums of sine and cosine functions. Before a particular solution can be obtained, conditions at the boundary of the rectangular source must be considered. Figure 2-11 schematically shows the sort of conditions one might expect in rectangular geometry. The top and bottom of the source in the y direction are dielectrics. Using the Chen boundary condition at the dielectric, the perturbed current, and thus the perturbed magnetic field must go to 0. The condition in (a) would satisfy that boundary condition, and so would (b). If external antenna elements had parallel currents as shown in the y drawing, the field from those elements would induce an additional node at the center, making the (b) condition more appropriate for that geometry. Therefore,

Figure 2-11. Boundary Conditions for Rectangular Source

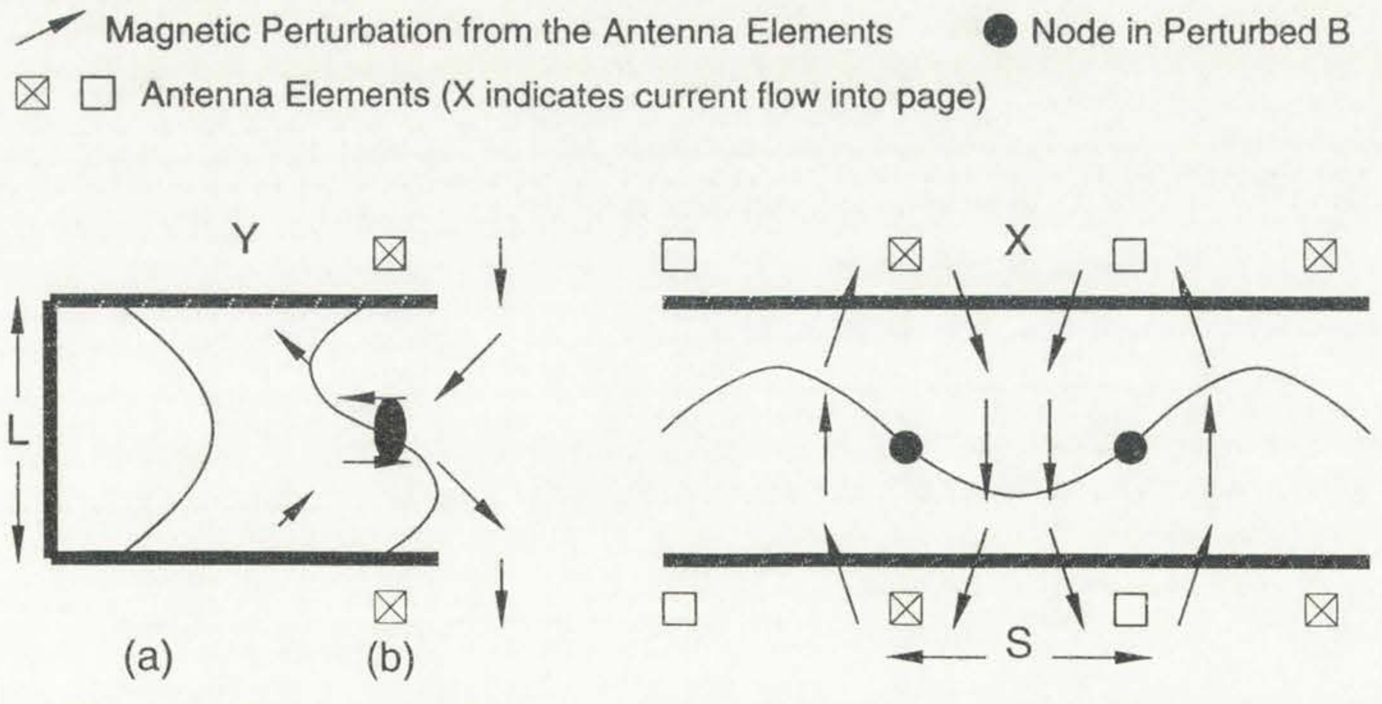

both sine and cosine variation in y are possible for (18), and n must be an integer multiple of Π/L. The walls have very little effect in determining conditions in x. Instead, the antenna plays a more important role. An antenna like the one pictured in Figure 2-11 would create a node between each parallel current segment. Solutions to (18) equation would then require that m have values of $(2M-1)\Pi/s$, where M is an integer. These two sets of boundary conditions place a constraint on the wave number in the Z direction, given by the following

$$k^2 = \alpha^2 - \left(\frac{N\Pi}{L}\right)^2 - \left(\frac{(2M-1)\Pi}{S}\right)^2 \qquad (21)$$

where α is also a function of k, and N and M are positive integers. (21) is the dispersion relation for waves traveling along magnetic field lines in rectangular geometry.

2.8 FUTURE RESEARCH

Helicon sources are being used in research plasma tools from lasers to fusion to plasma processing. They are remarkably efficient at producing plasma over a wide range of magnetic fields and pressure conditions. Unexplored areas where such sources may be useful include geometries which are not cylindrical, excitation of lasing gases with helicon waves and solid state applications. Commercial applications, even in the oldest research areas, are few, owing to the relatively short period of time over which research has been performed. However, helicon reactors may become the tool of choice for semiconductor manufacturing in the next decade as damage becomes a greater concern in the move to smaller device geometries. Helicon sources may also drive plasmas in commercial fusion reactors when that technology is mature.

3. DESIGN OF THE LARGE AREA HELICON SOURCE

The construction of a new type of helicon source involved the selection of extended source dimensions and materials, and design of an appropriate antenna. The antenna had to uniformly excite plasma along the entire source length and needed to be constructed simply to allow for any needed changes to be made quickly. In addition, the source design needed to allow convenient access for diagnostics. A large diffusion chamber was designed to attach to the new source for study of plasma behavior out of the source and for future processing work. Two major variants of the extended source were used: (1) a simple linear tool with a helicon source extending the length of one or both side(s), and (2) a cylindrical reactor with the plasma powered by an axial ring. The "Ring Source", not discussed in this dissertation, was developed subsequent to the simpler linear source. All of the experiments presented in this chapter focus on efficiently powering a plasma over the length of the linear source.

The source built for the first phase is shown in Figure 3-1. A long rectangular box (8.9 cm x 8.9 cm x 87 cm), which functions as the source, opens into a large cylindrical vacuum vessel, which functions as the diffusion region. The back and sides of the source are constructed of metal. The top and bottom are grooved for o-rings to seal against a glass dielectric. The front of the source opens into the diffusion chamber. To facilitate easy access for diagnostics, ports are placed along the side, back, and top of the large cylindrical diffusion region. The motivation for the two-section design is to generate a dense plasma in the source, while independently controlling the bias on a substrate, located in the diffusion region.

Figure 3-1. The First Extended Helicon Source

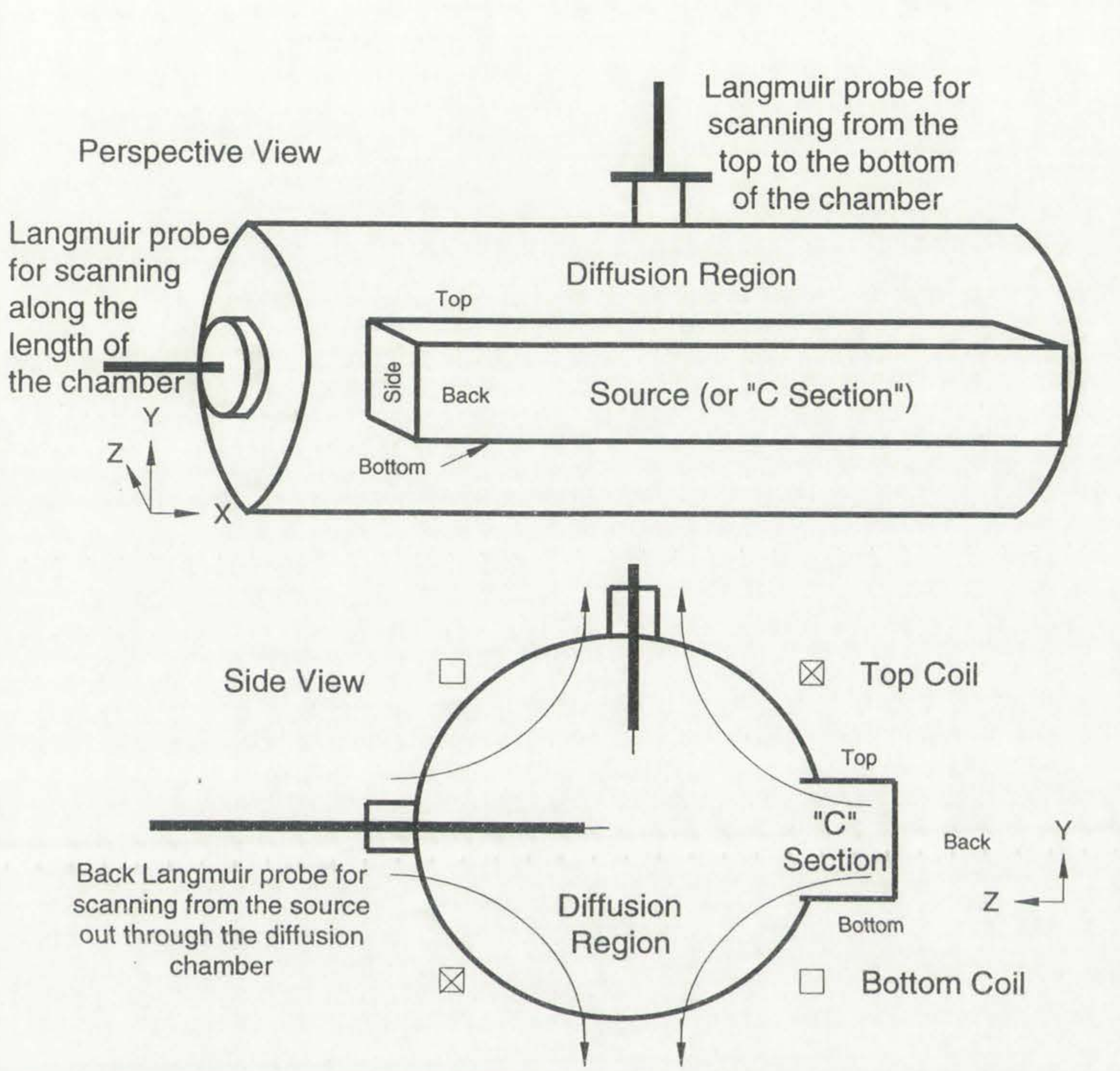

Magnetic field coils were constructed to produce two markedly different types of fields. The experiments presented in this chapter were performed with fields designed to simulate the operation of the ring source, that is, a cusp field. Later chapters cover operation with parallel field lines.

Langmuir probes were installed on the top, back, and side of the chamber to allow monitoring of plasma conditions along three lines through the chamber. Full current versus voltage scans were not done. Saturation current profiles from the Langmuir robe were initially used as a quick method for comparing perfor-

mance between various source and antenna configurations. Improved measurements were used as they became available to further quantify source performance, and eventually wave structure.

The linear source cross-section dimensions were chosen to be 8.9 cm x 8.9 cm. These dimensions are significantly smaller than previous helicon sources used for processing for the following reason. Using equation (21), and assuming a 40 Gauss parallel static magnetic field, a B_Y wavelength of 8 cm (1 wavelength across the source), a B_X wavelength of 20 cm, and a parallel wavelength of 14 cm, the theoretical density needed to be on the dispersion surface for helicon waves is 1.0×10^{12} cm^{-3}. This density is sufficient for many processing applications. A simple increase in the static field, or a change in the mode structure in the source could probably accommodate other processing conditions.

The work covered in this chapter focuses on source and antenna behavior. Some results from measurements made in the diffusion chamber are shown as related to antenna and source performance, but the majority of those measurements are left for chapters 4 and 5. A variety of antennas were tried to determine an optimum configuration. At low power, antennas couple power to the plasma via capacitive coupling across the sheath. Coupling to the helicon mode requires a change from capacitive to inductive coupling, and further requires that conditions in the plasma will allow a wave to propagate. There are several distinct regions of operation: capacitive mode, inductive modes where the wave cannot propagate, and helicon modes. For an antenna to couple into a helicon mode a change from capacitive to inductive mode would have to be induced. This was the criteria used to judge antenna performance in this chap-

ter. Tests were performed at several pressure and magnetic field settings.

Source aspect ratio was also examined to determine its effect on plasma parameters. A source with a moveable back wall was used for this purpose. In addition, a source constructed entirely of ceramic was used to examine back wall material effects. Both of these studies are included in this chapter.

Construction details will be discussed only briefly as they relate to the extended source design. The platform used for gas, vacuum, and gauge accessories differs little from those used on many other types of machines. The long period spent working on details of tuning box and antenna connections, and other matters of assembly can adequately be summarized by the statement "make the antenna to tuning box connections as short as possible". Therefore, this review begins with an antenna survey.

3.1 AN ANTENNA SURVEY

Early designs of the antenna and match box assembly placed the tuning box some distance from the source, to keep the source area clear for easy access. However, a significant voltage drop (more than 50%) was found between the tuning box and the antenna regardless of what type of power feeders were used. Circulating currents of more than 300 A (peak to peak) caused a significant portion of the applied power to be lost in the weakly resistive copper conductor between the tuning box and the antenna, which resulted in poor coupling between the antenna and the plasma. Therefore the first improvement on the linear source was to move the tuning box as close to the antenna as possible. A modified Π network was used in all of the early work; a schematic of which is

Figure 3-2. Tuning Arrangement

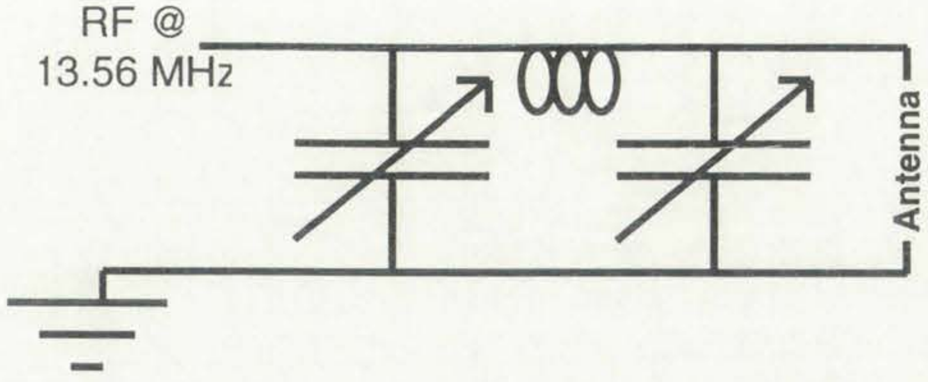

found in Figure 3-2.

When coupling changes from predominantly capacitive to inductive, there is a sharp change in the antenna voltage as a function of power. As the power is increased slowly up from 0 watts, the antenna voltage rises and the electric field forms an oscillating sheath in the weak plasma on the other side of the glass. Electrons are excited in this coupling mode through stochastic heating. But as the power is increased, the antenna current starts exciting a mirror current in the plasma underneath the glass. When this current becomes large enough, power is preferentially dumped into those electrons, and the antenna voltage drops sharply as the current it carries produces plasma more efficiently. By observing antenna voltage as the power is swept, the mode change can be observed. It was assumed that if a transition to inductive mode were induced, then helicon modes were also being excited. This assumption is not entirely true, and is addressed later in this study. Two features of the transition to inductive mode are[26]:

1. as pressure increases, the power where the discontinuity is observed becomes lower, and

2. at low pressure, the transition is very sharp and discontinuous; at high pressure, it is much smoother.

As an independent check of the above measurement, saturation current versus applied power was also measured. A sharp change in the density as a function of power should accompany a change in antenna coupling.

These experiments were carried out on a variety of antenna configurations, which are pictured in Figure 3-3. The motivation for moving between various antenna sets is explained in the discussion of experiments associated with each antenna.

3.1.1 Large Single-Loop Antenna

The first antenna set installed was simply a pair of large loops that extended the entire length of the source. The loops were electrically connected in parallel, and were located on the top and bottom of the source. The antenna was not designed to couple to any fundamental modes of the small source dimensions. It was thought that a uniform magnetic field perturbation over the entire length might be sufficient to excite those modes. Shown in Figure 3-4 and 3-5 are plots of antenna voltage versus forward power at low and high pressure, respectively. Measurements were taken with 5 A in the top static field coil, and -5 A in the bottom coil to create a cusp in the center of the chamber.

Two permanent magnet plates were available for installation in the back of the source. The two permanent magnet plates add 20 Gauss each in the source and tend to make the magnetic field more uniform through the source region.

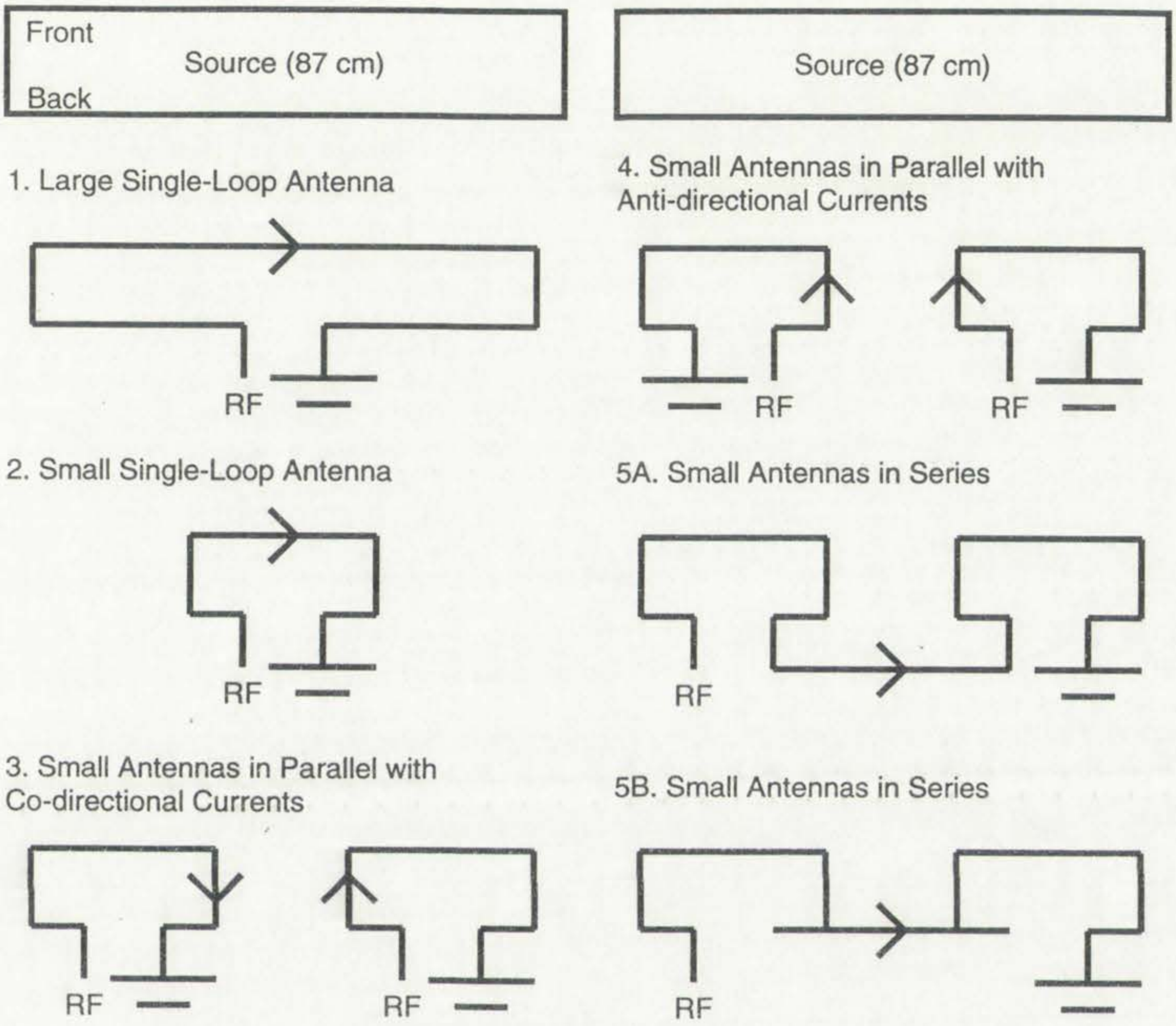

Figure 3-3. Progression through the Antenna Survey (Top View).
(Arrows indicate current direction when RF Voltage is Positive)

Use of these plates had little effect on source operation. The electromagnets were used with antidirectional current senses. They produce 50 Gauss in the source when carrying 5 A each. Although a cusp field is desirable for this phase of development (cylindrical ring source applications), a variety of field configurations were tried. The square root type of behavior of antenna voltage versus forward power in Figures 3-5 and 3-5 indicates that there is never a sharp change in the plasma impedance. The coupling mode exhibited no sharp changes over a wide variety of conditions. The coupling remained weak, and

Figure 3-4. Large Antenna. Peak to Peak Voltage vs Forward Power
1.2 mTorr Argon. 5 A Top, -5 A Bottom, w/Permanent Magnets.

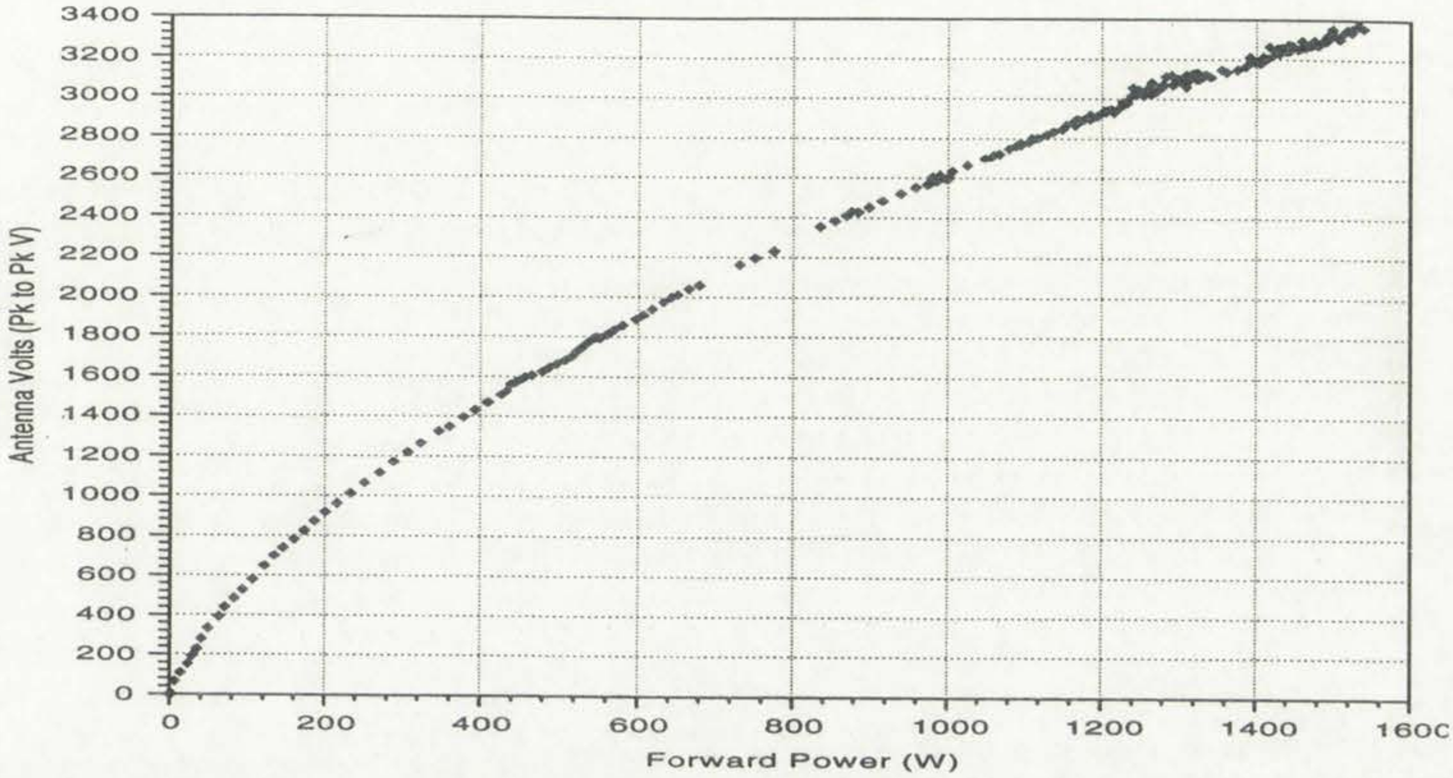

Figure 3-5. Large Antenna. Peak to Peak Voltage vs Forward Power
27 mTorr Argon. 5A Top, -5A Bottom, w/Permanent Magnets

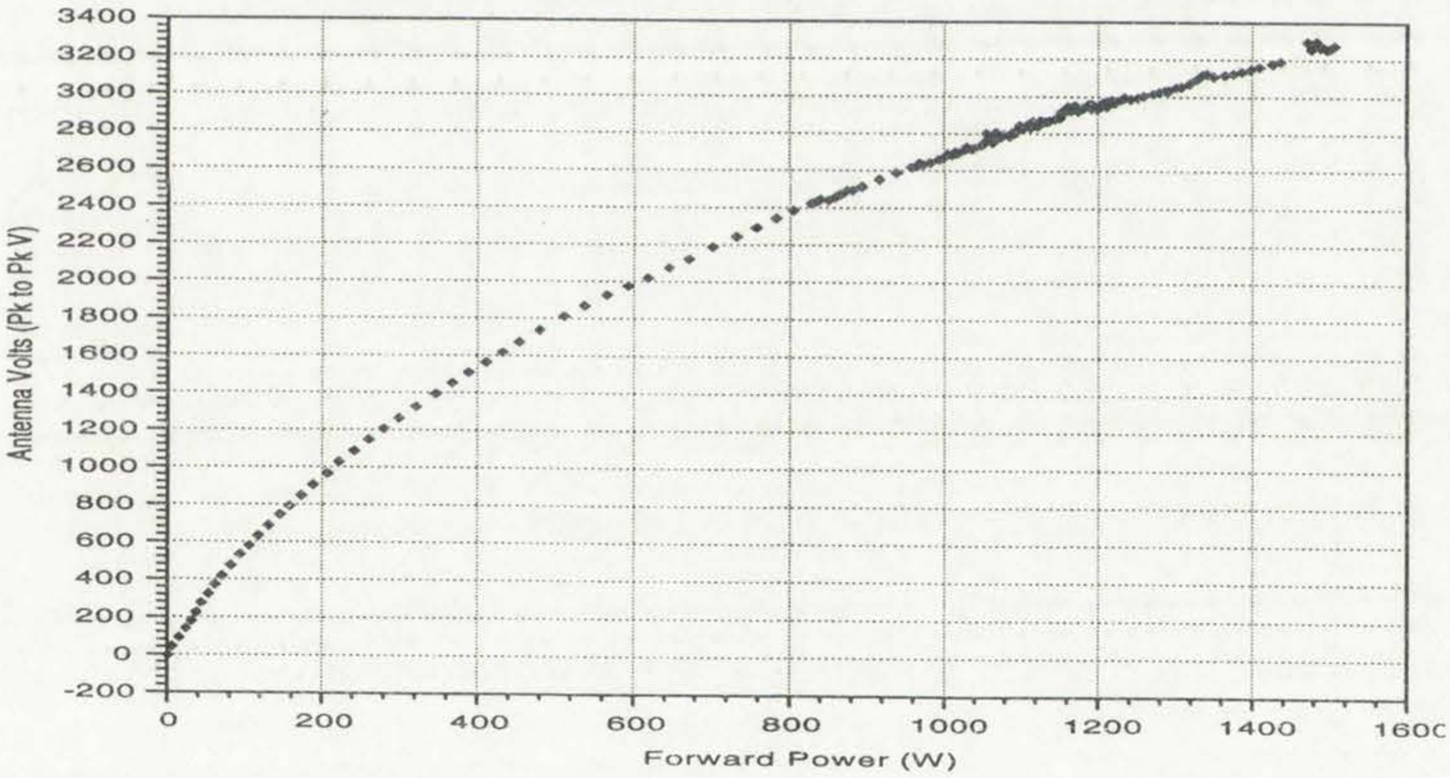

predominantly capacitive, which resulted in rather low density plasmas. Therefore, this antenna set was deemed unsatisfactory.

3.1.2 Small Loops on Top and Bottom of Source Driven in Parallel

A small antenna of the modified Boswell type of design was investigated next. The aim was to induce a mode change in a small portion of the source. An 8 cm x 6 cm loop pair was fabricated and placed on the source. The same antenna voltage studies were performed. Figure 3-6 shows that there is a distinct discontinuity at 600 Watts at a pressure of 1 mTorr. This transition was accompanied by a significant increase in the plasma brightness, as well as in the saturation current measured in the center, 5 cm outside of the source with a Langmuir probe (see Figure 3-7). Mode shifts observed in other helicon sources occur at lower power with higher pressures. Experiments were performed at several pressures to see if this behavior was also observed in the new machine. Graphs of antenna voltage versus forward power are shown for 3, 10, and 27 mTorr in Figures 3-8, 3-9, and 3-10, respectively. The corresponding density

Figure 3-6. Small Antenna. Peak to Peak Voltage vs Forward Power
1 mTorr Argon. 5A Top, 1A Bottom, no Permanent Magnets

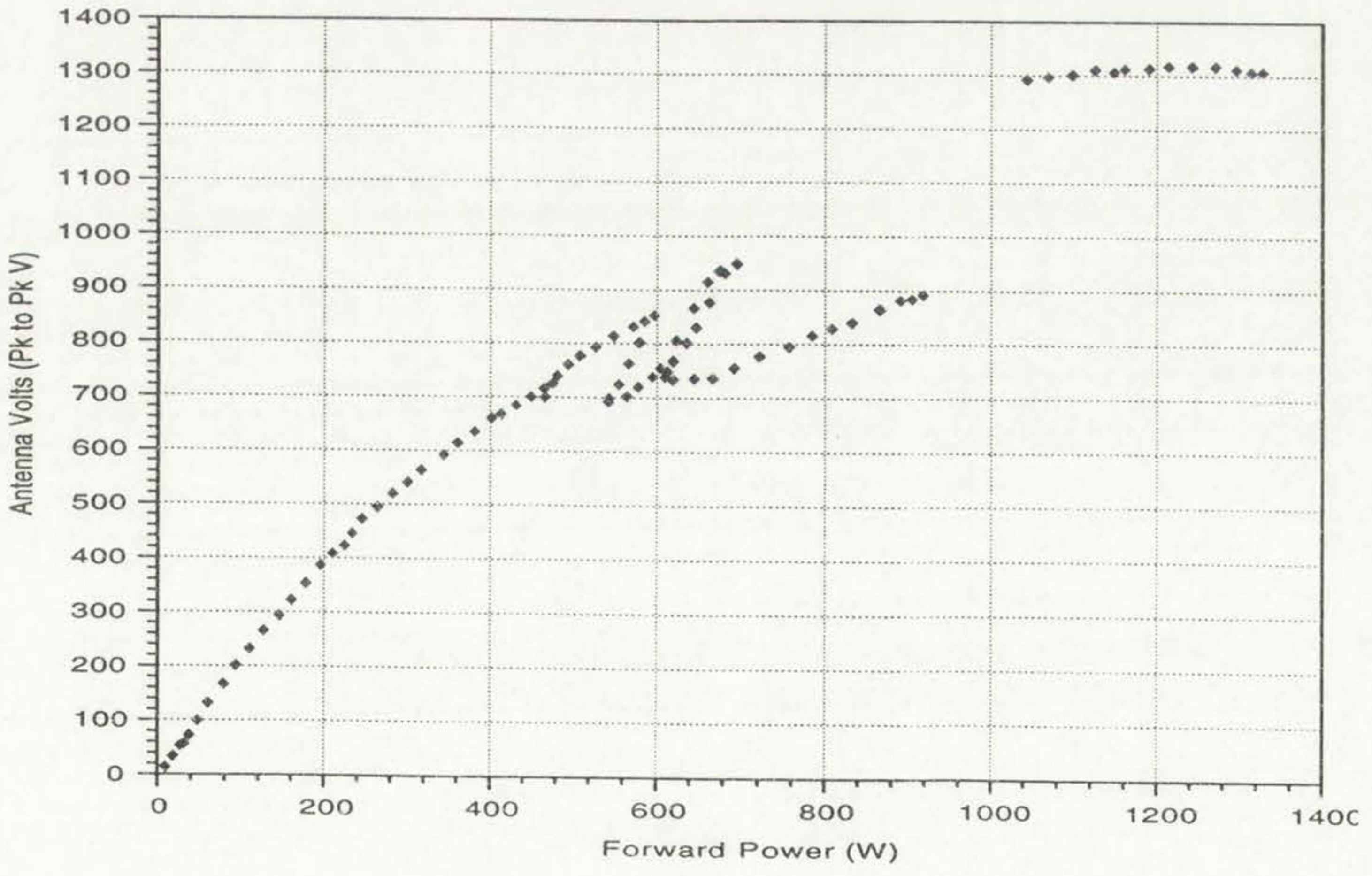

Figure 3-7. Small Antenna. Density vs Forward Power
1 mTorr Argon. 5A Top, 1A Bottom, no Permanent Magnets

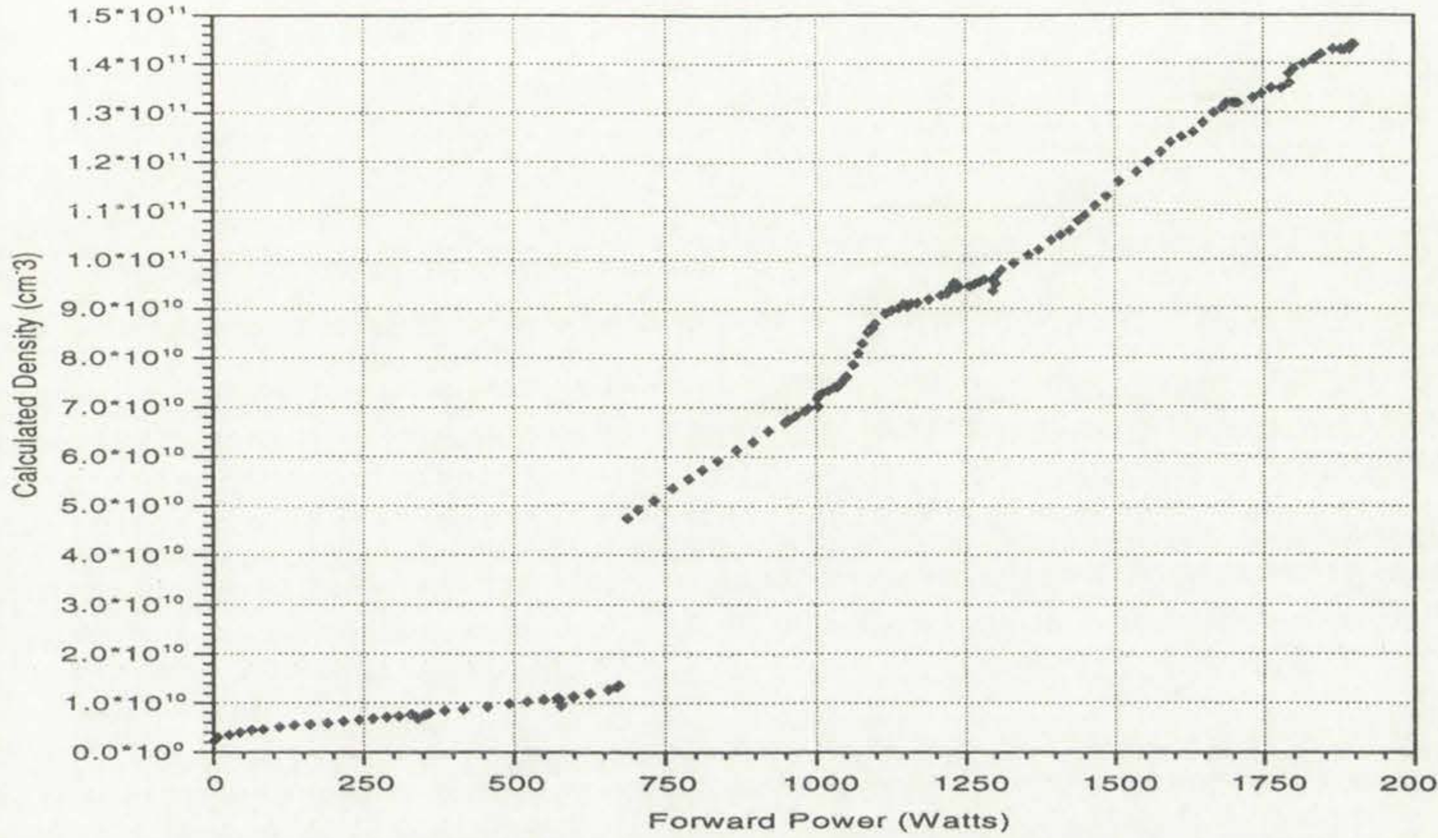

Figure 3-8. Small Antenna. Peak to Peak Voltage vs Forward Power
3 mTorr Argon. 5A Top, 1A Bottom, no Permanent Magnets

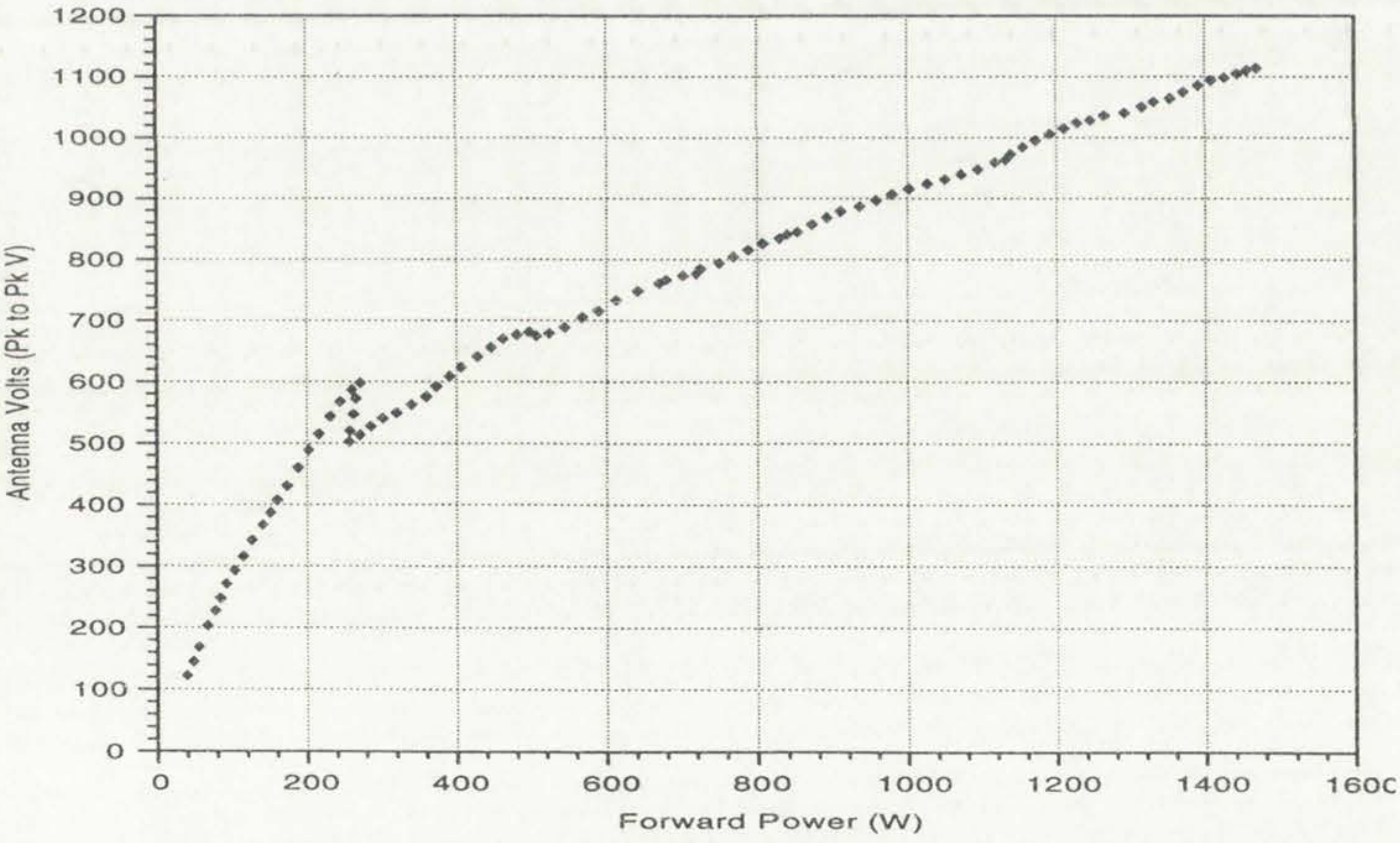

scans are shown in Figures 3-11, 3-12, and 3-13, respectively. This being the first antenna set to exhibit mode changes, a comprehensive examination of the

Figure 3-9. Small Antenna. Peak to Peak Voltage vs Forward Power
10 mTorr Argon. 5A Top, 1A Bottom, no Permanent Magnets

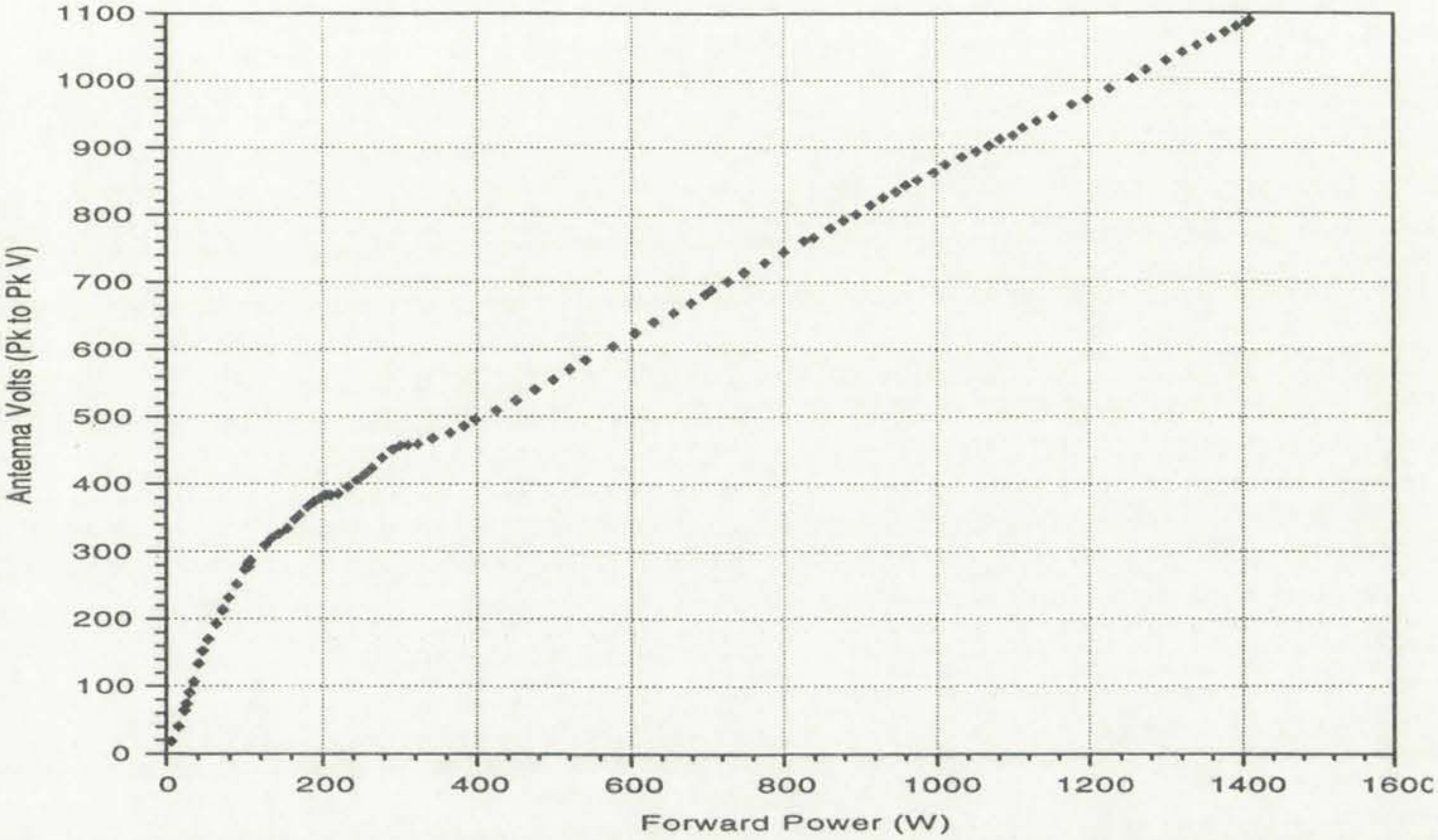

Figure 3-10. Small Antenna. Peak to Peak Voltage vs Forward Power
27 mTorr Argon. 5A Top, 1A Bottom, no Permanent Magnets

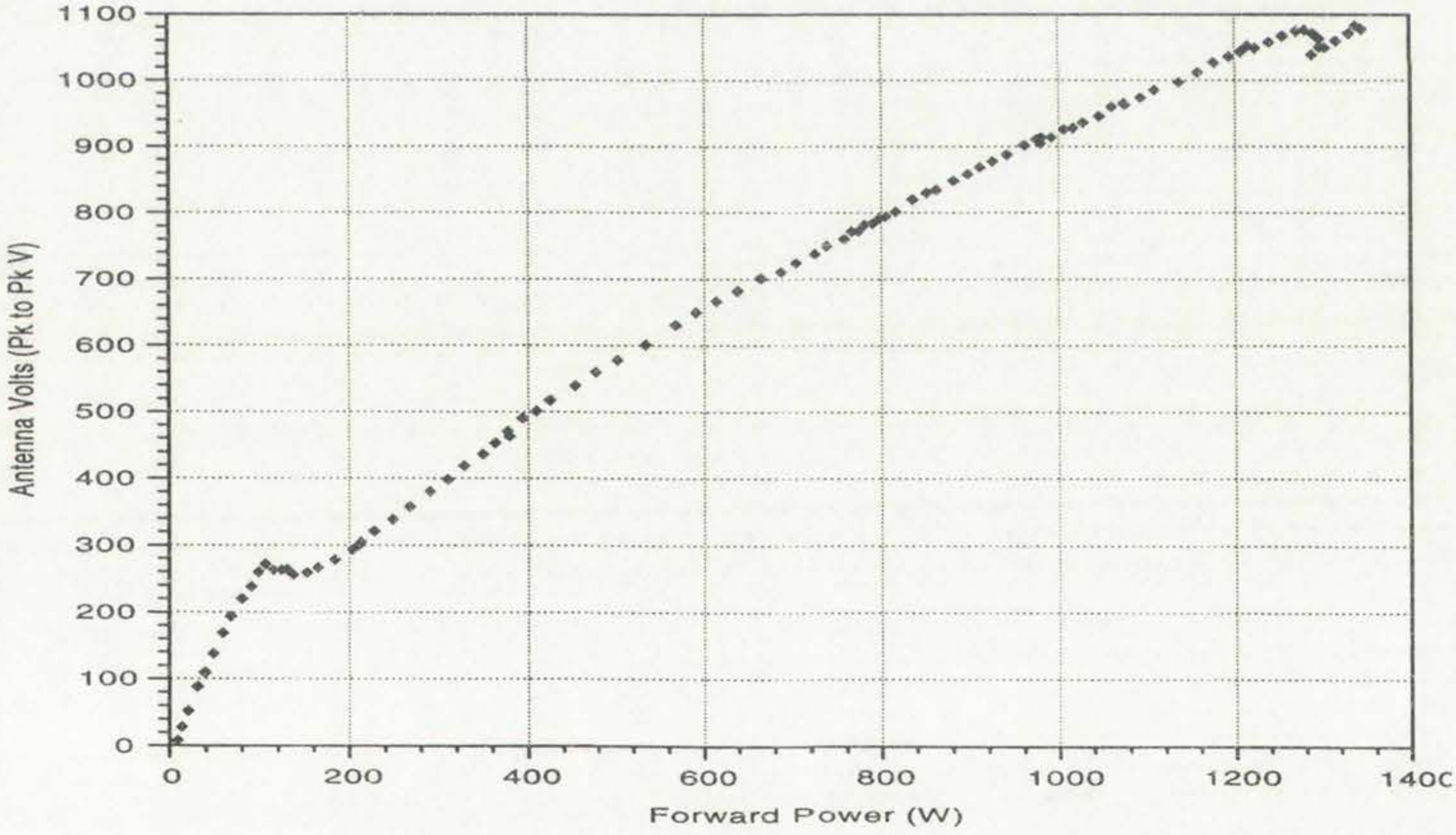

data will be presented; subsequent antennas will be treated with brevity.

Figure 3-11. Small Antenna. Density vs Forward Power
3 mTorr Argon. 5A Top, 1A Bottom, no Permanent Magnets

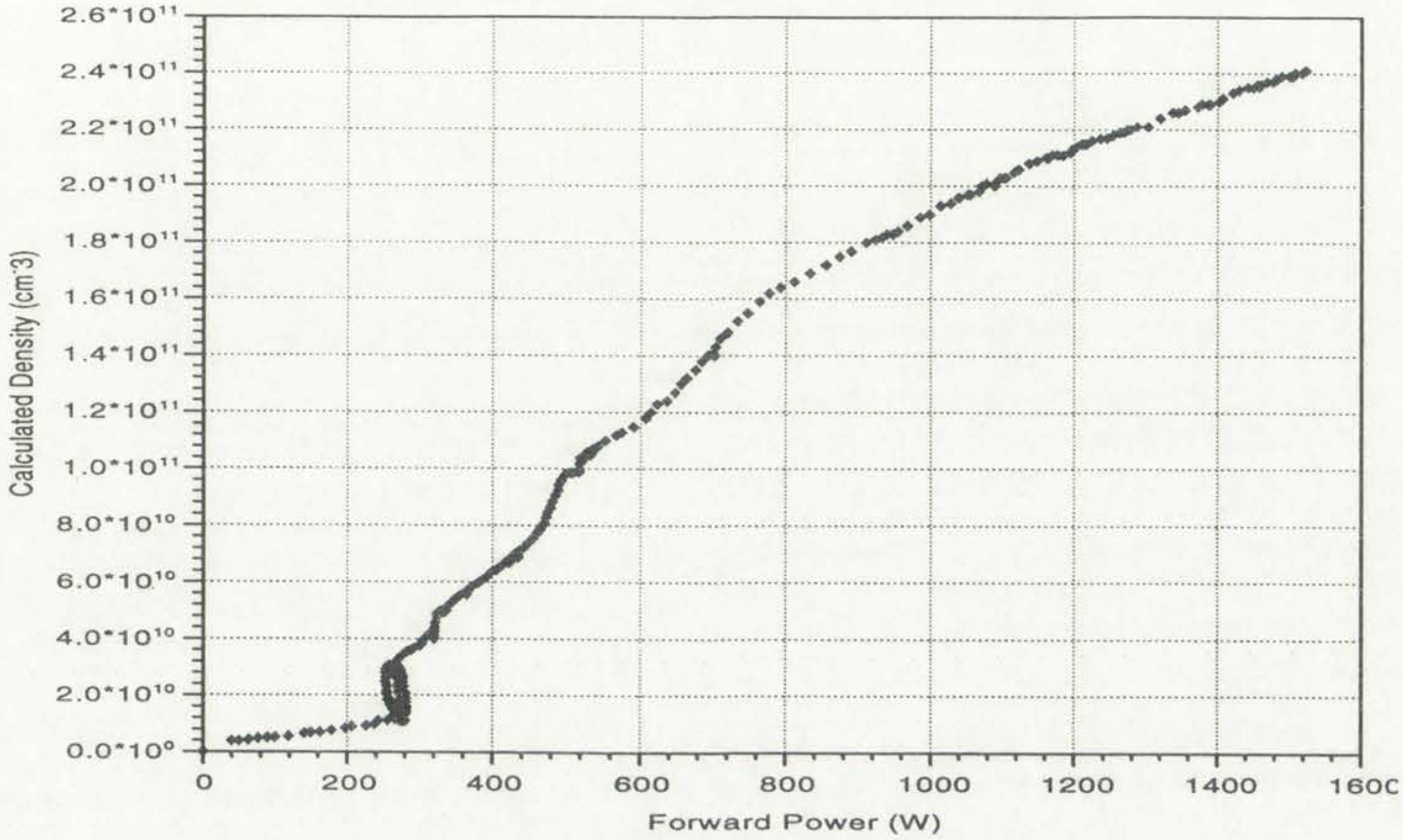

Figure 3-12. Small Antenna. Density vs Forward Power
10 mTorr Argon. 5A Top, 1A Bottom, no Permanent Magnets

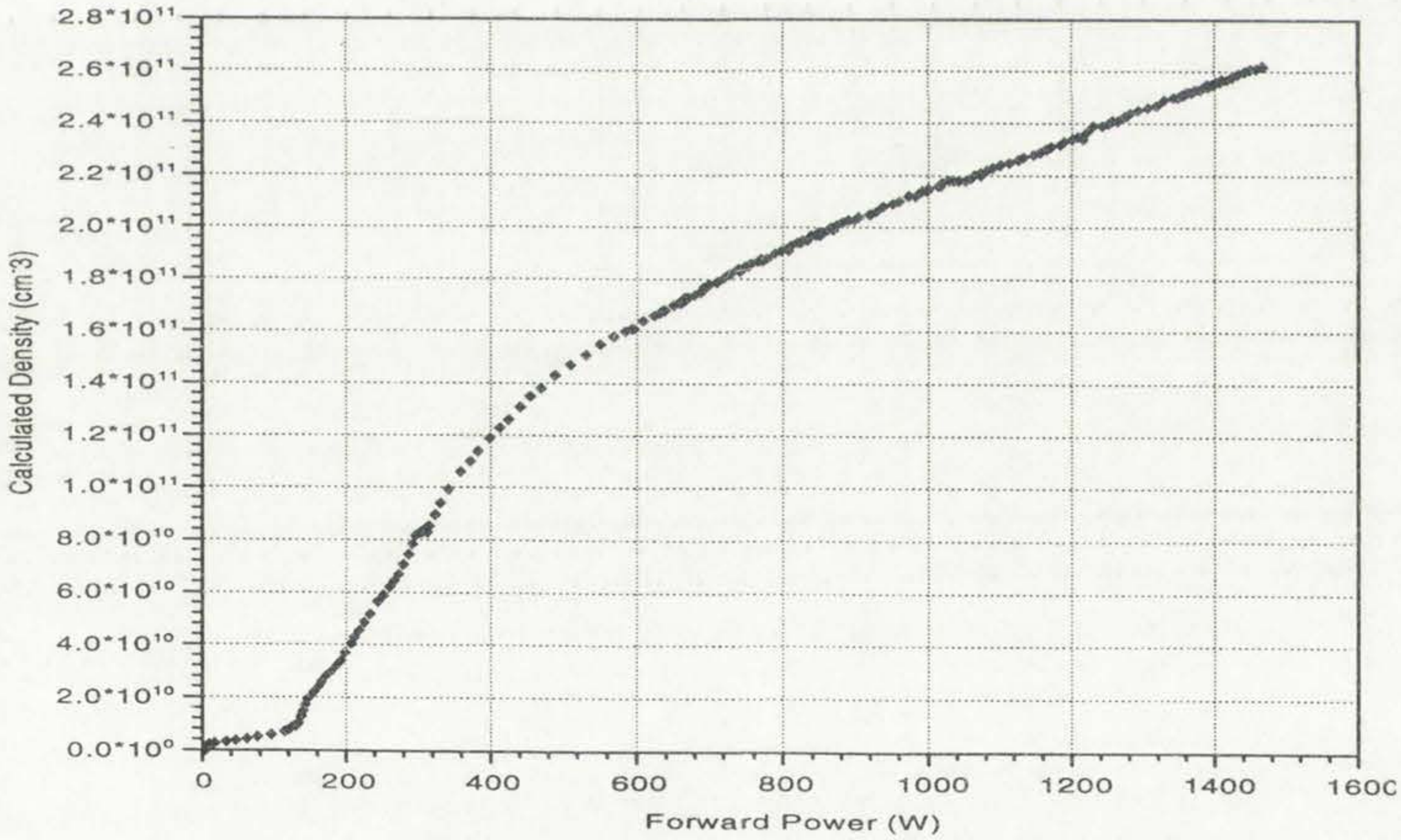

Note in Figures 3-8, 3-9, and 3-10 that as the pressure is increased, the mode shift occurs at lower powers and becomes smoother. This was the desired

Figure 3-13. Small Antenna. Density vs Forward Power
27 mTorr Argon. 5A Top, 1A Bottom, no Permanent Magnets

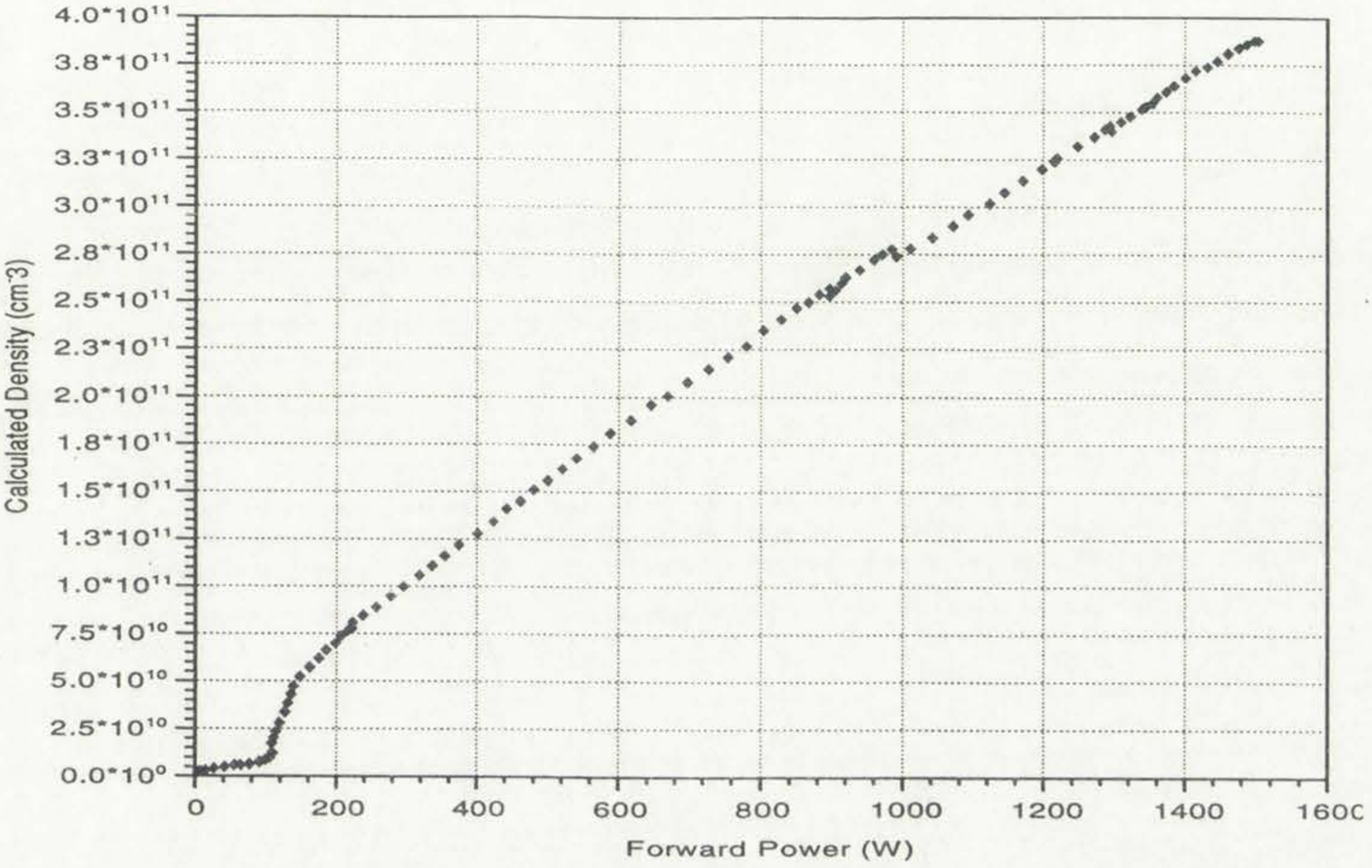

behavior. Subsequent designs would be based on powering various configurations of small antennas to attempt to generate plasma over the entire length of the source.

The Langmuir probes used to measure ion saturation current (and eventually electron temperature) were designed to move around the chamber. As the small antenna set produced behavior indicative of the desired mode shift, plasma conditions as a function of distance out of the source (**Z** direction) and position along the length of the source were measured. Figures 3-14 and 3-15 show variations in calculated density as a function of position in the chamber. Both plots were taken at 28 mTorr, with 5 A in the top coil, and -4 A in the bottom coil. The scan along the source in Figure 3-14 was performed with the probe centered between the top and bottom of the source, located 5 cm out from the mouth of the source. The small antenna pair generates a strongly center-peaked density

Figure 3-14. Small Antenna. Density vs Position Along the Source
28 mTorr Argon. 5A Top, -4A Bottom, no Permanent Magnets. 800 W

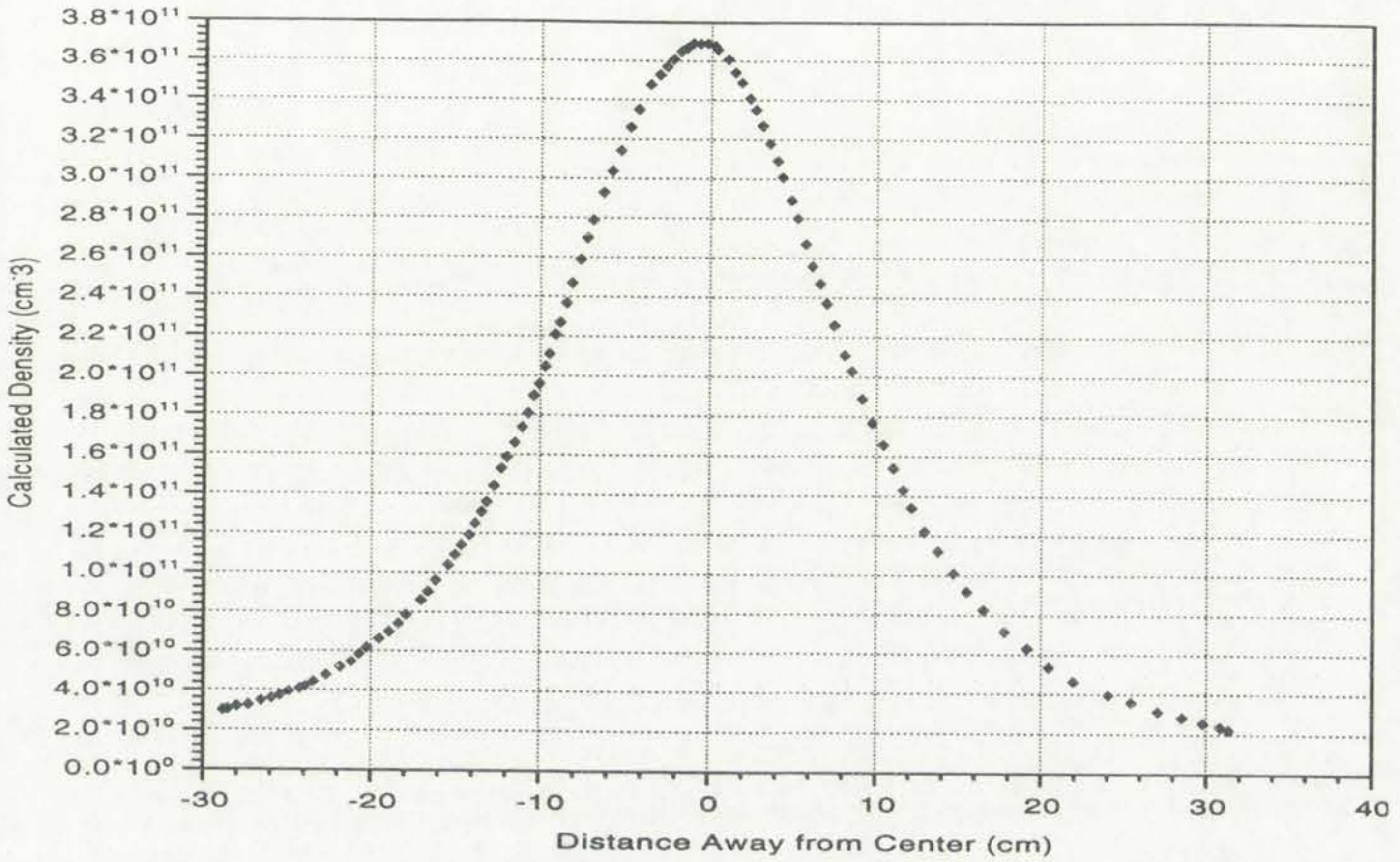

Figure 3-15. Small Antenna. Density vs Z Position
28 mTorr Argon. 5A Top, -4A Bottom, no Permanent Magnets. 800 W

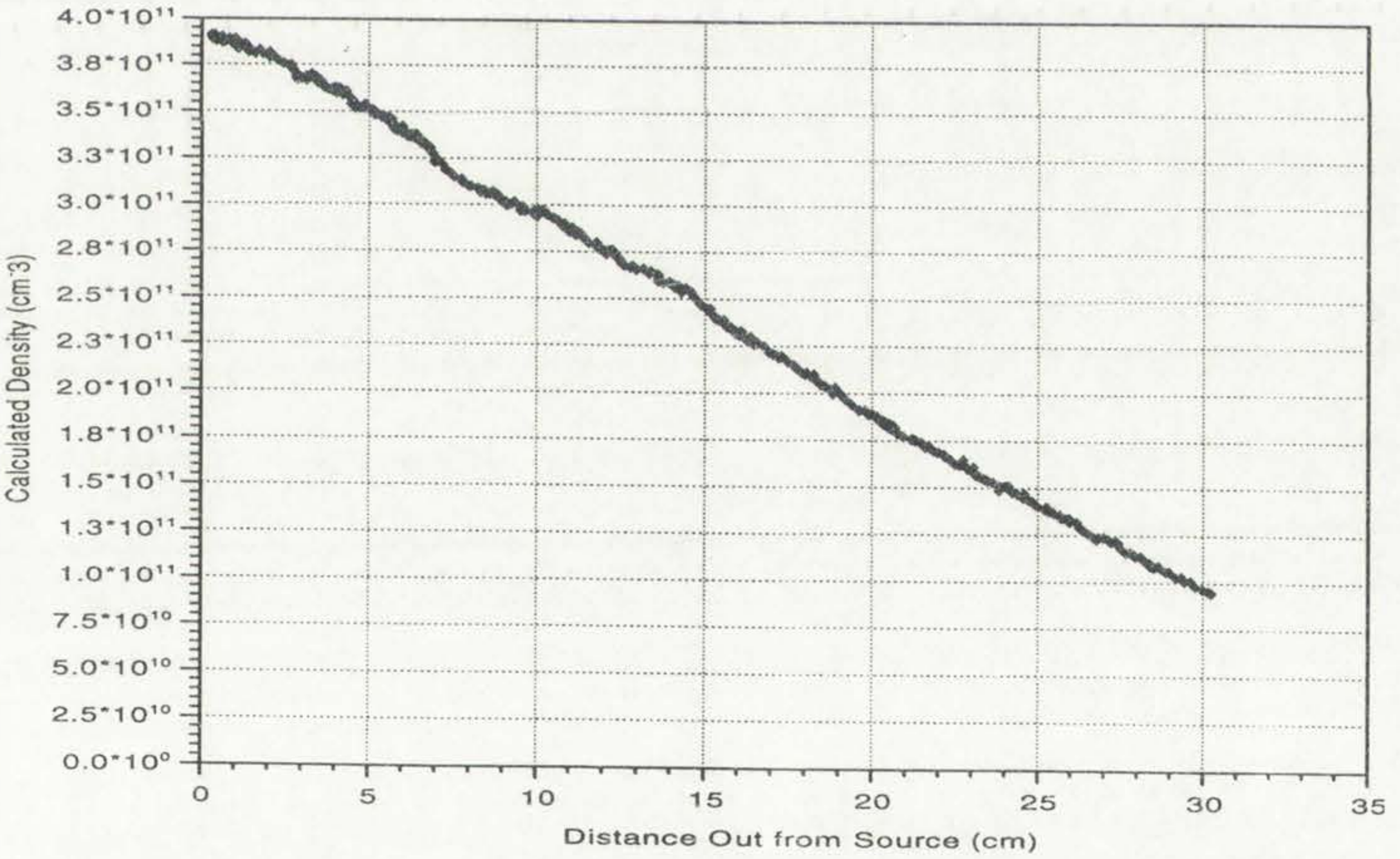

profile, as one might expect. The **Z** scan in Figure 3-15 was again taken with the probe centered between the top and bottom in Y, and centered between the two

sides in X. The linear decrease in density with increasing Z led to a rather novel double-source configuration, which will be discussed more fully later in this chapter.

3.1.3 Four Small Loops. Powered in Parallel, Co-directional Currents.

The natural progression from the first successful small antenna set was to place another set beside it. The method of powering the two pairs was not as clear. The next four antenna configurations presented here focused on how to distribute power between the two pairs. The best method would balance the power deposited in the plasma between all of the loops. The first attempt at powering multiple antennas was to place them all in parallel, with current senses in the same direction (Figure 3-3 [3]). Note that the region between the two loops on the top of the glass looks like an antenna loop with only two sides. The significance of this region became more apparent as development progressed.

A mode jump was easily obtained in this configuration, as is readily apparent in Figure 3-16. However, the mode discontinuity occurred at different powers for each antenna pair, resulting in jumps at 500 and 800W. This imbalance of power is reflected in the density versus position at 17 mTorr along the source shown in Figure 3-17. Density versus power scans at 3, 10, and 17 mTorr follow in Figures 3-18, 3-19, and 3-20. All of the density versus power scans were performed with no permanent magnets in place, with -5 A in the top coil, and -1 A in the bottom coil. Note that this is a slightly different magnetic field than was used in previous experiments. The choice of magnetic field was dictated by the density obtainable at the probe. Optimization was performed at the highest attainable power for the density vs power scans, and at a single intermediate

Figure 3-16. Small Co-directional Pairs. Density vs Power
1 mTorr Argon. -2.5A Top, -1A Bottom, no Permanent Magnets.

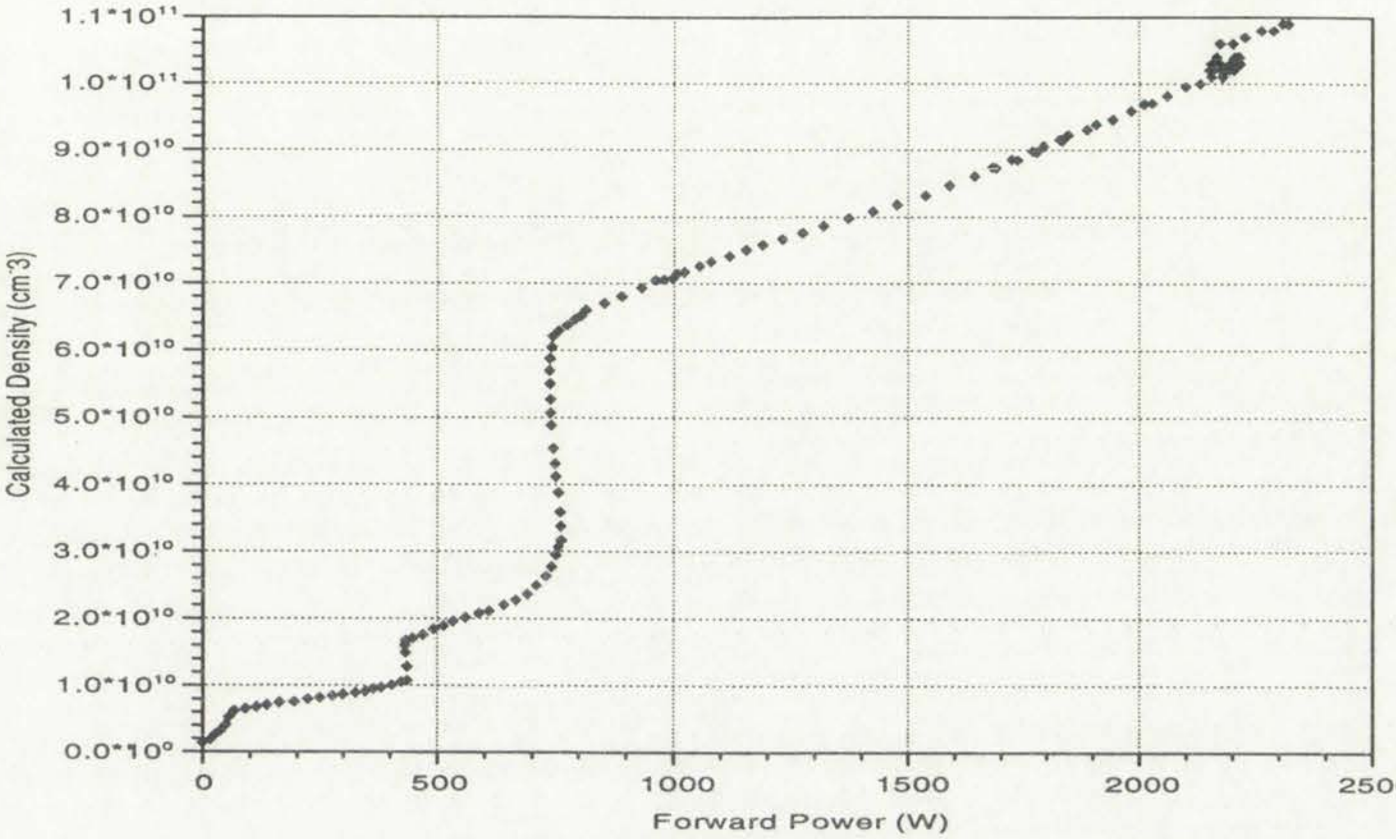

Figure 3-17. Small Co-directional Pairs. Density vs Distance Along Source
17 mTorr Argon. 0A Top, -1A Bottom, One Permanent Magnet Plate. 1200 W.

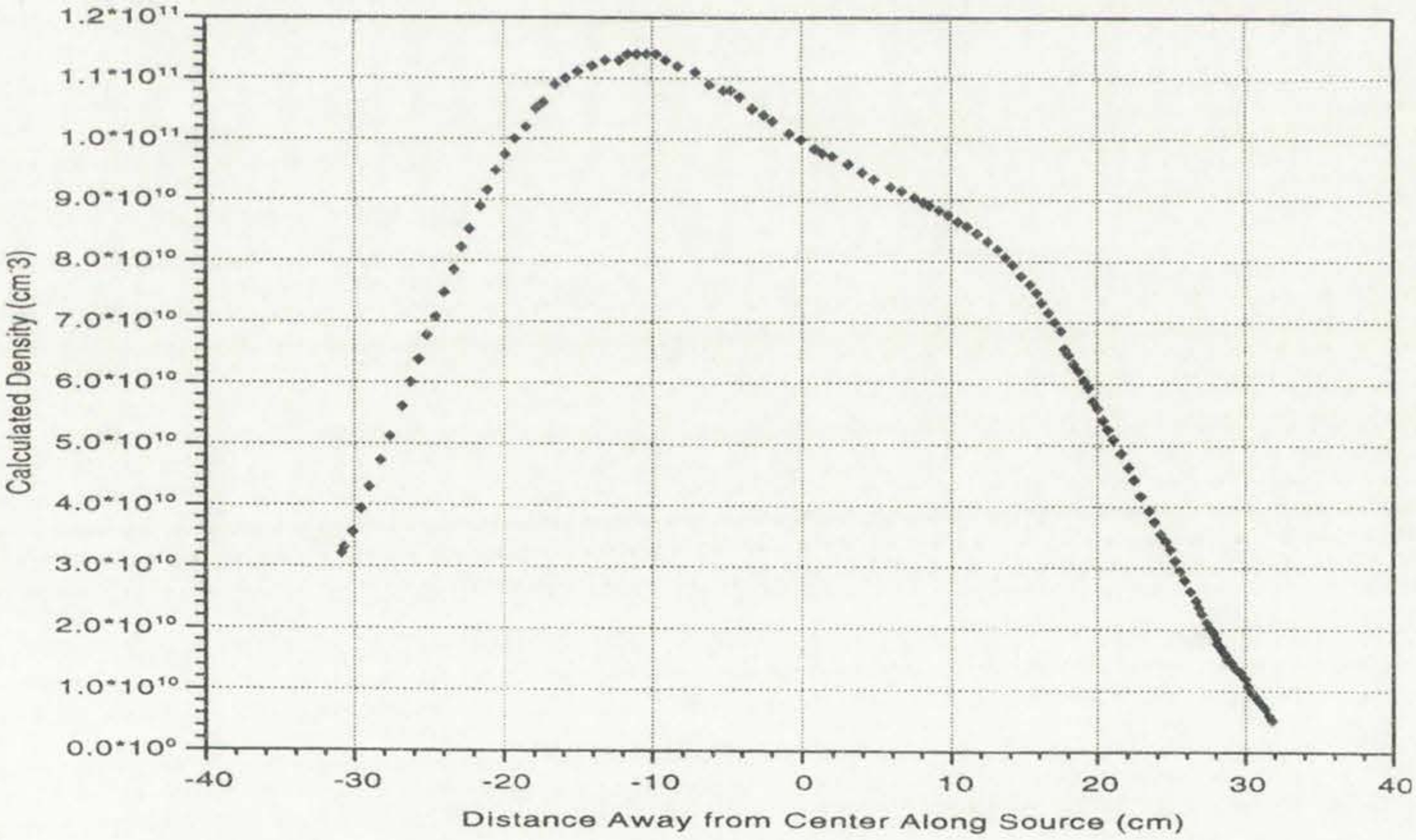

power for the density profiles. Magnetic field configurations were adjusted to obtain the highest saturation current to a probe centered in X and Y, located 5

Figure 3-[illegible]. Small Co-directional Plant. Density vs Power [illegible]

Figure 3-[illegible]. Small Co-directional Plant. Density vs Distance Along Source [illegible]

[illegible]

Figure 3-18. Small Co-directional Pairs. Density vs Power
3 mTorr Argon. -5A Top, -1A Bottom, no Permanent Magnets.

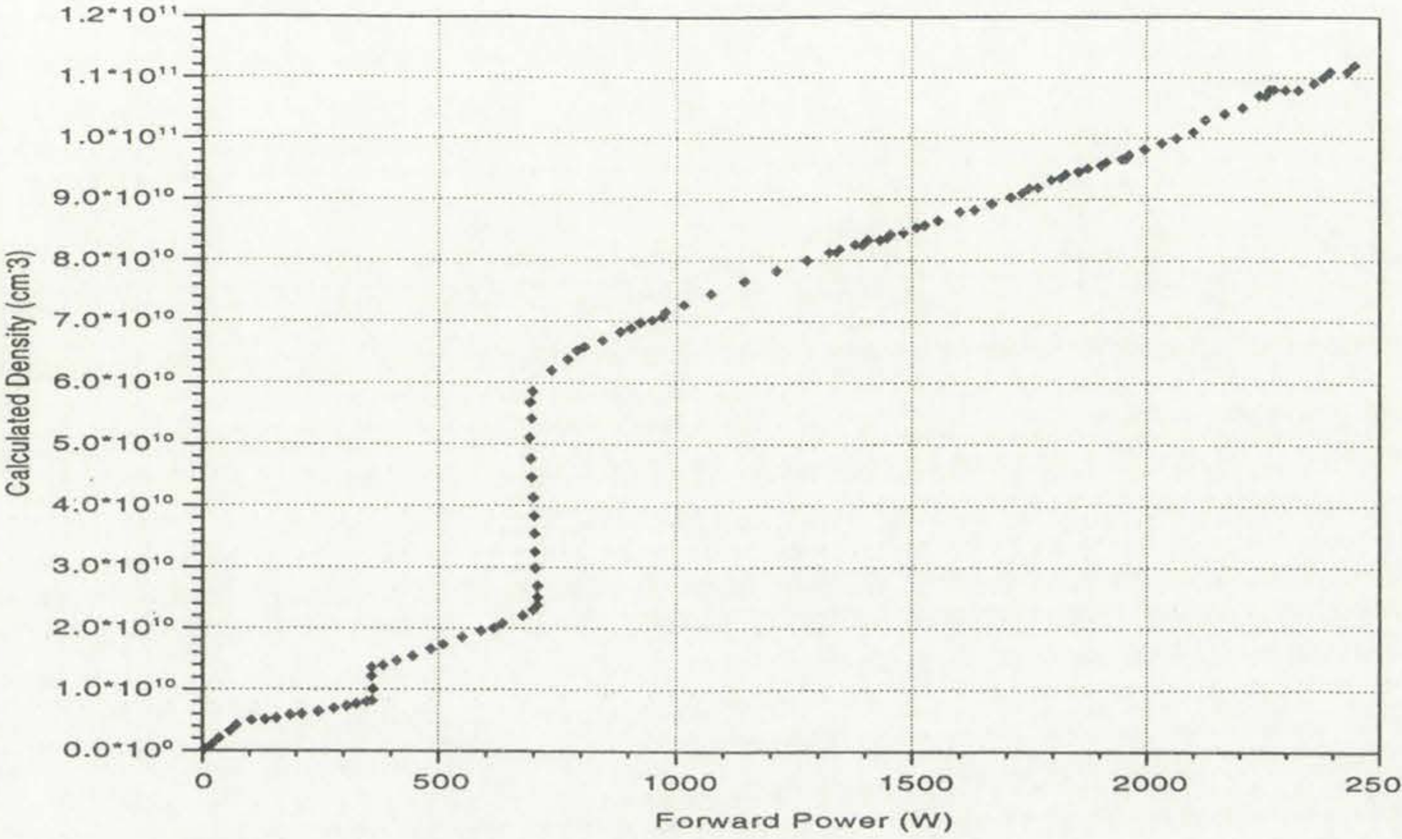

Figure 3-19. Small Co-directional Pairs. Density vs Power
10 mTorr Argon. -5A Top, -1A Bottom, no Permanent Magnets.

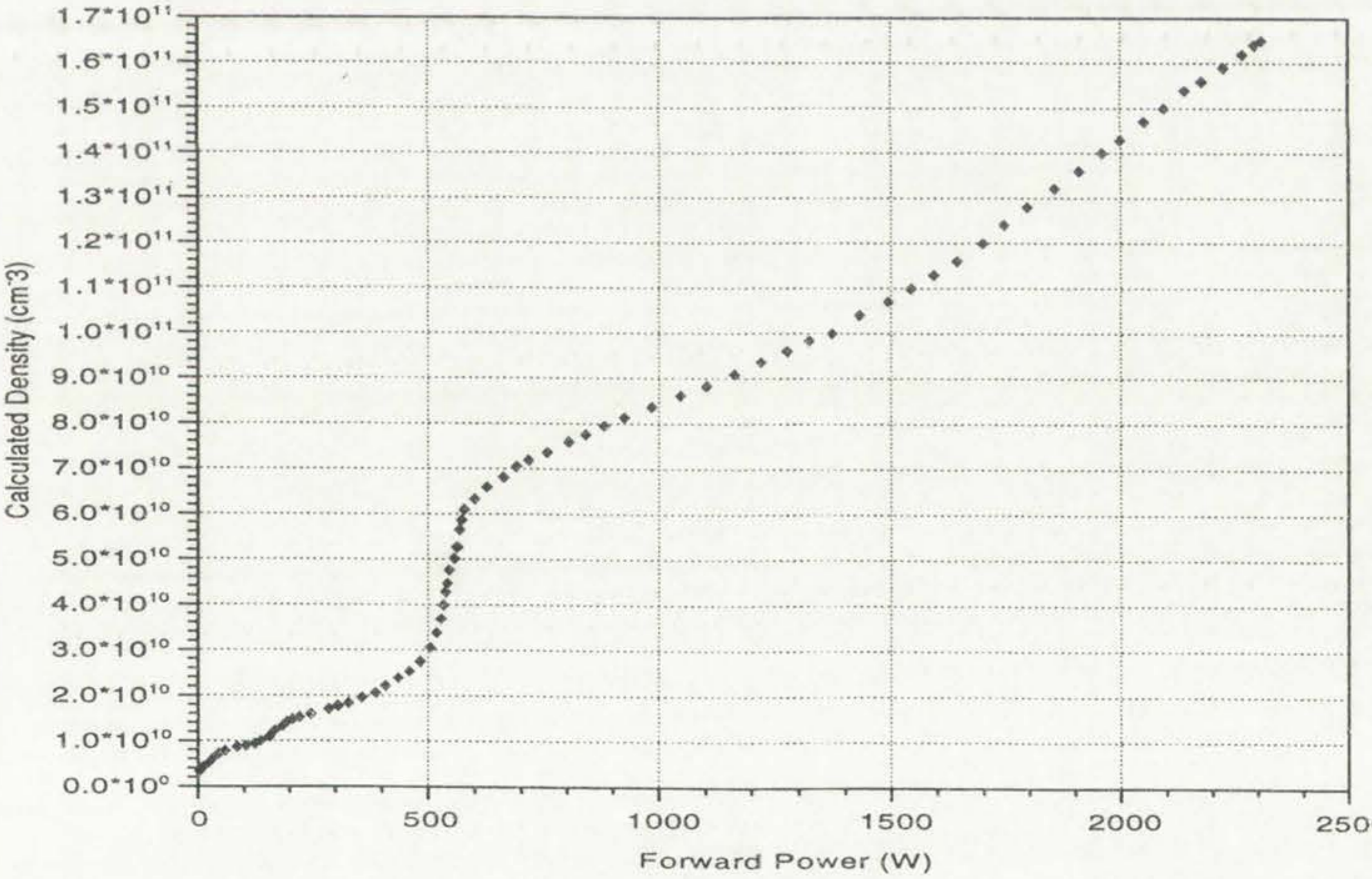

cm out from the source opening. The position scans in Figures 3-17 and 3-21 were made at 1000 Watts, at 17 mTorr, with 0 A in the top coil, -1 A in the bottom

Figure 3-20. Small Co-directional Pairs. Density vs Power
17 mTorr Argon. -5A Top, -1A Bottom, no Permanent Magnets.

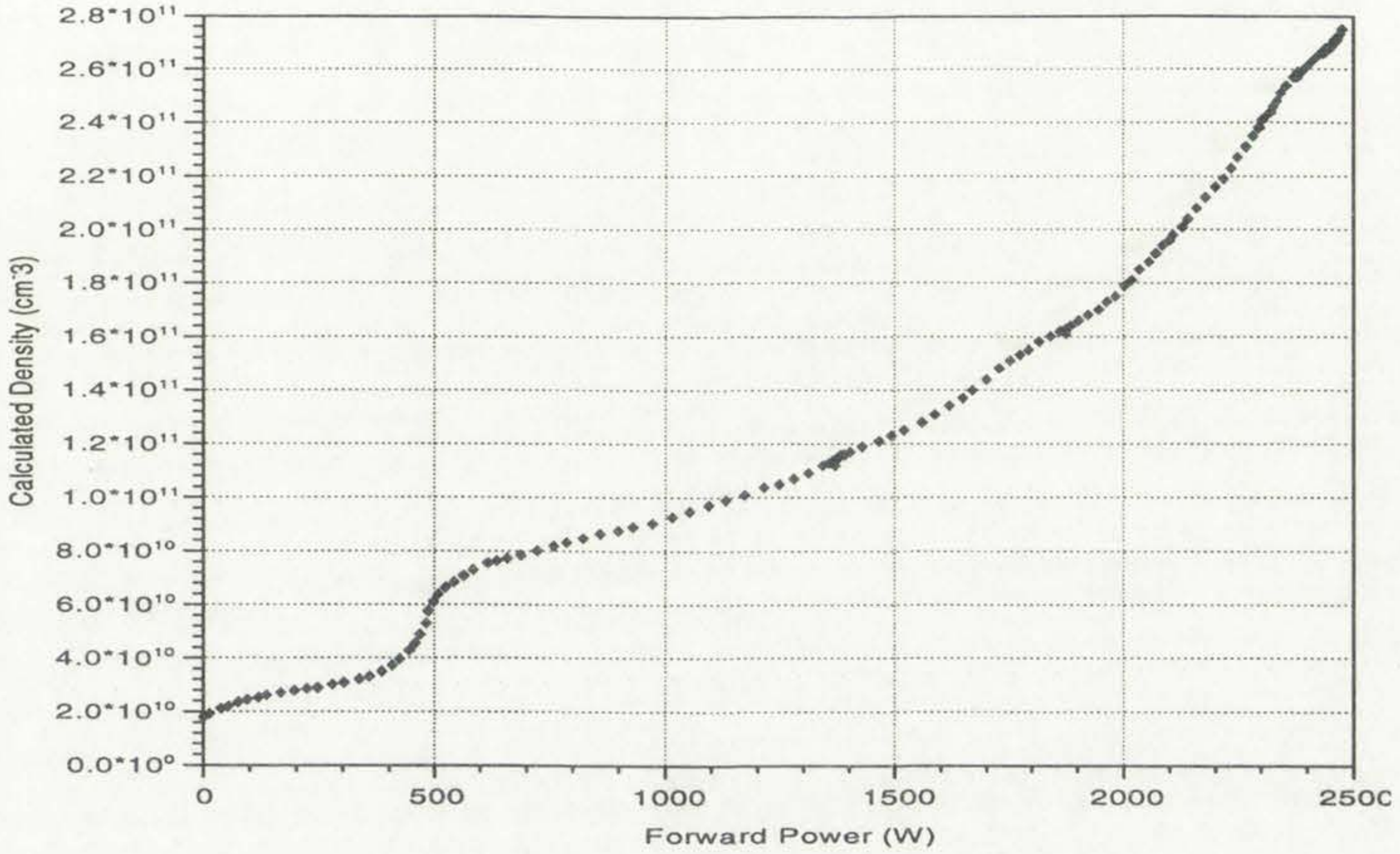

Figure 3-21. Small Co-directional Pairs. Density vs Distance out from Source
17 mTorr Argon. 0A Top, -1A Bottom, One Permanent Magnet. 1200 W.

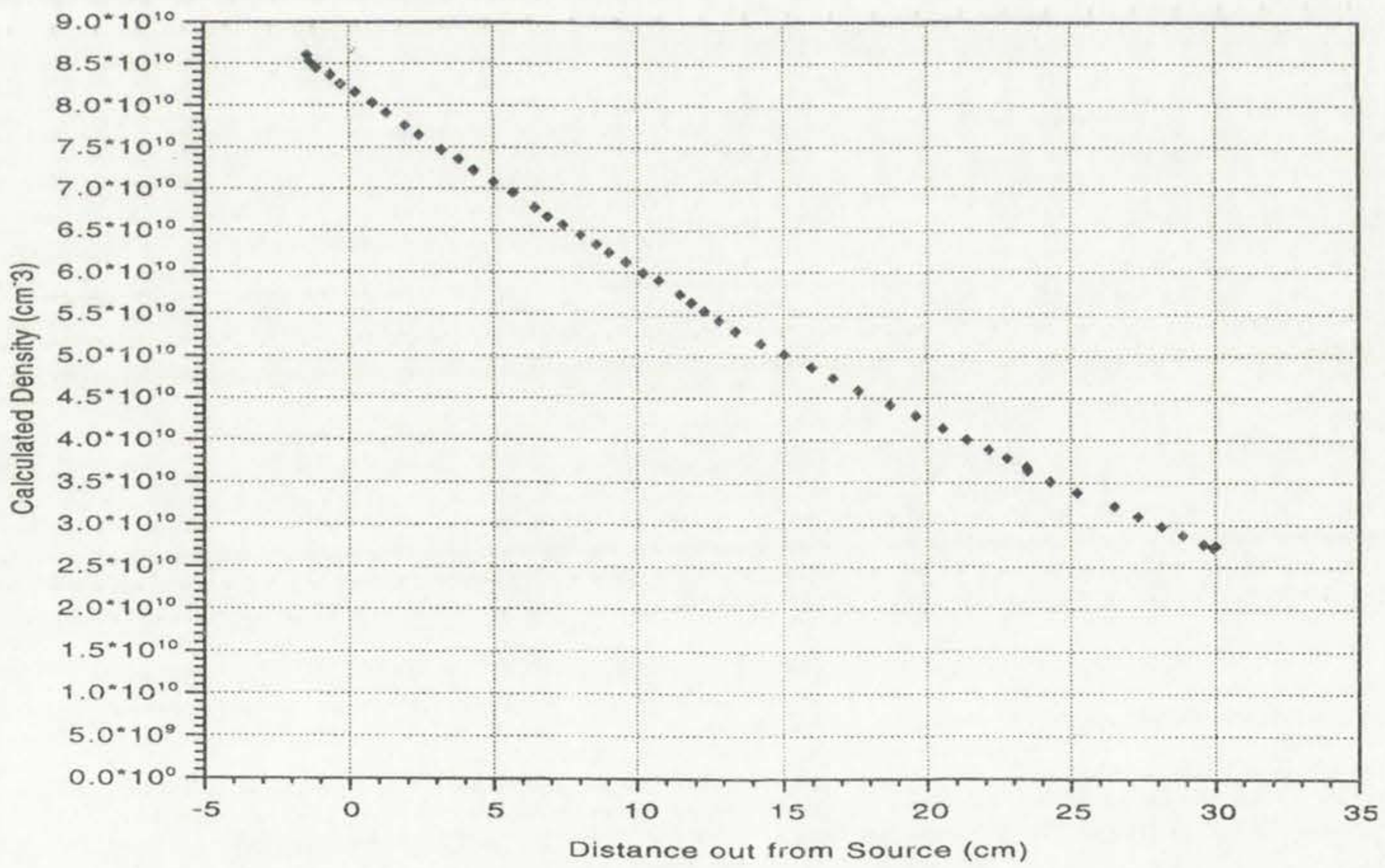

coil, and one 20 G permanent magnetic field plate installed. The scan of density versus **Z** position in Figure 3-21 was made along a center line out from the

source, where the density was not a maximum. This antenna set clearly produced plasma over a substantial fraction of the source length (although not uniformly, as was shown in Figure 3-17). The next section describes the same antenna set, with current senses changed.

3.1.4 Four Small Loops. Two Loops on the Top, and Two on the Bottom of the Source. All Four Loops in Parallel, Opposite Current Senses

Figure 3-22 contains a plot of measured density versus power for this antenna configuration. The same mode changes that were observed with the previous co-directional set are observed here. Given that these two cases have such similar geometries, it is not surprising that the behaviors are similar. However, the density scan along the source shown in Figure 3-23 shows a more marked separation of the regions excited by each of the antenna pairs. The separation

Figure 3-22. Small Anti-directional Pairs. Density vs Forward Power
17.5 mTorr Argon. 5A Top, -3A Bottom, No Permanent Magnets.

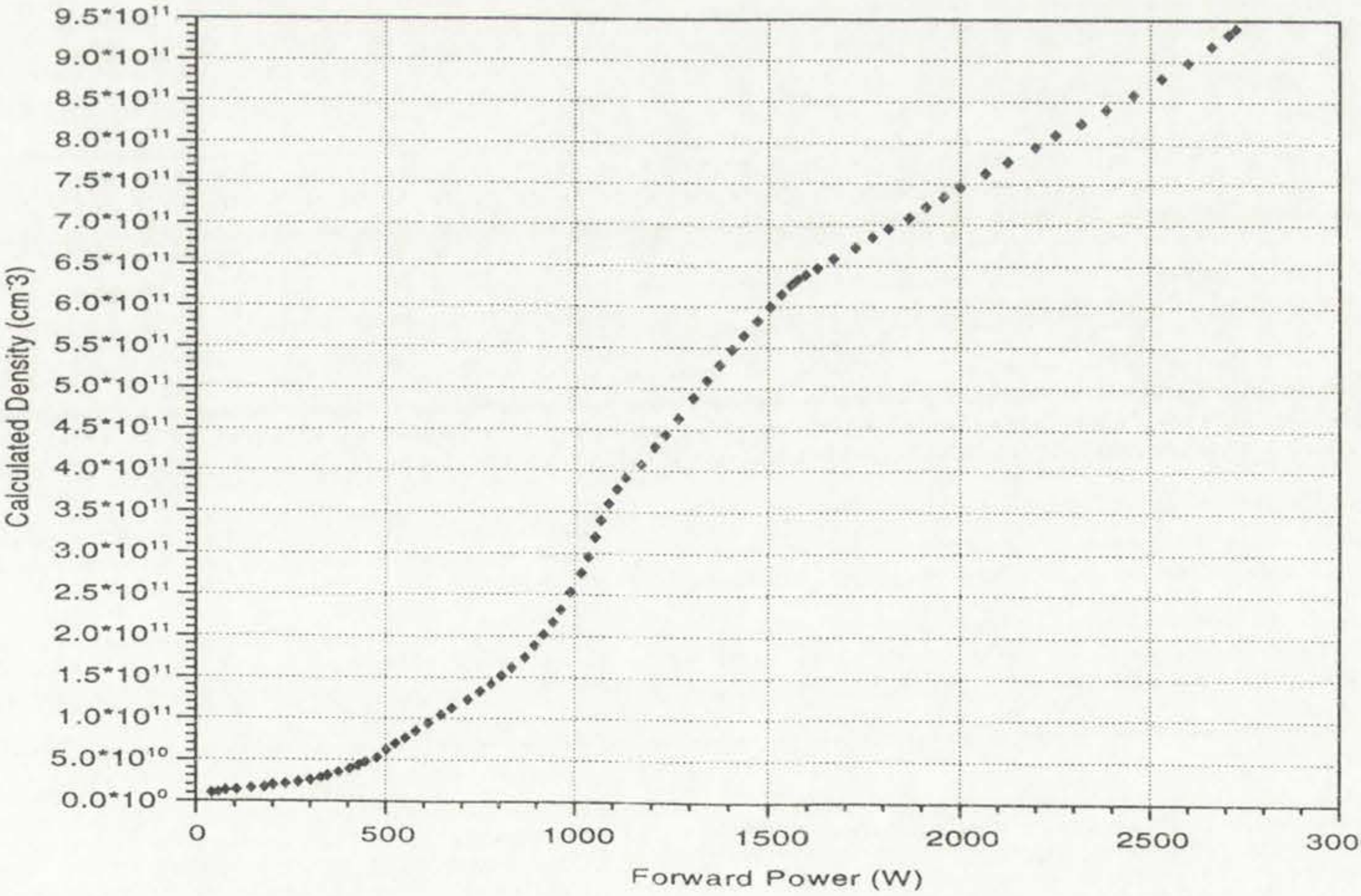

Figure 3-23. Small Anti-directional Pairs. Density vs Distance Along Source 17 mTorr Argon. 5A Top, -3A Bottom, Both Permanent Magnets. 1200 W

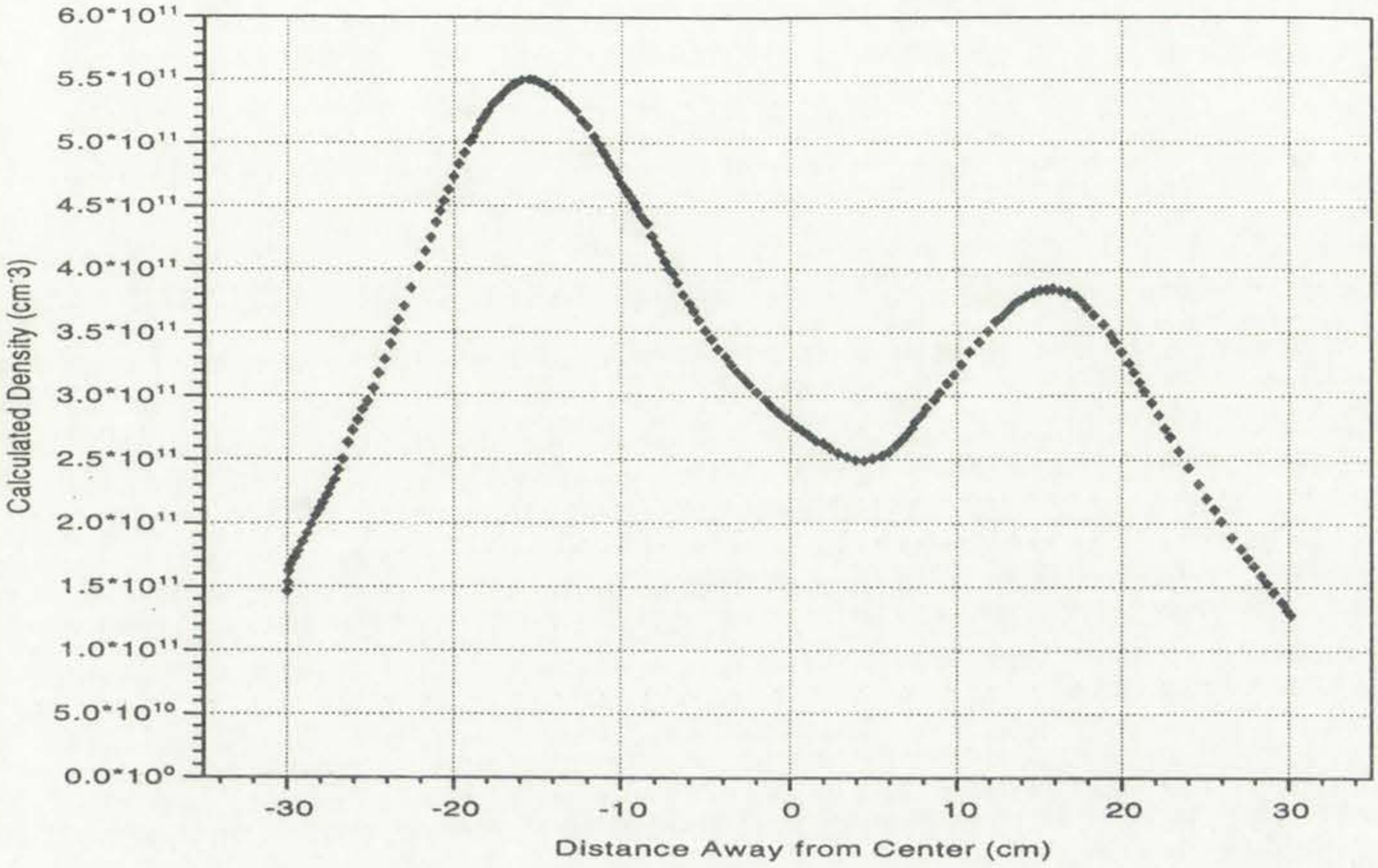

Figure 3-24. Small Anti-directional Pairs. Density vs Distance out from Source 17 mTorr Argon. 5A Top, -3A Bottom, Both Permanent Magnets. 1200 W

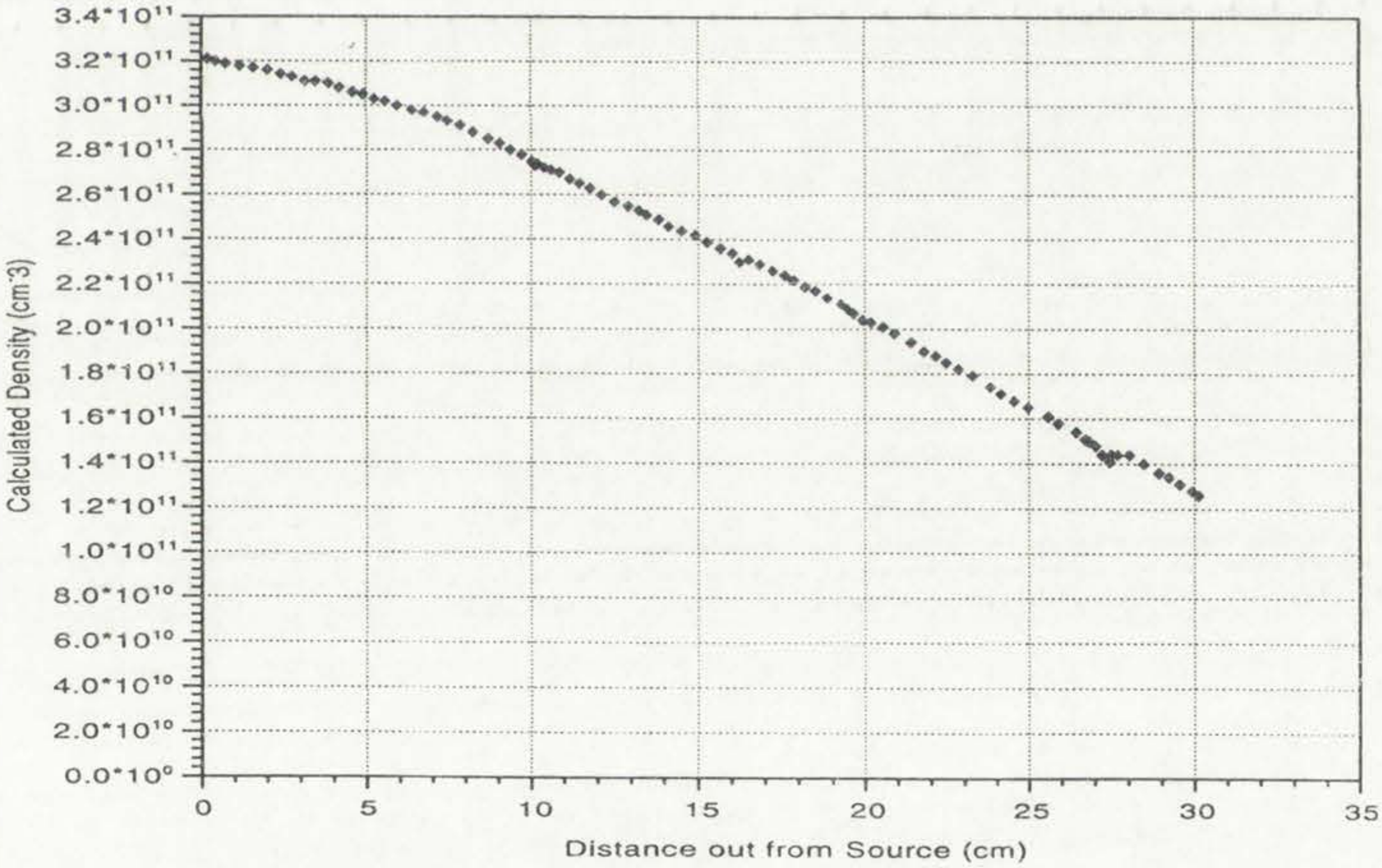

may be caused by the effect of having two co-directional current loops in close proximity to one another, as was mentioned in the previous section. The "virtual

loop" formed by the opposing current segments of the pairs in close proximity couples enough power into the gas underneath to cause a significant smoothing effect. This effect is apparent in the density differences at 0 cm seen between Figures 3-23 and 3-17. Note that the peak density for this case was substantially higher than for previous cases, and that the profile in the **Z** direction remained close to linear (Figure 3-24). The reason for the increased density remains unclear.

3.1.5 Two Small Current Pairs in Series. Same Current Sense.

Both of the previous antenna sets exhibited imbalances in the plasma density underneath the separated antenna pairs. Both sets were being driven in parallel, hence the current carried in one set could be quite different from that carried in the other. Different currents could arise from different antenna distance from the plasma, or slightly different loop areas. In an effort to address this problem, two of the parallel connections were changed to series. The loop pairs on either end of the source were connected in series with each other by joining them at the back of the source, as is shown in arrangement 5A in Figure 3-3.

Signs of hot spots in the tuning box led to a redesign of the box and its copper components. Ideally, all components of the tuning box, power connections and antennas should be free of any resistance. Unfortunately, there are always small resistances in the materials (copper) which make up the components, and in particular, in the connections made between components. Even small resistances from slightly oxidized parts become power sinks in the presence of the large circulating currents found in the tuning circuit. A major refit of all of the components was performed at this time, with a substantial improvement in power

Figure 3-25. Small Pairs in Series (A). Density vs Position along Source
50 mTorr Argon. 5A Top, -1A Bottom, No Permanent Magnets. 1500 W

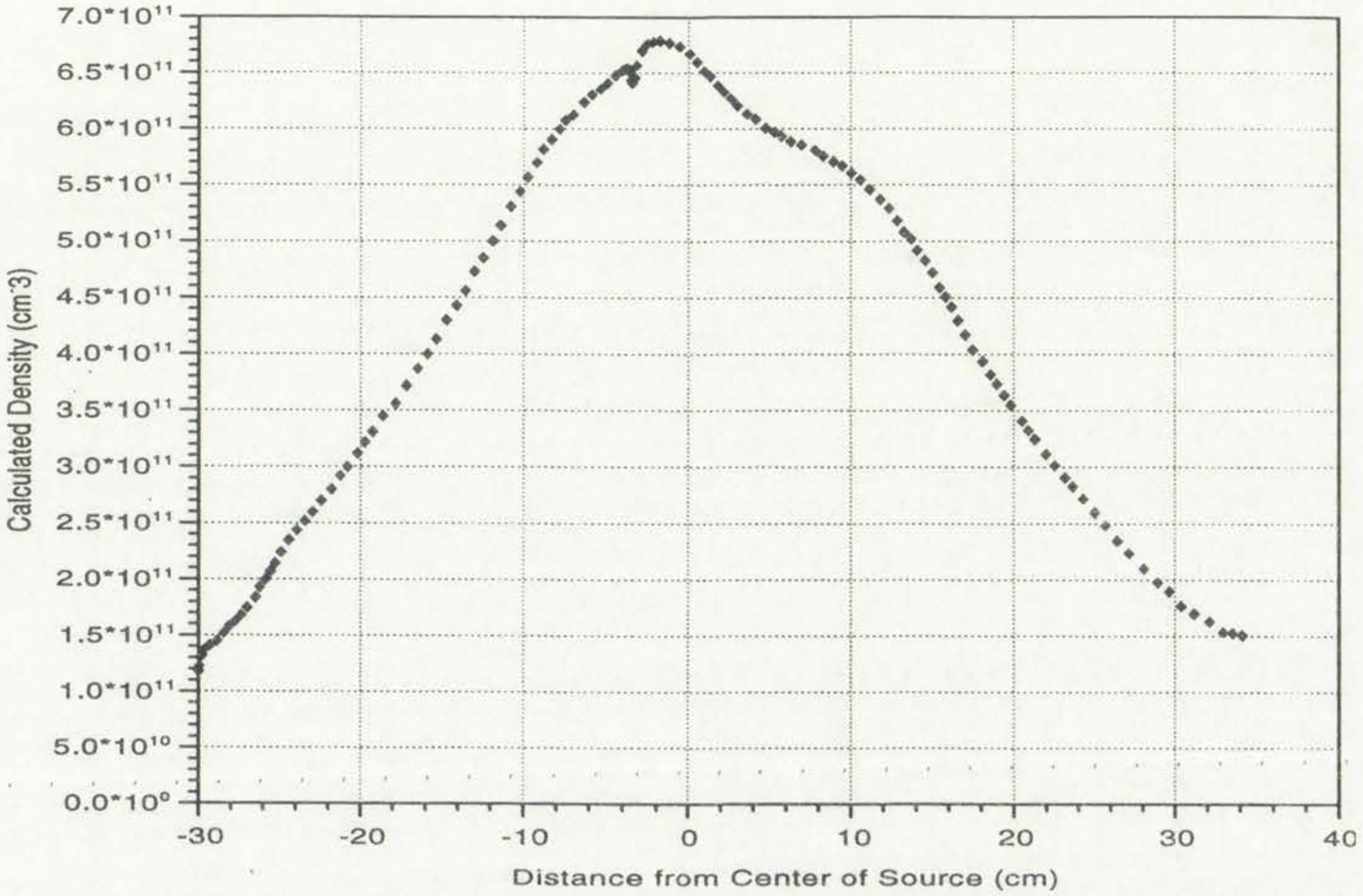

coupling and a reduction of heat dissipation in the tuning box. Connections between the tuning capacitors were replaced, with particular attention being given to making current paths shorter and wider. Contacts between capacitor and conducting elements were changed from single-screw type connections to large-area plates with multiple bolt attachments. Figure 3-25 illustrates the marked improvement in source performance after the refit. Plasmas at 50 mTorr prior to the refit were approximately one-half as dense.

Densities of up to 8 x 10^{11} cm^{-3} were observed with this set, which made it the most promising of the set. Coupling to the plasma was still nonuniform, as is evidenced in Figure 3-25. The strong central peak indicates that the center anti-parallel segments of the antenna set did contribute to excitation in the

Figure 3-[illegible] [illegible]

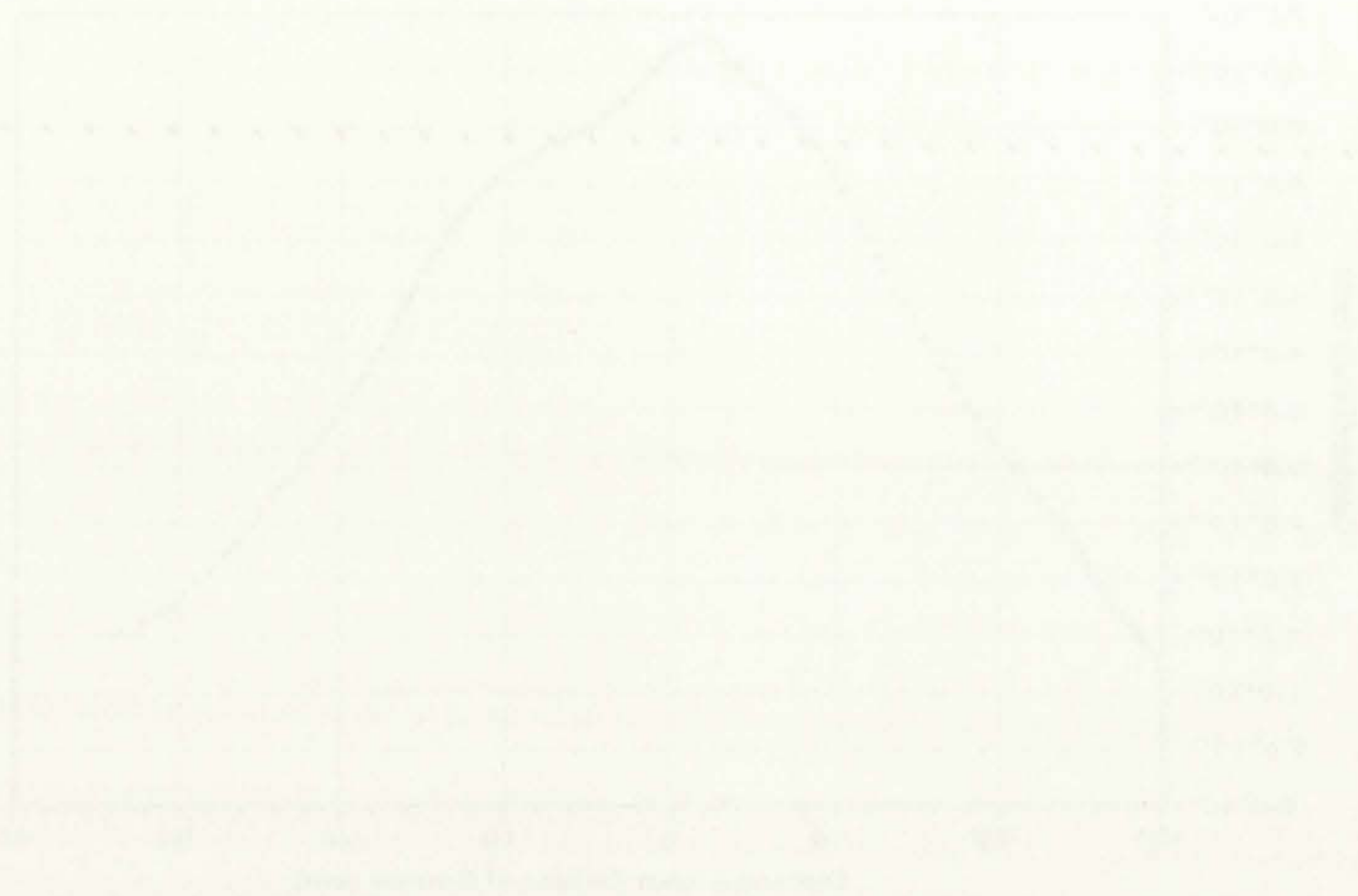

coupling and a reduction of heat conduction in the tuning [illegible]. Connections between the [illegible] capacitors were improved, with particular attention being given to routing current [illegible] and [illegible]. Contacts between capacitor and conducting elements were changed from single-screw type connections to large area clamps with multiple bolt attachments. Figure 3-[illegible] illustrates the marked improvement in [illegible] performance after the [illegible]. Pressures of [illegible] prior to the tests were approximately one-half as [illegible].

[illegible] of up to 3 x [illegible] were [illegible] with this test, which made it the [illegible] according to the [illegible] was still non-uniform, as is evidenced in Figure 3-[illegible]. The strong central peak indicates that the [illegible] plasma, in a manner similar to Figure 3-17. Because this configuration produced more dense plasmas, a further modification (shown in Figure 3-3 [5B]) was made by making the series connection between the antenna pairs part of the antenna itself. Version 5B gave the most dense plasma over the largest area, and led to the antenna choice used for the rest of the project. It will be discussed in detail in subsequent sections.

3.2 THE SERPENTINE ANTENNA AND OTHER SOURCE CONFIGURATIONS

The small looped antennas driven in series showed considerable promise for use in the large area tool. Plasma was generated over the entire source length, and each antenna pair appeared to be able to induce a mode change (albeit, rather independently of each other). Using what was known about the fundamental mode structure of the source, and the small antenna experiments, a new antenna was proposed. The antenna was made of individual semicircles designed to excite the fundamental modes in X and Y. The series of semicircles

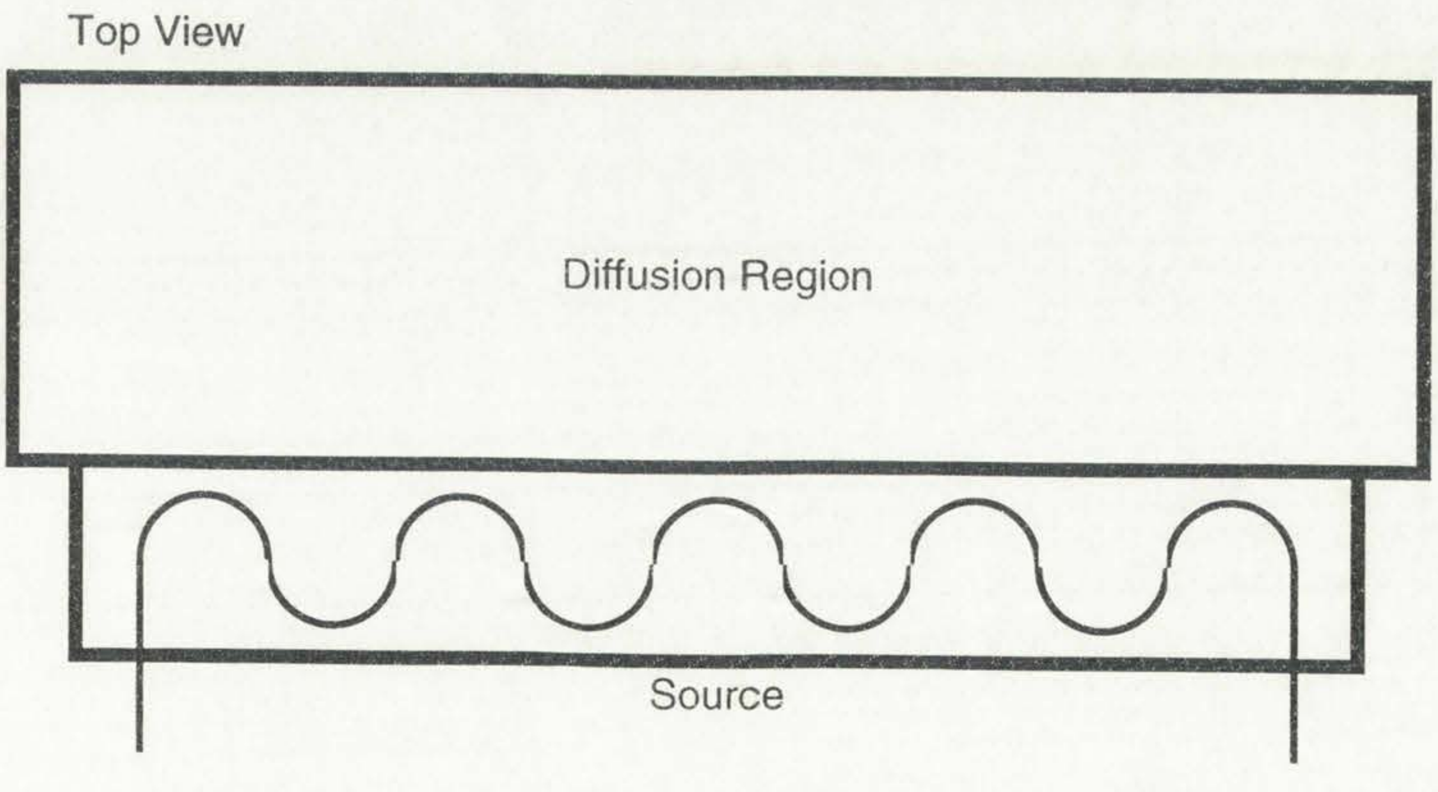
Figure 3-26. Serpentine Antenna on Source

joined together were dubbed "the serpentine antenna". Figure 3-26 shows a schematic of the serpentine antenna as it appeared mounted on the source. The antenna was constructed of 1 cm wide copper strap formed into 8 cm radius loops. Experiments were performed with a serpentine installed on the top and the bottom of the source. A typical plot of density variation versus position along the source powered with this antenna is shown in Figure 3-27. Note that the density profile is quite uniform over 33 cm. That is not to imply that the desired large area uniformity was present, as the density again dropped off considerably as the probe was moved out from the source (Figure 3-28). If this device were going to be used in a manufacturing environment in its present configuration, clearly the wafer could not be processed parallel to the **Z** axis. A wafer could, however, be processed perpendicular to the **Z** axis because the density variation

Figure 3-27. Serpentine Antenna. Density versus Position along the Source 7.05 mTorr Argon. 5 A Top Coil, -1.5 A Bottom Coil. 2000 W

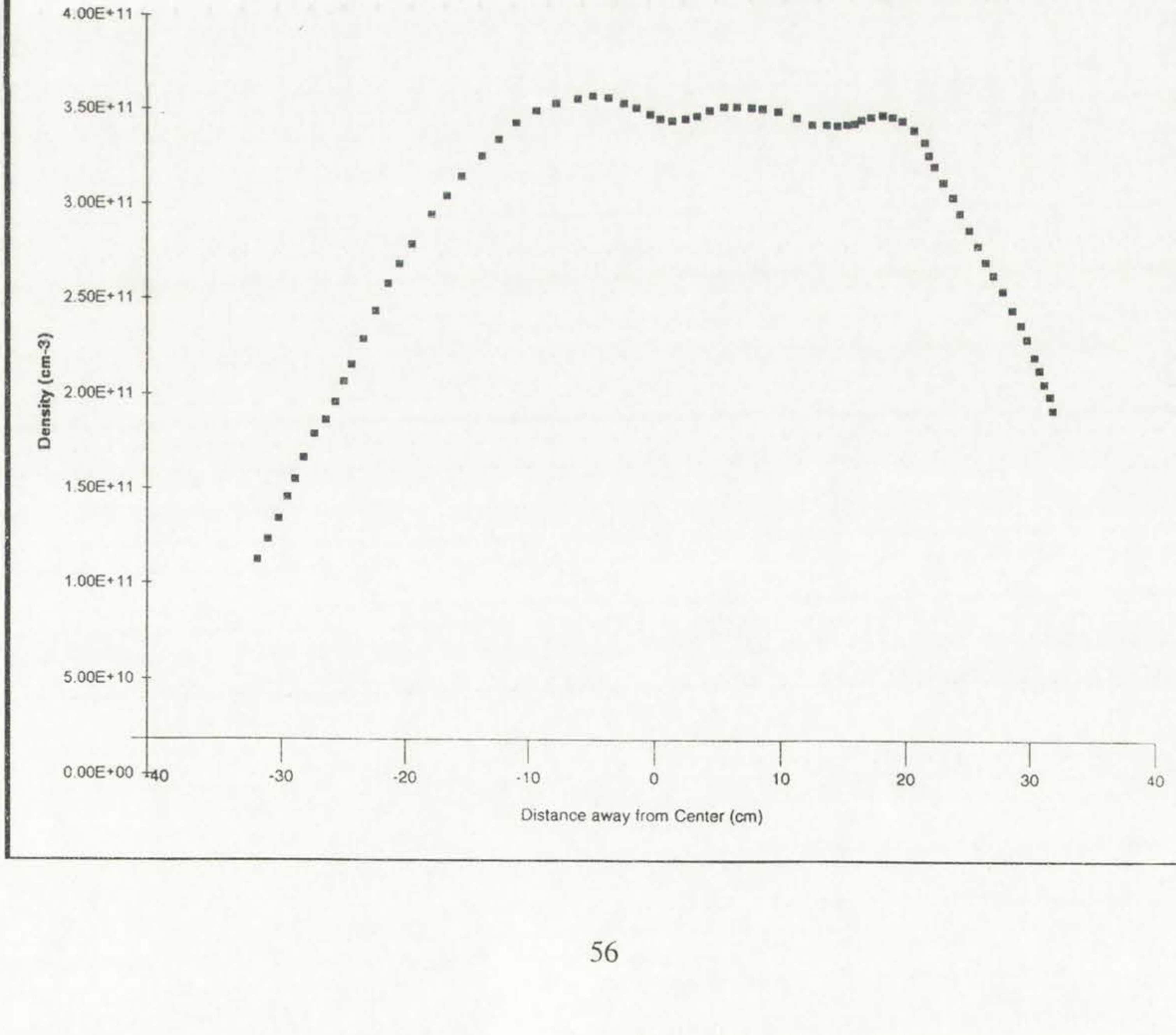

Figure 3-28. Serpentine Antenna. Density versus Distance out from Source
7.05 mTorr Argon. 5 A Top Coil, -1.5 A Bottom Coil. 2000 W

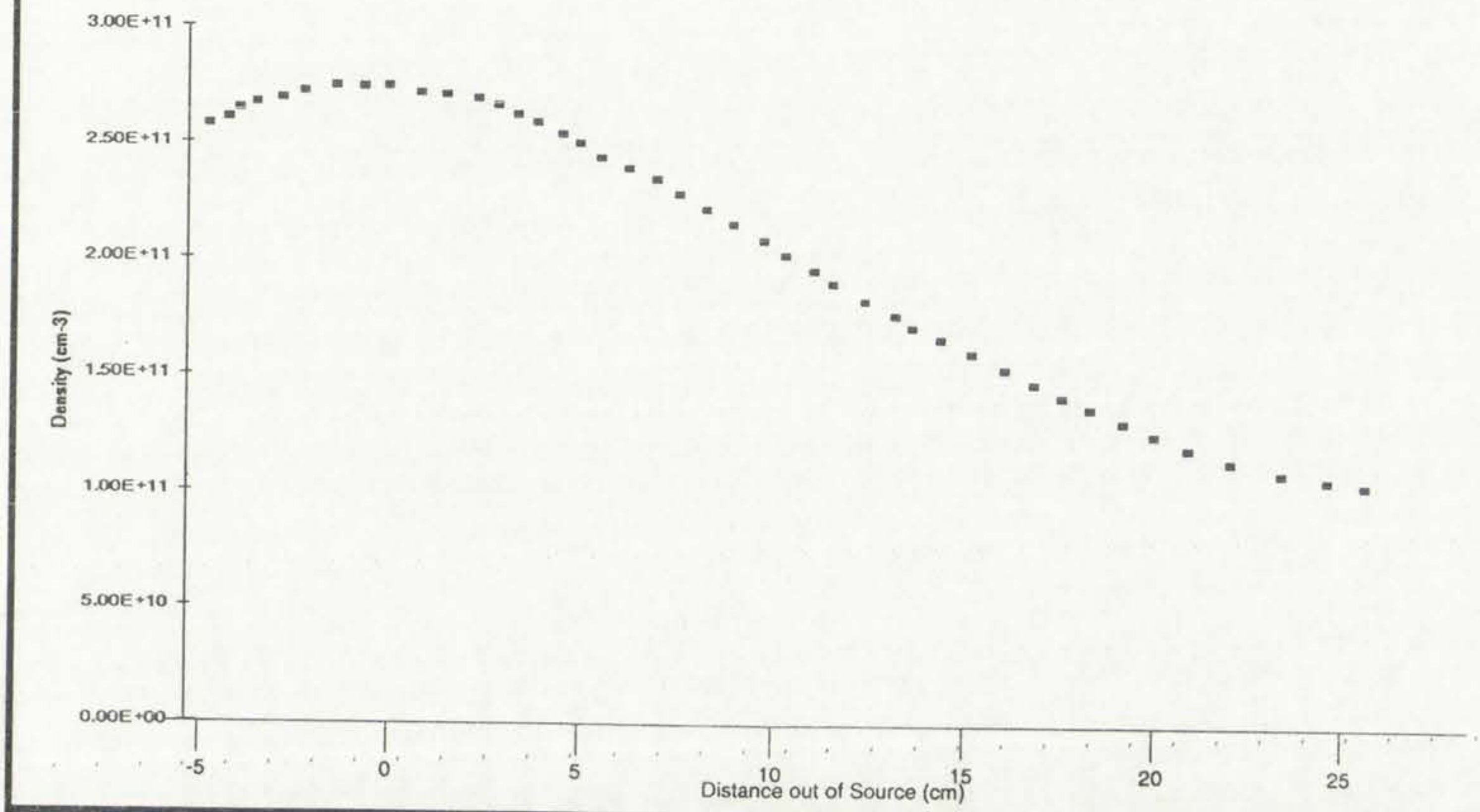

Figure 3-29. Serpentine Antenna. Density versus Height
7.05 mTorr Argon. 5 A Top Coil, -1.5 A Bottom Coil. 2000 W

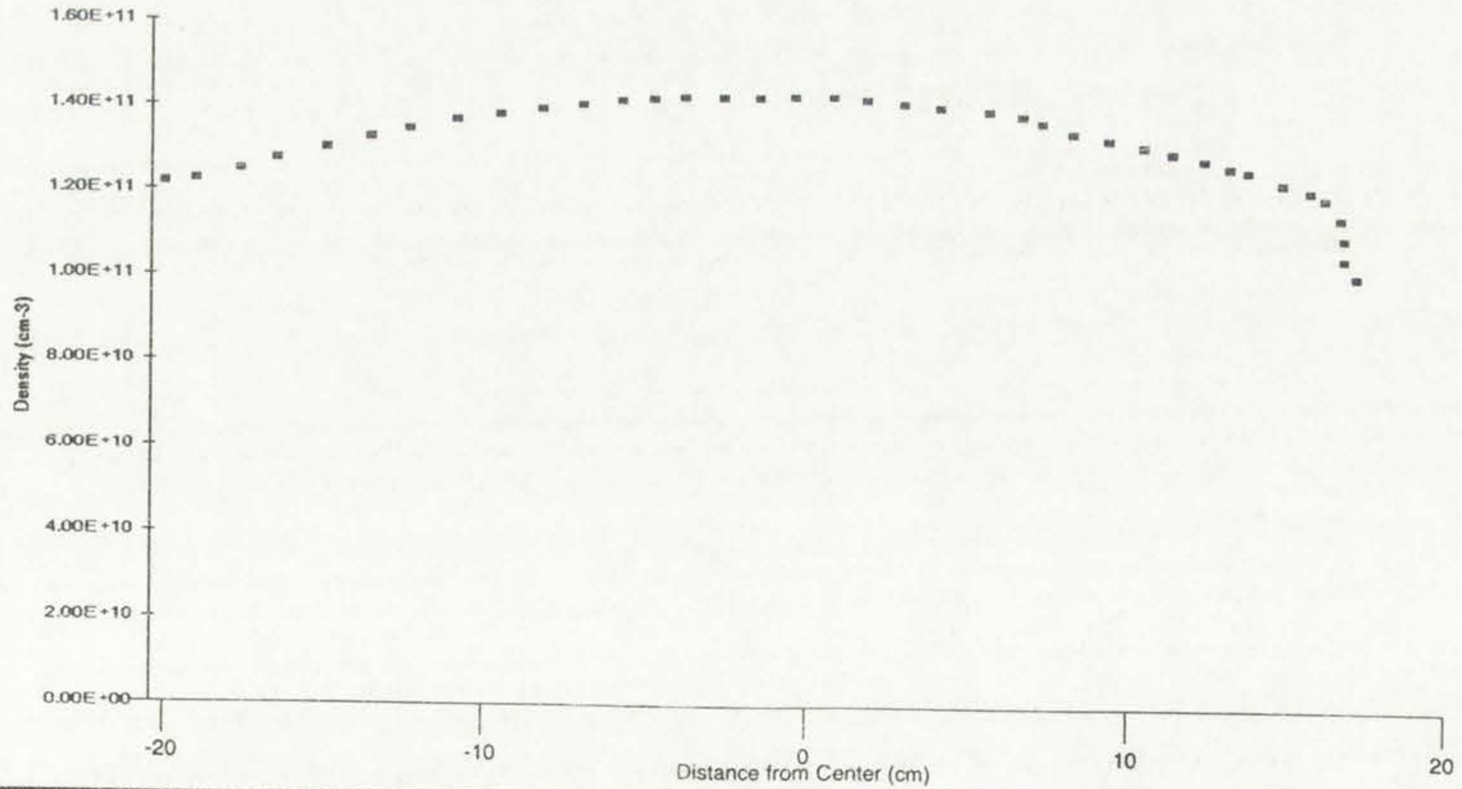

with height in the chamber is minimal (see Figure 3-29). The serpentine antenna was used throughout the rest of the linear tool characterization.

In the following set of experiments, the scans with the serpentine antennas located on the top and bottom of the source in 3-27, 3-28, and 3-29 were used as a base line, and measurements were made in the following 4 arrangements:

1. glass dielectrics on the top and bottom, but only the top antenna segment installed,

2. top antenna segment installed, bottom glass dielectric replaced with an aluminum plate,

3. an all ceramic source (one and two antenna segment experiments repeated), and

4. using a source with a moveable aluminum back wall to change the aspect ratio. Three wall positions were used.

The remarkable feature of each of the new arrangements was the similarity they had to the original profiles. The material composition of the source and the parallel wave number (which is limited by the position of the back wall) seemed to have very little to do with the source performance, at least in terms of density profiles. Individual results for all four of the experiments will not be exhaustively reproduced here, but rather a sample of five different profiles is presented to show the similarities. Figure 3-30 shows the variation of density with position along the source powered by a single-sided serpentine antenna, with a dielectric in place on the bottom. The very similar plot shown in Figure 3-31 is the same

antenna configuration, with the bottom dielectric replaced by the conducting aluminum plate. Finally, Figure 3-32 shows the same general behavior for the all ceramic source (except for a small increase in density, which may be attributed to the use of antenna segments on both the top and bottom of the source). All of the scans along the chamber length were taken at a distance of 5 cm out from the mouth of the source, as before.

The density profile as a function of distance out from the source was not effected by whether the source was composed of dielectric or conducting material, but had a slight dependence on whether the source was powered by an antenna pair (top and bottom), or a single-sided antenna. Density profiles in **Z** for single-sided sets in Figure 3-28 tended not to be as flat as when powered with an antenna pair. Rather, the profile appeared to have an inverse dependence on distance out from the source as is evidenced in Figure 3-33. Note that the probe used in

Figure 3-30. Single Serpentine Antenna. Density versus Distance away from Center. 7.12 mTorr Argon. 5 A Top Coil, -1.5 A Bottom Coil. 2000 W, Glass Source Bottom

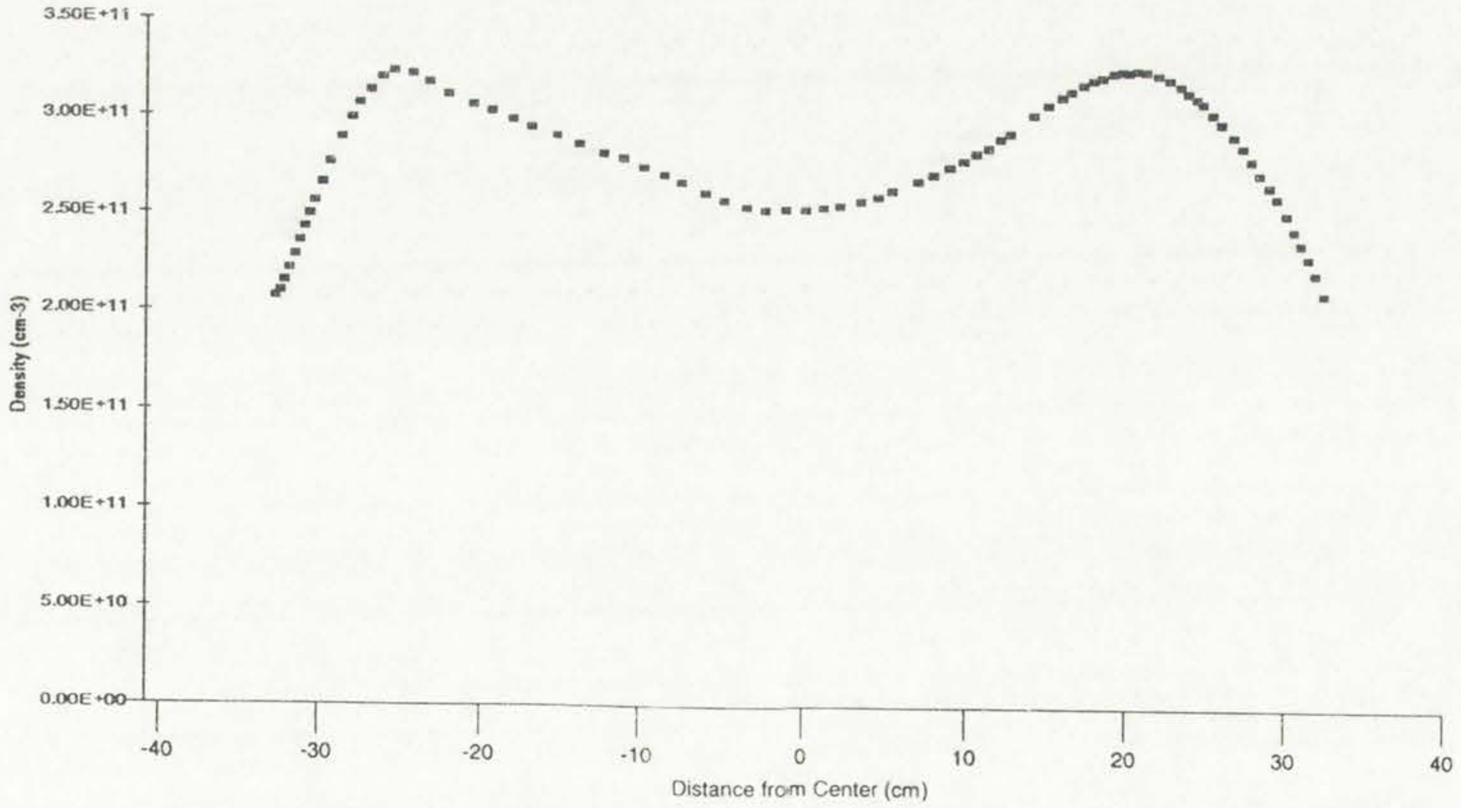

Figure 3-31. Single Serpentine Antenna. Density versus Distance away from Center. 7.12 mTorr Argon. 5 A Top Coil, -1.5 A Bottom Coil. 2000 W, Aluminum Source Bottom

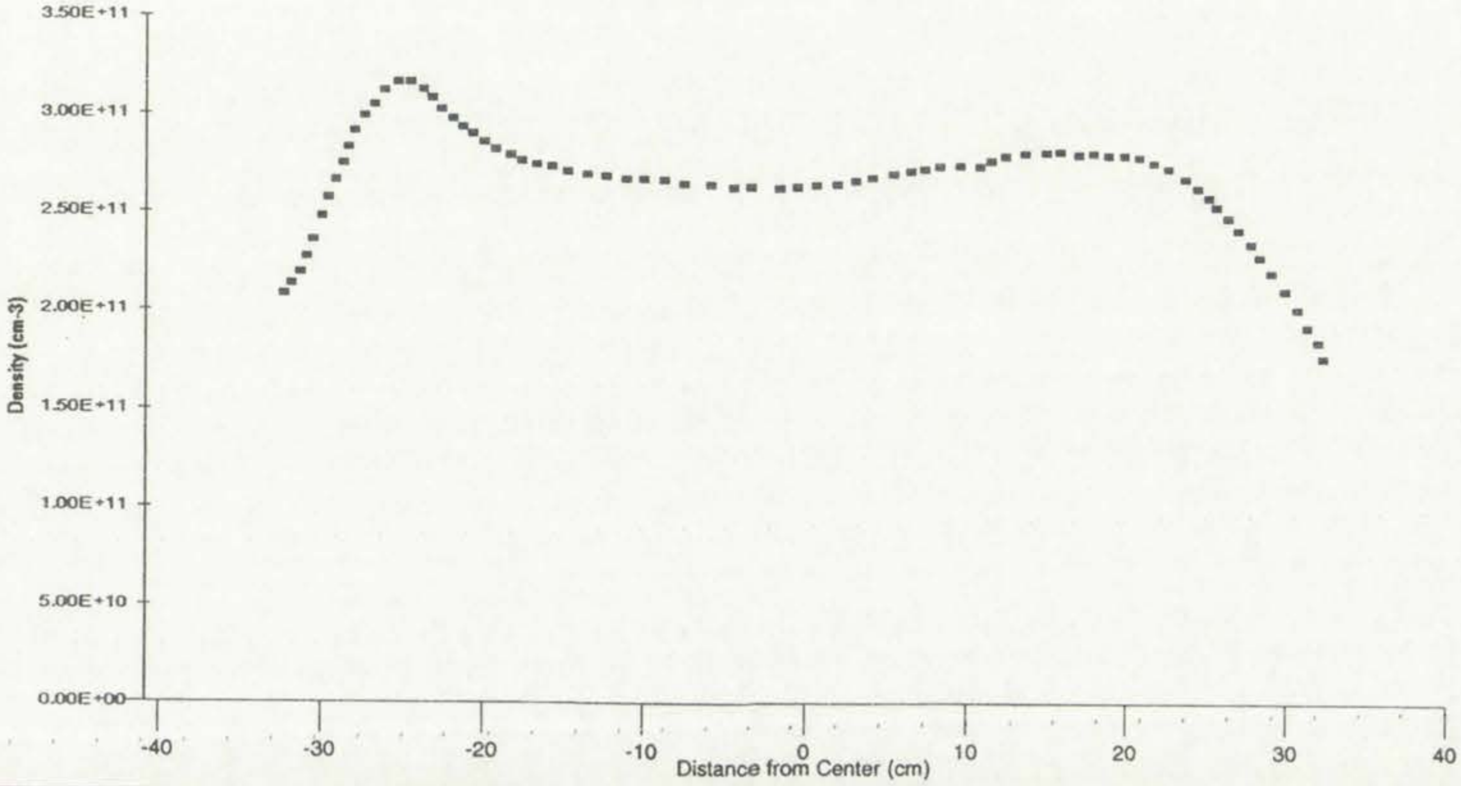

Figure 3-32. Double Serpentine Antenna. Density versus Distance away from Center. 7 mTorr Argon. 5 A Top Coil, -1.5 A Bottom Coil. 2000 W, All Ceramic Source

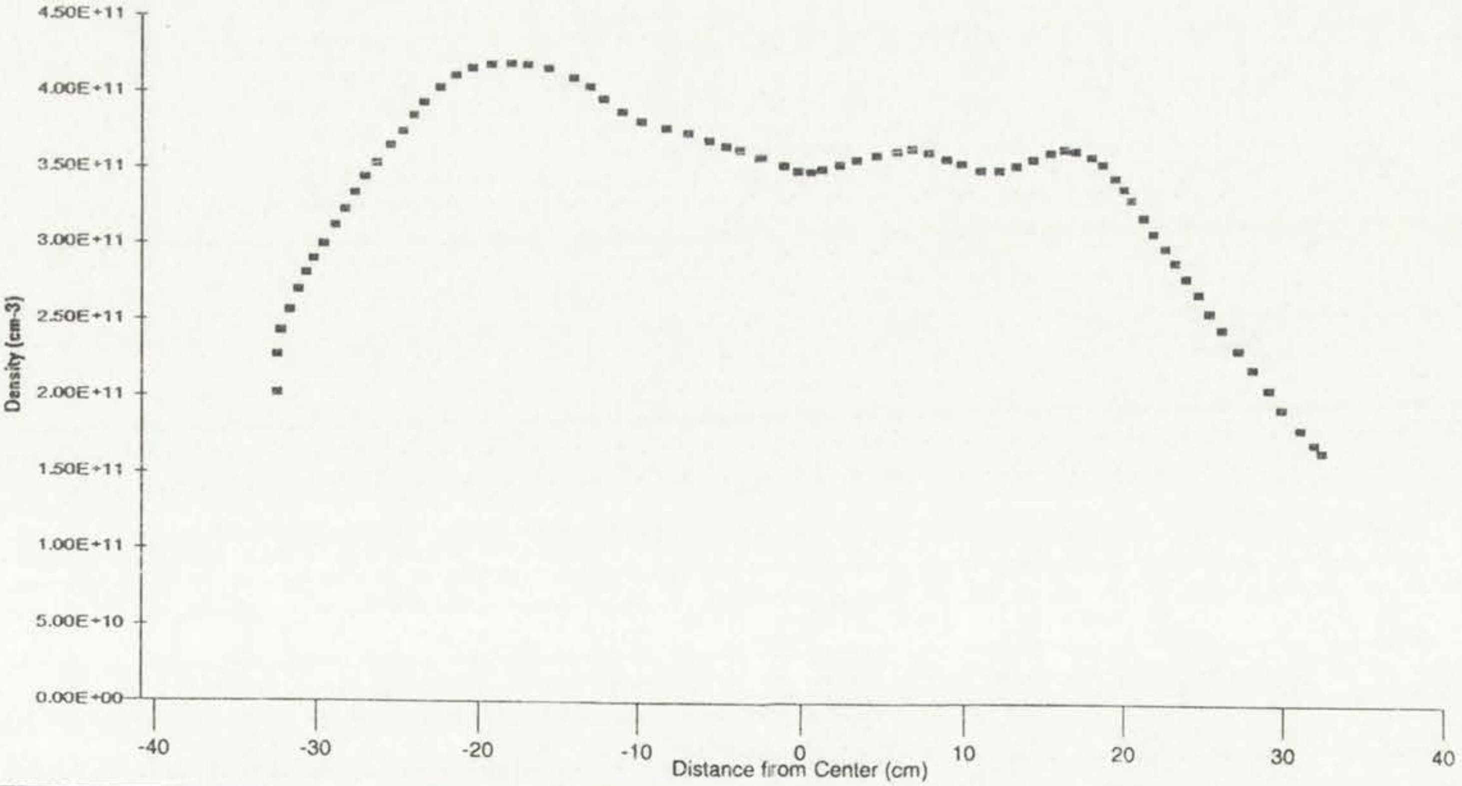

previous measurements of saturation current has been replaced with a longer probe, with an inductive filter constructed into the tip (whose purpose will

become apparent in the next chapter). Although it was able to extend into the source (hence the negative positions in Figure 3-33), it was not able to cover the same distance in the diffusion chamber. Whether the inverse distance dependence of the density is important is unclear at this time, particularly given that profile will look different if this source (or antenna) is ever used in a cylindrical ring source.

For the two source experiments, the diffusion chamber was replaced by a chamber which could have sources mounted on both sides, diametrically opposed to each other. That is, it could be configured with one source facing another source mounted on the opposite side. The second source was fitted with a moveable back wall, designed to examine aspect ratio effects. Shown in Figure 3-34 are density profiles as a function of **Z** position for three different aspect ratios. Scans were made with the source 12 cm, 8 cm, and 6 cm (recall

Figure 3-33. Single Serpentine Antenna. Density versus Distance out from Source. 7.12 mTorr Argon. 5 A Top Coil, -1.5 A Bottom Coil. 2000 W, Glass Source Bottom

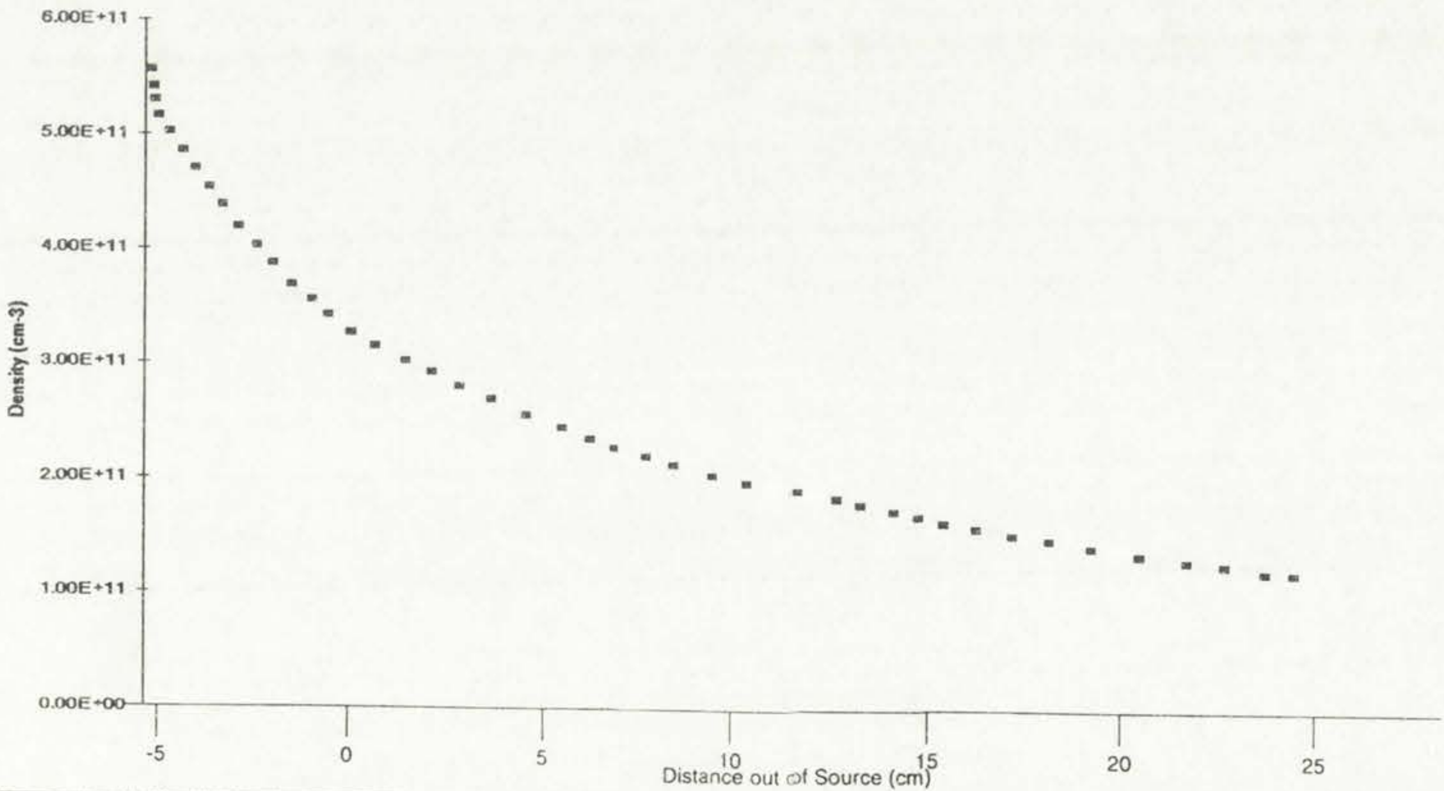

Figure 3-34. Aspect Ratio Changes. Density versus Distance out from Source. 10 mTorr Argon. 4.2 A Top Coil, -1.4 A Bottom Coil. 1500 W

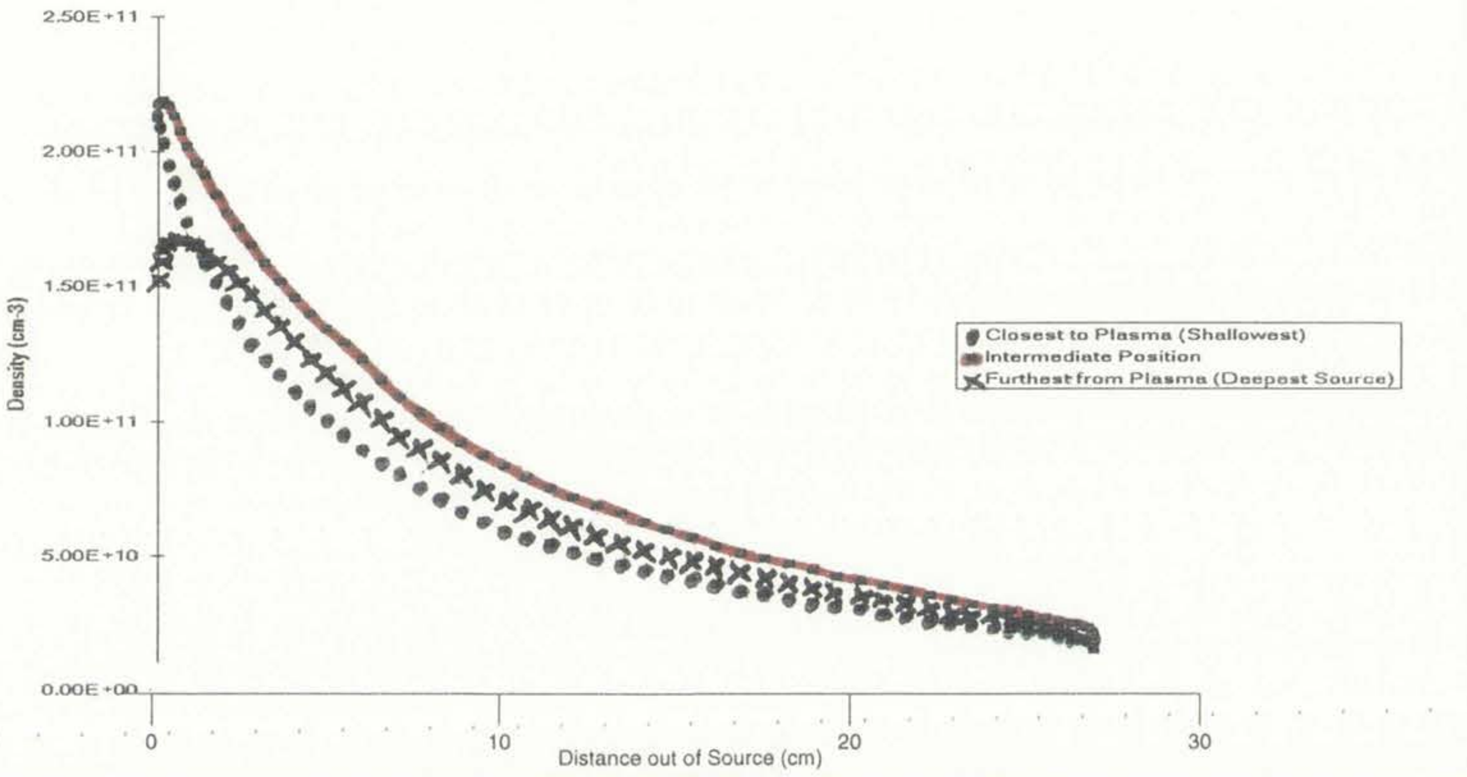

that the original source depth was 8cm). As is apparent, the profile in the chamber is little effected.

The idea for adding a second source on the opposite side of the machine arose from the observation of a linear decrease in density with increasing **Z** observed in Figures 3-15, 3-21, 3-24, and 3-28. If two sources could operate opposite each other, and produce this same flat behavior, the addition of the individual profiles of the two sources should be a flat density profile in Z. Figure 3-35 illustrates the profile that would be obtained if the radial profile from Figure 3-15 is used for each source. A flat profile in both Z and X would certainly make this source attractive as a processing tool. The prediction of a linear profile hinges on two assumptions: (1) the sources do not influence each other, and (2) the power coupled into the plasma is balanced between each of the sources.

Figure 3-35. Ideal Two Source Behavior. Density versus Z Position
10 mTorr Argon. -4 A Top Coil, 5 A Bottom Coil.
2200 W Each Source

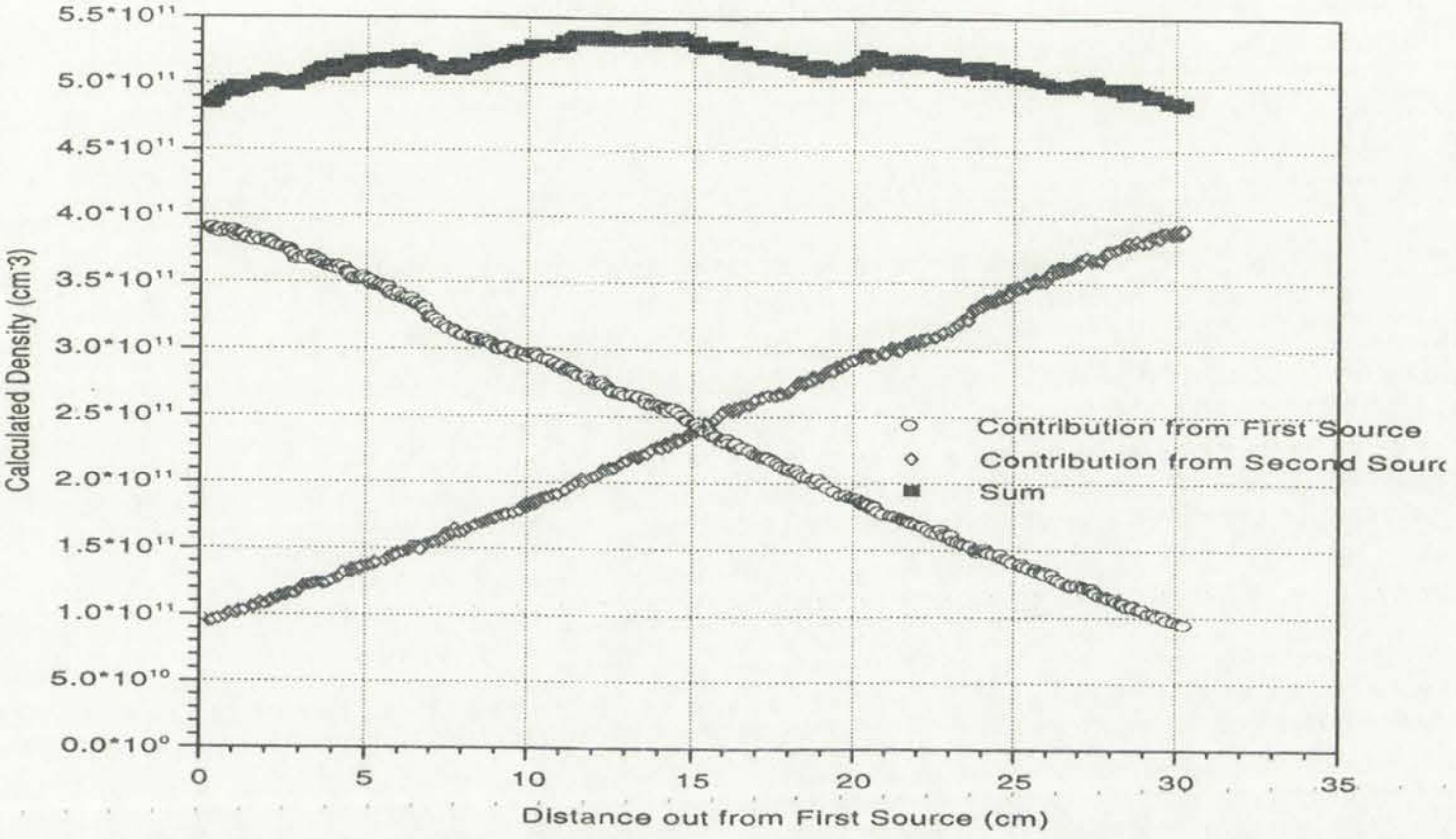

Unfortunately, there was only a brief period of time during which to observe the behavior of the dual source configuration, and many important questions remain unanswered. Power was first divided between the two sources via a series of feeders from a central tuning box. Previous experience about locating the tuning box as close to the antenna as possible was set aside in favor of trying the most economical route. If only one rf generator were used, the machine would cost much less, and there would be easy phase control between sources. However, the use of only one generator necessitates the use of long power feeders from the tuning box to the chamber. The antenna current was so low using the long feeders that a dense plasma was never generated. Most of the power was resistively dissipated or radiated in the long feeders before ever reaching the antenna.

Hence, the machine was reconfigured with two separate matchboxes, and two

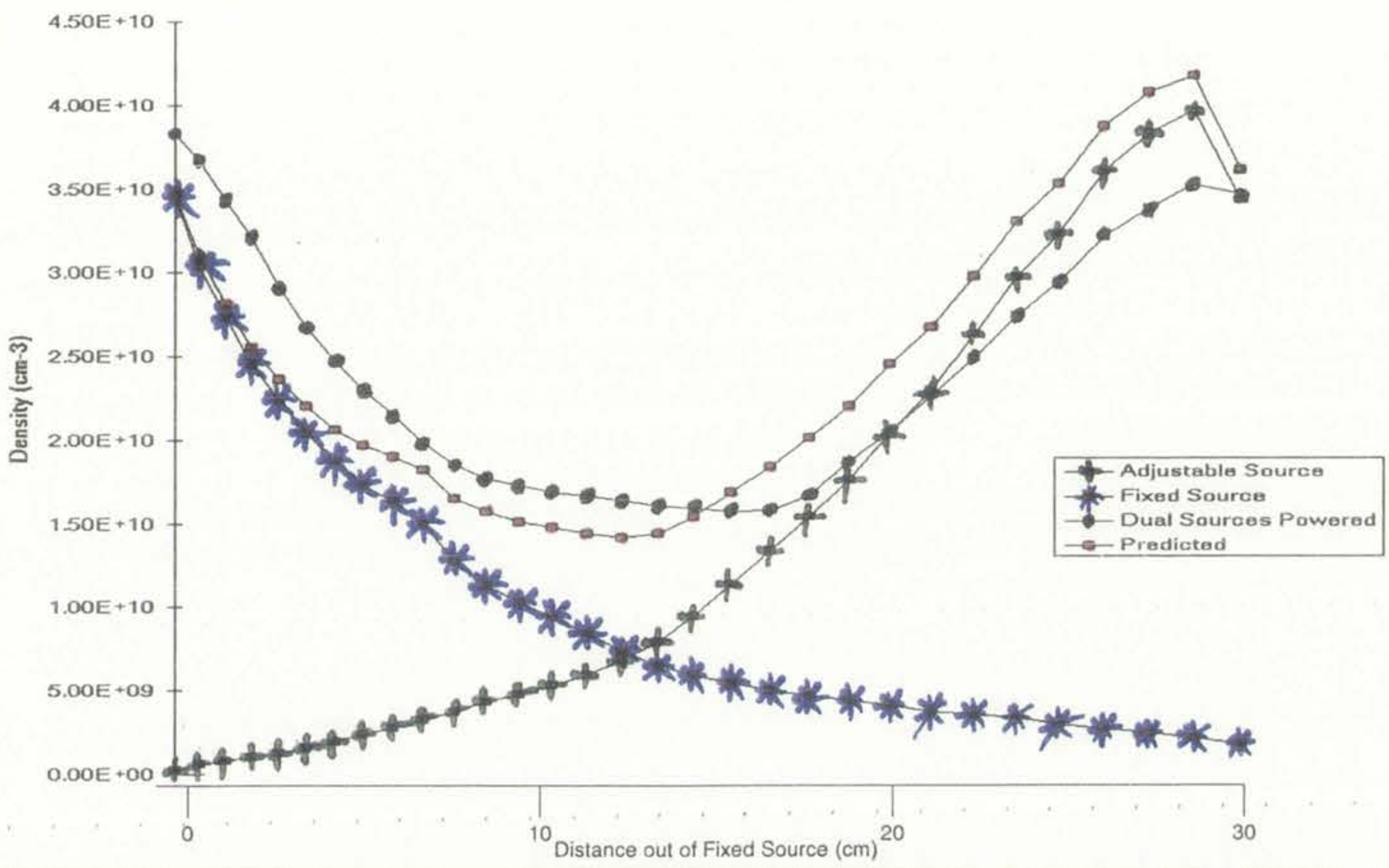
Figure 3-36. Actual Two Source Behavior. Density versus Z Position
10 mTorr Argon. 4.2 A Top Coil, -1.4 A Bottom Coil.
1.5 KW Each Source

RF power supplies, which were not phase referenced. Only a couple of profile scans were done, with little to no optimization. Although remarkable densities were not achieved, the question of source interaction was addressed. A plot of the density profiles for each source operating independently, as well as together is contained in Figure 3-36. Each source was configured with top and bottom serpentines for a total of four antenna segments. Included in the plot is the addition of the two scans with the sources operating independently. If the sources were operating independently, then the density profile with both sources powered should look similar to sum of the individual profiles. It does, and independent operation was confirmed.

In retrospect, any worries that waves launched from one source would interact with the other source in cusp geometry were unfounded. A helicon wave can not propagate from a region of higher magnetic field through a region where the

absolute value of the field strength drops to 5 Gauss, because this point corresponds to the electron cyclotron resonance frequency of 13.56 MHz. Wave energy would be completely absorbed before this region by electrons spiralling around field lines. Measurements presented in the next chapter vividly illustrate the wave absorption. Waves generated in one source had no way of ever reaching the other source.

3.2.1 Pressure Effects

Figure 3-37 shows the dependence on pressure of the density as calculated from the ion saturation current at two different points in the chamber. the chamber was configured with a single source, which was fitted with a serpentine segment on the top and bottom. The higher densities are measured 5 cm outside the source. The second measurement point is 15 cm out from the source, in the center of the chamber. The density was a maximum at a somewhat higher

Figure 3-37. Calculated Density versus Pressure
4.2 A Top Coil, -1.4 A Bottom Coil. 1.5 KW

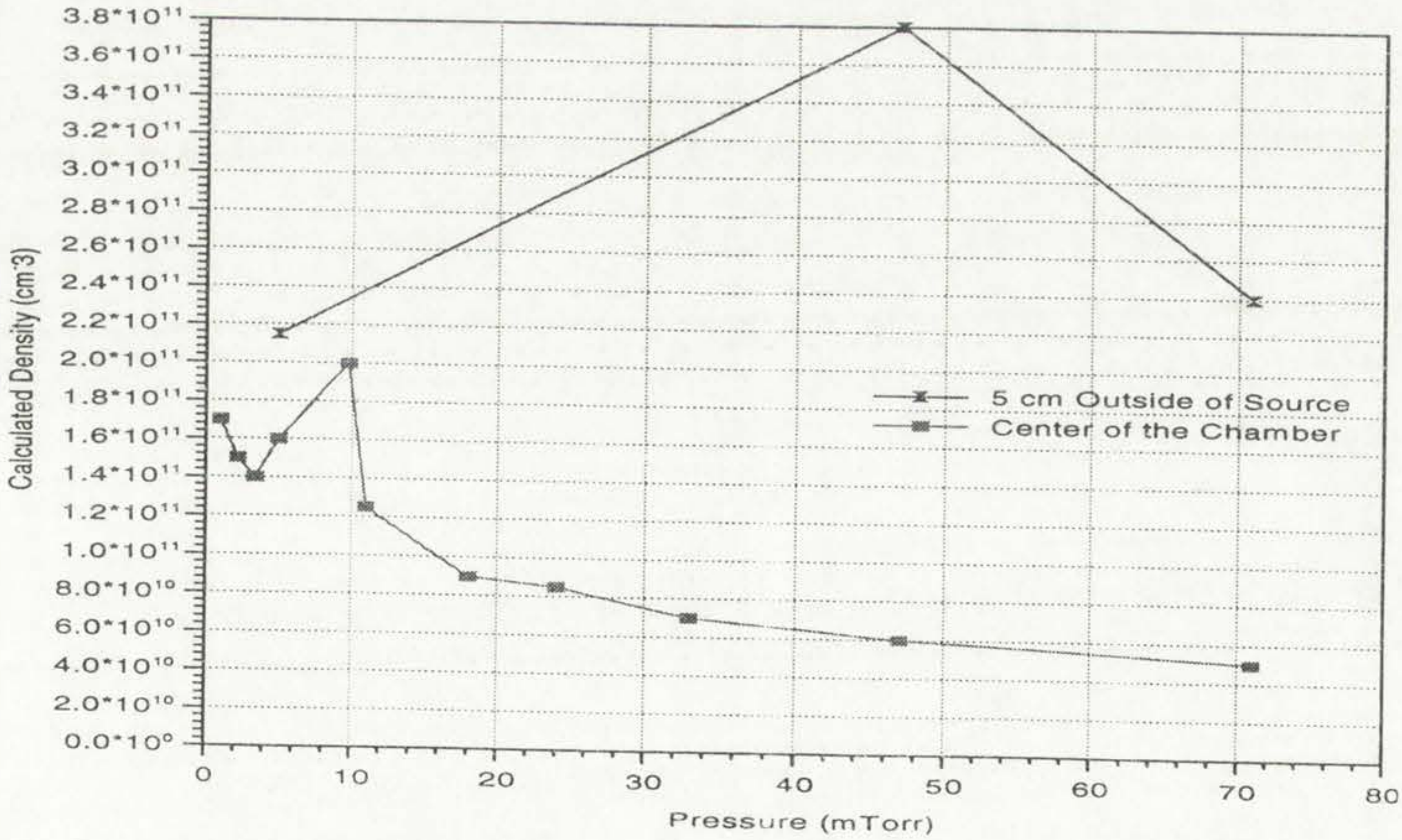

pressure (~45 mTorr) just outside the source, and at ~7 mTorr in the center of the chamber. This behavior is typical of source-diffusion chamber interaction, and is largely due to increasing collisional effects at higher pressures.

3.3 SUMMARY OF ANTENNA EXPERIMENTS

The purpose of these experiments was to determine the best antenna configuration for powering an extended source. A significant number of experiments requiring substantial modification of the source and antenna components of the new extended machine were performed in the space of a single year. The linear source demonstrated an ability to produce relatively dense plasmas over an extended length. Even so, the densities obtained up until this point were a factor of 5 less than that regularly achieved in argon in cylindrical helicon machines. Mode changes had been observed in the source, but it was not possible to determine if the antenna was coupling to a helicon mode, or even exciting a helicon wave in the plasma. Source material effects were investigated fairly completely, with the conclusion that the materials that make up the source have relatively little effect on the densities achievable. Antenna shape, and power connections play more important roles in how well power is coupled into the plasma.

The linear source, with the serpentine antenna, was shown to be able to produce plasma along its entire length, but very little was known about how it was produced. A fuller understanding of source behavior was needed, with the eventual goal to improve the applicability of the source for manufacturing processes. In order to better achieve this goal, emphasis was turned toward the development of appropriate diagnostics to probe the operation characteristics of the new

source. In particular, Langmuir and B-dot probes were constructed, and the role of the static magnetic field reexamined. Problems that needed to be addressed could be summarized as follows:

1. plasma produced in the source does not seem to diffuse into the chamber, and

2. whether the high density mode(s) of the source were inductive or helicon was not known. A way to distinguish between the two was needed.

With these two problems in mind, efforts were focused on building some new probes.

4. MEASUREMENTS IN CUSP FIELD GEOMETRY

The goal of the helicon source project was to develop a source that could process large areas. Scaling a traditional source, like the Boswell source, would make the pumping requirements prohibitive or substantially reduce throughput. The pumping volume of a conventional source would scale with the $^{3}/_{2}$ power of the desired processing area. The ring source, and, to a lesser extent, the linear source, could be enlarged by scaling with the desired processing area. Further, both the linear and ring sources could be scaled up without changing the actual source geometry. The dispersion relation would be the same in a large machine, as in a small machine, as long as the c-sections had the same cross-sections. In order to explore the viability of the extended source to create large areas of uniform plasmas, the source was configured to operate in two distinct magnetic field configurations. This chapter focuses on the extended source as it might be applied in a ring source. Therefore, measurements of plasma characteristics and wave structure were performed on the linear tool with a cusp static magnetic field geometry. The cusp field is the most likely geometry to be used in a ring source.

With focus of experiments on the new source moving from source design to source optimization, there was a recognized need for better diagnostics. Therefore, discussion of the operation of the chamber with cusp field geometry starts with a discussion of the probes used to characterize its behavior. The Langmuir probes used for density profile information were only being used as saturation current diagnostics. Density calculations from those probe traces involved two assumptions: (1) electron energy distributions in the plasma can be described by a 3 eV Maxwellian, and (2) the saturation current measured at a high negative

bias was the Bohm current (from which the density could be inferred). Neither of these assumptions results in a gross error, but they ignore non-thermal distributions expected in the source region of high density plasmas (Sheriden, et al.[15]). In addition, properly analyzed Langmuir probe traces provide valuable information about floating potential and plasma potential, as well as energy distribution functions and density. Hence, improved Langmuir probe measurement and analysis were given high priority.

Also of considerable interest was the choice of antenna for use in powering the source. An extensive array of designs had already been evaluated. Although a serpentine antenna pair produced a uniform plasma along the length of the source, it was still unclear at this point whether the antenna was exciting helicon waves in the discharge. In order to better evaluate antenna performance, and to determine whether helicon waves existed in the plasma, development of **B**-dot probes was imperative to measure time-dependent magnetic field in the plasma. A single-loop antenna pair (located on the top and bottom of the source) was installed to provide a simple benchmark for detailed study of the serpentine antenna developed in the last chapter.

The final element in the diagnostics focus was the measurement of the static field configuration in the existing chamber. A system for calculating field strength and geometry had been developed before experimental work began, but actual measurements with the magnetic field coils on the chamber had not been done. Since the magnetic field has a direct relationship to helicon wave propagation, measurements with a Hall effect probe were made.

If all of the above diagnostics tools could be implemented on the linear source, a better understanding of the operation of the extended helicon source would be achieved. Specifically, the following issues could be addressed:

1. measured static magnetic field, wavelength, and density would provide immediate comparison to the relevant theoretical predictions for a helicon-excited source,

2. electron energy distribution and wavelength measurements could help explain the source excitation mechanism, and the power deposition pattern in the chamber,

3. **B**-dot probe measurements in the center of the source directly measure the field driven into the plasma by the antenna and better determine optimal antenna shape, and

4. Langmuir probe traces provide information about plasma potential, floating potential and electron energy distribution. All of these parameters directly effect etching or deposition characteristics of a plasma tool.

An understanding of the physical processes occurring in the chamber would provide ways to improve the applicability of the new source to industrial processes.

4.1 LANGMUIR PROBE DEVELOPMENT

Rather than immediately disassemble the probes already in place on the machine, a preliminary set of current versus bias voltage traces were taken, and

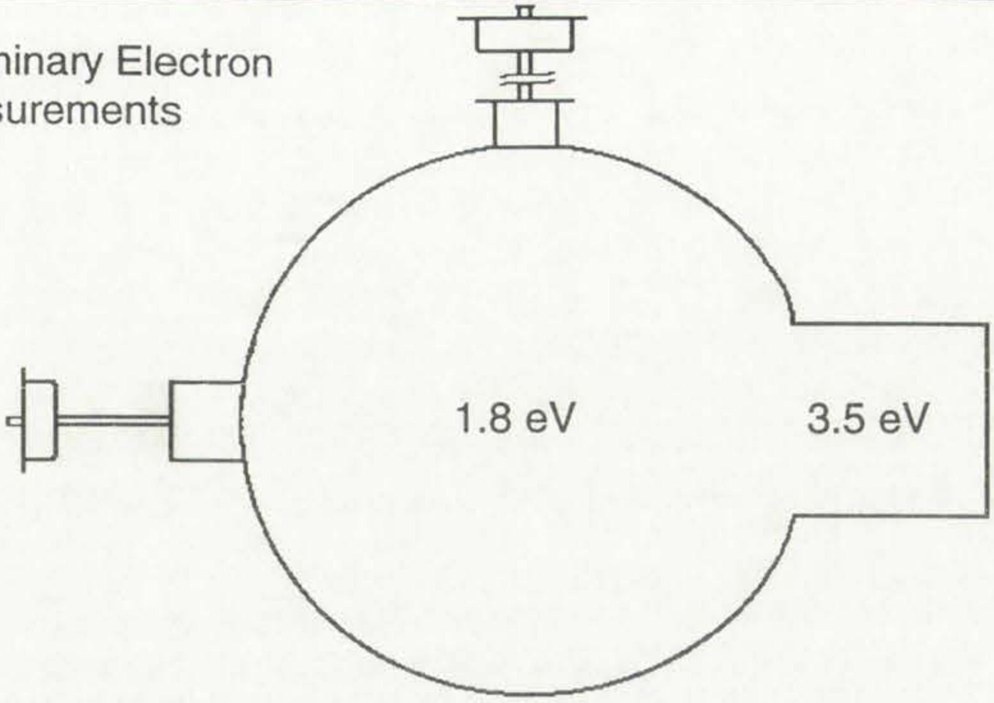

Figure 4-1. Preliminary Electron Energy Measurements

the resulting curves analyzed to obtain a rough estimate of electron energy. Any measurements taken with these probes are only regarded as approximate, as the large body of data on probe measurements in magnetized plasmas was being neglected. The experiments were performed merely to get a rough idea of how careful subsequent measurements needed to be. Electron populations were assumed to be Maxwellian, and the results are shown in Figure 4-1. These results indicated that there appeared to be a significantly cooler electron population in the diffusion region than in the source.

A review of the theory of probes in rf plasmas was performed to determine what features were desirable to have in a Langmuir probe. At their simplest, Langmuir probes are wires immersed in a volume of charged particles, and the flux to such a wire is given by

$$\Gamma = \sum_j n_j \iiint f_j(v)\ v_p d\vec{v} \qquad (22)$$

where Γ is the total flux, n_j is the density of the j^{th} charged species, f_j is the veloc-

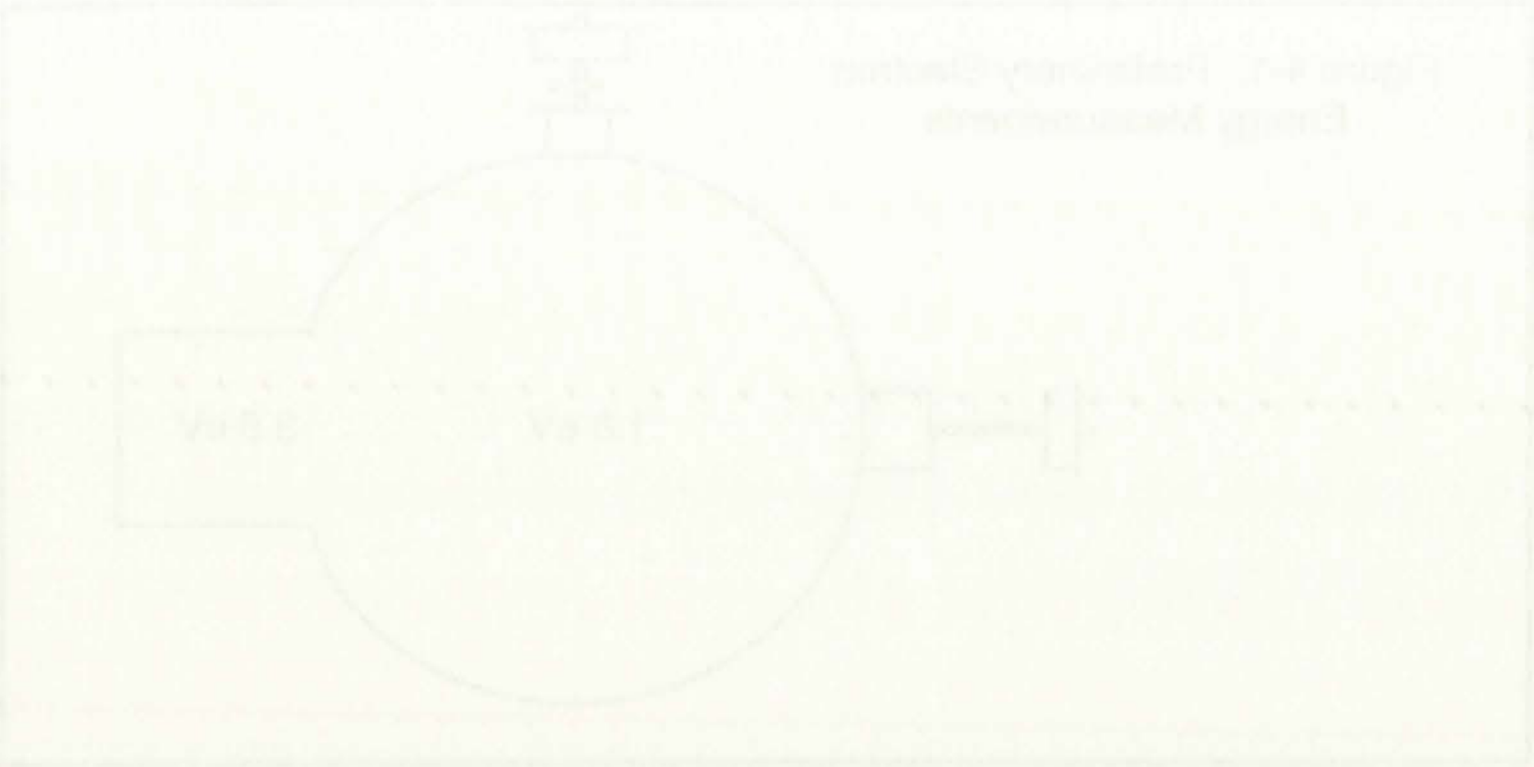

Figure 4-1. Preliminary Electron Energy Measurements

the resulting curves analyzed to obtain a rough estimate of electron energy. Any measurements taken with these probes are only regarded as approximate, as the large body of data on probe measurements in magnetized plasmas was being neglected. The experiments were performed merely to get a rough idea of how careful subsequent measurements needed to be. Electron populations were assumed to be Maxwellian, and the results are shown in Figure 4-1. These results indicated that there appeared to be a significantly cooler electron population in the diffusion region than in the source.

A review of the theory of probes in rf plasmas was performed to determine what features were desirable to have in a Langmuir probe. At their simplest, Langmuir probes are wires immersed in a volume of charged particles, and the flux to such a wire is given by

$$\Gamma = \sum_i n_i \iiint f_i(v)\, v \cdot dA \qquad (22)$$

where Γ is the total flux, n_i is the density of the i^{th} charged species, f is the veloity distribution function for the jth species, and v_p is the velocity normal to the probe surface. The integral is over all of the allowed velocities in 3-D space. One can treat the electron population as bi-Maxwellian, and simulate the expected I(V) current to the probe as a function of the applied voltage. f(v) is modeled as

$$f(v) = (1-a)\left(\frac{m_e}{2\Pi K_B T_{e1}}\right)^{\frac{3}{2}} e^{\left(\frac{-m_e v^2}{2K_B T_{e1}}\right)} + a\left(\frac{m_e}{2\Pi K_B T_{e2}}\right)^{\frac{3}{2}} e^{\left(\frac{-m_e v^2}{2K_B T_{e2}}\right)} \qquad (23)$$

where a is the ratio of electrons with a higher temperature, T_{e2}, to the total population. K_B is the Boltzman constant. When the probe is biased at $V<V_p$, the plasma potential, then only electrons with sufficient energy to overcome the sheath potential between the probe and plasma will be collected. That is, only electrons that satisfy $\frac{1}{2} m_e v^2 \geq q_e(V_p-V)$ will contribute to the probe current. Substituting f(v) into the expression for Γ_e, and integrating over the collecting range, the following solution is obtained

$$\Gamma_e = \left[\begin{array}{ll} n_e\left((1-a)\left(\frac{K_B T_{e1}}{2\Pi m_e}\right)^{\frac{1}{2}} e^{\frac{e(V-V_p)}{K_B T_{e1}}} + a\left(\frac{K_B T_{e2}}{2\Pi m_e}\right)^{\frac{1}{2}} e^{\frac{e(V-V_p)}{K_B T_{e2}}}\right) & \text{for } V < V_p \\ n_e\left((1-a)\left(\frac{K_B T_{e1}}{2\Pi m_e}\right)^{\frac{1}{2}} + a\left(\frac{K_B T_{e2}}{2\Pi m_e}\right)^{\frac{1}{2}}\right) & \text{for } V \geq V_p \end{array}\right. \qquad (24)$$

Figure 4-2. Schematic of First Langmuir Probe Designed for Full I-V Characteristics

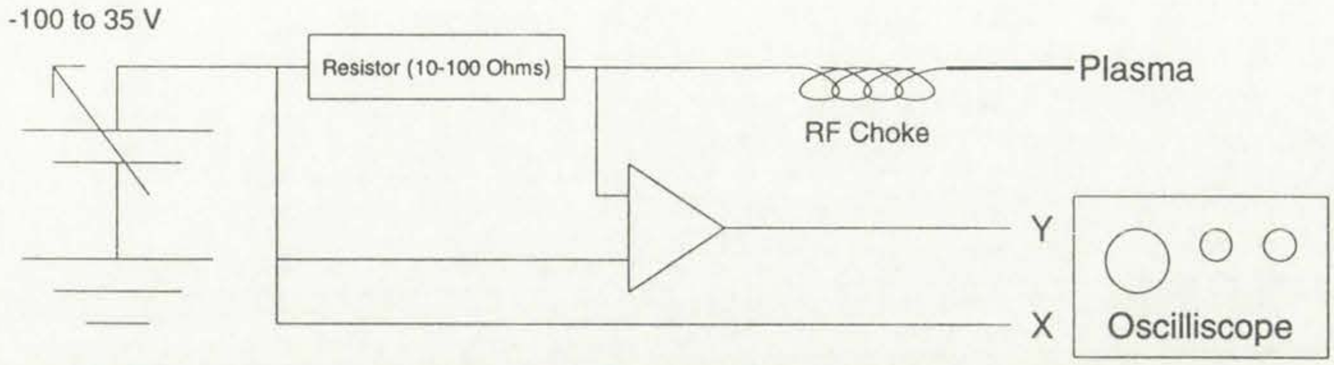

The first probe built for these measurements is shown schematically in Figure 4-2. The bias supply was a programmable amplifier, which was driven by a small signal generator at 100 Hz. The differential voltage measurement, which is proportional to the current, made across the resistor is very susceptible to noise and common mode gain. A custom circuit was designed and built to minimize noise. The signal was relatively noise free at low sampling frequencies (a limitation of the programmable amplifier), and had a linear response over more than 4 decades of voltage values. An rf choke, whose self-resonance was at 13.56 MHz, was constructed into the end of the probe to allow the tip to follow any oscillations present in the plasma and to obtain only the DC component of the probe signal. The oscilloscope used had only 8 bit resolution, and some of the important features of helicon sources that were hoped to be observed were contained in only the first few digitization levels. Therefore, a set of two traces for each condition was taken in rapid succession. The first scan was performed at a gain low enough to obtain the entire trace. The other was taken at 10-100 times the gain to resolve the finer features of the trace. The lower resolution portions of the whole trace were given no weight when combining the two traces, preference being given to the high resolution trace. If the original trace is mapped into 256 levels, and a second trace at the same resolution is taken over the region comprising four of those levels, then the spacing between digitization points in that section of the trace is equivalent to the spacing of the entire trace mapped

onto 16384 levels. This is equivalent to 14 bits. Conservatively, the estimated virtual resolution of the combined traces is 12 bits.

There are presently two widely accepted techniques used to analyze I-V traces. The method used by Godyak et al.[27,28] starts by taking the second derivative of the I-V trace, which removes any 0th and 1st order probe effects (and ideally removes any ion current effects). The resulting curve crosses 0 at the plasma potential, and the rest of the curve represents the velocity distribution function around the plasma potential. Further, the integral of this curve from very low bias voltage to the plasma potential enables one to calculate a corresponding electron density. A sample velocity distribution function is presented in Figure 4-3. Unfortunately, numeric differentiation has a tendency to magnify any noise present in the tabulated function. This effect becomes particularly troublesome when the derivative changes substantially over the space of a few data points. In order to minimize problems with differentiation, many data points were gathered over the voltage sweep, such that changes in the trace from one voltage point to another are gradual. Further efforts to minimize effects of noise during

Figure 4-3. Sample Velocity Distribution. Plasma Potential = 19.5 V, Maxwellian Temperature = 2.7 eV

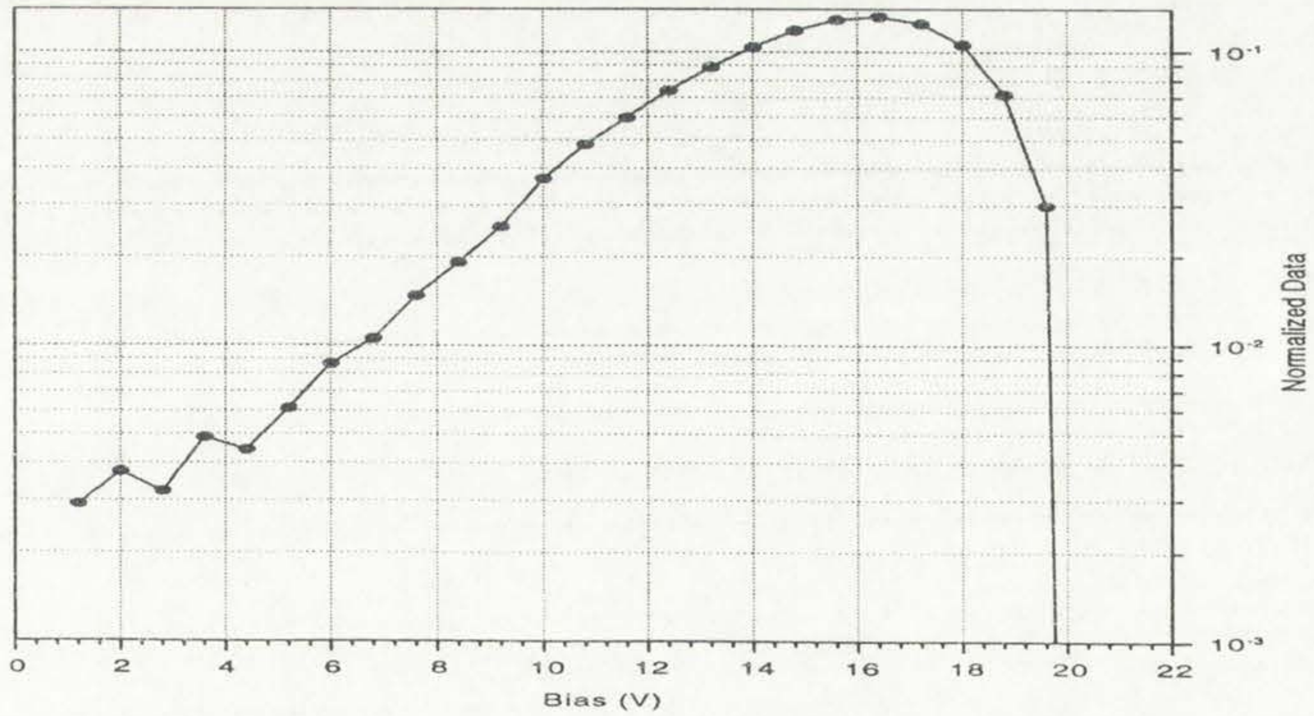

data gathering and analysis include the use of multiple averages of the I-V sweeps at a given position and use of a moving polynomial window technique to obtain the derivative and second derivative. Still, there is room for systematic error to creep in, and a discussion of some possible sources of that error and their effects on measured plasma parameters is included with discussions of the actual measurements.

Sheriden, et al.[15] use a second way of looking at I-V characteristics which is widely accepted, but is perhaps a bit more prone to systematic errors than the previous method. Analysis of this type generally proceeds as follows:

1. be certain that the negative bias portion of the I-V trace sweeps to a sufficiently low value such that electron current is a negligible fraction of the collected current,

2. fit a straight line to the lowest bias portion of the characteristic, and subtract that current off. The resulting trace should closely resemble what would have been gathered had the probe only been able to gather electrons, and

3. examine the remaining trace to decide how best to describe the gathered electron current. In low pressure magnetized plasmas, single- and dual- temperature Maxwellian models are commonly used.[15,29,30]

A rough indicator for the credibility of an I-V trace is the difference between floating and plasma potentials. Both can be obtained using a simple analysis of the

trace. The floating potential is the point at which the average ion and electron currents balance, i.e. where the net current is zero. The plasma potential is the point at which $^{dI}/_{dV}$ is a maximum. For the purposes of this rough indicator, the electron energy distribution is considered to be Maxwellian while ions are cold. Ion and electron densities are the same. Ions entering the sheath region at the edge of a plasma have the Bohm velocity of

$$u_B = \left(\frac{K_B T_e}{m_i} \right)^{\frac{1}{2}} \qquad (25)$$

where m_i is the ion mass. Therefore, the total flux of ions to the probe is given by $\Gamma_i = n_i u_B$, where n_i is the ion density. The electron current to a wall is given by[2]

$$\Gamma_e = \frac{1}{4} n_e \left(\frac{8 q_e T_e}{\Pi m_e} \right) e^{\frac{V_s}{T_e}} \qquad (26)$$

where V_s is the sheath potential, n_e is the electron density, and m_e is the electron mass. Since integrated ion flux must balance the integrated electron flux for any surface, the average V_s can be obtained by setting $\Gamma_i = \Gamma_e$. Doing so reveals the following relation

$$V_S = \frac{T_e}{2} ln \left(\frac{m_i}{2 \Pi m_e} \right) \qquad (27)$$

For argon, $V_s \cong 4.7\ T_e$, with T_e in eV. But the sheath potential V_s is the difference between the plasma potential V_p and the ground reference V_f. Measurements at 7 mTorr of argon give T_e=2.2eV, V_p=9.95V, and V_f=-0.65V. Hence, V_s calculated from equation 27 yields 10.34V, which is close to V_p-V_f=10.6V. If the measured value of V_p-V_f differed substantially from 4.7 Te then the simple theory could not be used and the effects of rf and magnetic field would have to be considered.

Systematic error in the analysis can be introduced in step 2, when the fitted ion current is subtracted from the original trace. If the ion current is linear with probe bias in this region, there is no problem. If, however, there are some second order effects, then those would remain buried in the electron current. This same problem is found in the afore mentioned 2nd derivative technique as well, and is usually so small that it can be ignored. A more complete analysis will be included in Chapter 5, where EEDF's are obtained.

There are two other sources of error which should be mentioned, and they are effects of rf ripples in the plasma, and magnetic field. Rf ripples of ~1V peak to peak have been measured in helicon reactors[31]. Therefore, the actual current to a probe at some set bias V_{bias} is the average of the currents to the probe as the plasma potential fluctuates with respect to the probe. That is $I_{measured}=\langle I[V_{bias} + V_{ripple}(t)]\rangle$. Cui et al.[32] have shown that when

$$V_{ripple} < \frac{2K_B T_e}{q_e} \tag{28}$$

For argon, V_p≈5.2 T_e with T_e in eV. But the sheath potential [illegible] is between the plasma potential V_p and the ground reference [illegible] of argon gave T_e=2.5eV, V_p≈25V, and [illegible] from equation 27 yields 10.3eV, which is close to V_p–[illegible]. The value of V_p–[illegible] affected substantially [illegible] that [illegible] be used and the effects of the magnetic field would need to be considered.

Systematic error in the analysis can be introduced in step 2, when the ion current is subtracted from the original trace, if the ion current is [illegible] bias in this region, there is no problem. If, however, [illegible] order effects, then there would remain buried in the electron current. This same problem is found in the above mentioned 2nd derivative [illegible] and it is usually so small that it can be ignored. A more complete [illegible] is included in Chapter 6, where EEDFs are obtained.

There are two other sources of error which should be mentioned, and they are effects of rf ripples in the plasma, and magnetic fields. rf ripples of [illegible] peak have been measured in helicon reactors[illegible]. Therefore the current drawn to a probe at some set bias V_{bias} is the average of the currents [illegible] the plasma potential fluctuates with respect to the probe. That is [illegible] V_{bias}(t)]>. Cui et al.[illegible] have shown that when

$$\frac{2eV_{rf}}{kT_e}[illegible]$$

which is the case here, rf effects can be ignored when treating the electron energy distribution as Maxwellian or bi-Maxwellian. A simulation of rf effects is included in the discussion of EEDF measurements in Chapter 5.

The presence of a static magnetic field presents one other complication to the I-V measurements in the extended source, as has been shown in the general treatment above. The effect of the magnetic field on derived properties of the plasma are twofold[9]: (1) depression of V_p, and (2) a change in V_p along the magnetic field lines impinging on the probe surface. Both of these effects present problems for large Langmuir probes[32], since the probe gathers a significant population of electrons. Field effects can be minimized by using probe tips smaller that the electron mean free path (~3 cm). The use of small tips and proper rf compensation has the further advantage of minimizing the perturbing effects of Langmuir probe measurements[33].

An interactive computer code was written to perform Langmuir probe analysis on a variety of traces. A computer disk containing the source code and executables (for OS/2) is included as an appendix to this work. The code is interactive to allow analysis by both of the afore mentioned techniques, and to allow the user to treat signals with varying degrees of noise, made on a wide variety of machines. A full discussion of the techniques used in the code would be inappropriate here, as the majority of its functions are direct adaptations of code found in Numerical Recipes in C[34]. The heart of the code (which does the nonlinear least squares) does deserve some attention, as it represents a significant departure from the Levenburg-Marquardt routine presented in the book. Nonlinear-least-squares fitting involves minimizing the total deviation of a nonlinear function of several modifiable variables with a set of empirical data points. In this

case there are 3 variables given by a1, a2, and a3 in the following formula:

$$\mathrm{F}(a1,a2,a3) = I_{V_p}\left((1-a2)\, e^{\left(\frac{V-V_p}{a1}\right)} + a2\, e^{\left(\frac{V-V_p}{a3}\right)} \right) \tag{29}$$

where a1 is the bulk electron temperature in eV, a2 is the ratio of warm to cool electrons, and a3 is the warm electron temperature in eV. I_{V_p} is the current measured at the plasma potential, and F(a1,a2,a3) is a shorted version of the current expression for a probe biased below the plasma potential and immersed in a two temperature plasma. Note that a2 should range from 0 to 1, and that a1 and a3 should always be positive. The standard nonlinear routines have no way to constrain the fitting parameters, and this particular function changes drastically for small changes in the adjustable values. Further, one might want to try large changes in one variable while letting the other variables change only slightly. Application of unmodified nonlinear least squares techniques often resulted in singular matrixes, or no convergence, unless the first guess for the fitting parameters was remarkably accurate. In order to address the problem, the definition of the fitting variables was changed. Each variable was redefined with the following transformation:

$$\mathrm{aN}^{*} = Arcsin\left(\frac{aN - aN_{min}}{aN_{max} - aN_{min}} \right) \tag{30}$$

In the transformed state, all of the fitting parameters were on equal footing, with each variable constrained to move about the -1 to +1 domain of the sine function. Desired small changes in one variable were obtained by adjusting the

maximum and minimum allowed values. Also, the fitting parameter definition was changed. Any calls to the nonlinear function routine returned the function value and its derivatives according to the original definition, not the transformed one. This was remedied by back shifting the fitting parameters to the untransformed state just before the call to evaluate the function. The chain rule was then used to properly evaluate the derivatives after the values are returned. The use of this technique had the added advantage that if one value has wandered close to the limit of its allowed range, changes are made to that value much more slowly, allowing other fitting parameters to be varied. Convergence using this transformation typically occurred in less that $1/3$ the number of iterations required in the untransformed state. Further, in conditions where convergence using the prior definition had been unstable, fitting in the new coordinate space was stable.

4.2 B-DOT PROBE DEVELOPMENT

The linear source geometry was chosen such that the induction current from the antenna would excite helicon waves in the chamber, which would propagate along the static magnetic field lines. A **B**-dot probe was designed to slide inside a glass tube inserted from the far wall of the chamber to the back wall of the source (along the entire **Z** axis). The circuit is shown in Figure 4-4. The solid squares are Mini-Circuit's phase detectors (RPD-1), and the solid triangles are Mini-Circuit's power splitters (LRPS-2-1). Considerable care was taken to ensure proper termination and isolation from any external circuit. The probe was checked for frequency response, and no appreciable attenuation was found up to ~50 MHz. The 5 small loops slide in the glass tube immersed in the plasma. Current induced in the loops couples through a small transformer to the external circuit. The external circuit compares **B**-dot signal amplitude to a reference rf

Figure 4-4. Schematic of the 1-D B-Dot Probe

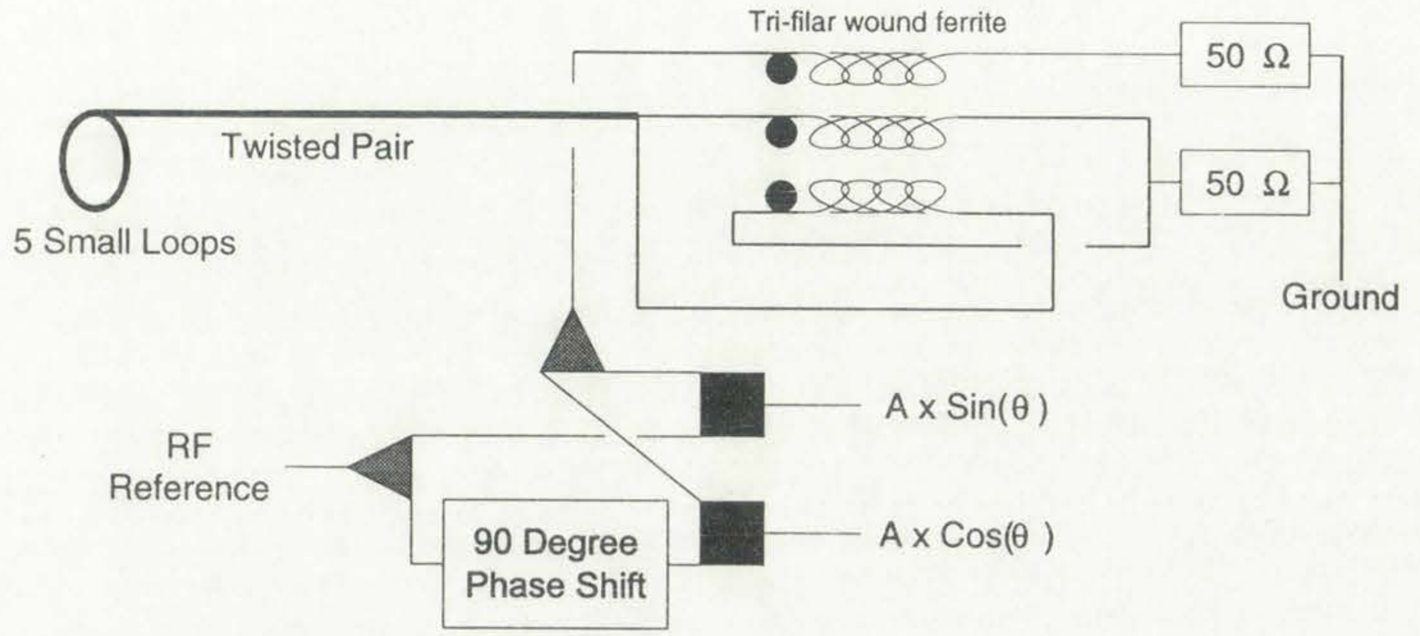

signal from the power supply. Both amplitude (A) and phase (θ) information are contained in the two signals, and a simple mathematical transformation can easily separate them.

$$Amplitude \propto \sqrt{(B\cos(\Theta))^2 + (B\sin(\Theta))^2} \qquad (31)$$

$$\text{Phase} = Arctan\left(\frac{B\sin(\Theta)}{B\cos(\Theta)}\right) \qquad (32)$$

where B is the signal amplitude, and Θ is the phase of the signal with respect to the reference rf signal. The amplitude of the trace is not equal to the actual coil current, but is only proportional to it. The Mini-Circuit's phase detectors output a signal which is defined by the product of the two signal amplitudes and the cosine of the phase between them. If the rf reference signal amplitude is known, then it is a simple matter to obtain the original B-dot signal amplitude from the output of the measurement circuit.

A tri-filar transformer winding was used to reduce pickup from electric field oscillations in the plasma. When the probe is immersed in the plasma, not only is current induced in the wire by changing magnetic flux through the loop, but current due to capacitive coupling to small electric field fluctuations is also induced. Fortunately, it is possible to separate the two effects. Current in the wire arising from electric field pickup would travel in the same direction in both wires of the twisted pair, whereas current induced from changing magnetic flux would be traveling in opposite directions. Winding both leads from the twisted pair in opposite directions around the ferrite results in a cancellation of the effects of co-directional currents, and amplifies the anti-directional components by a factor of 2. Further amplification can be obtained in the third winding of the ferrite, if desired. For the purposes of this experiment, the factor of two amplification was sufficient. Another commonly used method of isolating the probe from electric field effects is to use a piece of shielded coaxial cable for the probe. The ground sheath of the coax is left nearly intact to shield the inner conductor from electric field pickup. But a small break in the outer conductor prevents loop currents in the shield section, such that the inner conductor picks up that signal. This style B-dot probe was not used in the extended source experiments.

4.3 SOURCE PERFORMANCE IN CUSP FIELD GEOMETRY

One of the intended purposes of the extended source was to excite a ring-fed cylindrical source for processing disk substrates. Helicon waves propagate along magnetic field lines, and so any helicon source must be designed with the lines of force parallel to the intended direction of propagation. In the ring source, the ideal field line orientation would resemble the spokes in a bicycle wheel. Such an arrangement is not physically possible, but can be approximated using

a set of two coils forming a magnetic cusp. The cusp could be shaped even more like spokes by the addition of several concentric magnetic loops on the top (and mirrored on the bottom), but the simple two-loop arrangement was chosen for the next set of source experiments in the interests of cost and simplicity.

A method was developed to calculate the static field in the cusp geometry. (A fully functional code was already developed for the intended cylindrical geometry by Nelson and Porteous[35]). Such a code was not available for the linear tool, and so a simple analytic solution for the field strength along a center line through a rectangular coil was used. Comparisons between Hall Effect probe measurements and the code are shown in Figure 4-5. There is good agreement between the predicted and measured values. The code was used to calculate field values for other coil currents.

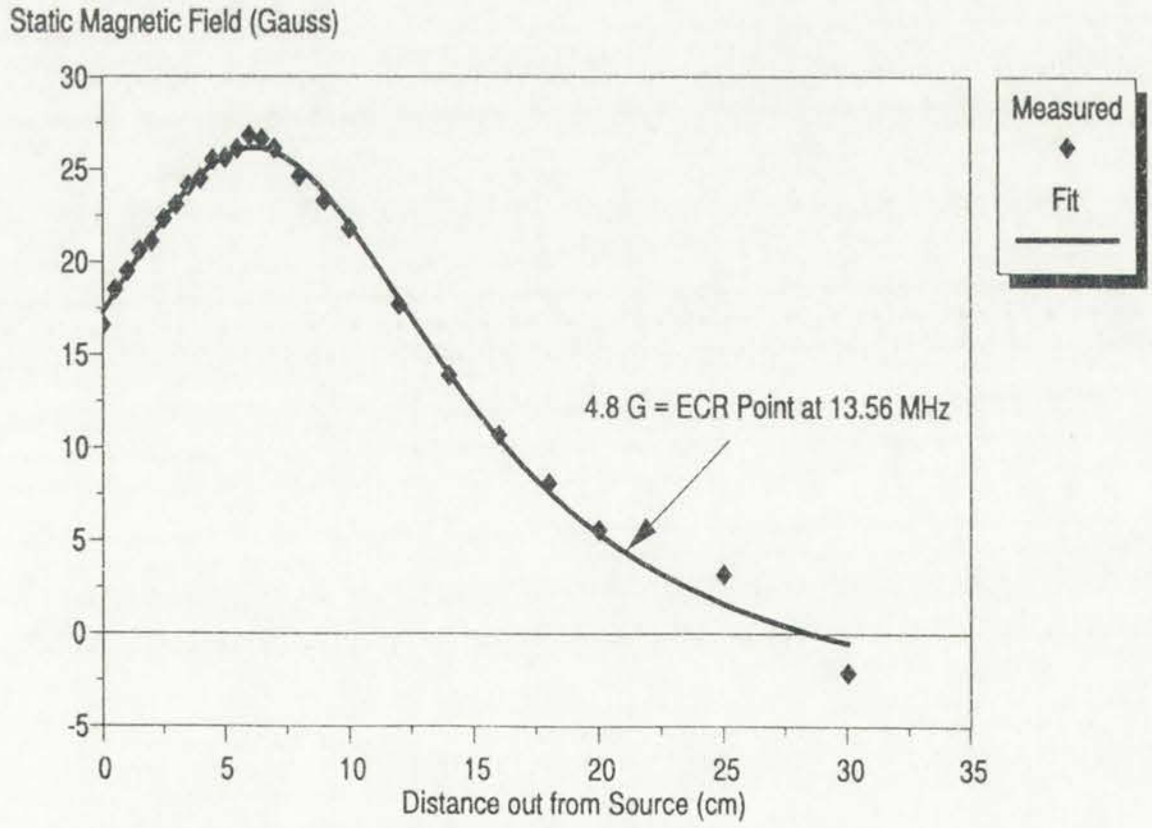

Figure 4-5. Static Magnetic Field Strength in the Z direction versus Z Position

Figure 4-6. Wave Structure in Cusp Field Geometry
2000 W, 3 mTorr of Argon, 5A Top Coil, -1 A Bottom Coil

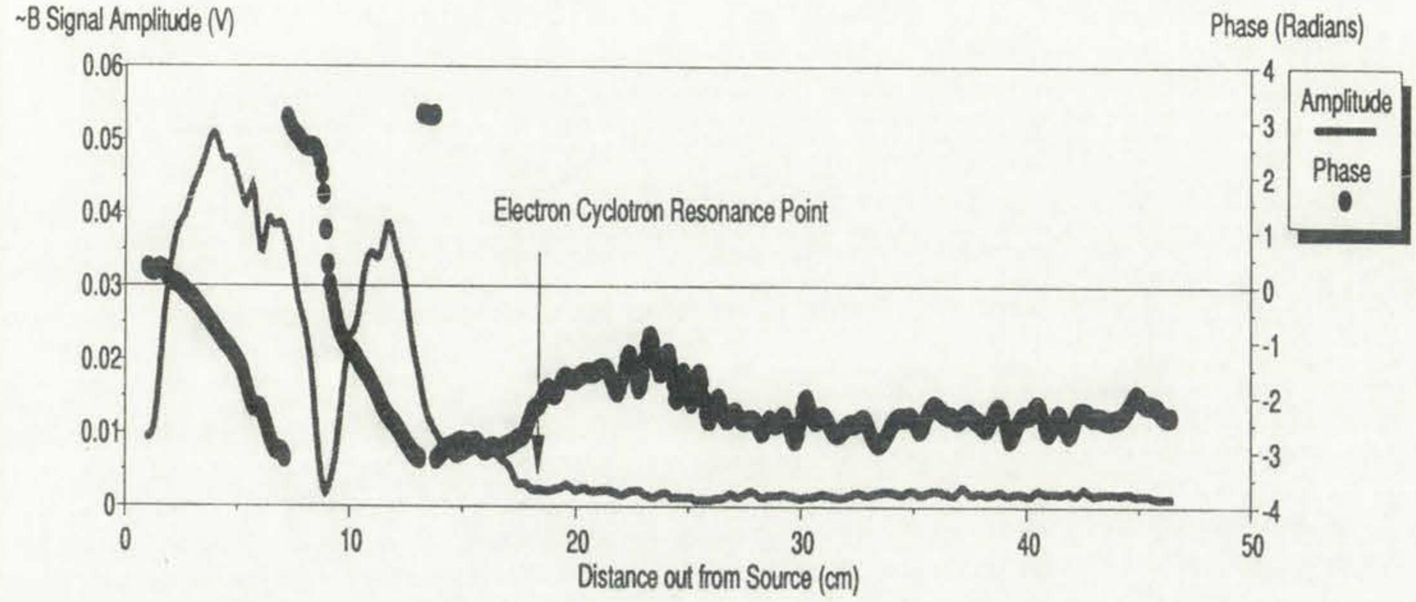

The **B**-dot probe was first used to characterize wave structure with the static magnetic field in this cusp arrangement (unchanged from the previous configuration). Amplitude and phase measurements from the B-dot probe provided information about wave structure as well as antenna performance.

Figure 4-6 shows the typical variation in wave structure as a function of position in the chamber. The source extends from 0 cm to 10 cm on the plot, with the rest of the chamber filling the remaining 10 to 46.5 cm distance. Note that although there is extensive penetration by the antenna magnetic field in the source (which excites the plasma), just 10 cm outside the source all ~**B** excitation is absorbed, and no excitation extends into the rest of the chamber. This behavior appears odd until it is compared to the static field strength as a function of position shown in Figure 4-5, where it is evident that the magnetic field drops to the electron cyclotron resonance (ECR) point at the same position. In a cold plasma, a RHCP wave cannot propagate past the ECR point (where the phase velocity goes to 0)[36]. Notice also that the phase of the antenna perturbation changes sign at 8.0 cm. This point is right between a curve of the top serpentine

Figure 4-8: Wave Amplitude [illegible] Geometry

[illegible]

The B-dot probe was first used to characterize wave structure with the static magnetic field in the cusp configuration (unchanged from the previous configuration). Amplitude and phase measurements from the B-dot probe provided information about wave structure as well as antenna performance.

Figure 4-8 shows the typical variation of wave amplitude as a function of position in the chamber. The source extends from 0 cm to 13 cm on the plot, with the rest of the [illegible] the remaining 13 to 48.5 cm distance. Note that although there is [illegible] by the antenna magnetic field in the source [illegible] the plasma, but [illegible] outside the source an [illegible] oscillation is apparent, and an oscillation extends into the rest of the chamber. The behavior of amplitude [illegible] is compared to the static field strength as a function of position [illegible], where it is evident that the magnetic field drops to the electron cyclotron resonance [illegible] at the same position. In a cold plasma, whistler waves cannot propagate past the ECR point [illegible] the phase velocity goes to [illegible]. Notice also that [illegible], the antenna [illegible] 4.5 cm. This [illegible] of the [illegible]

Figure 4-7. Theoretical Dispersion Surface for Helicon Waves in Infinite Geometry, Expressed in More Physical Terms of B, Density, and Wavelength

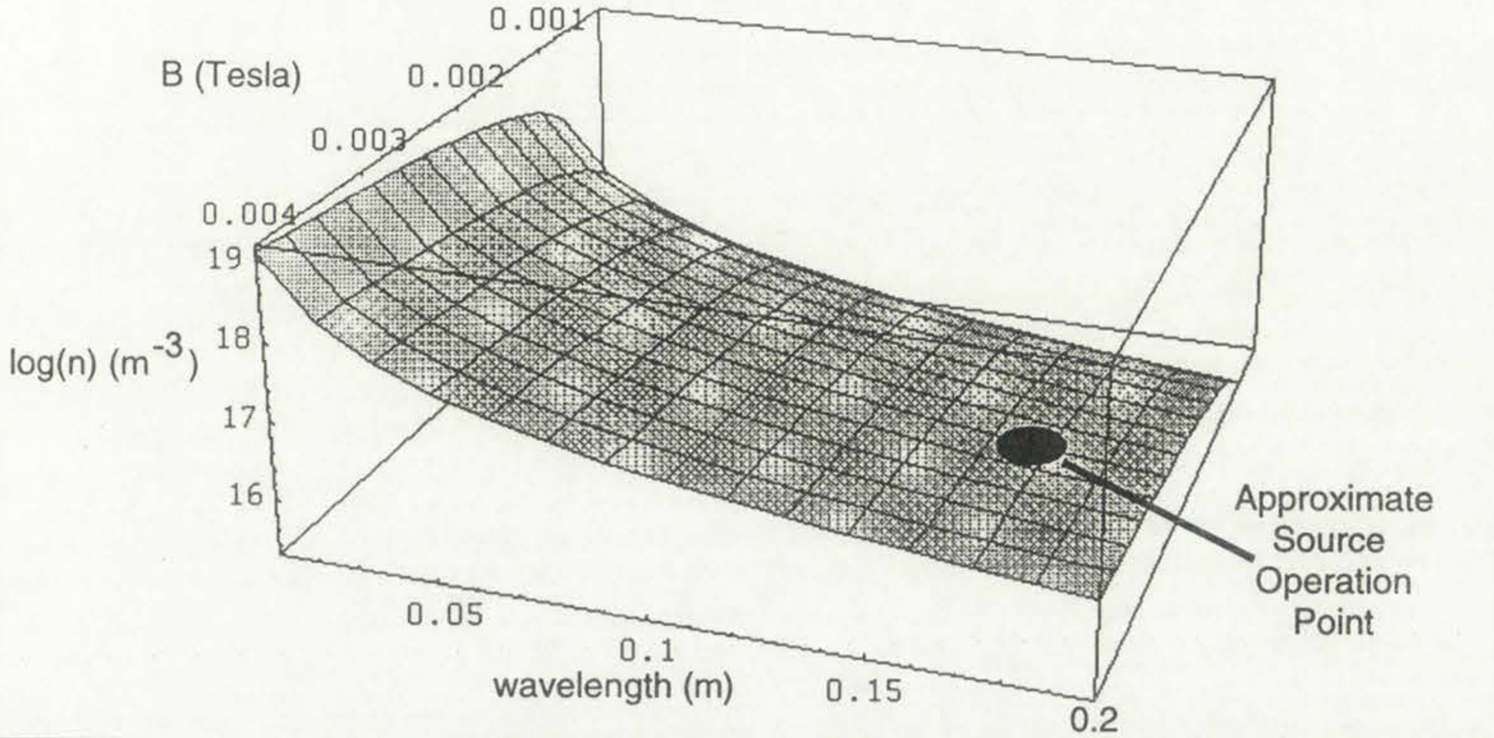

that passes closest to the chamber wall, which is mirrored by the bottom serpentine segment. This point forms a node, on either side of which the excited field changes sign. The lowest order mode that would have a node at 8 cm and at the back conducting wall of the source is a 16 cm wave. This is the first indication that the antenna in use could be launching helicon waves. Since the wavelength excited, magnetic field present, and the plasma density in the source all fit nicely on the theoretical dispersion surface shown in Figure 4-7, it is likely that helicon waves are being excited.

Before making a definite assertion that the source is launching a helicon wave, one should note the following. The magnetic field (and the dispersion relation) changes markedly over lengths comparable to the wave field of the antenna. Therefore, the wave structure in this region changes over such a short distance that the $k_{//}$ spectrum is severely distorted, and hence wave propagation effected. It is evident that an increase in the static field strength and a smoother field geometry could enhance formation of helicon waves in the source, enabling

Figure 4-7. Theoretical Dispersion Relation for Helicon Waves in Argon [illegible] Compared to Some Physical Parameters: Density and Wavelength

wall passing closest to the chamber wall, which is mirrored by the bottom segment. This point forms a node, on either side of which the excited field changes sign. The lowest order mode that would have a node at 5 cm and at the back conducting wall of the source is a 10 cm wave. This is the first indication that the antenna in use could be launching helicon waves. Since the wavelength, the magnetic field present, and the plasma density in the source all fit nicely on the theoretical dispersion surface shown in Figure 4-7, it is likely that helicon waves are being excited.

Before making a definite assertion that the source is launching a helicon wave, one should note the following. The magnetic field (and the dispersion relation) changes markedly over lengths comparable to the wave field of the antenna. Therefore, the wave structure in the region changes over such a short distance that the k-spectrum is relatively distorted, and helicon wave propagation obscured. It is evident that an increase in the static field strength and a smoother field [illegible]

Figure 4-8. Amplitude of -B Field versus Position and Decreasing Static Magnetic Field. 3 mTorr of Argon, 2000W

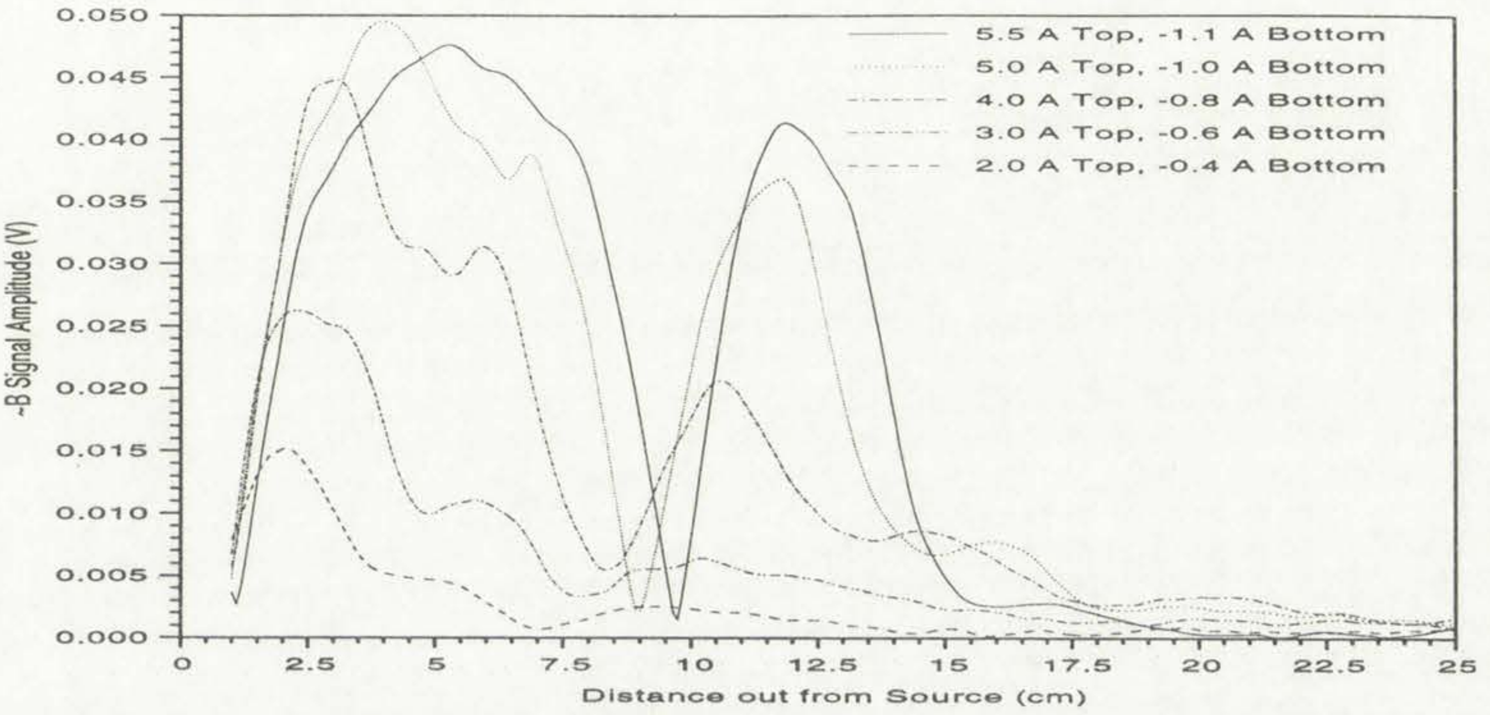

propagation into the chamber, but a coherent wave structure is probably not present in the cusp geometry.

The antenna appeared to be performing well. From Figure 4-6, there was significant penetration of the antenna magnetic field into the middle of the source. Whether source characteristics, in particular static field strength, allowed optimum penetration was still unclear. A variety of antenna shapes were described in the previous chapter, but will be addressed here once more. The variation of the excited fields in the plasma versus static field strength is shown in Figure 4-8. There was an increase in penetration as the field was increased, which indicates that higher static fields would enhance antenna coupling.

Phase measurements are not included in Figure 4-8 (for clarity), but are included in Figure 4-9. The sign change of the phase information of the excited field as it passes through the source opening always occurs at 8.0 cm (or slightly lower as the static field is decreased). This sign change is another indication that a $-\mathbf{B}_z$

Figure 4-9. Wave Structure versus Position for the 5 Conditions in Figure 4-8.

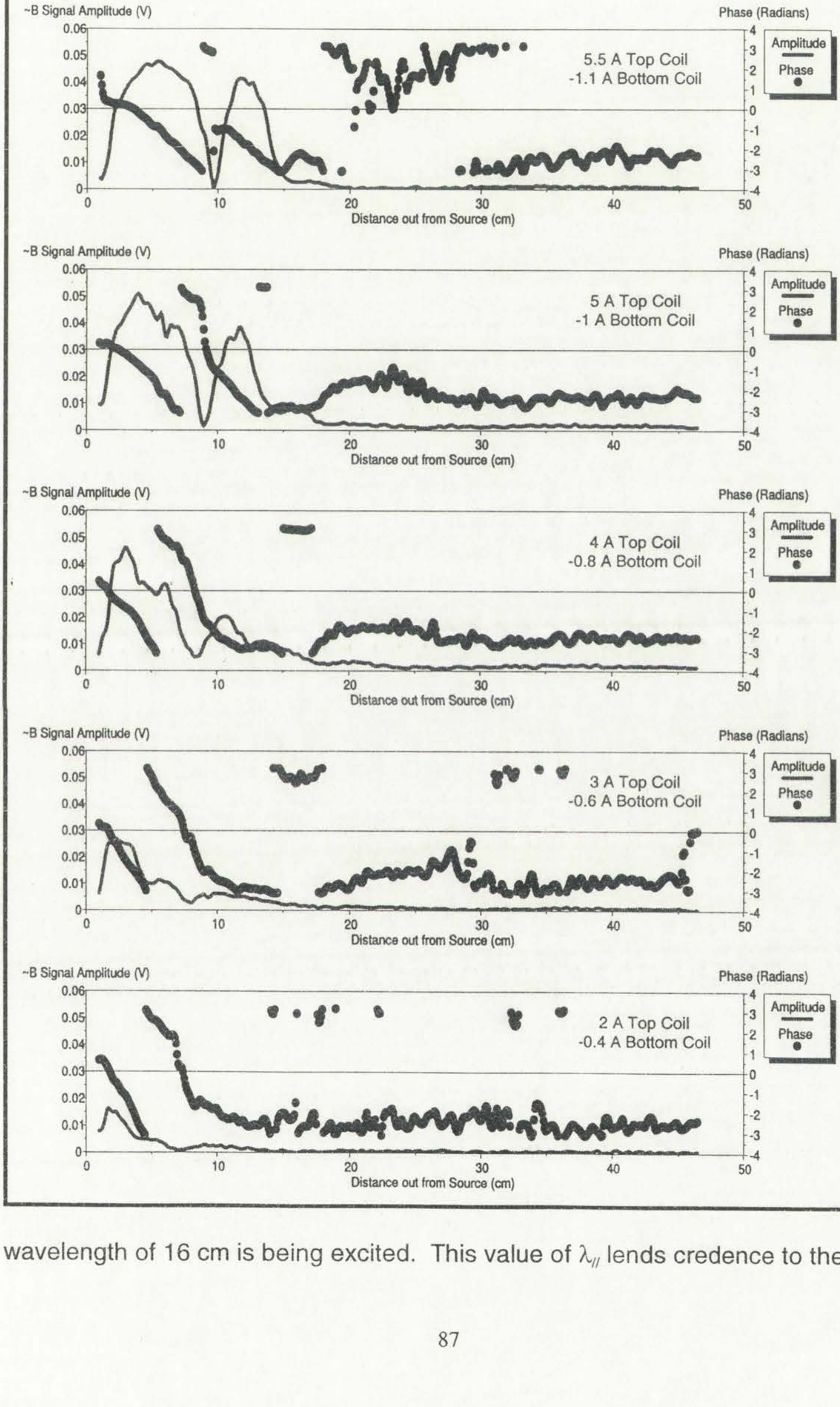

wavelength of 16 cm is being excited. This value of $\lambda_{//}$ lends credence to the

boundary conditions used in the theoretical treatment in chapter 2.

If a helicon source were only able to excite helicon waves at a particular wavelength, it would not be very useful. Even with flexible density and magnetic field characteristics, the source could cause some unwanted instability problems for an industrial application. Also, the antenna would have to capacitively (or inductively) couple to the plasma until the dispersion characteristics were favorable for propagation. Mode shifts, where the density changes markedly as the power is increased smoothly, were observed in prior work on the linear source, as well as in other sources[37]. It was thought that a changing $k_{//}$ was responsible for the mode shifts, but experimental evidence for this proposed mechanism was scarce. Variation of parallel wavelength as a function of power was investigated in the extended source, with the results displayed in Figure 4-10. At 100 W, the B_Z wavelength is 12.5 cm. The dispersion relation predicts shorter wavelengths with higher density. As more power is absorbed by the plasma in the source, higher densities can be found near the source. As the power is increased, the wavelength decreases; a 6 cm wavelength being observed at 1000 W. The **B**-dot probe provided a view of the source that was unavailable in previous experiments, and provided clues about source deficiencies and solutions.

The new Langmuir probe studies also offered novel insights into plasma characteristics, and proved to be an invaluable tool for furthering understanding of source behavior. The Langmuir probe analysis software had not yet been refined enough to use the second derivative technique discussed earlier, so the technique of Sheriden et al.[15] was followed. To be certain that some electron current was not accidently subtracted off in the process of removing the ion current, the probe voltage with respect to the chamber wall was swept from -100 V, boundary conditions used in the theoretical treatment in chapter 4.

If a helicon source were only able to excite helicon waves at a particular wavelength, it would not be very useful. Since both the plasma density and magnetic field dependence allows the tuning of [illegible] to avoid [illegible] instability problems in an industrial application. Also, the existence would need to [illegible] (truly couple to the plasma) until the dispersion characteristics were favorable for propagation. Hence jumps, where the density changes modestly as the power is increased smoothly, were observed in prior work on the helicon sources, as well as in other sources. It was thought that changing k, was responsible for the mode shifts, but experimental evidence for this process and mechanism was scarce. Variation of the axial wavelength as a function of power was investigated in the extended source, with the results displayed in Figure 4-16. At 100 W, the B_z wavelength is 15.5 cm. The dispersion relation predicts shorter wavelengths with higher density. As more power is absorbed by the plasma in the source higher densities can be found near the antenna. As the power is increased, the wavelength decreases, with a 6 cm wavelength being observed at 1000 W. The B-dot probe provided a view of the source that was unavailable to previous experiments, and provided more solid source conclusions and solutions.

The new Langmuir probe also has [illegible] novel insights into plasma characteristics, and showed to be an innovative tool for furthering understanding of source behavior. The Langmuir probe analysis software has not yet been refined enough to use the second derivative technique discussed earlier, so the technique of [illegible] is more favored. To be certain that some electron current was not accidentally subtracted off in the process of removing the ion current, [illegible]

Figure 4-10. Changes in wavelength as a function of power applied

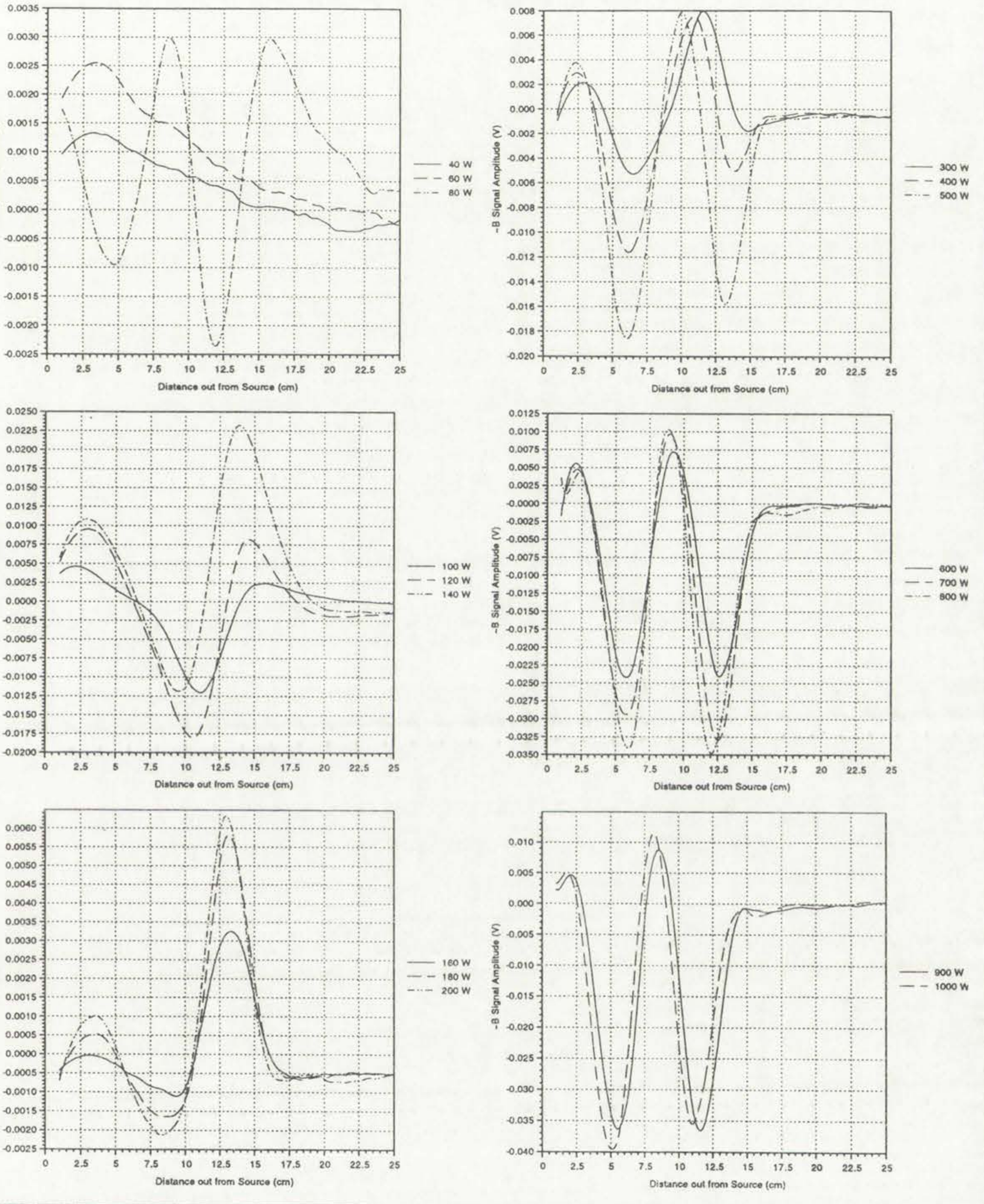

where it is well into the ion saturation region, to above the plasma potential. All of the current contribution comes from electrons at the most positive bias. A sample current versus bias voltage trace is shown in Figure 4-11. Figure 4-12 contains a semi-log plot of the trace after the ion current has been removed,

Figure 4-11. Raw Langmuir Probe Characteristic
at the Mouth of the Source
2000 W, 3 mTorr of Argon

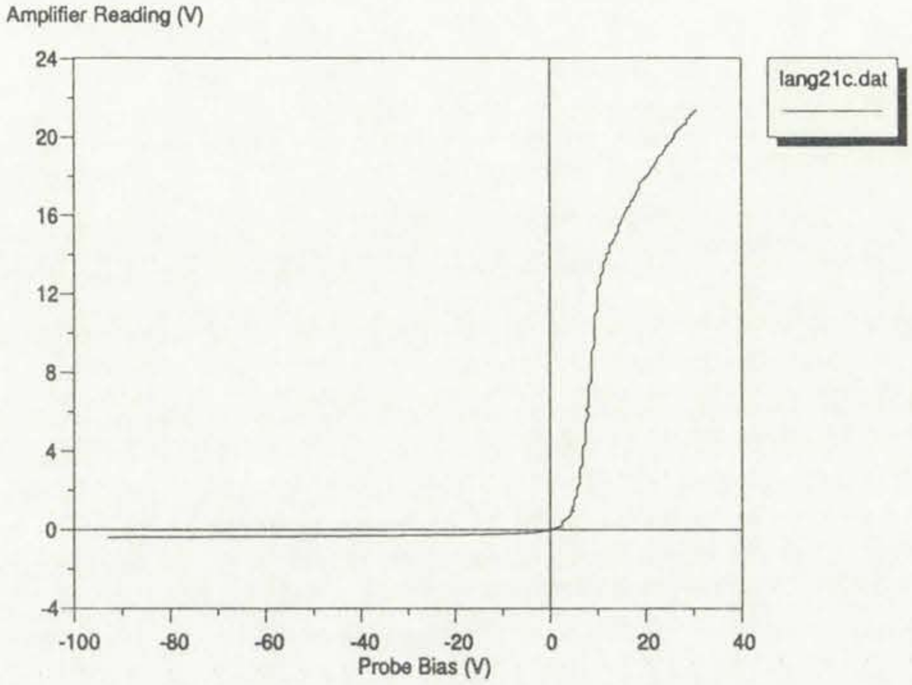

Figure 4-12. Extracted Electron Current
2000 W, 3 mTorr of Argon

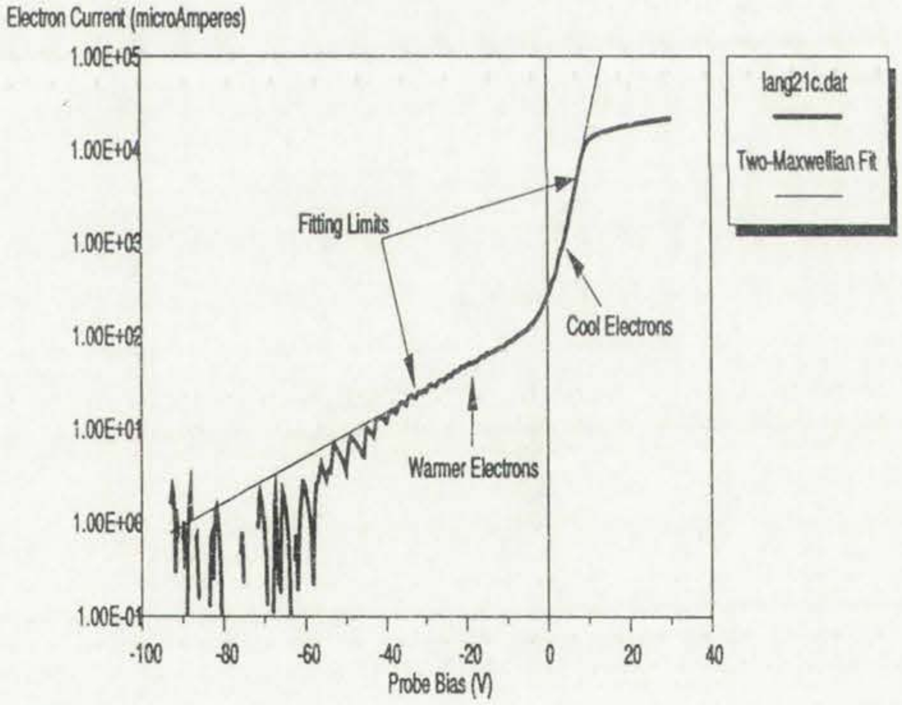

which should represent the electron current from the trace in Figure 4-11. Particularly exciting was the apparent presence of a significant population of electrons warmer than the bulk temperature. There are two distinct regions of linear variation, indicative of two distinct populations of electrons. It is not sufficient simply to apply a linear fit to the cool electron region, and hope the small

fraction of warm electrons have little effect. Rather, the presence of only 1% supra-thermal electrons at 18 eV can elevate the apparent temperature predicted by a single Maxwellian fit by as much as 25%. A Bi-maxwellian fit was implemented for our purposes, using the modified Levenberg-Marquardt[38] least-squares optimization technique discussed earlier. In Figure 4-12, warm electrons contribute 1.6% of the electron current with an energy of 17.8 eV. Bulk electrons have 2.03 eV. The floating and plasma potentials are 0.1 V and 10 V, respectively. Using the above values for the electron energy distribution, and the extrapolated ion current at the plasma potential, the ion density is 2×10^{12} cm^{-3}. A plot of the Bi-maxwellian fit is also shown as the solid line in Figure 4-12; it agrees remarkably well with the measured data over the fitting region from -35 V to 8 V.

The presence of supra-thermal electrons at these ratios increases the electron population with sufficient energy to ionize argon by a factor of 10. Further investigation of electron energy distributions, including discussions of possible sources of error, are included in the next chapter.

After the **B**-dot and Langmuir probes were completed, one more antenna experiment was performed. Recall that the small antenna pair was used to excite the plasma throughout this initial characterization segment. It was used in the early stages of this phase because its antenna field structure was less complicated than the serpentine antenna used at the end of the source development period. However, the small antenna could only excite plasma in a small portion of the source; hence, it was not an appropriate choice for the distributed source. The serpentine antenna does excite a plasma in the entire volume, but whether

Figure 4-13. Plasma Density versus Position for Serpentine and Small Antenna Pairs. 2000 W, 3 mTorr Argon, Cusp Field

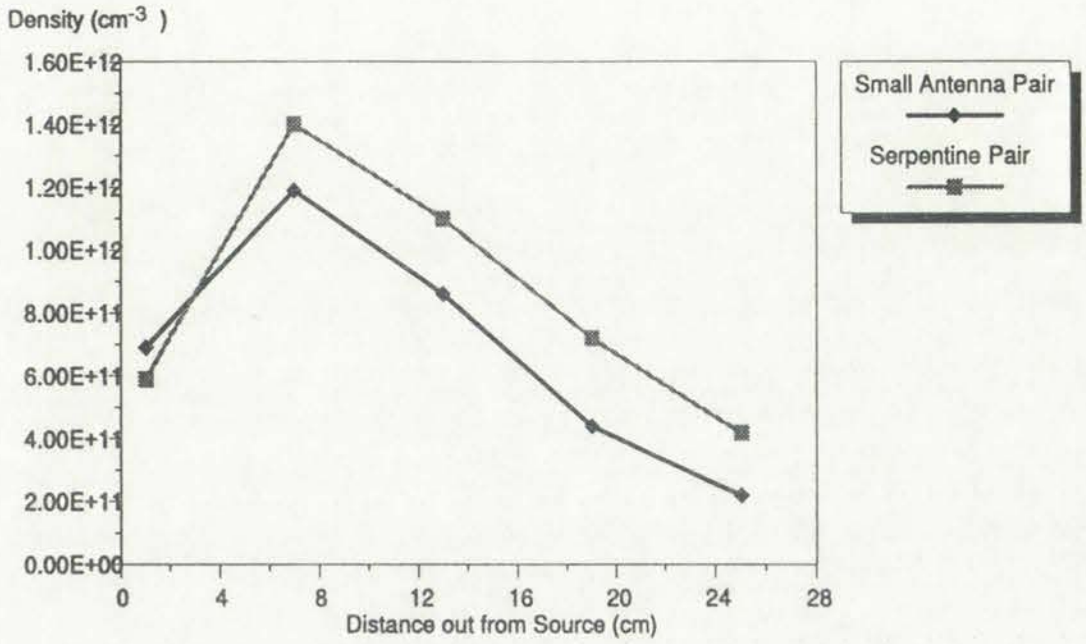

or not it performed better than the small antenna was still unclear. A comparison of the two antennas was done.

Figure 4-13 is a plot of ion density in the chamber (on a line in the **Z** direction out from the source) for the two antenna sets under identical conditions. It is clear that the serpentine antenna performs better than the small antenna even on a line through the center of the chamber, where the small antenna performs best. Because serpentine also fills the entire source length, as was shown in chapter 3, it was selected for use in the remainder of the experiments.

Measurements in cusp geometry revealed some unfortunate problems for the cylindrical ring source. Density drops from the source to the chamber are a direct result of the cusp geometry, which cools the plasma as it diverges, and prevents helicon waves from propagating out into the chamber. A ring source might be able to overcome these problems by exciting the plasma uniformly over the entire periphery, but that will require more development on an actual ring

tool. A different approach to solving uniformity problems was chosen for the linear tool. The prior results indicated that the helicon waves could not travel into the diffusion region in cusp field geometry. So, letting the data guide the design efforts, it was proposed that a new set of field coils be made that would provide parallel field lines throughout the chamber. Field shape could be varied as a function of position to adjust for any nonuniformities. The results of that series of experiments is the focus of the next chapter.

5. MEASUREMENTS IN PARALLEL FIELD GEOMETRY

A static magnetic field along the **Z** direction is required for helicon waves to propagate. The cusp field provided for experiments in the last chapter was shown to be rather inappropriate for the slab source, even though it is probably the appropriate static field for a cylindrical ring source. Knowing the limitations the cusp geometry places on diffusion into the slab chamber, a change in the magnetic field configuration was proposed to explore the potential of the existing slab tool. The simplicity of the slab geometry made that source attractive from a manufacturability point of view. Measurements presented in this chapter were performed on the slab source configured with a new set of field coils.

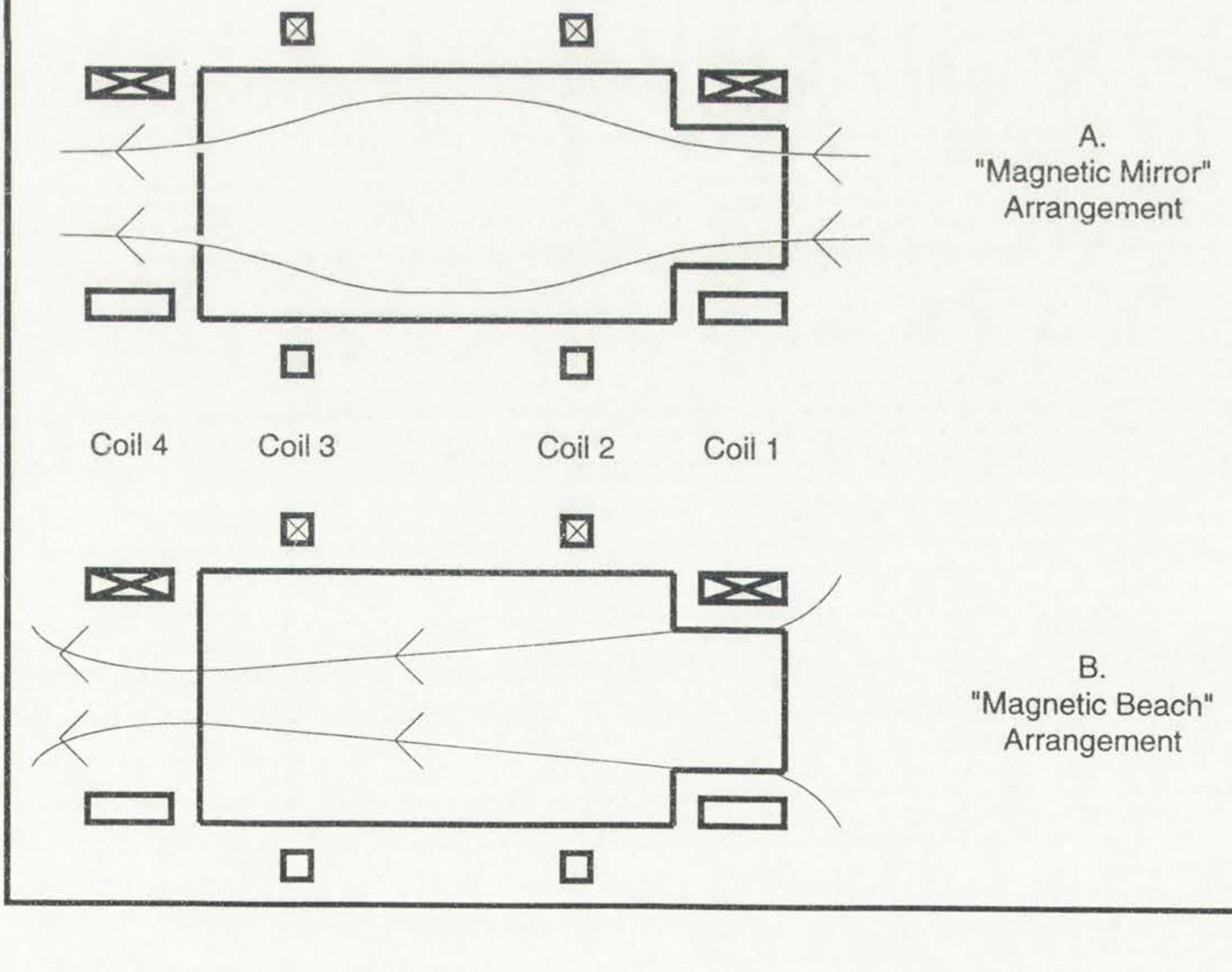
Figure 5-1. Cross Section View of New Magnetic Field Geometry

Figure 5-2. Sample Magnetic Field Configurations for New Coils (calculated)

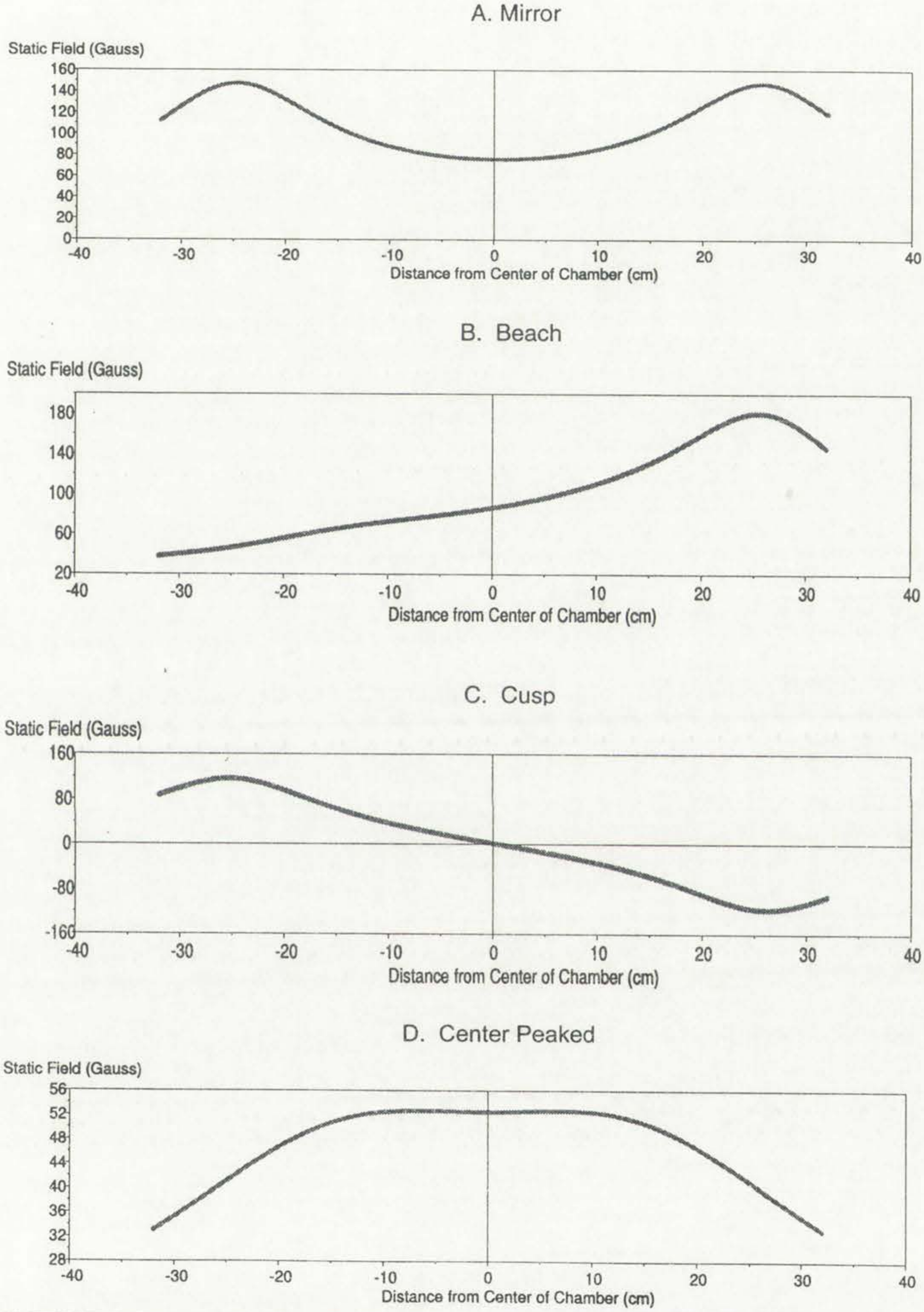

Rather than choosing a design which might not be optimum for use in a processing environment, a flexible set of 4 solenoid coils was designed and implemented

Figure 5-2. Various Magnetic Field Configurations for New Coils (Calculated)

A. Mirror

B. Beach

C. Cusp

D. Center Peaked

Rather than choosing a design which might not be optimum for use in a changing environment, a flexible set of 4 solenoid coils was designed and implemented.

as shown in Figure 5-1. The existing coils (coils 2 and 3 in the figure) were reoriented vertically, and two larger (600 turn) coils were added around the source and at the back wall. The best results were obtained in subsequent experiments by using the magnetic "mirror" and "beach" configurations. Figure 5-2 shows the value of the magnetic field in the **Z** direction for several operating modes. Note in 5-2(C) that the new coil set could be used to emulate the cusp geometry used in previous experiments. Figure 5-2(A) and 5-2(B) will be subsequently referred to as the "mirror" and "beach" arrangements.

Removing the cusp in the center of the chamber removed the ECR cutoff point and dramatically improved the performance of linear source. Figure 5-3 shows the **Z** component of the wave structure as a function of **Z** position in the new beach arrangement. Waves now appear throughout the chamber. Notice that the amplitude trace doesn't quite fall to 0 anywhere in the chamber. This behavior is indicative of a structure that has some travelling wave component and some standing wave component. The wavelength again appears to be consistent with helicon wave dispersion surface. Transitions between the top and bottom of the phase plot are null transitions, because -Pi is the same phase as +Pi. The fairly constant slope of the phase plot indicates traveling wave structure. Optimum densities at low pressures were obtained using the beach arrangement, but the mirror arrangement was optimal for higher pressures. Density measurements at 3 and 7 mTorr in the beach configuration, and at 20 mTorr in the mirror arrangement are shown in Figure 5-4. Recall that in cusp geometry, density always dropped as a function of distance out of the source. That behavior is no longer present. Instead, there is little variation in density as a function of position for the 7 and 20 mTorr cases, and an <u>increase</u> in density with distance for the 3 mTorr case. The antenna appears to be coupling more

Figure 5-3. Wave Structure with New Field Coils (Beach Configuration)
2000 W, 3 mTorr of Argon.

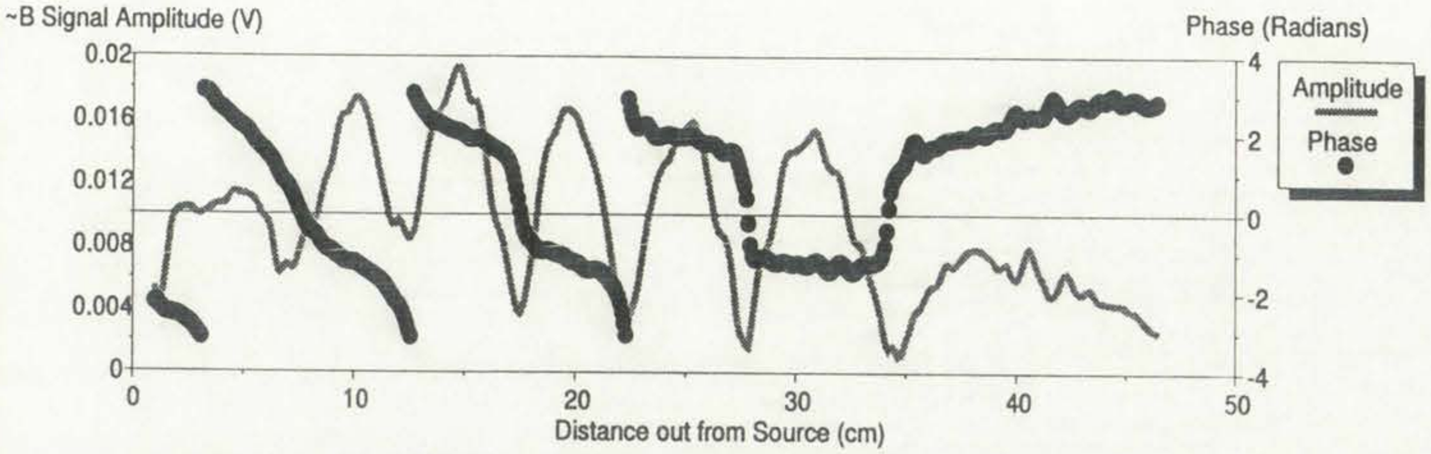

power into the bulk of the chamber, rather than losing most of it in the source. As a result, density is noticeable higher everywhere in the chamber.

Another of the performance criteria for the linear source was its ability to generate a dense plasma uniformly over the length of an extended source. Measurements of density versus **X**-position are shown in Figure 5-5. Measurements were made at a 5 cm distance outside the source at the left edge of the antenna (0 cm), the middle of the antenna (15 cm), and at the right side of the

Figure 5-4. Density vs Position (New Field)
2000 W, Argon.

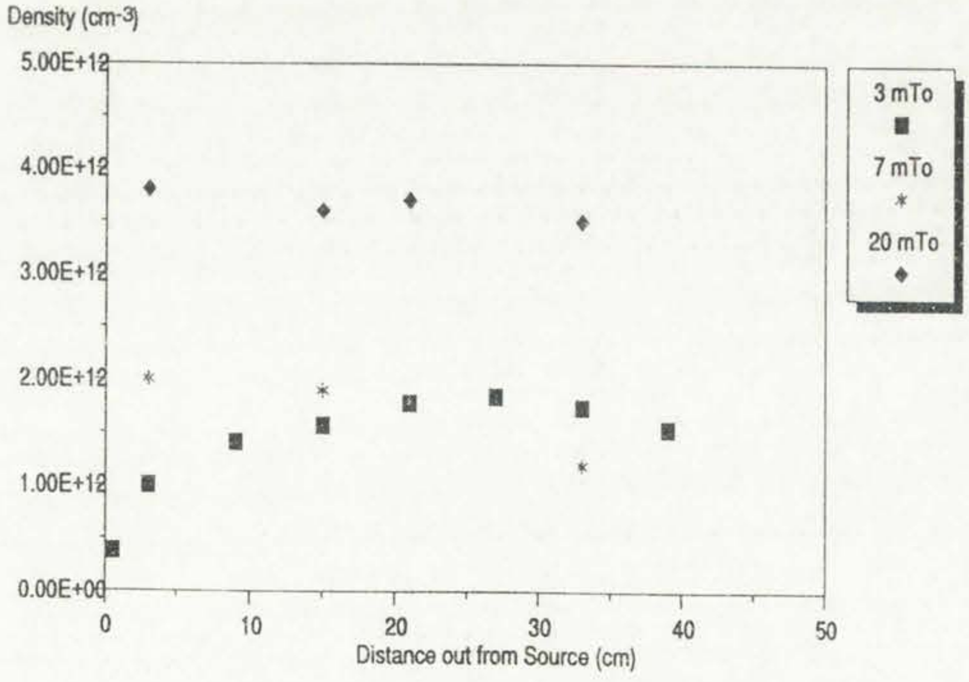

Figure 5-3. Probe Readings with New Field Coils (Sheath Correction) 2500 W, 3 m Torr of Argon.

power into the bulk of the discharge, rather than losing most of it in the sheath. As a result, density is noticeably higher everywhere in the chamber.

Another of the performance criteria for the linear source was its ability to generate a dense plasma uniformly over the length of an extended source. Measurements of density versus x-position are shown in Figure 5-4. Measurements were made at a 5 cm distance outside the antenna at the left edge of the antenna (0 cm), the middle of the antenna (12 cm), and at the right side of the

Figure 5-4. Density vs Position (New Field) 2500 W, Argon.

Figure 5-5. Density vs Position along Source (X dimension) 3 mTorr of Argon, 2000W Beach Field.

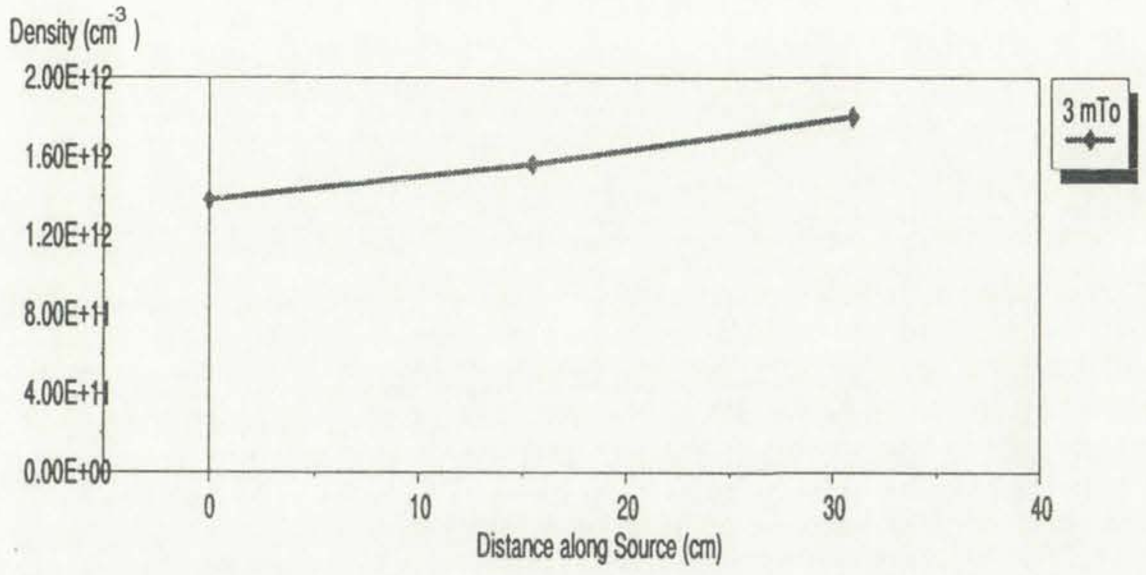

antenna (30 cm). The plasma is ± 15% uniform over a 30 cm distance, but there is a troubling trend toward higher densities as the probe moves toward the right of the antenna. Trends of this type could be caused by irregularities in the antenna shape. Perhaps one loop or side of the antenna was closer to the source than the other, resulting in better coupling. If this were the cause, then there should be some evidence of it in the B-dot probe measurements. A subsequent review of **B**-dot probe measurements taken across the source reveals the nonuniform coupling of the antenna, and appears to indicate a faulty loop. Figure 5-6 shows the amplitude and phase values of the excitation field just outside the source. The scan starts at the left side of the antenna (0 cm), moves past the first loop at 9 cm, the second loop at 18 cm, and so on. There is an amplitude peak at 3 cm corresponding to the side of the first loop closest to the chamber, a sign change at 5 cm (apparent in the Pi phase shift), and another peak associated with the segment of the first loop closest to the back wall. The pattern repeats for the second loop up to 18 cm. But the back edge of the third loop results in a much higher peak than the two previous loops, which results in a density profile that shifts toward the right side of the source. The solution to

Figure 5-6. Wave Structure across Source
3 mTorr of Argon, 2000 W, Mirror Field.

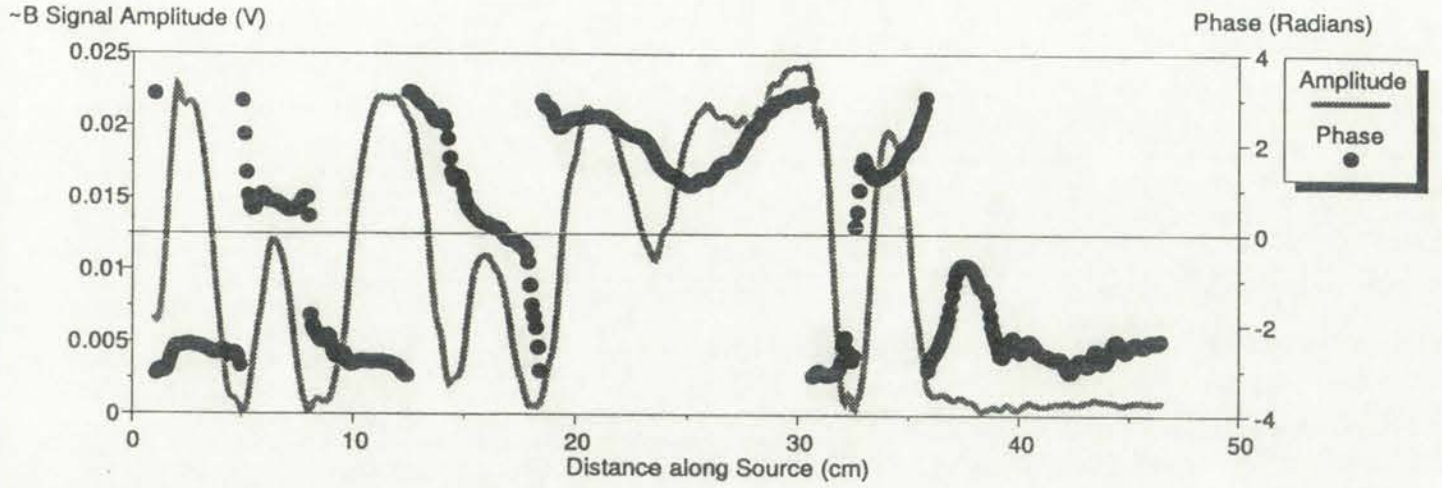

this nonuniformity probably lies in the careful machining of an antenna to more exact dimensions than the hand-bent model built for this experiment. Further experiments revealed that the effect changed with pressure, which indicated this problem was slightly more complex than was first thought. Another remarkable feature about the plot shown in Figure 5-6 is the contribution of individual segments of the antenna. Wave excitation from each segment is visible downstream, with seemingly very little cross-field contribution. Each component appears to launch waves independent of the other elements.

A very brief measurement of density in an electronegative gas (CF_4) was performed. With only a minimal amount of optimization, a density of 2.52×10^{11} cm^{-3} was derived from a Langmuir probe trace (3 mTorr of CF_4, 2000 W, Center of Chamber). The total number of ions present in the system must be higher, because a significant portion of the radicals present are negatively charged species. Negative species are not collected during the portion of the I-V characteristic when the probe is negatively biased, which is the section of the trace used to calculate ion density. Accordingly, a more accurate statement is that a positive ion density of 2.52×10^{11} cm^{-3} was measured in CF_4.

In a further effort to understand the operation of the slab source, a larger third chamber was built. It was not felt that building a source identical to the second source would be most beneficial to the ongoing source development. Rather, several design choices were made to allow this tool to have more room to perform large-substrate processing, and to explore a slightly higher range of magnetic field values. The third machine is pictured in Figure 5-7. Note that nearly all of the dimensions of the source have been scaled up, and that more ports have been added for diagnostic access. The magnetic field coils, which are not pictured in Figure 5-7, were designed to produce similar field shapes to the coils used on machine 2, but at double the strength. The rational for this increase is that once well above the ECR point, the density scales with the magnetic field (from equation 15). Although the densities achieved in the chamber were sufficiently high, it was thought that even higher density values could be traded for uniformity. Photographs of the third machine are included as Appendix II.

Figure 5-7. The Third Linear Source Chamber.

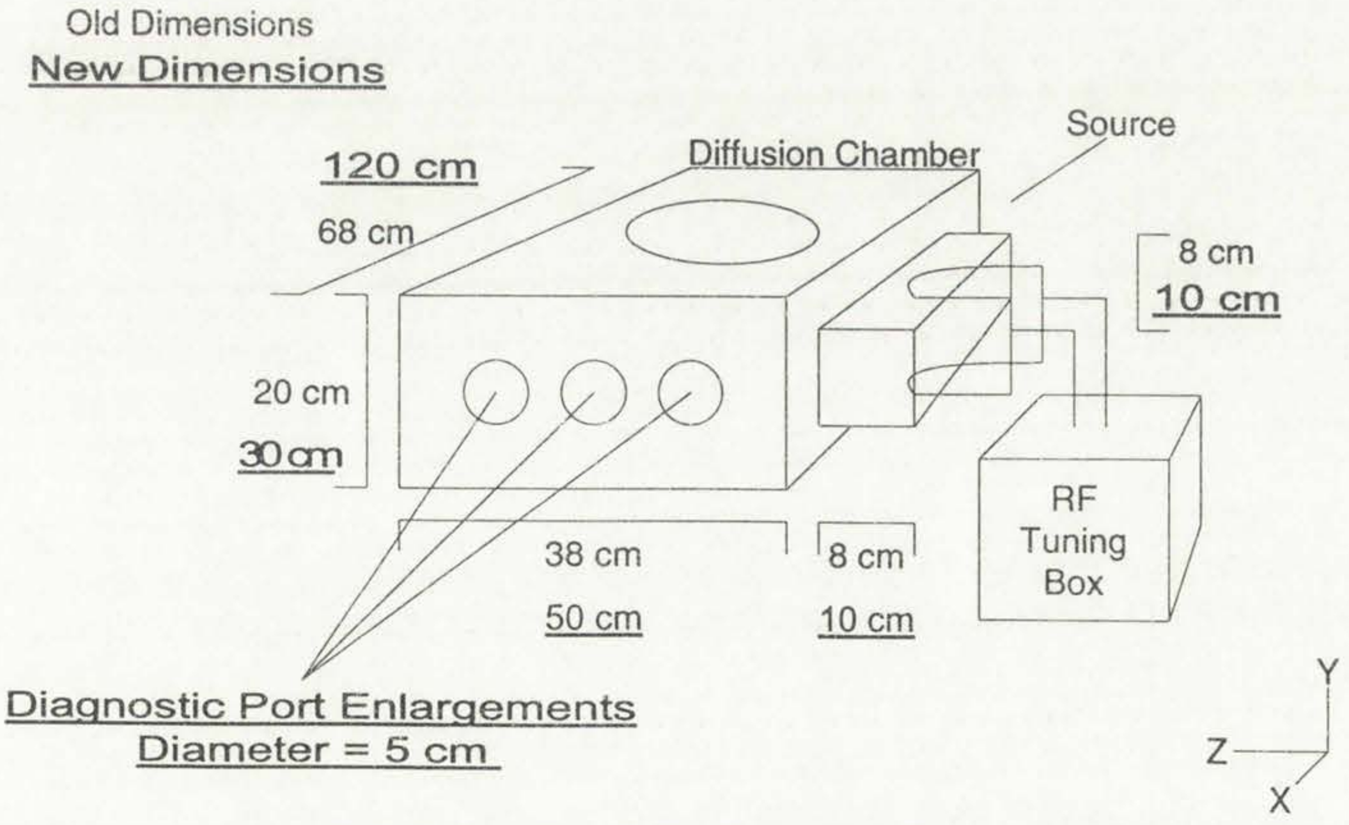

In a further effort to understand the operation of the disk source, a larger field chamber was built. It was not felt that building a source identical to the second source would be most beneficial to the ongoing source development. Rather, several design choices were made to allow this tool to have more room to perform [illegible] and to explore slightly higher levels of magnetic field values. The third machine is pictured in Figure 6-7. Note that nearly all of the dimensions of the source have been scaled up, and that more ports have been added for diagnostic access. The magnetic field coils, which are not pictured in Figure 6-7, were designed to produce similar field shapes to the coils used on machine 2, but at double the strength. The rational for this increase is that once well above the ECR point, the density scales with the magnetic field (from equation xxx). Although the densities achieved in the chamber were sufficiently high, it was thought that even higher density values could be traded for uniformity. Photographs of the third machine are included as Appendix B.

Figure 6-7. The Third Linear Source Chamber

The coils built for this project were designed around available power supplies, with the two strong field coils on the ends formed into a racetrack shape 126.3 cm x 22.34 cm inner dimensions. 340 turns of number 8 square cross-section layers were laid down with 17 turns per layer and a height of 20 layers. The coils were wound into a pre-constructed copper shield to allow operation close to the antenna with little RF interference. The field produced by a current of 20 A is 212 G in a direction perpendicular to the plane of the coil. Also constructed with the same number of turns were two "shaping" coils to be placed lengthwise around the chamber to enhance the solenoid type of behavior. For completeness, these were also shielded from RF by a conducting copper case. The field contribution of a single one of these coils carrying 10 A of current is 52.9 G. (The currents given are the maximum available from their respective supplies). A typical variation in field strength with **Z** position is shown in Figure 5-8.

Figure 5-8. Field Strength in the Z direction versus Distance Away from Center. Coil Currents 7.0, 4.0, 3.0 and 0.0 A, and positions 67.3, 53.58, 16.9, -3.4 cm

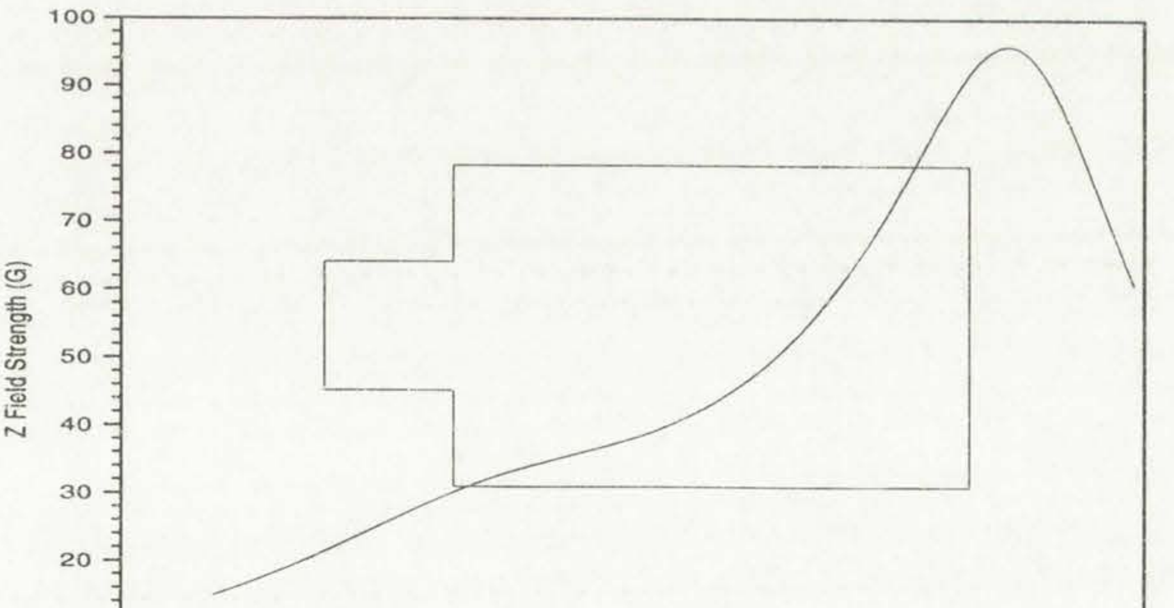

Before launching into a discussion of source characteristics, the diagnostics should be revisited, as there were significant changes made to the Langmuir and B-dot probes used on the third tool. Only minimal attention was given to RF compensation on the Langmuir probes used on the second machine. A small inductor whose self-resonance was very close to the fundamental RF frequency was constructed into the tip. However, since the plasma has a slight capacitance with the inductor in the tip, its in-circuit resonant frequency is slightly changed. RF effects were more carefully addressed on machine 3. The method used in this segment of experiments followed the technique of Paranjpe et al.[39], with some slight modifications. The plasma capacitively interacts with the probe tip. Because the sheath thickness changes with any change in bias between the probe and the plasma, the capacitance between the probe tip and the plasma also changes, and is a nonlinear effect. Rather than spend a considerable amount of time building an active feedback amplifier system (as others have done)[40], a passive component approach was used. The probe tip was constructed into a piece of ceramic rod with a large copper slug built inside, insulated from the plasma. The plasma also capacitively couples to the slug, but because sheath thickness changes are negligible compared to the thickness of the ceramic, a voltage independent capacitance to the plasma is obtained. The key is to make the slug to plasma capacitance much larger than the tip to plasma capacitance. See Figure 5-9 for a schematic representation of the probe circuit. C_t, and R_t represent the tip to plasma capacitance and resistance, respectively, and C_s is the slug capacitance to the plasma through the ceramic casing. There is also a probe to ground capacitance given by C_g, and an inductance, L_p, associated with the length of the probe. This is where the analysis used here differs from that of Paranjpe. The length of the probes for the slab tool introduces a significant inductance, which cannot be ignored. Finally, there are two adjust-

Figure 5-9. Schematic Representation of Probe Circuit

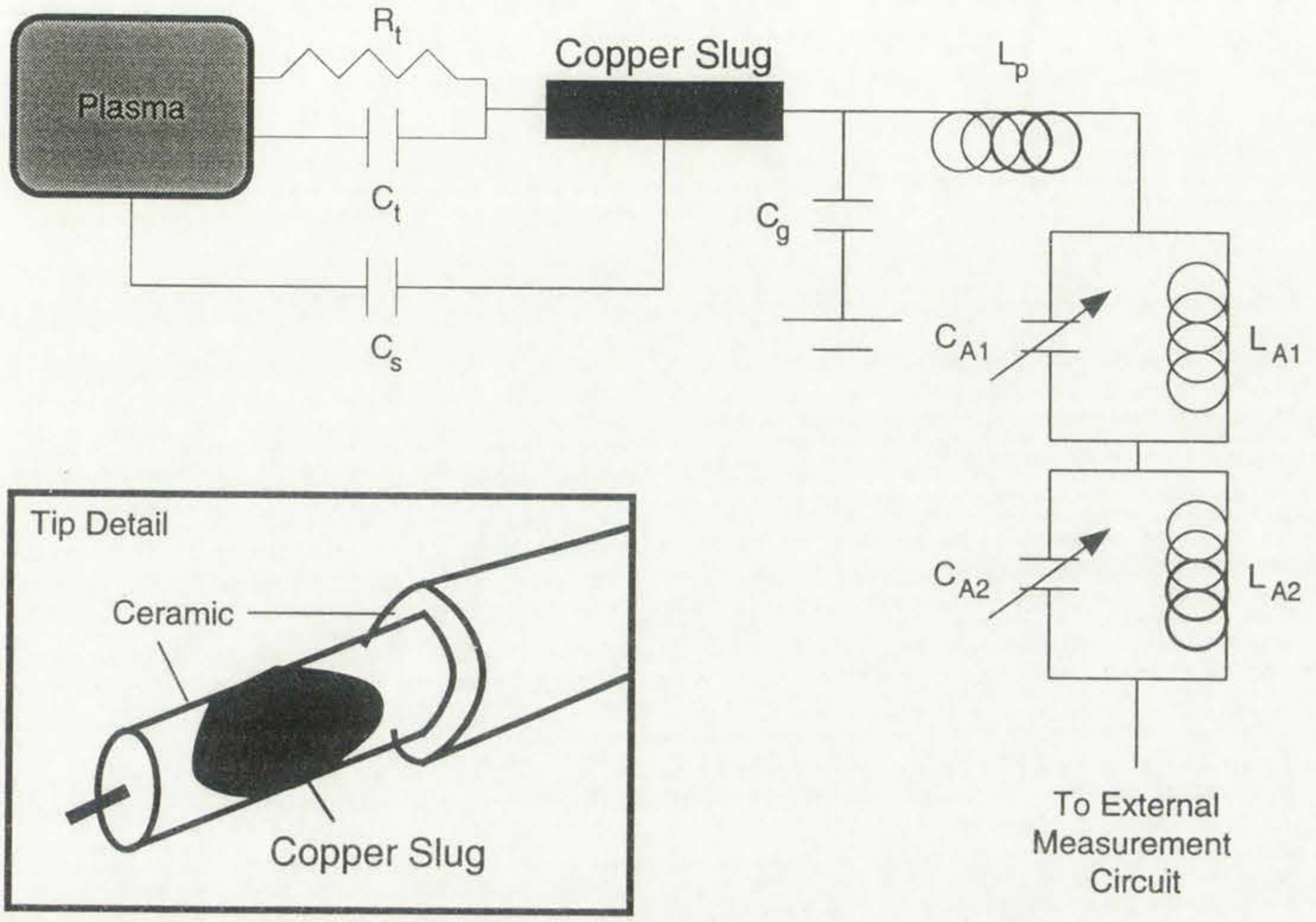

able L-C circuits to tune for resonance at the fundamental (13.56 MHz = 8.52 x 10^7 rad/sec), and at the first harmonic. This looks like a rather complicated circuit, but it can be modeled analytically; R_t can be estimated from a sample Langmuir probe trace at ~500 Ohms, and C_t was estimated by wrapping a piece of aluminum foil around the tip. The measured capacitance was less than 2 pF. The slug was designed to provide a linear capacitance of 15 pF with the plasma. Therefore, the capacitance of the tip-slug combination is given by $C_s + C_t \cong C_s$. The magnitude of the tip impedance is given by

$$\left|Z_{tip}\right| = \frac{R_t}{1 + w^2 C_s^2 R_t^2}\sqrt{1 + w^2 C_s^2} \qquad (33)$$

and the magnitude of the impedance of the rest of the probe circuit with a single

L-C filter in place is

$$\left|Z_{\text{probe}}\right| = \frac{wL_{A1} + wL_p(1 - w^2 L_{A1} C_{A1})}{1 - w^2 L_{A1}(C_{A1} + C_g) - w^2 L_p C_g (1 - w^2 L_{A1} C_g)} \quad (34)$$

L_p and C_g were measured and found to be 1.9 μH and 65.4 pF, respectively. Making the probe impedance 100 times that of the tip alone, using a 100 pF value for C_{A1}, the appropriate inductor was 0.123 μH. Following a similar analysis for the first harmonic, values of 100 pF and 1.27 μH for C_{A2} and L_{A2}, respectively, were found. Capacitors that were adjustable between 25 and 200 pF were chosen to account for any small effects which were not considered in the analysis. Adjustment of the two tuning capacitors was performed while watching the I-V trace on an oscilloscope, maximizing the potential where the trace moves into the electron current gathering region.

Figure 5-10 shows a schematic of the circuit used to bias the probe and measure the corresponding current. The Analog Devices AD202 Isolation Amplifier was configured with a gain of 1, where the amplifier had the best frequency response. The two current sense resistors provided sufficient gain. Of considerable importance is the use of a slow sweep time, and a sine wave driving input. Isolation amplifiers with high common mode rejection, like the AD202, usually have very poor high frequency performance. The AD202 cannot be used above 200 Hz without introducing significant attenuation and phase shift. A triangle wave contains several higher frequency components; in order to eliminate any problems associated with them, it is essential that the bias voltage be driven in sine wave fashion.

Figure 5-10. Langmuir Probe Biasing Circuit

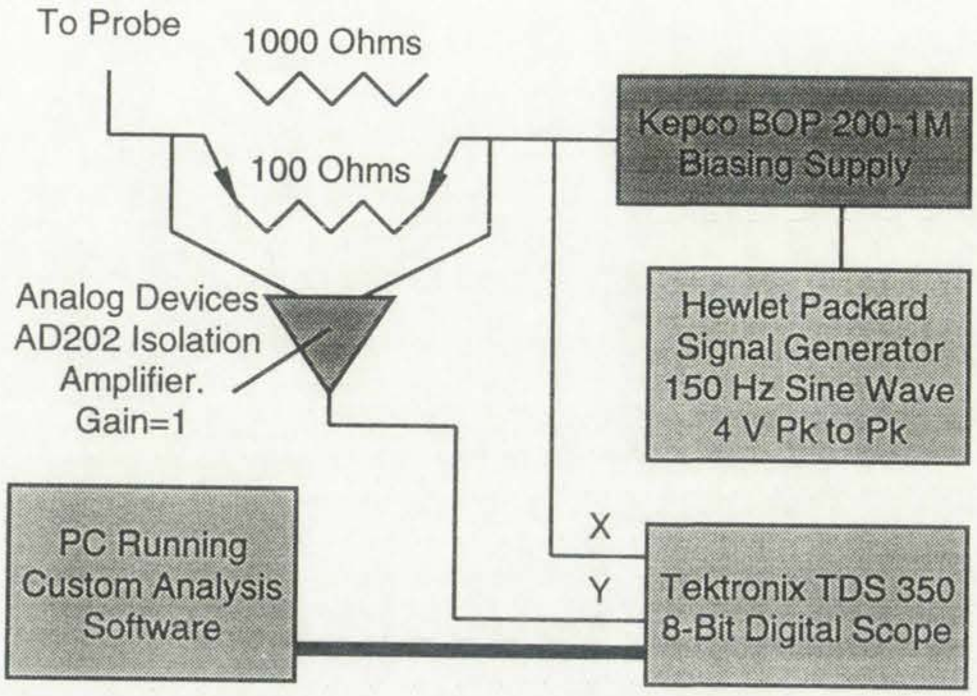

A final measure taken to improve the accuracy of the density measurements taken with the Langmuir probe was to make the collecting area of the probe tip very small. Miller, et al.[41] have shown that the use of large area probes results in an underestimate of the actual plasma density as compared to a microwave interferometer measurement. Accordingly, an area of 2.96 mm^2 was used.

Measurements with the new Langmuir probe, along with the improved analysis techniques, yielded some surprising insights in to the performance of the extended source. A typical density profile as function of distance out from the source is shown in Figure 5-11. The density peaks outside the source, but the density decreases more steeply with distance when compared with the second machine. Also, the density is lower, which is probably due to the lower operating power, and a higher chamber volume. (It was felt that operation at higher powers would present an implosion hazard on the new machine, because some small pits in the glass were observed near the high voltage end of the antenna.

Figure 5-11. Density versus Distance out from back of Source. 8 mTorr of Argon, 1250 W

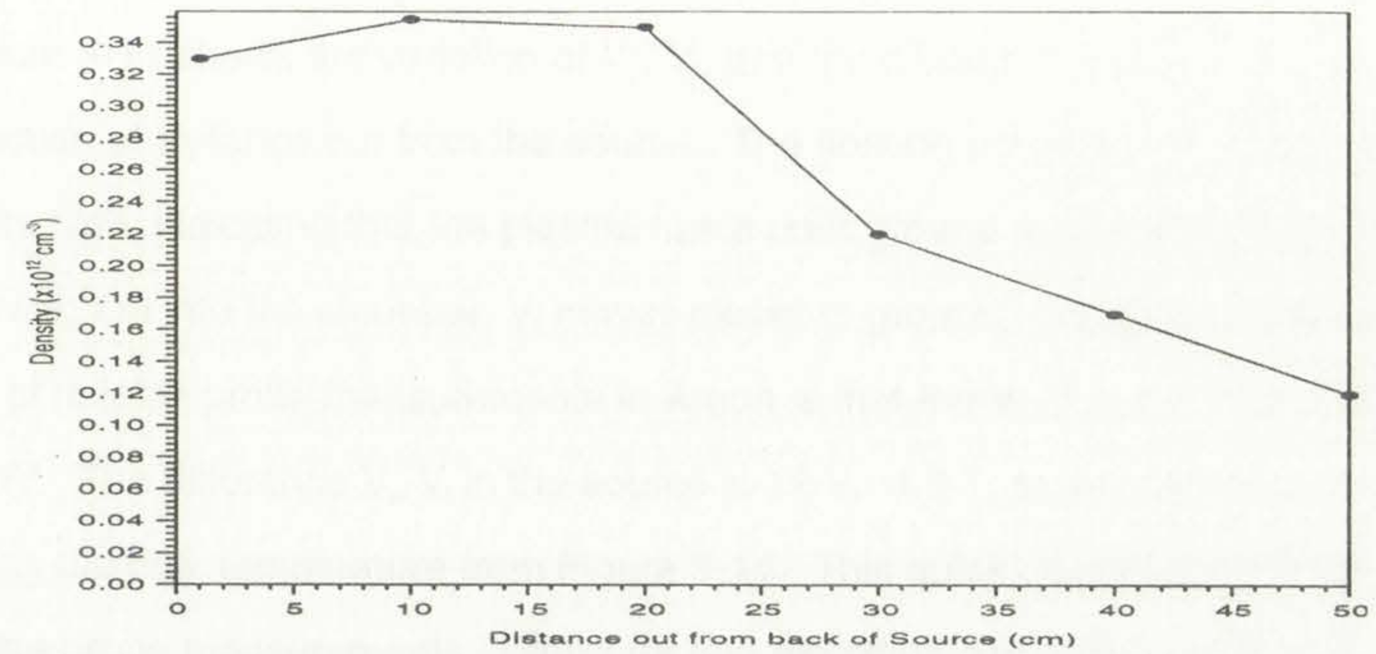

This danger would be minimized if the source dielectrics were replaced with ceramic, as has been done on the second machine). The magnetic field used for the 8 mTorr measurements in Argon is shown in Figure 5-12. Magnetic field values were again chosen so as to maximize density at 40 cm out from the back of the source. The same optimization technique was used in all subsequent experiments. The decrease in density as a function of Z position was not surprising, but the plasma potential (V_p), floating potential (V_f), and current

Figure 5-12. Bz Field Strength versus Distance out from back of Source. 8 mTorr Ar Conditions

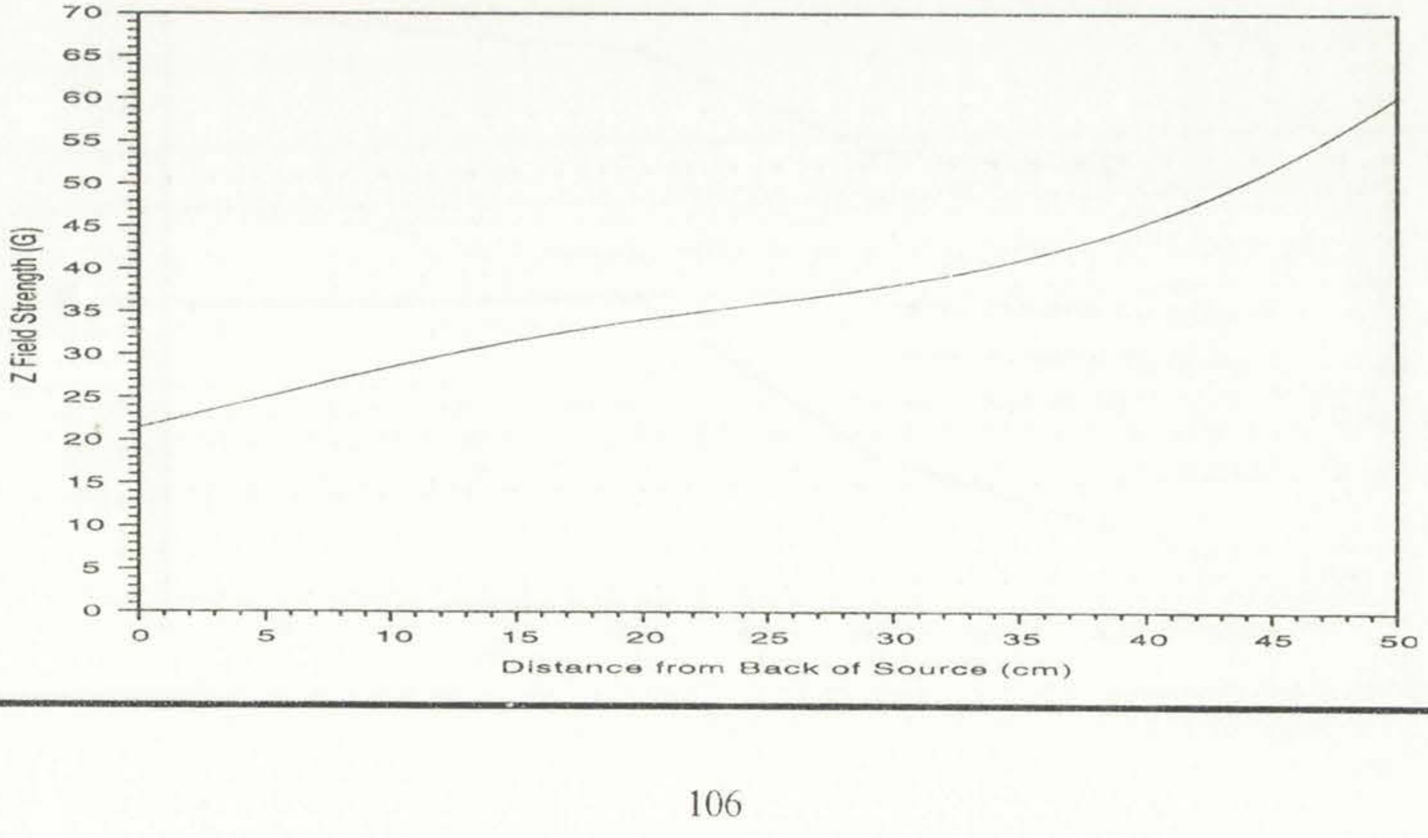

Figure 5-14. Electron Temperature versus Distance from back of Source. 8 mTorr Ar Conditions

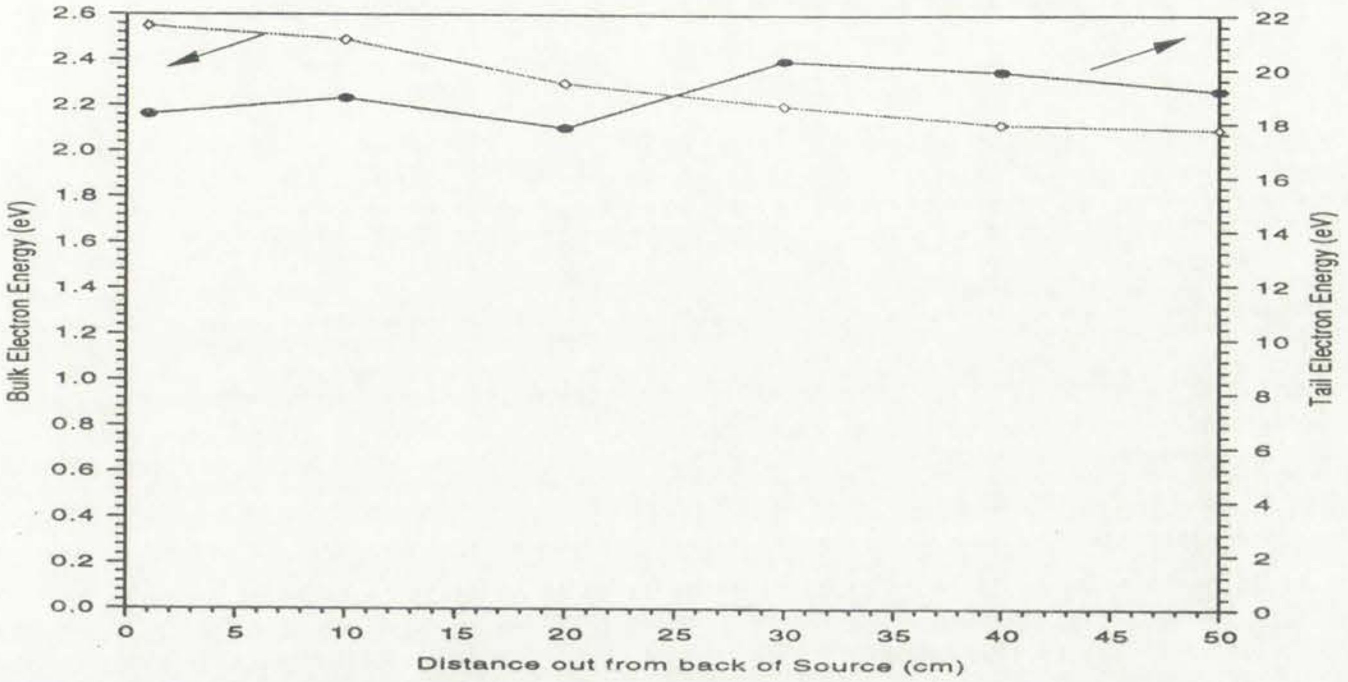

Figure 5-15. Percent of Total Electron Current due to Warm Electrons versus Distance from back of Source. 8 mTorr Ar Conditions

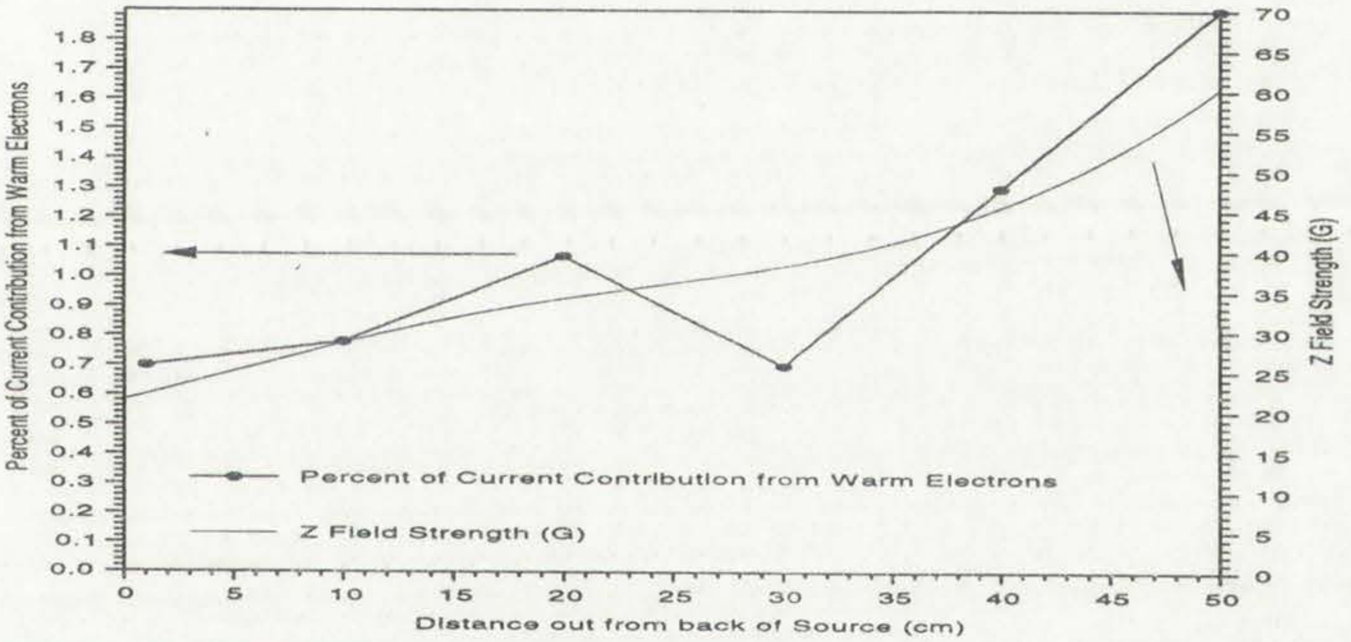

tion current at very negative probe bias. If not performed properly, this technique can cause some misinterpretation of the data, and lead to erroneous results. Therefore, any results used from this technique were checked using the Druyvesteyn second derivative routine.[33] Very good agreement between the two techniques was obtained.

Recently, Langmuir probe orbital-motion-limited (OML) theory has become

Figure 9-12. Electron Temperature versus Distance from Exit of Source, 3 mTorr Ar Conditions

Figure 9-13. Percent of Total Electron Current due to Warm Electrons versus Distance from Exit of Source, 3 mTorr Ar Conditions

ion current at very negative probe bias. If not performed properly, this technique will cause some misinterpretation of the data, and lead to erroneous results. Therefore, any results based from this technique were checked using the Druyvesteyn method (derivative model).[illegible] Very good agreement between the two techniques was obtained.

Recently, Langmuir probe orbital motion limited (OML) theory has become popular.[33] It was not used here, because some of the assumptions needed to satisfy the theory are rather difficult to obtain experimentally. They include:

1. a small probe and rare plasma, probe dimensions << the Debye length (λ_D),
2. no ion collisions in the probe sheath, $\lambda_D << \lambda_i$ (where λ_i is the ion mean free path). Orbital motion is extremely sensitive to (and destroyed by) ion collisions,
3. ions cold compared to electrons,
4. a Maxwellian EEDF, and
5. a one-dimensional cylindrical probe sheath. At high probe voltage, and low pressures, the sheath around a cylindrical tip looks approximately spherical. (OML theory gives $I_i[V_{bias}] \propto |-V_{bias}|$).

The accuracy of OML theory and the even more sophisticated Laframboise theory[42], which accounts for probe sizes of the order of the Debye length, and differing ion and electron temperatures, have been questioned in several recent works[43,44,45], so their use was shunned in favor of the simpler second derivative (or Druyvesteyn) approach. The Druyvesteyn approach requires collisionless electron motion around the probe, which implies that the probe dimensions and λ_D be much less than λ_e, (the electron mean free path). The Debye length in the linear tool is of the order of $1\text{x}10^{-5}$m for 3 eV electrons, and the electron-neutral mean free path is about 3cm at 5 mTorr. The probe tip is 2.0mm long, with 0.39mm outer diameter, so probe dimensions are less than the electron mean free path. Further, the area of plasma exposed to the tip can be approximated by the area of the tip because the Debye length is so small compared to the probe dimension. If the probe dimensions are not much less than λ_e, the plasma

density around the probe is depleted, since electron diffusion from the nearby plasma cannot compensate for electrons collected by the probe[46]. This leads to a distortion of the low-energy part of the EEDF[47].

The Langmuir probe used in these experiments was constructed so as to offer a high impedance to RF, but because the current perceived to be due to warmer electrons was only 1 to 2 percent of the total current, the effect of RF on probe measurements needed to be considered. RF perturbations in helicon plasmas are on the order of 1 V peak to peak[48]. Therefore, the actual bias of the probe with respect to the plasma is the sum of the applied bias and the RF oscillations. The first of these terms is part of the normal probe analysis, but the RF oscillations mean that the actual current measured on the probe is the average of the currents collected while the plasma oscillates at some RF voltage with respect to the probe. One can imagine an oscillation of the I-V characteristic along the bias axis, as is pictured in Figure 5-16. To determine what effect this oscillation has on the measured EEDF, a synthetic trace was used, assuming a 3eV Maxwellian electron distribution, and a 10 V plasma potential. Current at any given bias was considered to be the average of the currents if the bias were allowed to oscillate

Figure 5-16. RF Oscillations on an I-V trace

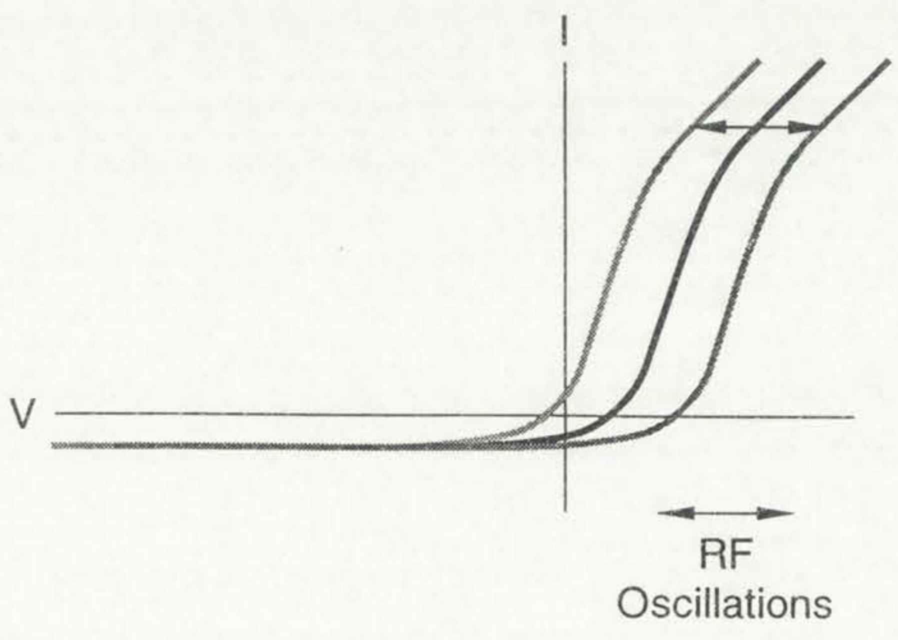

density measured [illegible] is obtained [illegible] from the floating potential [illegible] compensated [illegible] by the probes. The result is a distortion of the I-V characteristic of the probe.

The Langmuir probe used in these experiments was not designed so as to offer a high impedance to RF, so because the [illegible] due to [illegible] electrons and subject to [illegible] the effect of RF on probe measurements needs to be considered. RF perturbations in [illegible] plasmas are of the order of [illegible]. Therefore, the actual bias of the probe with respect to the plasma is the sum of the applied bias and the RF oscillations. The first of these terms is part of the regular probe analysis, but the RF oscillations mean that the [illegible] current measured by the probe is the average of the currents over the range of [illegible] RF voltages with respect to the probe. One can imagine an oscillation of the I-V characteristic along the bias axis, as illustrated in Figure 6-18. To ascertain what effect this oscillation has on the measured EEDF, a synthetic I-V was used, assuming a 3eV Maxwellian electron distribution, and a 10 V [illegible]. Currents at any given bias was considered to be the average of the currents if the bias were allowed to oscillate

Figure 6-18. RF Oscillations on an I-V trace

Figure 5-17. Simulated Distortion of EEDF's by RF

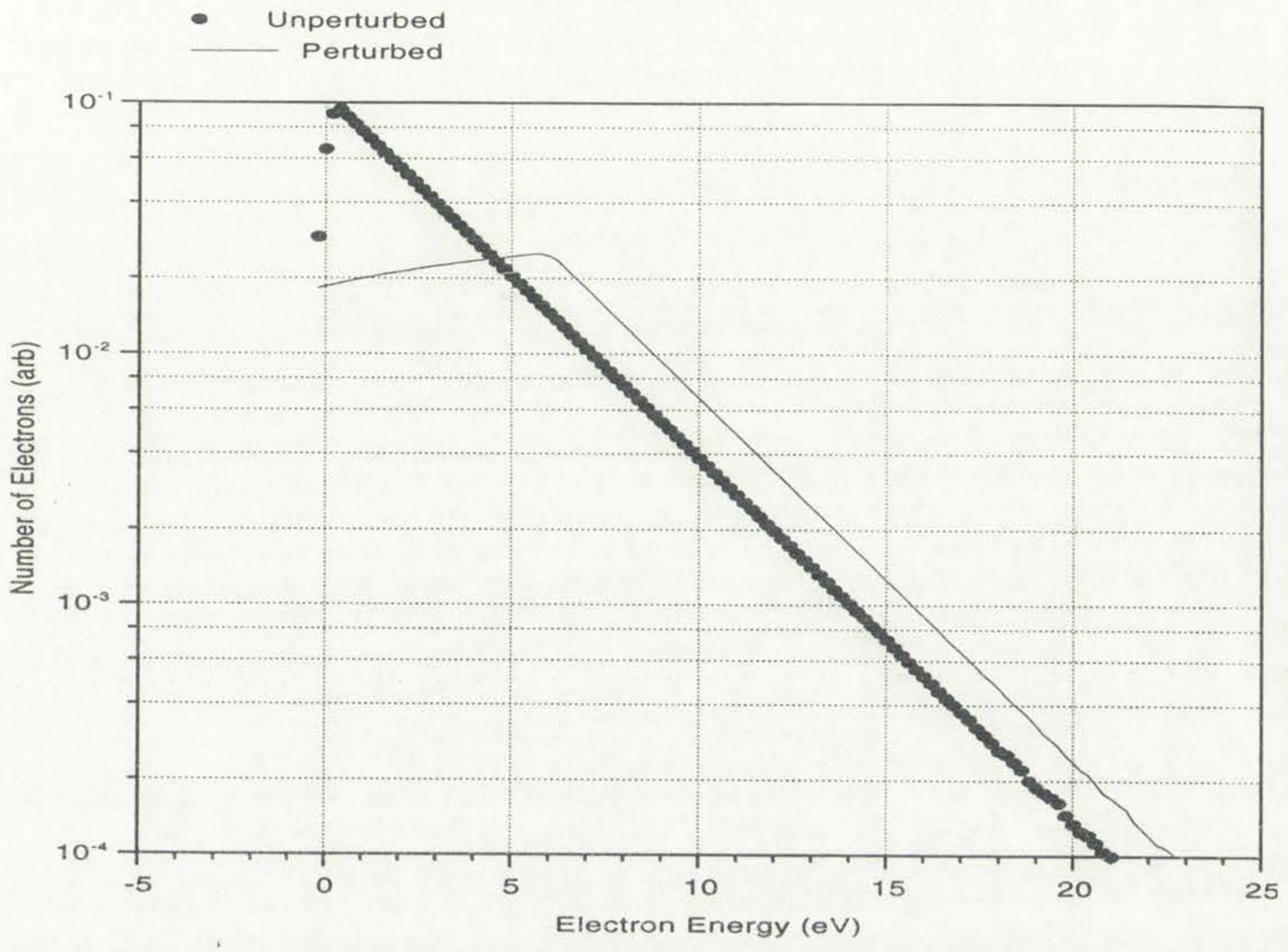

with 32 V peak to peak. Oscillations this large would almost never be observed in a real system, but the analysis needs to be robust.

Shown in Figure 5-17 are the unperturbed and perturbed EEDF's obtained from the simulation. Note that there is considerable error introduced in the low energy portion of the distribution below 6 eV. Higher energies are shifted up slightly from their initial population. The slope is the same in both of the traces, and both resemble 3 eV Maxwellian distributions. RF fluctuations present in the plasma introduce another source of error in the low energy portion of the EEDF, but leave the higher energy sections relatively intact. Similar analysis by other authors[39,49] has shown the same effect.

Two other sources of systematic errors which need to be considered before

presenting measured EEDF's in the new chamber are low frequency noise effects, and ion current effects. Godyak[50] has shown that low frequency plasma potential changes (usually due to RF power supply instabilities) can produce the same low energy distortions in the EEDF as is caused by RF in the plasma. Averaging over multiple probe scans can be used to minimize this effect, but because the fluctuations introduced are not truly random, this is only a partial solution. Active feedback techniques can be employed where this is a significant problem, but they were not necessary for the helicon source measurements. Second, the validity of the calculated EEDF in the ion current collecting region needs to be examined. It is assumed that for a large portion of the I-V trace, I''_i (the second derivative of the ion current) << I''_e (the second derivative of the electron current). It has been shown[13,51] that the dynamic range of an EEDF measurement is limited by the ion current contribution which is of maximal influence for light gases and cases where the probe size is of the order of λ_D. Using OML theory to obtain an estimate of the uncertainty limit for EEDF measurement gives the approximate usable range as $^{M}/_{m_e}$. For Argon, this is ~10^5. Therefore, for a Maxwellian distribution, the maximum usable energy is 11 T_e. At 11 T_e, the measured EEDF may be overestimated slightly (by a factor of no more than 2)[4]. With this dynamic range limitation in mind, and using averaging to minimize low frequency perturbations, EEDF's in the new chamber were obtained.

Figure 5-18 shows a sample EEDF taken just outside the source in Argon at 7 mTorr. Solid lines represent the fit made to the extracted electron current, and the points represent the second derivative of the actual probe trace. Note that the fit proves to be quite acceptable in the lower energy range, and although there appears to be a little noise present in the lower part of the trace, a warmer population of electrons can be found. The entire trace is contained within the 10^5

Figure 5-18. EEDF for 8 mTorr of Argon, 2000 W, 15cm from Source Wall

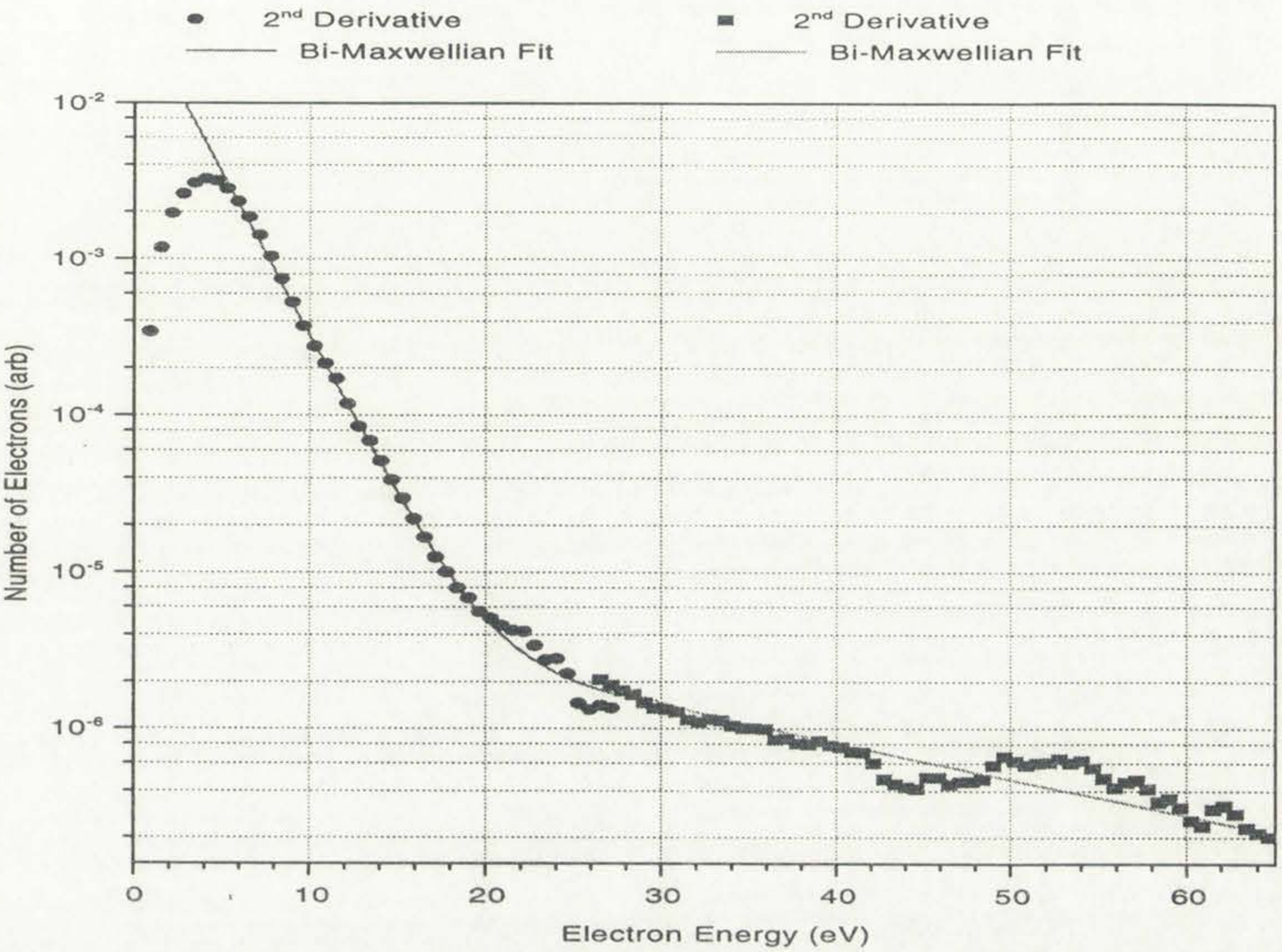

dynamic range limit set by the conservative method used above. Therefore it is unlikely that the second portion of the bi-Maxwellian is an artifact of the ion current. The fitted bi-Maxwellian temperatures were 2.0 eV and 18 eV, respectively, with the 18 eV electrons contributing 1.6% to the total electron current. In the low energy portion of the spectrum, note that there appears to be a bit of rounding in the 0 to 4 eV range. This is an artifact of taking the numerical second derivative. Its shape can be widened or narrowed by changing the width of the polynomial fitting window, or the order of polynomial used. A stiffer polynomial technique was used to resolve the higher energy portion than was used to examine the low energy portion, as is shown by the segment from 26 to 65 V in Figure 5-18.

The origin of the high energy tail is still unclear. Measurements of very similar distributions in argon in a capacitively coupled plasma tool have been made by Godyak, et al.[33] They attribute the presence of the warm tail to stochastic heating in the sheath, energy transfer from strong electric fields near plasma boundaries, and other mechanisms. It is entirely possible that capacitive coupling of the antenna to the plasma in the extended helicon source could drive the same mechanisms. Another possible explanation is the coupling of the helicon wave into a select group of electrons via Landau damping. The wavelength of perturbations in the static field along Z has been measured at ~12 cm. The phase velocity of that wave is given by ω/k (or λf), where f is the frequency. For f=13.56 MHz, the phase velocity is 1.63×10^6 m/s. For electrons to be moving at that speed, they must have an energy of 7.5 eV. There is certainly a population of electrons with that energy present in the plasma, but typical tail temperatures appear to be 18 eV. A further possible explanation is that there may be two distinct populations of electrons present on the machine: a low energy distribution with velocities principally parallel to the static field lines, and a warmer population with velocities perpendicular to field lines. High energy electrons whose velocity vectors are oriented perpendicular to the field lines have a longer residence time in the chamber than those with velocities parallel to field lines.

Unfortunately, the data do not clearly support any of these mechanisms over the others. If the presence of warm electrons is solely a function of field strength, then that trend should be evident in the data analysis. Shown in Figure 5-19 is the percentage of electron current due to warm electrons as a function of static field at various positions in the chamber. For all but the 2 mTorr pressure series, there is a tendency to see higher current proportions from warm electrons at higher field strengths. Even so, the field geometries are very similar for the three

Figure 5-19. Current due to Warm Electrons vs Static Field Strength. Argon, 1250 W

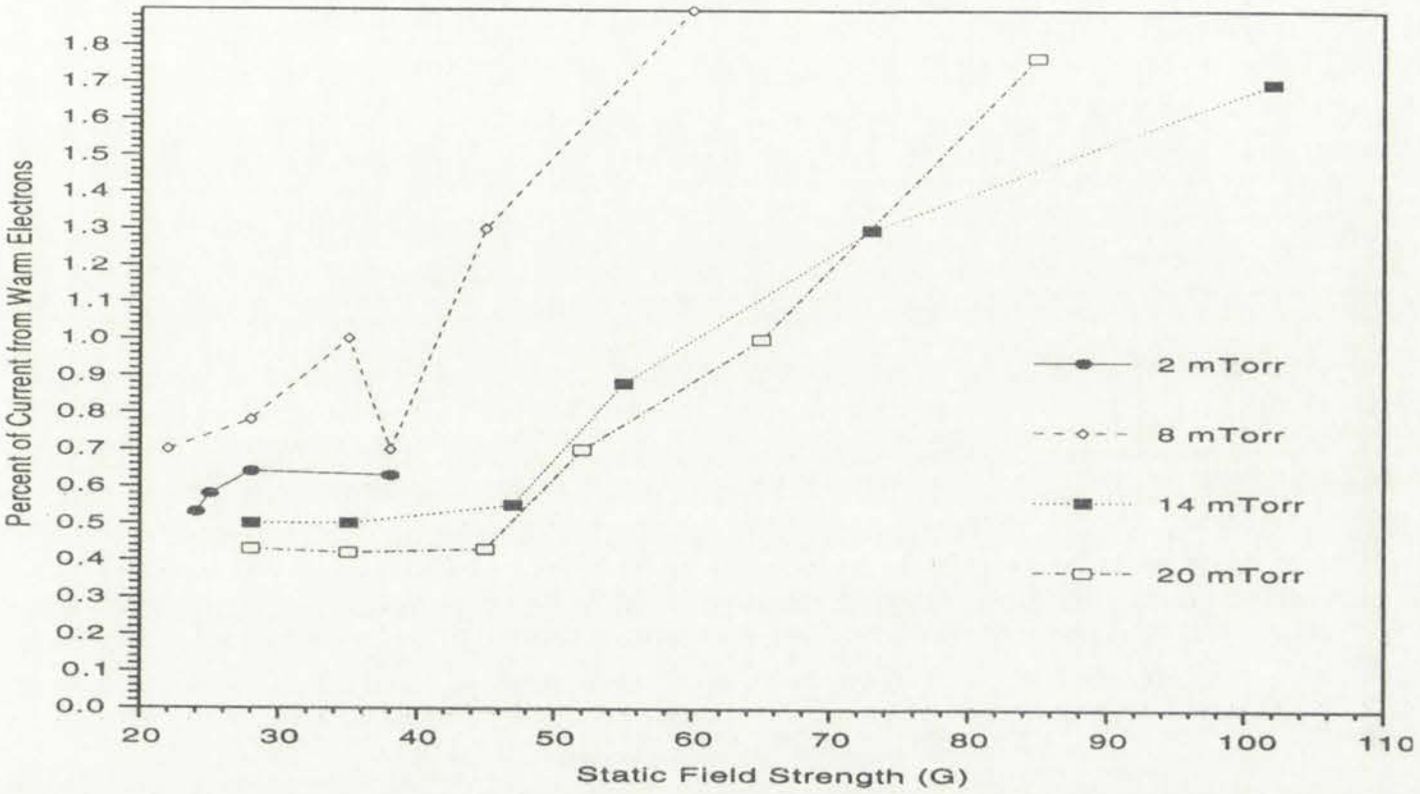

sets which leaves room for doubt about the explanation. Probe traces taken with the tip parallel and perpendicular to the field lines may produce different warm electron current ratios at the same position in the chamber. At 20 mTorr in the center of the chamber, a parallel measurement yields 1.0% warm electron current. The perpendicular measurement yields 0.87%. This ~10% discrepancy is not a convincing difference. At 8 mTorr, the difference is a bit higher: 0.76% measured perpendicular to B_0, and 1.3% parallel. Still, the differences are not strong enough to prove (or disprove) this theory.

If the heating mechanism were largely driven by capacitive effects, which result in large fields in the source and near the plasma edges, there should be a markedly larger population of warmer electrons in the source than in the relatively isolated diffusion region in the center of the chamber due to the mean free path of the electrons. Figure 5-20 shows that the opposite effect appears to be the trend. Finally, that Landau damping is the predominant mechanism is also not evident, as the warmer populations observed appear to have energies much

Figure 5-20. Current due to Warm Electrons vs
Distance from Source Back Wall.
Argon, 1250 W, 8 mTorr

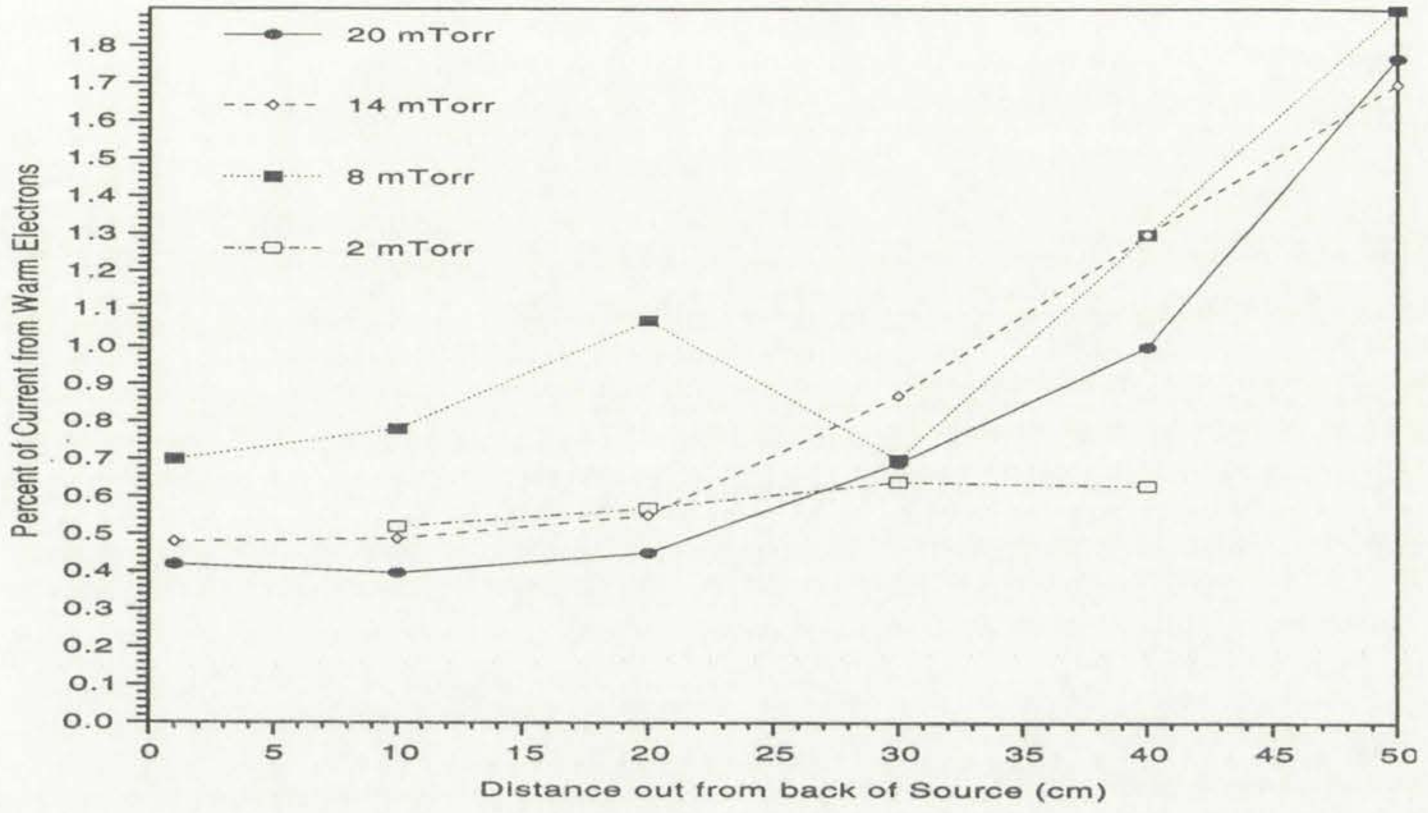

larger than could be obtained via Landau damping in this machine (18 eV distributions, compared to phase velocities that would interact with 7 eV electrons) . Further work will be necessary to fully address this question.

Measurements along the source exhibited some asymmetry from one end to the other. One explanation for this systematic behavior was that one antenna element was coupling to the plasma differently, as appeared to be evident in one of the B-dot probe scans. That the second source exhibited similar behavior with a new antenna set, and at different pressures, suggests that another mechanism is at work. Shown in Figure 5-21 is the density as a function of position along the source for 8 and 20 mTorr. While the variation in density over 40 cm is approximately ±10% at 8 mTorr, variation of more than ±25% is seen at 20 mTorr.

Improvements were also performed on the existing B-dot probe. Prior mea-

Figure 5-21. Uniformity across the Source
Argon, 1250 W

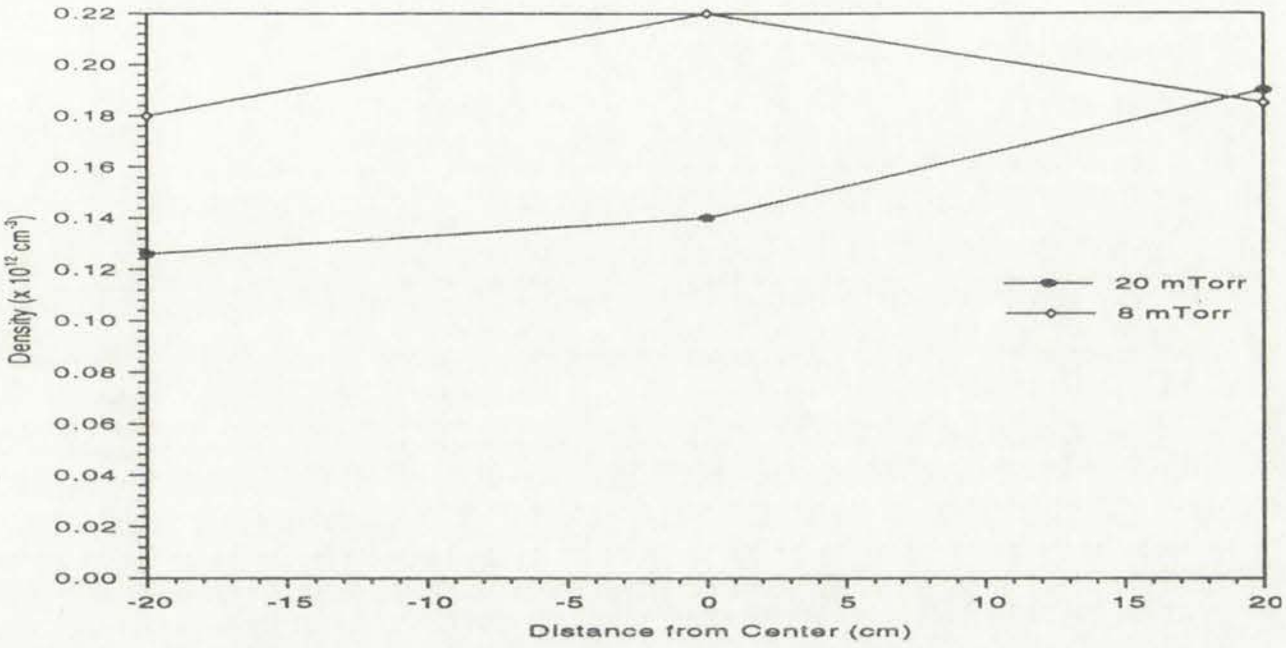

surements had been made only for B_z. Hoping to obtain information on the 3-d wave structure, a 3 channel probe was constructed using the same circuit components as were used for the single channel model. The tip of the probe was made with three loops of 5 turns each, each oriented perpendicular to the others. Twisted pairs carried the three signals back to a central box where comparisons were made to an RF reference. Connections were made from the box to a new data acquisition system installed in the PC. The seven data channels, one for position and two for each of the three loops (as before), were acquired and saved to a text file for later analysis. Amplitude and phase information could be determined individually for each of the three components of the wave, and a composite wave reconstructed. Figure 5-22 shows a sample data set taken at 2 mTorr of Argon. The probe was scanned from the source out along Z, along a center line through the chamber. The rotation of the wave is obvious, and the amplitude decreases slightly as the wave is absorbed with increasing distance from the source. Note that the wave does not have a constant rotation sense, but that it markedly changes rotation directions near 17.5 cm out of the source. This non-constant rotation is predicted by the derivation in section 2G. For clar-

Figure 5-22. 3-D Wave Amplitude vs Distance from Back Wall of Source

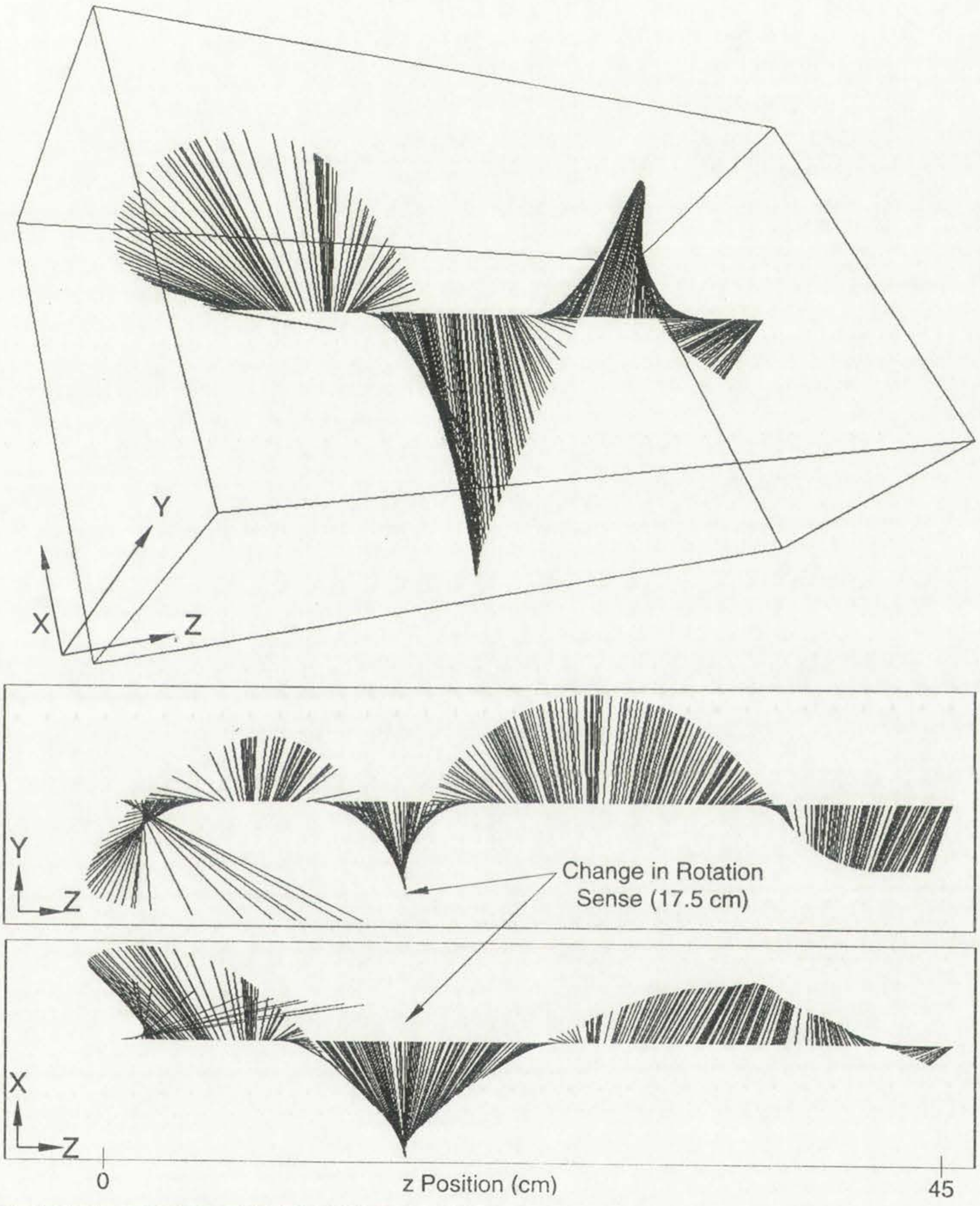

ity, individual components of the wave as a function of distance out from the source are shown in Figure 5-23.

Figure 5-23. Measured Components of the Helicon Wave versus Z Position. 2 mTorr of Argon, 1250 W.

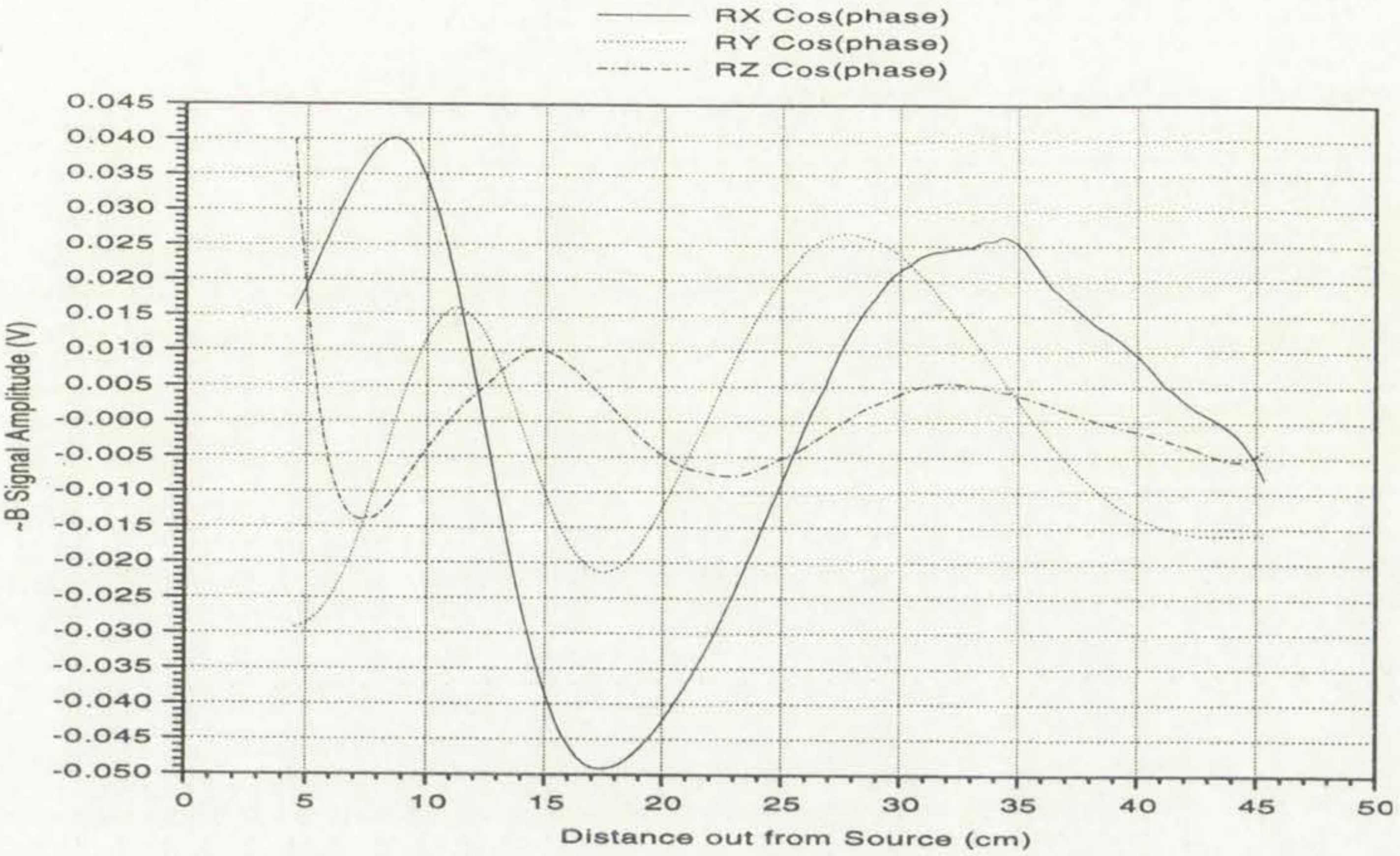

Figure 5-24. Measured Components of the Helicon Wave versus Z Position. 8 mTorr of Argon, 1250 W.

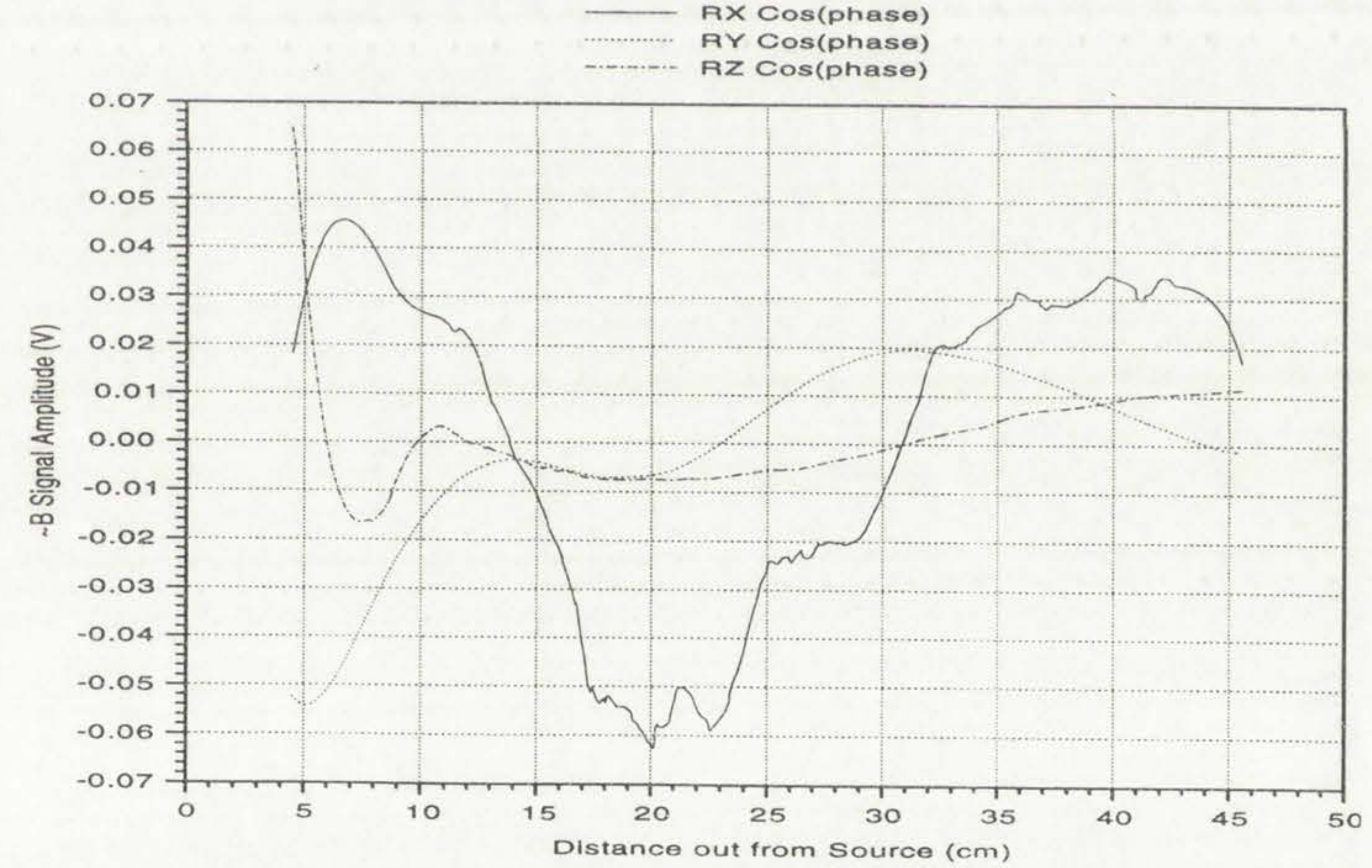

Wave structure at 8 mTorr exhibited more pronounced damping, as is shown in Figure 5-24. This damping is particularly evident in the perturbations in Z where

Figure 5-25. Measured Components of the Helicon Wave versus Z Position.
20 mTorr of Argon, 1250 W.

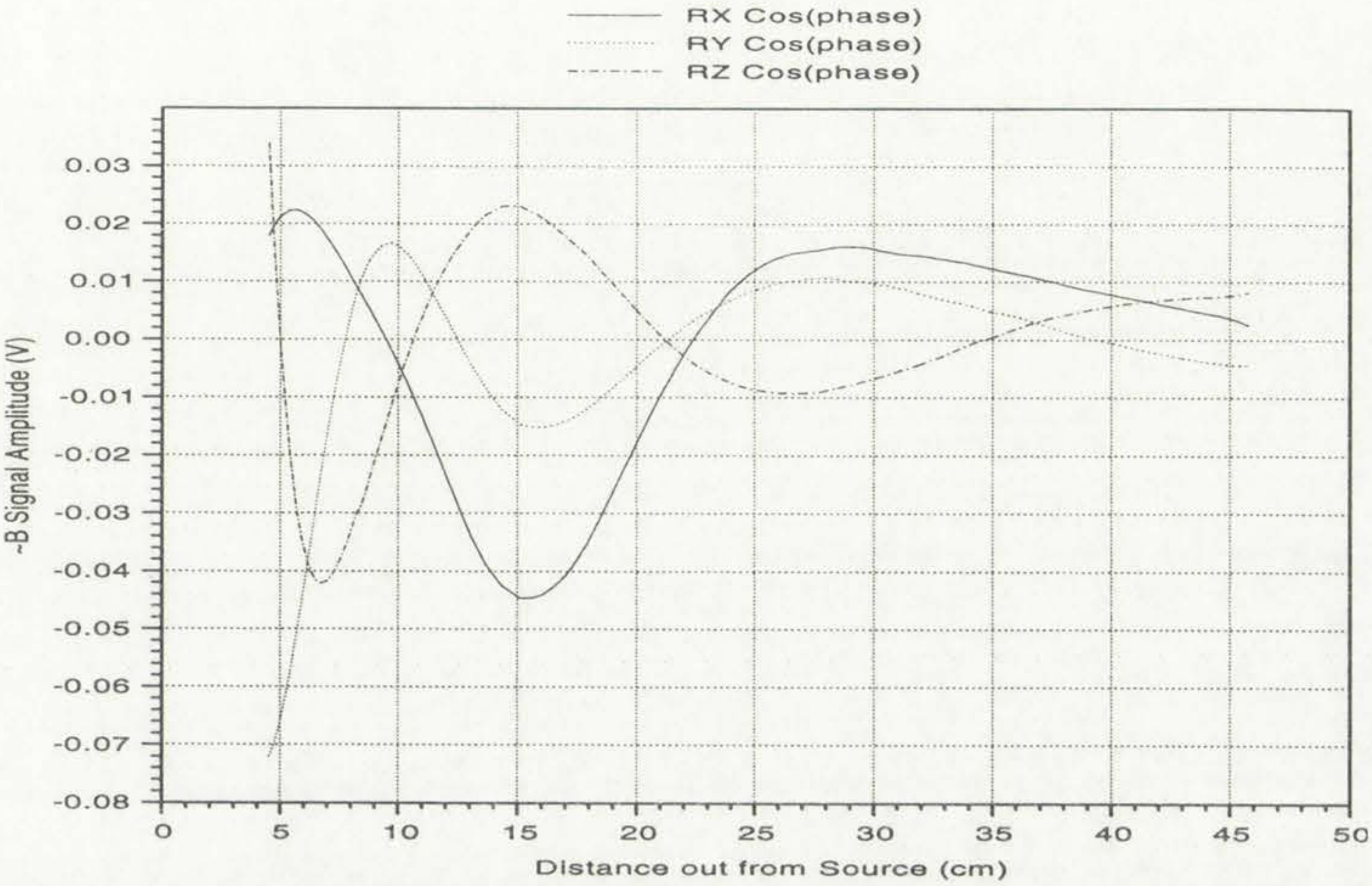

the amplitude falls to less than 10% of its original value 15 cm from the back wall (just 5 cm from the front edge of the antenna). Surprisingly, the 20 mTorr scan in Figure 5-25 did not continue this trend, but instead damped more gradually, in a manner similar to the 2 mTorr behavior. Both the RF compensated Langmuir and the 3-d B-dot probes performed as desired in characterizing the new tool in Argon.

The 3-D measurements of wave structure near the source show reasonable agreement with the theory presented in section 2.7 for conditions of relatively low gradient static field. Equation (21) predicts a wavelength in z of 11.8 cm for L=0.1 m (a wavelength of 0.1 m in y), S=0.1 m (a wavelength of 0.2 m in x), $n_0=1\times10^{18}$ m^{-3}, and $B_0=0.004$ T, conditions comparable to those in Figures 5-23, 5-24, and 5-25. Observation of non-constant phase between the perpendicular components of **B** is not inconsistant with the elliptically polarized waves shown to

be appropriate for finite rectangular geometry, where the phase difference depends on static field, density and boundary conditions. Further, if equation (18) is used with the measured magnetic field values in Figure 5-15, the structure shown in Figure 5-26 is predicted. The predicted structure looks remarkably similar to the measured wave structure as a function of z position shown in Figure 5-22. A reversal of rotation direction can even be found at z=30 cm.

Figure 5-26. Predicted 3-D Wave Structure in Rectangular Geometry

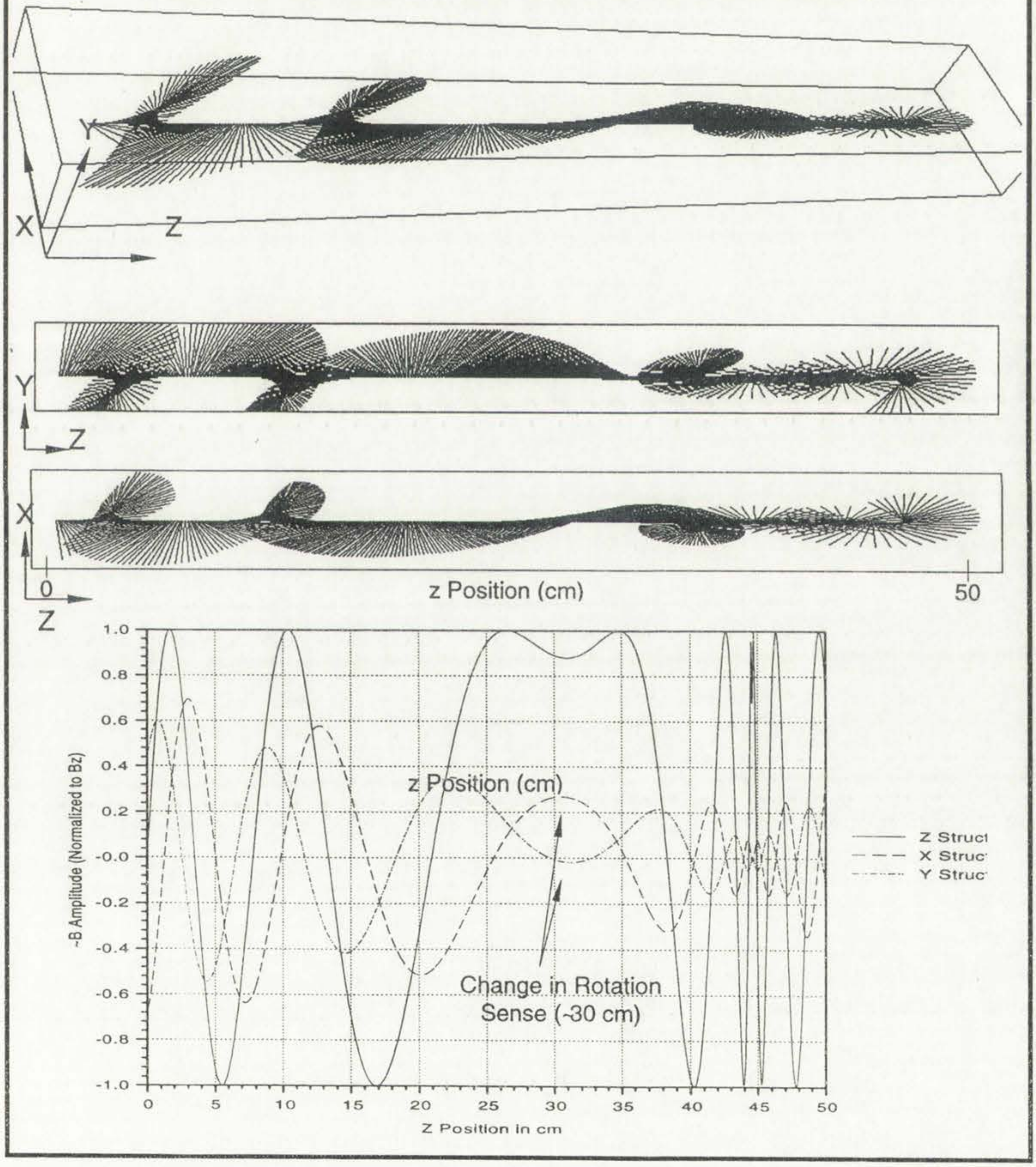

The probes were also used to look at discharges in CF_4, a gas more relevant for plasma manufacturing applications. Densities using CF_4 were markedly lower than in Argon, as was expected. At 1250 W forward power, and 5 mTorr, typical densities were of the order of 7.3×10^{10} cm^{-3} with bulk temperatures of 2-5 eV. Analyzing traces taken in CF_4 proved to be quite difficult. Whereas in Argon, the ion saturation region was reasonably well defined, with a slope much less than that of the electron gathering region, in CF_4, this was not the case. Ion saturation regions of the trace tended to have a steeper slope than in Argon. Since the technique used to evaluate densities is based on an extrapolation to the plasma potential of a fit to the ion saturation current, large errors can result from small changes in the slope. The presence of a significant slope on the ion side of the trace can also lead to inaccuracies in the measurement of electron energies. The 2 to 5 eV temperature given above is representative of some of the "best curves" which were able to be obtained. "Best curves" refers to I-V characteristics which appeared to have a well-defined exponential current region below the plasma potential, which allowed standard analysis to take place. The density value given above was obtained following the standard analysis on one of the better characteristics. Because systematic errors can be introduced in the analysis of I-V traces in electronegative gases, presented here are the unmodified saturation current measurements at several chamber positions for various pressures. It should be noted that using the ion saturation current to calculate density can result in large errors. Because the slope is significant in the ion saturation region, a factor of 2 change in calculated density can be obtained just by changing bias conditions by 10 V. Using the Bohm current approximation for electropositive plasmas to calculate density significantly overestimates the actual plasma density in this case. Therefore, this technique was not used for this analysis.

Figure 5-26 shows the variation in the ion saturation current as a function of distance out from the source for 5 and 20 mTorr of CF_4. Behavior is similar to that observed in previous experiments in the extended source; a very dense plasma is generated in the source, while much less diffuses into the chamber. Uniformity both in the Z direction and along the source (as shown in Figure 5-27) is good.

Figure 5-28 contains the corresponding B-dot probe scan for the 20 mTorr data in Figure 5-27. It is obvious that there is very little wave structure in the chamber, even though there seems to be sufficient field penetration within the source. The wave cannot propagate into the chamber because the density of CF_4 is not high enough to satisfy the dispersion relation, and there is no mechanism other than diffusion which can transfer energy from the source to the chamber plasma.

Figure 5-27. Ion Saturation Current vs Distance out from Source. CF4, 1250 W

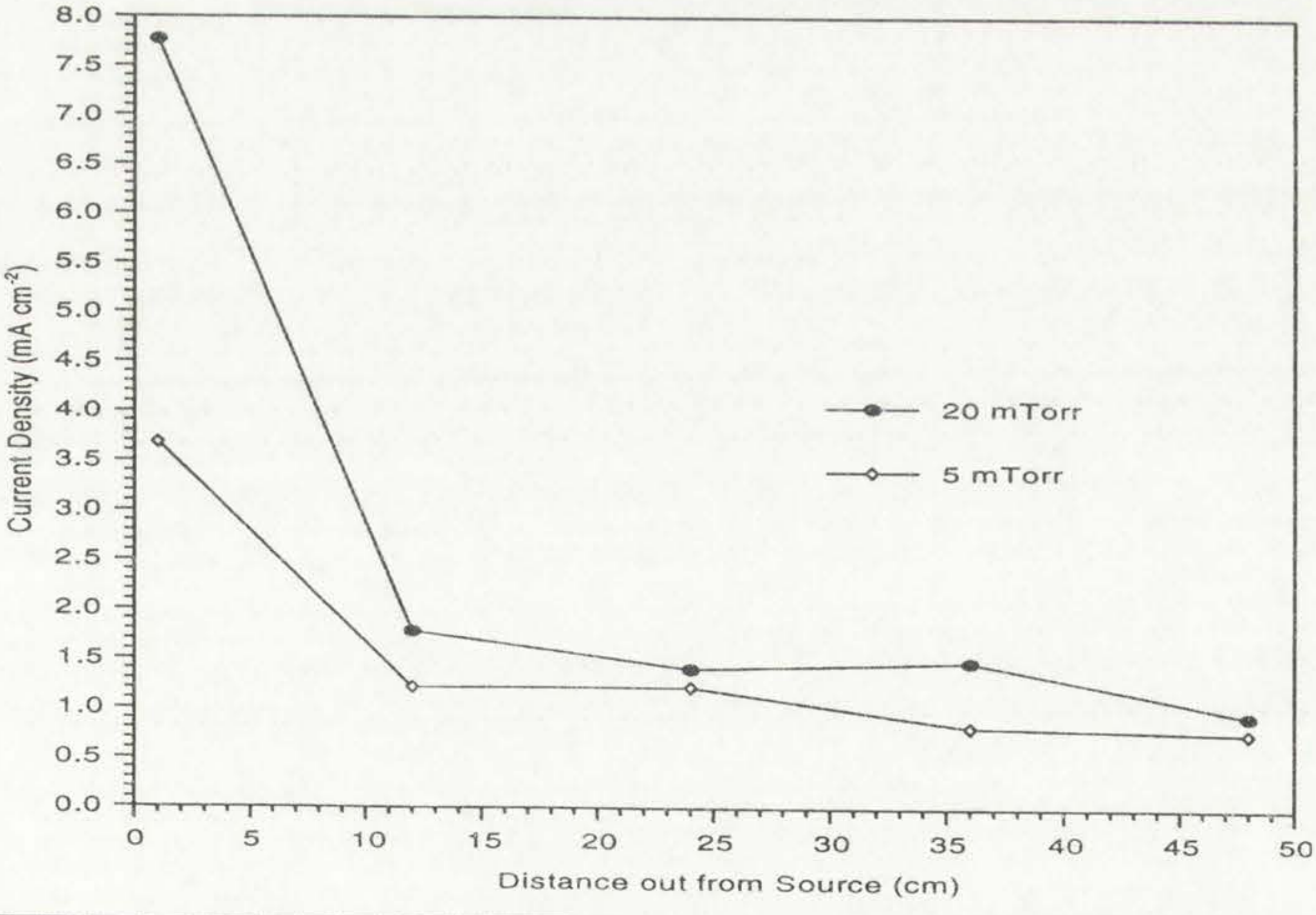

Figure 5-28. Ion Saturation Current vs Distance from Center of Antenna. CF4, 1250 W

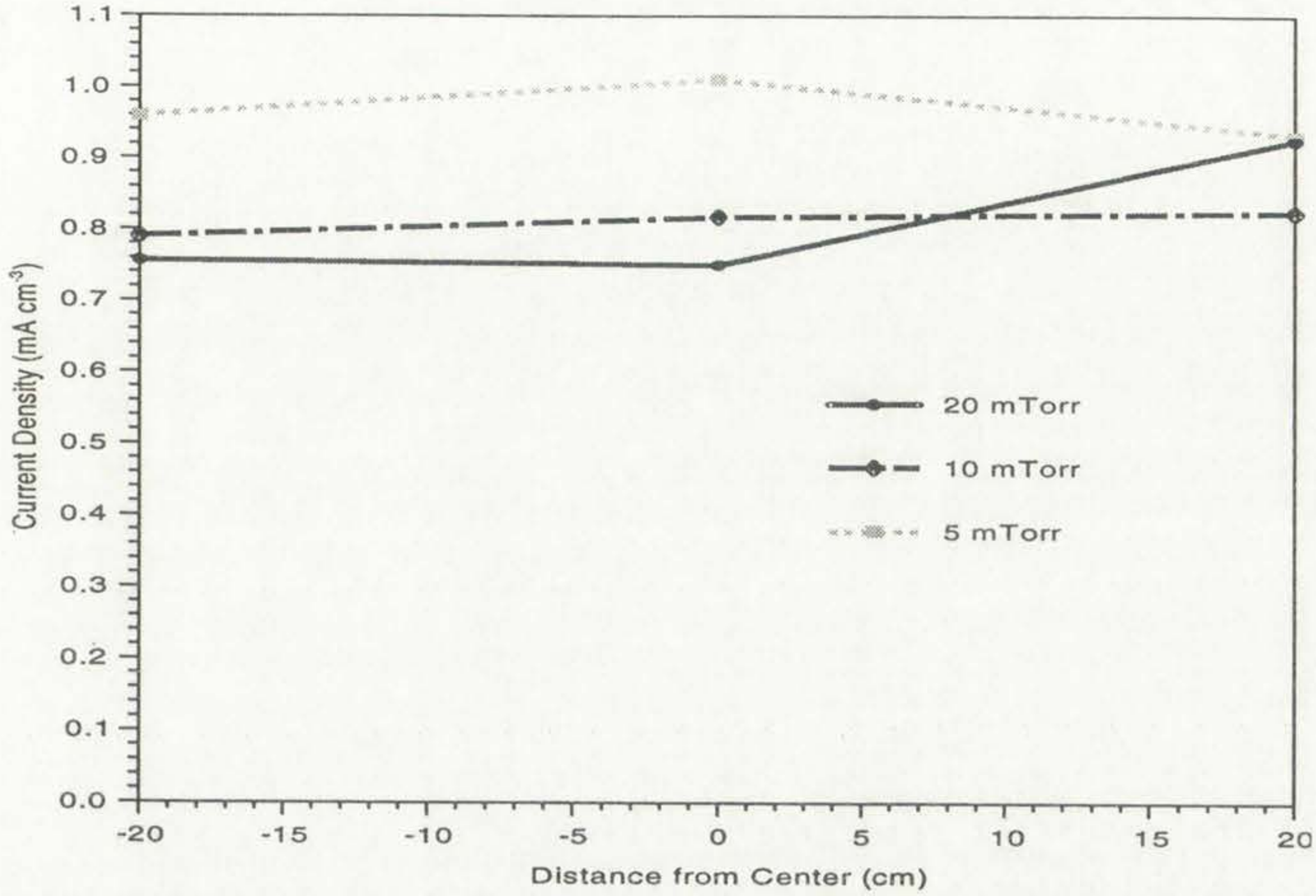

Figure 5-29. Wave Components vs Distance out from Source. 19 mTorr CF4, 1250 W.

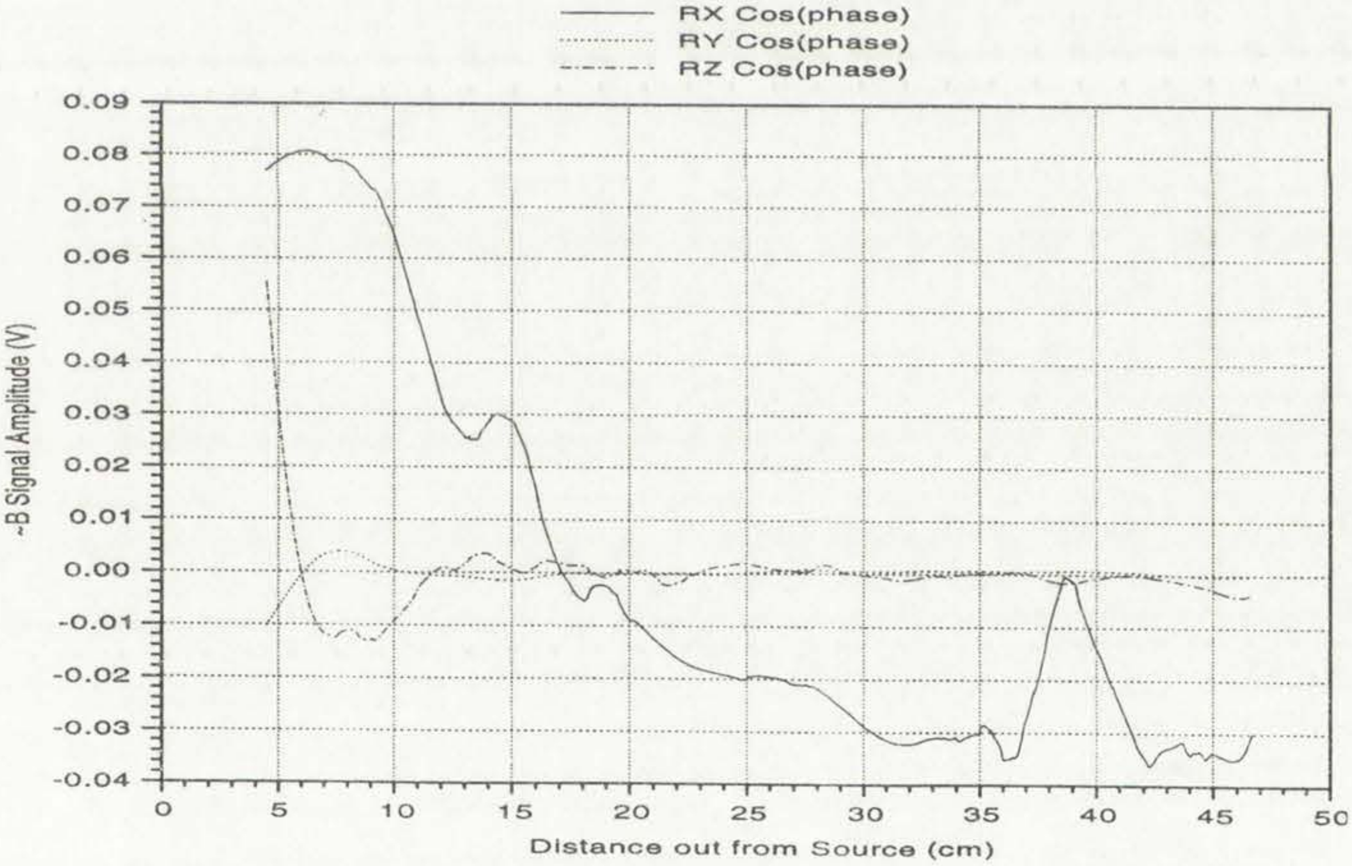

The experimental evidence to date suggests that the extended source helicon shows considerable promise as a large area processing tool. Large areas of

dense, uniform plasma, suitable for processing 30 x 20 cm substrates, have been produced in Argon in a variety of conditions. However, there are still some technical problems, such as efficient plasma production in CF_4, which must be overcome before this tool can be applied to industrial processes.

The extended linear source design has been shown to achieve greater than expected plasma densities (~4 x 10^{12} cm^{-3}) with ~14 % uniformity over 35 cm in 20 mTorr of Argon. Preliminary investigations with electronegative CF_4 gases demonstrate that the tool is capable of producing sufficient densities at a substrate surface (2.5 x $10^{11}cm^{-3}$) to be relevant for plasma processing of much larger dimension substrates. Present high density source designs cannot meet such criteria for large area processing. It has been shown that the serpentine antenna design is the most appropriate configuration (of those tested) for achieving this level of performance, and that two of the key performance control variables are the chamber static magnetic field shape and strength. A flexible set of field coils (a "chamber solenoid") has been designed which can be used to even further optimize reactor performance, or tailor performance to specific processing needs. The marked increase in plasma density with increased pressure suggests that the tool may also have a more flexible operational parameter space than current high density source tools, and that with further optimization, such a reactor may provide lower operating costs for plasma processing. In short, proof-of-principle for the extended source helicon design has been achieved. Further, a modest understanding of the source physics was attained in the process. Contained in Table 2 is a summary of the results obtained in the linear helicon source. A further discussion of the extended source accomplishments and shortcomings to date, as well as a discussion of possible improvements and further research topics is presented in the next chapter.

Table 2. Summary of Experiments and Theory.

Property	Theory	Experiment
Wavelength at 2 mTorr Argon, L=0.1 m, S=0.1 m , $n_0=1\times10^{18}$ m^{-3}, and $B_0=0.004$ T	11.8 cm	12.0 cm
EEDF	probably not Maxwellian	bi-Maxwellian
Wave Structure	elliptically polarized waves, non-constant phase between perpendicular components.	elliptically polarized waves, non-constant phase between perpendicular components.
Electron Tail Temperature	7-8 eV (phase velocity)	18 eV

6. CONCLUSIONS

The work contained in this dissertation focused on three principle areas: (1) constructing a helicon source and antenna that coupled power into a distributed source and diffusion region, (2) developing appropriate diagnostics to quantify source performance, and (3) comparing measured plasma parameters with the appropriate theory.

Powering the extended "C-section" source required the right choice of antenna. A small modified Boswell antenna was shown to exhibit a mode change with increasing power. Through an iterative experimental program, that small antenna led to the distributed serpentine antenna used in later experiments. Uniform power deposition, as evidenced by uniform density over the source length, was achieved with the serpentine antenna. Changes in aspect ratio had little effect on the ability of the source to produce plasma. The choice of back wall materials also had very little effect. Rather, the antenna shape played the most important role. Only when the antenna coupled into fundamental modes of the source, in a magnetic field geometry favorable for helicon wave propagation, was a dense plasma achieved. The presence of helicon waves as measured by B-dot probes was associated with higher and more uniform plasma densities.

A set of tools for evaluating source performance was constructed. Considerable effort was placed on building Langmuir probes with RF compensation, and developing a robust system for analyzing data from those probes. EEDF's were obtained that showed the presence of a small warm population of electrons existing with a large, cool bulk distribution. Changes were made to existing nonlinear curve fitting techniques to facilitate stable data analysis, and a

bi-Maxwellian treatment described the observed distributions very well. Construction of a B-dot probe allowed direct observation of the wave structure in the chamber.

Modeling of a cylindrical ring source with the linear tool revealed some fundamental problems with powering a helicon source in cusped field geometry. If wave propagation is the primary means of energy transport from the source to the rest of the chamber, then the 4.8 G ECR cutoff for 13.56 MHz waves found in any cusp geometry prevents energy transport past that point. It can be argued that having an ECR point in the machine would ensure full absorption of the energy of the waves. While this is true, the Larmor radius of a 3 eV electron in a 4.8 G field is 1.2 cm. Electrons heated by ECR absorption would be lost to the walls after only a few collisions. Therefore, a cusped field geometry is undesirable for wave propagation. Uniform density was achieved along the source length in X, and in the vertical direction Y. Unfortunately, density as a function of Z always decreased.

The use of a parallel field geometry with the linear tool greatly improved the plasma density throughout the chamber. Waves were readily launched along field lines. Two different sized sources were built. The smaller source produced higher densities, but both were able to excite dense, uniform plasmas in argon. Flat density profiles were obtained along the source in X, and out from the source in Z.

Some rather surprising results were found when the dispersion relation for waves traveling parallel to B_0 was derived. The unexpected result was that the wave

structure in rectangular geometry is not strictly circularly polarized. Instead, the wave numbers are different in the X and Y directions. The vector perpendicular to $\mathbf{B}_0$ described by $(\mathbf{B}_x + \mathbf{B}_y)$ rotates first one way, and then the other, depending on the starting phase difference between the X and Y components. Measurements with the 3-D B-dot probe verified the predicted changes in rotation sense. Measurements of λ_z compared well with those predicted by theory for similar conditions.

Application of the source to CF_4 plasmas was not as successful as with argon. Dense plasmas were generated in the source, but there was very little diffusion into the chamber region. For the densities inferred from saturation currents to the Langmuir probes, it was clear that the dispersion relation for helicon waves was not satisfied. The helicon wave could not propagate out of the source because the density was so low in the chamber. Therefore, the only energy transport to the plasma outside the source had to occur by diffusion, which resulted in the dramatic drop in density with distance away from the source.

The first problem which needs to be addressed in any future experiments is how to better couple power into CF_4, or another electronegative gas. Source performance in argon is acceptable because densities in the machine rise to a point where the dispersion relation is satisfied, and waves propagate. The density in CF_4 never gets that high, so any perturbations induced by the antenna are contained within the source. Three possible solutions are the use of higher power, use of a powered chuck, or the use of two independent sources in a parallel field. Each of these solutions forces more power into the CF_4 plasma in order to raise the plasma density. If the density could be raised sufficiently, then helicon

waves could contribute to the energy flow into the chamber.

The plasma and floating potentials drop substantially when moving from the source to the chamber, which is indicative of a second problem in the linear tool. The plasma has a poor ground reference in the source. Non-uniformities in the plasma potential could cause damage or non-uniformity problems in a manufacturing system. One possible way to address this problem is to introduce a biased chuck into the chamber. The large surface of a chuck or wafer would help define V_p over a large region of the plasma, and help to smooth out any variations observed.

The performance goals for this prototype tool were all met or exceeded. Densities in excess of 1×10^{12} cm^{-3} were readily obtainable in argon, and generation of plasma over the 40 cm source length was demonstrated. Plasmas were generated over pressures ranging from 0.5 mTorr up to 146 mTorr, with varying degrees of uniformity. The source showed most uniform operation between 2 and 30 mTorr.

More important than the performance goals, though, was the proof of concept. The intent of this work was to use what was known about existing helicon sources to learn how to build a new source. The new source would not only be able to process large area substrates, but would also be scalable. Applying the new source to a new size would largely consist of building an appropriate processing chamber. The physics of a 100 cm^2 processing tool would largely be the same as a machine designed to process 5000 cm^2. That source has been built. Further, the successful prototype was evaluated within a strong experimental atoms, could contribute to the energy [illegible]

The plasma and floating potentials [illegible] the substrate [illegible] source to the chamber, which is [illegible] The plasma has a poor ground reference in the [illegible] plasma potential could cause damage [illegible] ating system. One possible way to [illegible] biased chuck into the chamber. The large [illegible] help define V_s over a large region of the [illegible] variations observed.

The performance goals for the [illegible] ties in excess of 1 x 10^{11} cm^{-3} were [illegible] plasma over the 45 cm source length [illegible] ated over pressures ranging from 0.[illegible] degrees of uniformity. The source [illegible] and 30 mTorr.

More important than the performance goals, [illegible] The intent of this work was to use [illegible] sources to learn how to build a new source. [illegible] able to produce large area uniform [illegible] new source to a new site would [illegible] cessing chamber. The physics [illegible] same as a machine design [illegible] Further, the successful [illegible] and theoretical framework, and has demonstrated an ability to generate large area plasmas.

APPENDIX I

Custom Source Code for Langmuir and B-dot Probe Analysis

Contained on the supplied disk is the source code and OS/2 executable for the custom analysis software developed for this project. The code supplied is written in C, and makes extensive use of the OS/2 presentation manager interface to provide an intuitive user interface. Immediate graphical and statistical feedback is shown on the screen for any fitting operation. Other tools include integration, differentiation (polynomial interpolation and dy/dx methods), FFT and Inverse FFT, and smoothing (via FFT window, spline fitting, or polynomial interpolation). Support is included for Langmuir probe analysis using single- and dual-temperature Maxwellians, and a second derivative routine is provided to allow determination of arbitrary EEDF. The B-dot probe section allows conversion of raw probe signal data to wave structure information.

The code contains a flexible parser, which can read most ASCII data files without modification. A small section of a sample data file is included here for reference.

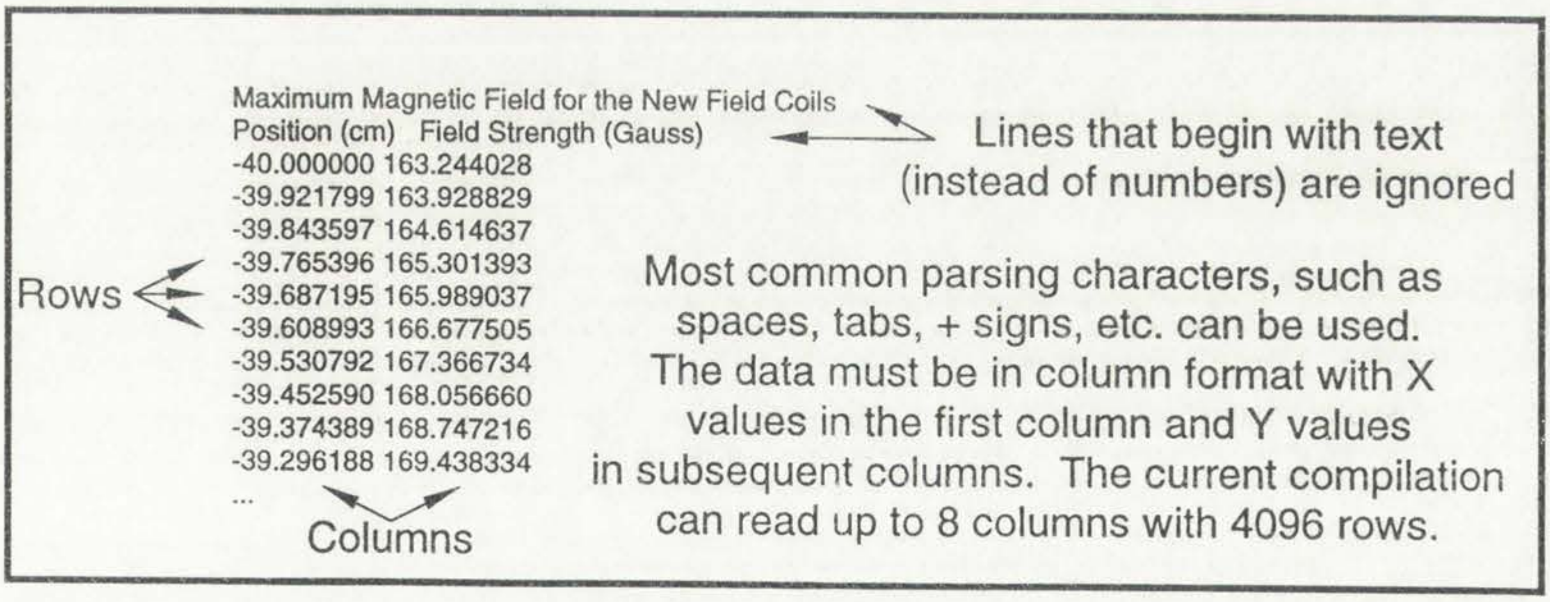

```
Maximum Magnetic Field for the New Field Coils
Position (cm)   Field Strength (Gauss)
-40.000000 163.244028
-39.921799 163.928829
-39.843597 164.614637
-39.765396 165.301393
-39.687195 165.989037
-39.608993 166.677505
-39.530792 167.366734
-39.452590 168.056660
-39.374389 168.747216
-39.296188 169.438334
...
```

Lines that begin with text
(instead of numbers) are ignored

Most common parsing characters, such as
spaces, tabs, + signs, etc. can be used.
The data must be in column format with X
values in the first column and Y values
in subsequent columns. The current compilation
can read up to 8 columns with 4096 rows.

APPENDIX I

Custom Source Code for Langmuir and B-dot Probe Analysis

Contained on the supplied disk is the source code and OS/2 executable for the custom analysis software developed for this project. The code supplied is written in C and makes extensive use of the OS/2 presentation manager interface to provide an intuitive user interface. Immediate graphical and statistical feedback is shown on the screen for any fitting operation. Other tools include integration, differentiation (polynomial interpolation and dy/dx methods), FFT and inverse FFT, and smoothing (via FFT window, spline fitting, or polynomial interpolation). Support is included for Langmuir probe analysis using single- and dual-temperature Maxwellians, and a second derivative routine is provided to allow determination of arbitrary EEDF. The B-dot probe section allows conversion of raw probe signal data to wave structure information.

The code contains a flexible parser, which can read most ASCII data files without modification. A small section of a sample data file is included here for reference.

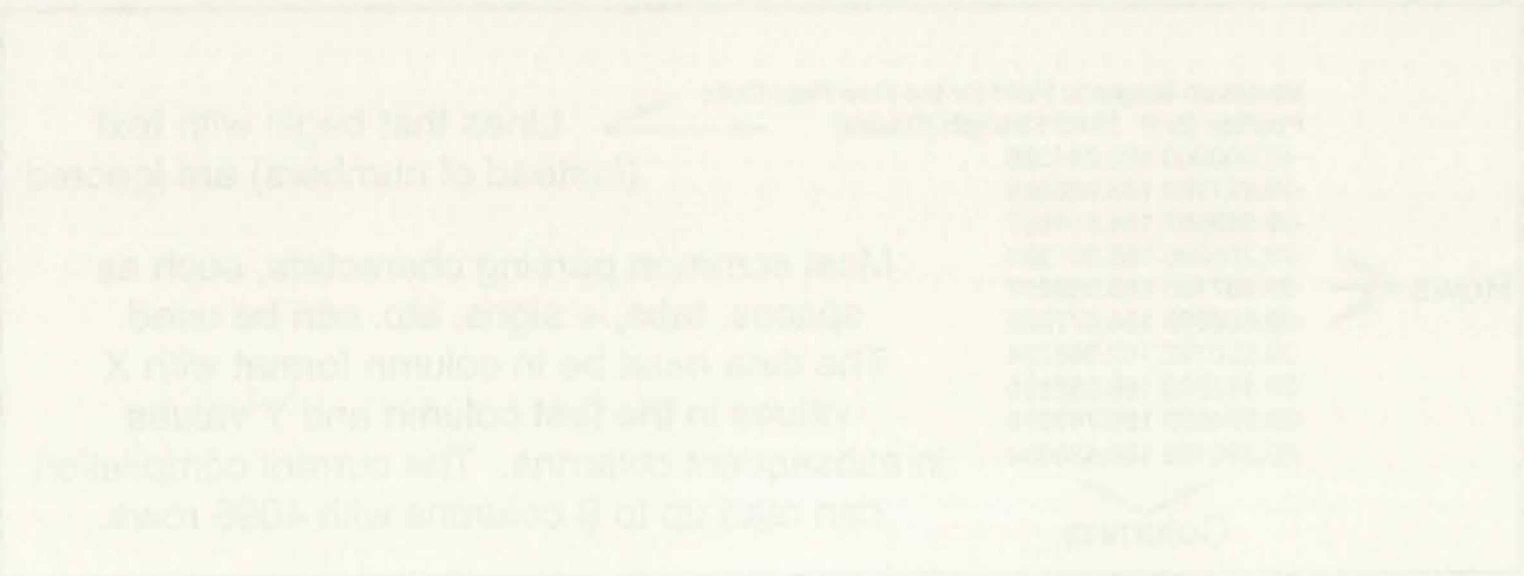

The enclosed source code is copyright Rusty Jewett, 1995, but is freely distributable. If further copies are needed please contact Dr. Harold Anderson at the University of New Mexico, Department of Chemical and Nuclear Engineering. Albuquerque, New Mexico. 87131.

APPENDIX II

Photographs of the Linear Helicon Plasma Processing Tool

The linear tool was constructed on a rather generic pumping platform which could accommodate a variety of chamber configurations. Although rather peripheral to the focus of this project, the construction of the tool may be of interest to other experimentalists, so a practical description is included here. Much in the way of verbal description can be replaced by these five photographs.

Figure A-1 shows the tool fully assembled. The main rectangular processing chamber rests on top of a welded steel frame, which encloses the majority of the equipment necessary to provide vacuum and diagnostic access. The chamber is pumped through a slit-type flange which also supports an Osaka Vacuum Magnetically Levitated Turbo-molecular Pump. Cooling for the magnets is provided by the Neslab refrigeration unit in the left bottom of the frame, and RF power is supplied by the 2.5 KW Solid State ENI supply.

Figure A-2 is a view of the top of the chamber which highlights the static magnetic field coils, which were described in the text. The flange in the top of the chamber allows future access for 20 x 40 cm substrates. A side view of the chamber is contained in Figure A-3, which again highlights the shape of the static magnetic field coils.

Figures A-4 and A-5 show the chamber source with the RF shielding in place, and removed (respectively). In A-5, the serpentine antenna is clearly visible as it sits on the top and bottom source glass pieces. Note that the power distribution feeds (which are attached to the antenna leads) are located close to the

grounded rear conductor of the chamber. This arrangement helps to lower the self-inductance of the power feed such that the antenna provides the dominant inductance for the circuit. Transformation of the plasma-antenna load to the 50 ohm load required for the RF generator is performed by the Comdel Pi network contained in the box attached to the bottom of the source case.

Figure A-1

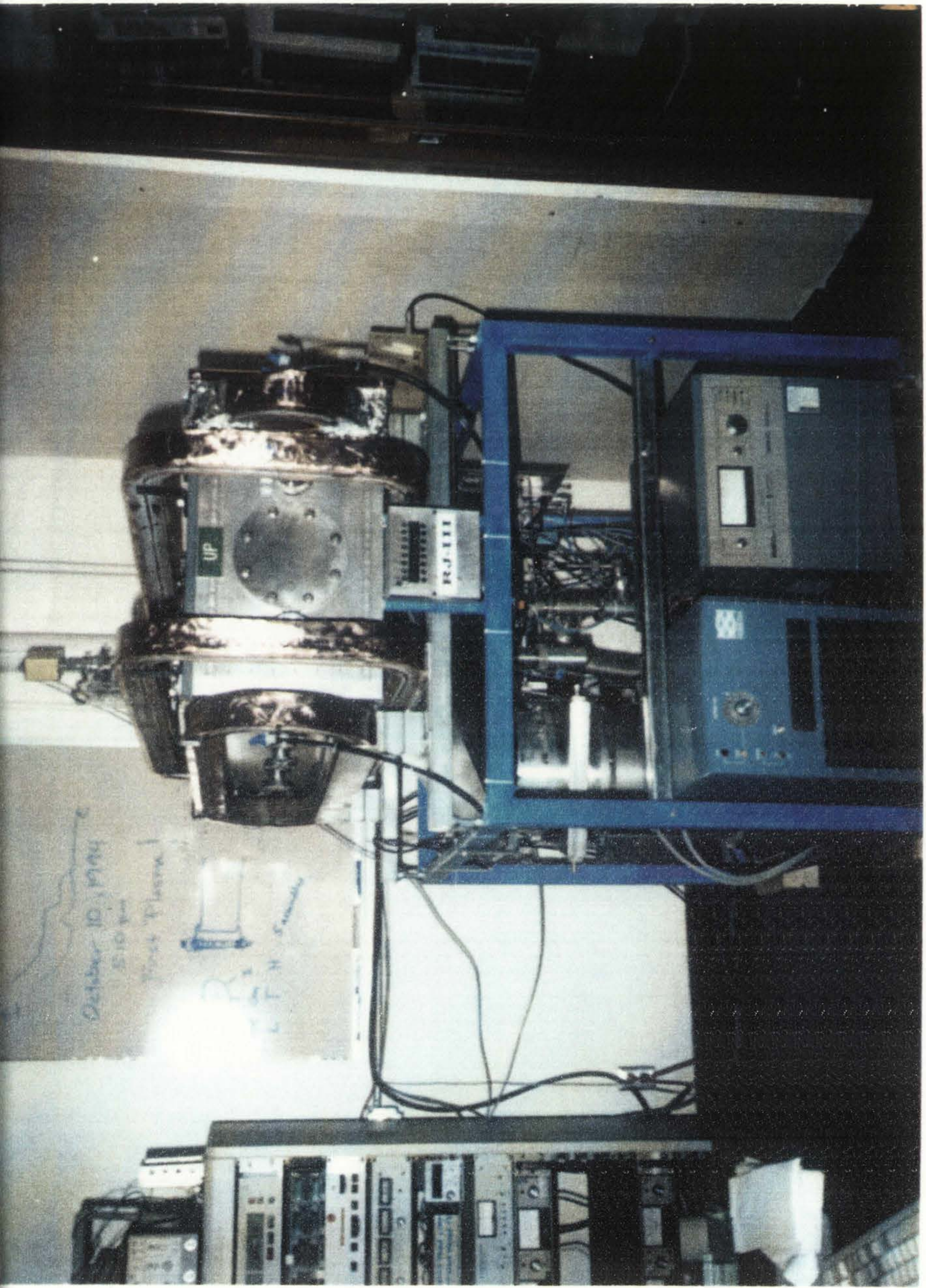

Figure A-2

Figure A-3

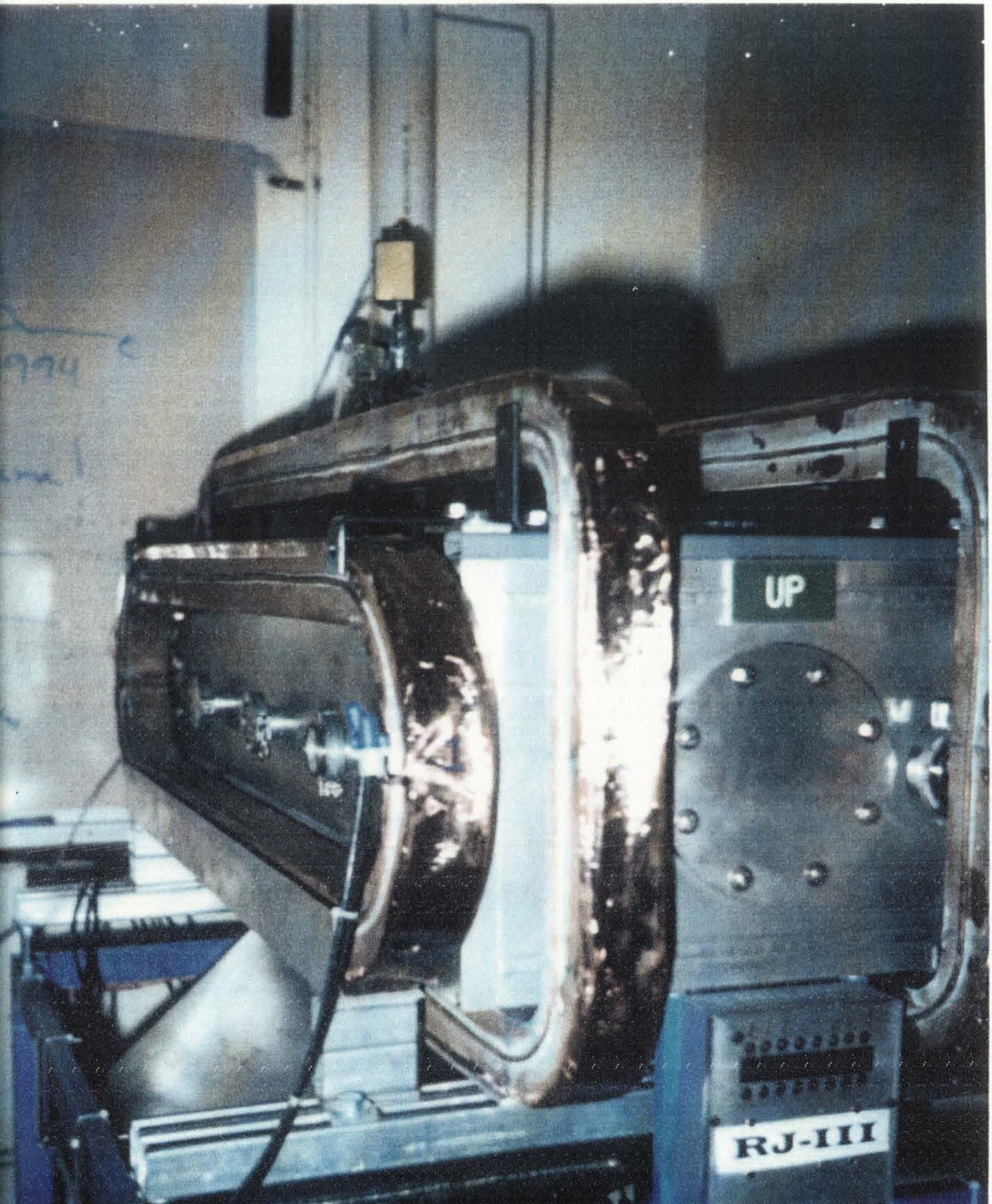

Figure A-4

Figure A-5

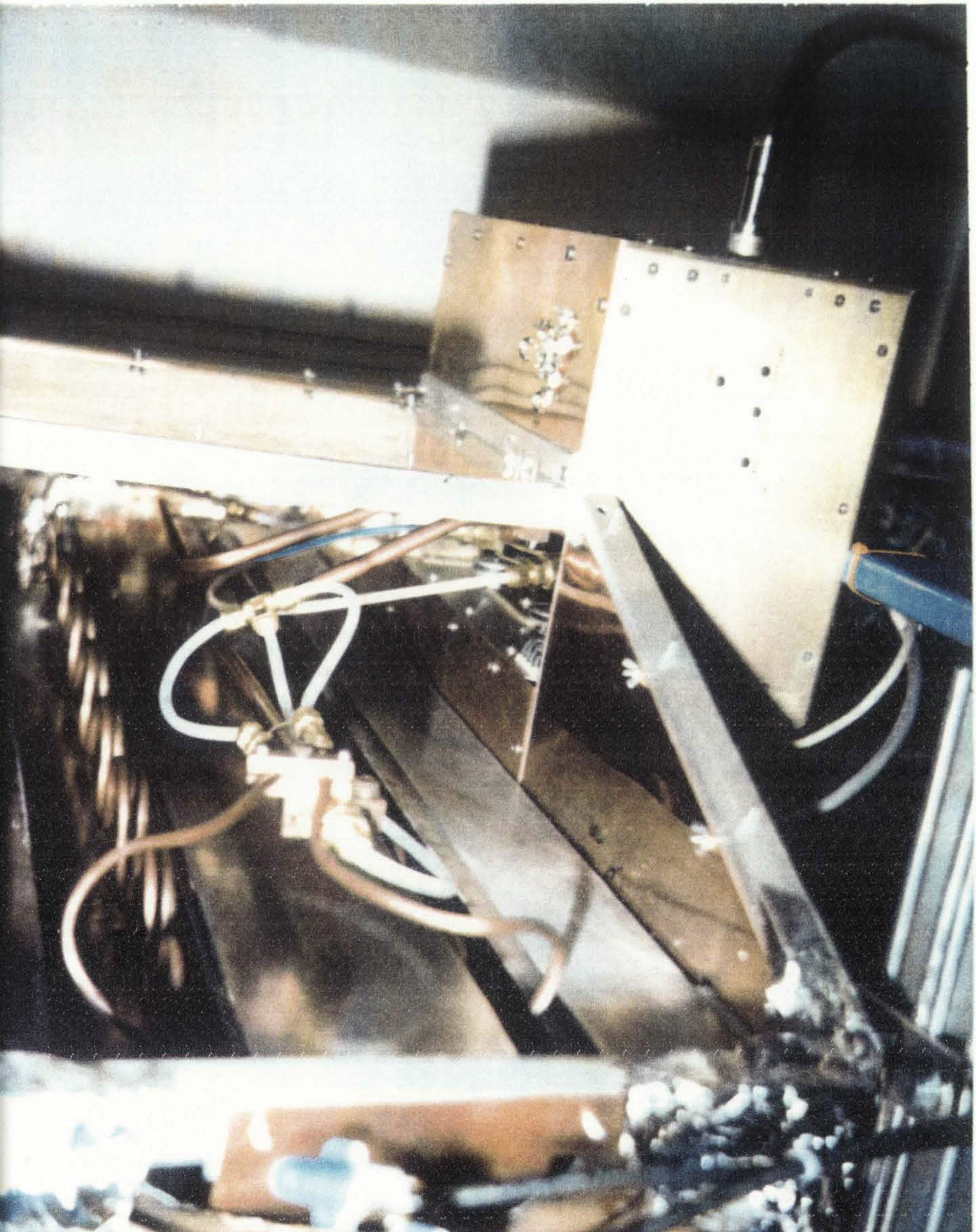

REFERENCES

1 Semiconductor Technology Workshop Working Group Reports. Semiconductor Industry Association. (1993).

2 M. A. Lieberman and R. K. Gottscho, Physics of Thin Films: Advances in Research and Development, (Academic Press, San Diego, 17, 1993).

3 R. W. Boswell and R. K. Porteous, Appl. Phys. Lett. **50**, 17, 1130, (1987).

4 A. J. Perry, D. Vender, and R. W. Boswell, J. Vac. Sci. Technol. B. **9**, 2, 310, (1991).

5 F. F. Chen, Plasma Phys. Controlled Fusion **33**, 4, 339, (1991).

6 B. Davies, J. Plasma Physics, **4**, 1, 43, (1970).

7 R. W. Boswell, Phys. Lett., **33A**, 457, (1970).

8 J. D. Jackson, Classical Electrodynamics, (John Wiley and Sons, 1975), p. 295.

9 D. G. Swanson, Plasma Waves, (Academic Press, Inc., 1989), p. 58.

10 F. F. Chen, J. Vac. Sci. Technol. A, **10**, 4, 1389, (1992).

11 P. Zhu and R. W. Boswell, Phys. Fluids B, **3**, 4, 869, (1991).

12 F. F. Chen. Introduction to Plasma Physics and Controlled Fusion. 2nd ed., (Plenum Press, New York, 1990).

13 G. Dilecce, M. Capitelli, and S. De Benedictis, J. Appl. Phys., **69**, 1, 121, (1991).

14 R. Piejak, Private Communication.

15 T. E. Sheriden, M. J. Goecker, J. Goree, J. Vac. Sci. Technol. A, **9**, 3, 688, (1991).

16 P. A. Miller, G. A. Hebner, K. E. Greenburg, P. D. Pochan, and B. P. Aragon, Preprint, Private Communication.

17 T. Intrator, S. Meassick, and J. Browning, Nuclear Fusion, **29**, 3, 377, (1989).

18 A. R. Ellingboe, Private Communication.

19 C. Charles, J. Vac. Sci. Technol. A, 11, 1, 157, (1993).

20 C. Charles, R. W. Boswell, and R. K. Porteous, J. Vac. Sci. Technol. A, 10, 2, 398, (1992).

21 A. J. Perry and R. W. Boswell, Appl. Phys. Lett., **55**, 2, 148, (1989).

22 R. W. Boswell and D. Henry, Appl. Phys. Lett., **47**, 10, 1095, (1985).

23 R. Jewett, A.J. Perry, R.W. Boswell, and H.M. Anderson, paper JB-1, 47th GEC, Bull. Am. Phys. Soc. 39(6) (1994).

24 T. Tsukada and H. Nogami, J. Appl. Phys., **74**, 9, 5402, (1993).

25 P. K. Loewenhardt, B. D. Blackwell, R. W. Boswell, G. D. Conway, and S. M. Hamberger, Phys. Rev. Let. **67**, 20, 2792, (1991).

26 R. W. Boswell, Private Communication

27 V. A. Godyak, Soviet Radio Frequency Discharge Research. (Delphic Association, Falls Church VA, 1986)

28 V. A. Godyak and A. S. Khanneh, IEEE Trans. Plasma Sci. **PS-14**, 112, (1986).

29 M. B. Hopkins and W. G. Graham, Rev. Sci. Instrum., **57**, 2210 (1986).

30 N. Hershkowitz, M. H. Cho, C. H. Nam, and T. Intrator, Plasma Chemistry and Plasma Processing, **8**, 35, (1988).

31 A. J. Perry. Private Communication

32 C. Cui, Doctoral Dissertation, Australian National U. (1993).

33 V. A. Godyak, R. B. Piejak, and B. M. Alexandrivich, Plasma Sources Sci. Technol. **1**, 36, (1992).

34 W. H. Press, Numerical Recipes in C, (Cambridge University Press, N.Y., 1992).

35 B. A. Nelson and R. K. Porteous, Lam Internal Progress Report (Unpublished).

36 F. F. Chen, Introduction to Plasma Physics and Controlled Fusion. 2nd Ed. (Plenum Press, 1984).

37 A. J. Perry, Private Communication.

38 W. H. Press, Numerical Recipes in Pascal, (Cambridge University Press, New York, 1989).

39 A.P Paranjpe, J. P. McVittie, and S. A. Self, J. Appl. Phys. **67**, 11, 6718 (1990).

40 B. Piejak, Private Communication.

41 P. A. Miller and G. A. Hebner, An inductively coupled plasma source for the GEC RF Reference Cell. To Be Published. (1995).

42 J. G. Laframboise, University of Totonto Institute for Aerospace Study Report, No 100.

43 M. W. Allen, B. M. Annaratone, and J. E. Allen, Proc. 9th Int. Conf. on Gas Discharges and their Applications (Venice) (Pavoda, Italy: Benetton Editore), 487, (1988).

23 [illegible] handbook, pages 10-17 (19[illegible]).

[illegible] Bull. Am. Phys. Soc. [illegible] (19[illegible]).

24 [illegible] and T. Nogami, J. Appl. Phys. 74, 9, 5462, (1993).

25 P. K. Loewenhardt, B. D. Blackwell, R. W. Boswell, G. D. Conway and S. M. Hamberger, Phys. Rev. Lett. 67, 20, 2792 (1991).

26 R. W. Boswell, Private Communication.

27 V. A. Godyak, Soviet Radio Frequency Discharge Research (Delphic Associates, Falls Church VA, 1986).

28 V. A. Godyak and A. S. Khanneh, IEEE Trans. Plasma Sci. PS-14, 112, (1986).

29 M. B. Hopkins and W. G. Graham, Rev. Sci. Instrum., 57, 2210 (1986).

30 N. Hershkowitz, M. H. Cho, C. H. Nam, and T. Intrator, Plasma Chemistry and Plasma Processing, 8, 35 (1988).

31 A. J. Perry, Private Communication.

32 C. Cui, Doctoral Dissertation, Australian National U. (1992).

33 V. A. Godyak, R. B. Piejak and B. M. Alexandrovich, Plasma Sources Sci. Technol. 1, 36 (1992).

34 W. H. Press, Numerical Recipes in C, Cambridge University Press, N.Y. [illegible]

35 [illegible] and S. K. [illegible], Lam Internal Progress Report (Unpublished).

36 F. F. Chen, Introduction to Plasma Physics and Controlled Fusion, 2nd Ed. (Plenum Press, 1984).

37 A. J. Perry, Private Communication.

38 W. H. Press, Numerical Recipes in Pascal, Cambridge University Press, New York, 1989.

39 A. P. Paranjpe, J. P. McVittie and S. A. Self, J. Appl. Phys. 67, 11, 6718 (1990).

40 R. [illegible], Private Communication.

41 P. A. Miller and G. A. Hebner, An electrostatically coupled plasma source for the GEC RF Reference Cell, To be Published (1993).

42 [illegible], University of Toronto Institute for Aerospace Studies Report No. 100.

43 M. W. [illegible] and [illegible] on the [illegible] of Gas Lasers and their Applications [illegible]

44 E. R. Mosburg. Rev. Sci. Instrum., **52**, 1182, (1981).

45 E. F. Jaeger, L. A. Berry, and D. B. Batchelor, J. Appl. Phys., **69**, 10, 6918, (1991).

46 J. F. Waymouth. Phys. Fluids, **9**, 801, (1966).

47 J. D. Swift and M. J. R. Schwar, Electrical Probes for Plasma Diagnostics (New York: American Elsevier), (1969).

48 A. J. Perry, Private Communication.

49 V. A. Godyak, Soviet Radio Frequency Discharge Research, (Falls Church, VA; Delphic Associates), (1986).

50 V. A. Godyak, Plasma-Surface Interaction and Processing of Materials Nato Advanced Study Institutes, Ser. E, (Dordrecht: Kluwer Academic), **176**, 95, (1990).

51 V. A. Dovzhenko, A. P. Ershov, and G. S. Solntsev, Sov. Phys.-Tech. Phys., **19**, 851, (1974).

fr